Multi-fluid Dynamics for Supersonic Jet-and-Crossflows and Liquid Plug Rupture

by

Ezeldin A. Hassan

A dissertation submitted in partial fulfillment
of the requirements for the degree of
Doctor of Philosophy
(Aerospace Engineering)
in the University of Michigan
2012

Doctoral Committee:

Professor Wei Shyy, Co-Chair
Professor Ken Powell, Co-Chair
Professor James F. Driscoll
Professor Hong G. Im
Douglas L. Davis, Air Force Research Laboratory

To my wife and my family

Acknowledgment

I would like to thank my advisor Prof. Wei Shyy for his unwavering support and advice both academically and personally. He has always made his students a priority and set an example that is very hard to follow. I consider myself lucky to have received such valuable well-rounded mentoring that served to shape the essence of the person I am today. I would also like to thank my co-chair Prof Ken Powell and my committee Prof. James Driscoll, Prof. Hong Im and Dr. Doug Davis for their help with my dissertation.

I would like to thank Dr Doug Davis also for being my mentor at AFRL propulsion directorate and for his insight and inspirational research support. I would like to thank Dr. John Boles at AFRL for continuous help and research collaboration regarding supersonic jet and crossflow interaction. I would like to thank all the research scientists who have helped me through my internships at AFRL; Dr. Mark Hagenmaier, Dr. Daniel Risha, Dr. Dean Eklund, and others. I would like to thank Dr. Tom Jackson and the propulsion directorate as a whole for accepting to serve as my sponsoring facility and showing interest in my research and future collaboration with AFRL. I would like to also thank HPCMO-DSRC for computer time.

I would like to thank my research collaborators specifically Dr. Hikaru Aono for his assistance, sincere advice, and collaboration with supersonic jet and crossflow interaction research and other issues, Dr. Emre Sozer for invaluable discussion and insight regarding CFD code development and numerical methods, and Dr. Jaeheon Sim for assisting in multiphase flow research. I would like to thank Dr Eray Uzgoren, Dr. James Grotberg and Dr. Hideki Fujioka for their collaboration on the plug flow problem.

I would like to thank Dr. Ed Luke, Dr. Jeff Wright and Dr. ST Thakur for their support with Loci-Chem. They have helped me with many questions regarding code structure and development.

I would like to thank my group members, office mates in FXB2211, and students in the other side of the FXB for the continuous friendship and support. Especially, I

would like to thank Dr. Chang-kwon Kang for his help in dissertation formatting issues, Dr. Amit Gupta, Dr. Pat Trizila, and Dr. Chien-Chou Tseng, Dr. Young-Chang Cho, Wenbo Du, Chih-Kuang Kuan, and Dr. Hicham Alkandry.

I would like to thank the SMART program for funding and supporting my research and for linking me with AFRL. I would like to thank SMART staff specifically; Alexis Becker and Danielle Rinderknecht for their help and support with the lengthy SMART paperwork. I would like to thank Brian Padilla my security officer for helping me with numerous security issues.

I would like to thank the staff in the aerospace department not only for their work, but also for creating a friendly environment in the FXB building, in particular Cynthia Enoch, Dave McLean, Denise Phelps, Michelle Shepherd, Sue Smith, and Lisa Szuma.

Finally, I would like to thank my family and friends. I would like to thank my wife, my parents, and my brothers and sister for their endless support and love. Furthermore, I would like to thank all those that I have not named.

Table of Contents

Dedication ii
Acknowledgment iii
List of Figures viii
List of Tables xiii
List of Symbols xiv
List of Abbreviation xviii
Abstract xix
Chapter 1. Background and Motivation 1
1.1 Introduction and Scope 3
1.2 Motivation 5
1.3 The SCRAMJET Engine 7
1.3.1 SCRAMJET Engine Components 8
1.3.2 SCRAMJET Advantages and Challenges 10
1.4 Mixing and Structure of Supersonic Jet and Crossflow 12
1.5 Experimental Studies of Supersonic Jet and Crossflow 15
1.6 Scaling Efforts for Supersonic Jet and Crossflow 19
1.7 Computational Approaches for Jet and Crossflow 20
1.8 Mixing of Liquid Jets 29
1.9 Plug Flow and Rupture Problem 30
1.10 Multiphase Flow Methods 35
1.11 Objectives and Proposed Models 36
1.11.1 Jet and Crossflow Interaction 36
1.11.2 Plug Propagation and Rupture 39
Chapter 2. Governing Equations and Numerical Methods 40
2.1 Governing Equations 40
2.1.1 Instantanous Balance Equations 40
2.1.2 Equation of State 41
2.1.3 Averaged and Filtered Navier-Stokes Equations 42
2.1.4 Turbulence Closure 44
2.2 Turbulence Modeling 45
2.2.1 RANS: Menter-SST 47

2.2.2 LES: Smagorinsky Lilly Model 51
2.2.3 Hybrid RANS/LES: NC State Model 52
2.2.4 Detached Eddy Simulation (DES) 54
2.2.5 Filter Based Approach 56
2.3 Current Modeling Approach 58
2.3.1 Multi-scale Turbulent Treatment 59
2.3.2 Adaptive Turbulent Schmidt Number Extension 67
2.4 Numerical Methodology 70
2.4.1 Base CFD Code 70
2.4.2 Implementation of Current Model 72
Chapter 3. Multi-scale Turbulence Modeling for Supersonic Jet and Crossflow 77
3.1 Experimental Setup 77
3.2 Computational Parameters 79
3.3 Nozzle Simulation 82
3.4 Sonic Injection Cases 83
3.4.1 Baseline Case: 90^o, q=0.5 [Cases 1-8] 85
3.4.2 Non-Baseline [Cases 9-14] 104
3.5 Assessment of Multi-scale Model Performance 112
3.6 Summary 115
Chapter 4. Adaptive Turbulent Schmidt Number in Turbulence Modeling 117
4.1 Implications of The Adaptive Approach 117
4.2 Baseline Case: 90^o,q=0.5 [Cases 15-19] 120
4.2.1 Adaptive **Sct** multi-scale and comparison to constant **Sct** multi-scale and RANS results 121
4.2.2 Effect of Numerical Viscosity on Turbulent Diffusivity 124
4.2.3 Adaptive Turbulent Schmidt Number Effect on Solution and Mixing 129
4.3 Inclined Case : 30^o, q=0.5 132
4.4 Summary 138
Chapter 5. Propagation and Rupture of Incompressible Liquid Plug in a Tube 139
5.1 Model Description 140
5.2 Computational Procedure 141
5.2.1 Surface Tension Treatment 143
5.2.2 Interface Reconstruction Scheme 144
5.2.3 Local Refinement of Eulerian Grid 148

5.2.4 Adaptive Time Stepping 149
5.3 Results and Discussion 150
5.3.1 Pre-Rupture Dynamics 150
5.3.2 Rupture Dynamics 155
5.3.3 Effects of Pressure Drop and Laplace number 163
5.4 Summary 167
Chapter 6. Concluding Remarks 170
6.1 Summary and Conclusions 170
6.2 Future Work 176
6.2.1 Jet and Crossflow Interaction 176
6.2.2 Plug Propagation and Rupture 178
Bibliography 179

List of Figures

Figure 1-1 Specific Impulses for Several Engine Cycles[56] 8

Figure 1-2 Diagram of a SCRAMJET engine, highlighting major components[57] 9

Figure 1-3 Model of transverse underexpanded jet in a supersonic crossflow (a)Full 3D schematic from Portz and Segal[60] (b) cross section schematic near injector from Gruber et al [8] 13

Figure 1-4 Indented Barrel shock with recirculation regions in normal sonic air injection into Mach 4 crossflow from Viti et al [17] 14

Figure 1-5 Temporally-resolved shadowgraphs of Mach 1.6, q=1.7 Air/Air jet and crossflow by VanLerberghe et al[50] 17

Figure 1-6 Penetration heights compared to the experiment for 3 turbulent models from Tam et al[19] 23

Figure 1-7 Experimental, RANS and Hybrid RANS/LES concentration comparison from Boles et al[27] 26

Figure 1-8 Live-dead staining of human pulmonary epithelial cells after 10(a),50(b), and 100(c) plug propagation events from Tavana et al [99] 31

Figure 1-9 Interface representation by marker points (a) line segments in 2D (b) triangular elements in 3D (c) indicator function used to smear properties across the interface with values varying from 0 to 1[48] 35

Figure 2-1 NC State blending function and velocity boundary-layer in wall coordinates 53

Figure 2-2 Filter functions for FBM, multi-scale models and proposed filter 63

Figure 2-3 Cell-neighbor notation in an unstructured grid 71

Figure 2-4 Flow chart of the solution procedure using the multi-scale model 74

Figure 2-5 Flow chart of the solution procedure using multi-scale model with the adaptive approach 76

Figure 3-1 Injector shape and placement for (a) normal injection and (b) inclined injection 78

Figure 3-2 Pressure probe data at x/D=5, y/D=0.25 and z/D=0.25 for 30 degree injection. Flow is considered statistically converged and iterations are used to collect average 81

Figure 3-3 Computational domain and boundary conditions for jet and crossflow interaction and nozzle simulations 82

Figure 3-4 Nozzle simulation(right): outflow boundary-layer axial velocity and turbulence kinetic energy, grid distribution for outflow boundary(left)..... 83

Figure 3-5 Grid distribution and boundary conditions for normal injection (top). Center plane cut: coarse, intermediate and fine grids in order 85

Figure 3-6 Pressure iso-surface (bow shock), midline average ethylene mole fraction (midline plane), and selected streamlines showing spilled vortex (baseline case, intermediate grid)..... 86

Figure 3-7 Snapshot of Mach number on the midline plane showing the barrel shock. White line outlines the jet profile at ethylene mole fraction of 0.05 (baseline, intermediate grid)..... 87

Figure 3-8 Average ethylene mole fraction results for RANS with different turbulent Schmidt numbers comparison with experiment. (baseline case)..... 89

Figure 3-9 Sample NOPLIF images for the baseline case for x/D=5 (top) and x/D=25 (bottom)..... 90

Figure 3-10 mean and variance of fuel concentration for RANS, multi-scale and experimental NO PLIF images(baseline case)..... 90

Figure 3-11 Instantaneous snapshots of ethylene mole fraction contours for coarse, intermediate, and fine grids(baseline case)..... 91

Figure 3-12 Instantaneous snapshots of eddy viscosity contours for coarse, intermediate, and fine grids(baseline case)..... 92

Figure 3-13 Average ethylene mole fraction results for grid refinement study(baseline case) 94

Figure 3-14 Centers for fuel penetration((a) height, (b)widths) for experiment, RANS, and multi-scale models (baseline case)..... 95

Figure 3-15 Pressure on the center plane. Comparison between RANS and multi-scale computation(baseline case)..... 96

Figure 3-16 Axial velocity on center plane. Comparison between RANS and multi-scale(baseline case)..... 97

Figure 3-17 Contours of P/P_∞ on bottom wall. RANS and multi-scale predictions compared to PSP (baseline case) 98

Figure 3-18 P/P_∞ on the surface at z/D=0(baseline case) 98

Figure 3-19 Turbulence kinetic energy (K_{Res}, bottom) and ratio of unresolved turbulence kinetic energy to total turbulence kinetic energy (K_{Ratio}, top) (baseline case).... 101

Figure 3-20 Instantaneous y vorticity snapshots on the center plane for multi-scale (intermediate grid on top and coarse grid on the bottom) and MILES (coarse) approaches. Maximum and minimum limited to 100, -100..... 102

Figure 3-21 Mass and momentum eddy viscosities based on resolved field at the center plane (baseline case) 103

Figure 3-22 Mass and momentum eddy viscosities as well as effective turbulent Schmidt

number based on resolved field for *x*/*D*= 5 intermediate grid (baseline case).... 105

Figure 3-23 Baseline ethylene mole fractions comparison, intermediate grid (baseline case) 106

Figure 3-24 Grid distribution and boundary conditions for inclined injection (top). Center plane cut: RANS and multi-scale grids in order(bottom) 107

Figure 3-25 Average ethylene mole fractions comparison, RANS and multi-scale (90^o, q=1.5) 108

Figure 3-26 Average ethylene mole fractions comparison, RANS and multi-scale (30^o, q=1.0) 109

Figure 3-27 Average mole fraction predictions for RANS and multi-scale compared to experimental Raman scattering at 3 different axial locations. (30^o,q=0.5)..... 110

Figure 3-28 Centers for fuel penetration((a) height, (b)widths) for experiment, RANS, and multi-scale models (30^o,q=0.5) 111

Figure 3-29 Vorticity in the y plane (out of the paper) for different injection configurations on the center plane Maximum and minimum limited to 100, -100 113

Figure 4-1 Adaptive turbulent Schmidt number contours for grid 1(top) and 2 (bottom) at different x/D locations (baseline case) 122

Figure 4-2 Fuel mole fraction contours at x/D= 5 for experimental and different numerical approaches. In multi-scale simulations grid 1 results are on top and grid 2 on the bottom 123

Figure 4-3 Fuel mole fraction contours at x/D= 25 for experimental and different numerical approaches. In multi-scale simulations grid 1 results are on top and grid 2 on the bottom 124

Figure 4-4 (repeated from 3-16) Instantaneous y vorticity snapshots on the center plane for multi-scale (grid 2 on top and grid 1 on the bottom) and MILES (grid1) approaches. Maximum and minimum limited to 100, -100..... 126

Figure 4-5 Instantaneous fuel mole fraction snapshots on the center plane for multi-scale (grid 2 on top and grid 1 on the bottom) and MILES (grid1) approaches (baseline case) 127

Figure 4-6 Fuel mole fraction predictions for the multi-scale adaptive Sct approach with numerical viscosity correction. Experimental measurements on the top, grid 1 in the middle and grid 2 on the bottom 128

Figure 4-7 Average bow shock pressure iso-surface and fuel streamlines for case 6. Average fuel mole fractions iso-surfaces for cases 5, 18, and 6..... 130

Figure 4-8 Average fuel mole fractions at center plane for cases 5, 18, and 6..... 131

Figure 4-9 Center plane pressure contours for cases 6 and 18. Injector is located at x/D= 0..... 131

Figure 4-10 Center plane axial velocity contours for cases 6 and 18. Injector is located at

x/D= 0 132

Figure 4-11 Mean intensity of PLIF images (2 separate images taken) compared to fuel mole fraction contours in grey scale of RANS ,multi-scale, and adaptive models(30^o,q=0.5). 133

Figure 4-12 Variance of intensity of PLIF images(2 separate images taken) compared to fuel mole fraction variance contours in grey scale of RANS , multi-scale, and adaptive models(30^o,q=0.5). 134

Figure 4-13 Fuel mole fraction predictions for multi-scale with/without the adaptive approach compared to experimental Raman scattering at 3 different axial locations(30^o,q=0.5). 136

Figure 4-14 Centers for fuel penetration((a) height, (b)widths) for experiment, RANS, and multi-scale with and without the adaptive approach (30^o,q=0.5)..... 137

Figure 4-15 Adaptive turbulent Schmidt number contours for at different x/D locations(30^o,q=0.5). 137

Figure 5-1 Computational setup and the boundary conditions, x axis attached to plug center before rupture and to the wall afterwards. Plug moves to the right 140

Figure 5-2 Identification of necking, a possible cause for topological change 145

Figure 5-3 Summary of the reconstruction algorithm in 2D and 3D 146

Figure 5-4 Reconstruction scheme. (a) Two interfaces come close so that the distance for red markers are less than critical length, (b) forming a single interface by updating the connectivity information 147

Figure 5-5 Geometry based grid refinement around the interface at various resolutions149

Figure 5-6 Plug length variation in time for various initial precursor film thickness values. Solid lines represent present study while dots represent study of [53]. (b) shows a more confined time domain to show details 151

Figure 5-7 Course of plug speed, defined as the capillary number, in time for various initial precursor film thickness values. Solid lines represent present study while dots represent study of [53]. (b) shows progressively zoomed in views of the plot in (a) 152

Figure 5-8 (a)Pressure and shear stress variation at the airway walls before plug rupture when Lp = 0.3, ΔP = 1, and λ = 1000. Solid lines represent present study while dots represent study of [53] (b) Pressure contours and velocity vectors near the wall corresponding to 156

Figure 5-9 Snapshots of pressure contours before and after rupture. h_2 = 0.06, ΔP = 1, and λ = 1000. 157

Figure 5-10 Pressure contours, velocity vectors and wall pressure and wall shear stress prior to rupture for h_2=0.06. View is zoomed at the location of minimum film thickness 158

Figure 5-11 Pressure contours, velocity vectors and wall pressure and wall shear stress

after rupture for h_2=0.06. View is zoomed at the location of minimum film thickness. 158

Figure 5-12 Snapshots of pressure contours before and after rupture. h_2 = 0.05,0.08, ΔP = 1, and λ = 1000. 160

Figure 5-13 Pressure and shear stresses at the airway walls before and after the rupture. h_2 = 0.06, ΔP = 1, and λ = 1000. 161

Figure 5-14 Variation of minimum and maximum wall shear stress in time. ΔP=1 and λ=1000 161

Figure 5-15 Maximum minimum difference in wall pressure(a) and wall shear stress(b) in time. ΔP=1 and λ=1000 162

Figure 5-16 Location of maximum wall shear stress and minimum wall pressure versus ruptured plug. ΔP=1 and λ=1000 162

Figure 5-17 Maximum variations in wall pressure(a) and shear stress(b) varying initial pressure drop. λ=1000 and h_2=0.05 165

Figure 5-18 Rupture time versus initial pressure drop (data connected using spline). λ=1000 and h_2=0.05 166

Figure 5-19 . Maximum wall pressure and shear stress variations versus initial pressure drop. λ=1000 and h_2=0.05 166

Figure 5-20 . Maximum variations in wall pressure (a) and shear stress(b) varying Laplace number. ΔP=1 and h_2=0.05 167

Figure 5-21 . (a) . Rupture time versus Laplace number. ΔP=1 and h_2=0.05 (b) . Maximum wall pressure variations versus Laplace number. ΔP=1 and h_2=0.05 167

List of Tables

Table 1-1 A comparison of several relevant parameters between subsonic and supersonic combustion based ramjets during Mach 12 flight[10, 12] 11
Table 1-2 Selective summary of experimental studies of jet and crossflow interaction . 16
Table 1-3 Selective summary of computational studies of jet and crossflow..... 21
Table 3-1 Experimental conditions for cases considered 78
Table 3-2 Loci-Chem Computational Parameters 80
Table 3-3 Sonic injection cases considered for multi-scale model testing 84
Table 4-1 Advantages and limitations of the adaptive approach..... 120
Table 4-2 Baseline injection cases considered for adaptive approach..... 121
Table 5-1 Summary of cases run for parametric study 164

List of Symbols

A	*A constant used in NC state hybrid model to shift transition point between RANS and LES*
A_f	*Area of cell face, f*
C_4	*Constant used in RANS modeling, FBM, and multi-scale modeling*
C_{DES}	*Constant used in DES modeling*
c_{P_m}	*Heat capacity for species m*
C_s	*Constant used in Smagorinsky sub-grid model*
C_μ	*Constant used in RANS modeling*
Ca	*Capillary number*
D, D_i	*Injector diameter*
D_k	*Laminar diffusion in the k direction*
d_w	*Distance to the nearest wall (used in DES)*
D_{DES}^k	*TKE destruction term used in DES modeling*
$D_{i_m}^R$	*Reynolds diffusion in i direction for species m*
D_{RANS}^k	*TKE destruction term used in RANS modeling*
e	*Specific internal energy*
f, f_d	*Generic filter function*
F_1	*First blending function in Menter SST*
F_2	*Second blending function in Menter SST*
$f_{d_{DES}}$	*Effective filter function used in DES*
$f_{d_{FBM}}$	*Filter function used in filter based model*
$f_{d_{MS}}$	*Multi-scale filter function of Nichols and Nelson*
$f_{d_{MS}}{}^*$	*Effective multi-scale filter function of Nichols and Nelson*
$f_{d_{proposed}}$	*Proposed filter function*

$\boldsymbol{F_s}$	*Surface tension force*
$G(x_i, \Delta)$	*A generic spatial filter used in LES*
H	*Total Enthalpy*
h	*Specific enthalpy*
h_1	*Liquid film thickness trailing liquid plug*
h_2	*Liquid film thickness in front of liquid plug*
k	*TKE, turbulence kinetic energy*
k_{res}	*Resolved TKE*
K_{res}	*Averaged resolved TKE*
K_{ratio}	*Averaged ratio of modeled TKE to total TKE*
l	*Length scale (used in scaling)*
$\tilde{l}$	*DES length scale*
L_G	*Grid length scale*
$l_{k-\omega}$	*DES length scale associated with Menter SST*
L_p	*Critical length for plug rupture*
L_T	*Turbulence length scale*
$L_{T_{NN}}$	*Turbulence length scale of Nichols and Nelson*
M	*Mach Number*
$\vec{n}, \boldsymbol{n}$	*Normal vector*
$\vec{n}_f$	*Normal vector to face ,f*
NS	*Total number of species*
P	*Absolute Pressure*
P_w	*Non dimensional wall pressure (in plug flow)*
Pr	*Prandtl number*
Pr_T	*Turbulent Prandtl number*
q	*Momentum ratio* $\frac{\rho_i u_i^2}{\rho_\infty u_\infty^2}$*, or heat flux*
R_m	*Gas constant for species* m
R^*	*Tube radius (in plug flow)*
r	*Non dimensional radial coordinate (in plug flow)*

R_{ij}	*Fluctuation correlation defined as* $-\overline{\rho u_i'' u_j''}$
Re	*Reynolds number*
$S, \lvert S \rvert$	*Magnitude of strain Rate,* $\lvert S_{ij} \rvert$
s	*Mass fraction of fuel in fuel stream*
S_{ij}	*Strain rate tensor*
Sc_T	*Turbulent Schmidt number*
$Sc_{T\,Res}$	*Resolved turbulent Schmidt number*
T	*Absolute temperature*
t	*Time coordinate (non-dimensional in plug flow)*
$t_{rupture}$	*Time of rupture (in plug flow)*
u	*Velocity scale or axial velocity component*
$u_i, \boldsymbol{u}$	*Velocity vector*
V_m	*Diffusion velocity for species* m
$\boldsymbol{X}$	*Position within Dirac delta function*
X_m	*Mole fraction for species* m
$\boldsymbol{x}, x_i$	*Position vector*
y	*Coordinate aligned with penetration height*
Y_m	*Mass fraction for species* m
Z	*Mixture fraction*
z	*z coordinate*
z_p	*Non dimensional z location of the plug center (in plug flow)*
β^*	*A constant associated with DES and RANS modeling usually =0.09*
γ	*Anisotropy factor, specific heat ratio*
Γ	*Blending function used in NC state hybrid model*
δ	*Boundary layer thickness or Dirac delta function*
δ_{ij}	*Kronecker delta function; 1 if* $i = j$ *, 0 otherwise*
Δ	*Measure of cell size*
ΔP	*Non dimensional pressure drop across plug (in plug flow)*
ϵ	*Turbulence dissipation rate*
θ	*Injection angle*

$\boldsymbol{\kappa}$	*Curvature (used in calculation of surface tension force)*
λ	*Taylor micro-scale or Laplace number (in plug flow)*
μ	*Viscosity coefficient*
μ_t	*Eddy viscosity*
$\mu_{t_{SGS}}$	*Sub-grid model eddy viscosity*
μ_{num}	*Numerical viscosity*
ν	*Kinematic viscosity coefficient*
ν_t	*Kinematic eddy viscosity*
$\nu_{t_{RANS}}$	*RANS model kinematic eddy viscosity*
$\nu_{t_{mass}}$	*Mass kinematic eddy viscosity*
$\nu_{t_{mom}}$	*Momentum kinematic eddy viscosity*
ρ	*Fluid density*
σ	*Surface tension*
τ_{ij}	*Shear stress tensor*
τ_w	*Wall shear stress*
ϕ	*Any arbitrary variable or primitive variable*
ψ_{c_0}	*A limiter function applied within cell* $,c_0$
Ω	*Absolute vorticity*
ω	*Specific dissipation per turbulence kinetic energy*
$\dot{\omega}$	*Chemical source terms*
$(\ \ )^*$	*Dimensional variables (in chapter 5)*
$(\ \ )', (\ \ )''$	*Fluctuation quantity* $\Phi' = \Phi - \bar{\Phi}$*,* Φ *is a truly instantaneous*
$(\ \ )^R$	*Resolved quantity* $\Phi^R = \Phi - \bar{\Phi}$*,* Φ *is the solution at one iteration*
$\overline{(\ \ )}$	*Time averaged quantity*
$\widetilde{(\ \ )}$	*Filtered quantity*
$\widetilde{(\ \ )}$	*Favre averaged quantity*
$(\ \ )_l$	*A property of a liquid*
$(\ \ )_\infty$	*Property associated with freestream conditions*

List of Abbreviation

AFRL:	Air Force Research Lab
CFD:	Computational Fluid Dynamics
DES:	Detached Eddy Simulation
DNS:	Direct Numerical Simulation
FBM:	Filter Based Model
LES:	Large Eddy Simulation
NC State:	North Carolina State University
NO-PLIF:	Nitrogen Oxide Planar Laser Induced Fluorescence
PSP:	Pressure-Sensitive Paint
RANS:	Reynolds Averaged Navier-Stokes
SMART:	Science, Mathematics and Research for Transformation
SST:	Shear Stress Transport
TKE:	Turbulence Kinetic Energy
UM:	University of Michigan

Abstract

Multi-fluid dynamics simulations require appropriate numerical treatments based on the main flow characteristics, such as flow speed, turbulence, thermodynamic state, and time and length scales. In this thesis, two distinct problems are investigated: supersonic jet and crossflow interactions; and liquid plug propagation and rupture in an airway.

Gaseous non-reactive ethylene jet and air crossflow simulation represents essential physics for fuel injection in SCRAMJET engines. The regime is highly unsteady, involving shocks, turbulent mixing, and large-scale vortical structures. An eddy-viscosity-based multi-scale turbulence model is proposed to resolve turbulent structures consistent with grid resolution and turbulence length scales. Predictions of the time-averaged fuel concentration from the multi-scale model are improved over Reynolds-averaged Navier-Stokes models originally derived from stationary flow. The response to the multi-scale model alone is, however, limited, in cases where the vortical structures are small and scattered thus requiring prohibitively expensive grids in order to resolve the flow field accurately. Statistical information related to turbulent fluctuations is utilized to estimate an effective turbulent Schmidt number, which is shown to be highly varying in space. Accordingly, an adaptive turbulent Schmidt number approach is proposed, by allowing the resolved field to adaptively influence the value of turbulent Schmidt number in the multi-scale turbulence model. The proposed model estimates a

time-averaged turbulent Schmidt number adapted to the computed flow field, instead of the constant value common to the eddy-viscosity-based Navier-Stokes models. This approach is assessed using a grid-refinement study for the normal injection case, and tested with 30 degree injection, showing improved results over the constant turbulent Schmidt model both in mean and variance of fuel concentration predictions.

For the incompressible liquid plug propagation and rupture study, numerical simulations are conducted using an Eulerian-Lagrangian approach with a continuous-interface method. A reconstruction scheme is developed to allow topological changes during plug rupture by altering the connectivity information of the interface mesh. Rupture time is shown to be delayed as the initial precursor film thickness increases. During the plug rupture process, a sudden increase of mechanical stresses on the tube wall is recorded, which can cause tissue damage.

.

Chapter 1.
Background and Motivation

The dynamics of multi-fluid interactions can vary greatly depending on the flow regime, the amount of turbulence and the thermodynamic state of the fluids involved. In the subsonic regime, jet and crossflow interactions have been studied by many researchers [1-5] for different applications, including gas turbine combustor [6] and ground effect of a V/STOL aircraft[7], among others. For these studies, the large and fine scales of the flow structures between the two streams, along with their interplay with the ground surface and jet exit characteristics, are of substantial interest. In this study, we expand the scope to focus on the supersonic flow regime.

In highly turbulent supersonic regimes, turbulent eddies carry fluid packets that are further broken down for efficient mixing [8-10]. Shock wave discontinuities and their interaction with the boundary layer [11] and recirculation zones create distinct regions of different mixing qualities[11, 12] The dynamics of such processes require sophisticated experimental measurements at high temporal and spatial resolution to capture fluctuations in velocity[13], pressure[14, 15] and mass fraction[16] . These experiments are costly and limited to specific regions where the measurements are taken. CFD simulations, on the other hand, can provide detailed information about the flow[17, 18] including discontinuities and complex 3D structures. RANS methods are the standard of the industry and have shown some success in multi-fluid simulations [19-21]. They are limited because they do not explicitly resolve turbulent features in the flow and are

usually overly dissipative[22-24]. LES is a good alternative in solving fluid-fluid interaction providing much more detailed information about the turbulent features[25, 26]; however, in high-speed flows, it becomes prohibitively expensive near walls[24, 27, 28]. Hybrid RANS/LES methods where, RANS is used near the wall and LES is used elsewhere, currently offer the best compromise and have shown great success in simulations of multi-fluid in high-speed flows [27, 29-31]. Within hybrid RANS/LES methods, it is desirable to model the flow economically with the flexibility of unstructured non-uniform grids and complex geometries to allow the simulation and design of practical design problems.

When two or more phases are involved in the interaction, an interface is present and should be tracked or modeled accordingly[32]. The interface can be tracked indirectly using an Eulerian method [33-37], where the interface is located using a scalar function on a stationary grid. This method is computationally economical and can easily handle topology changes; however, challenges for this method include ambiguous interface geometry and difficulty in imposing boundary conditions[38]. Lagrangian methods[39, 40] force the grid to conform with the boundary, thus interface geometry is uniquely defined and boundary conditions are clearly imposed. Lagrangian methods, however, require tedious pre-processing of the grid, and possible re-gridding due to movement of the interface. Radical changes in interface shape may produce meshes with bad grid quality that cannot yield an adequate solution[41, 42]. Eulerian-Lagrangian methods [43-46] utilize a separate grid representing the interface on a stationary grid. The interface grid can move freely based on the solution obtained on the stationary grid. Eulerian-Lagrangian methods allow for accurate representation of the interface without

re-gridding. Topological changes are allowed to occur with the interface grid deforming based on specific reconstruction criteria[46, 47]. Adaptive meshing maybe used on the background grid near the interface to increase interpolation accuracy of the coupling between the background grid and the interface. These methods have shown success in simulation of many multiphase problems, including plug flow and rupture[47], fuel tank draining[48] and instability under oscillating thrust[49]

1.1 Introduction and Scope

In this thesis, two distinct problems are investigated: supersonic jet and crossflow interactions; and liquid plug propagation and rupture in an airway. The jet and crossflow interaction is involves highly complex unsteady turbulent flow that requires special modeling beyond the standard RANS models. Experimental studies[16, 50, 51] show large degree of segregation between the jet and crossflow which results in large variances in fuel concentrations. The mean fuel concentrations are , therefore, not representative of the actual mixing and may appear to be overly mixed beyong single instantanous snapshots. Additionaly, RANS models showed limitations in correct prediction of mean profiles. LES is currently impractical for use near the wall in supersonic flows due to prohibitively expensive grid needed near the wall[28]. This gave rise to hybrid RANS/LES methods that use a combination of RANS and LES to resolve turbulent structures with managable grid reslutions[27, 52].

In the literature the hybrid RANS/LES methods usually lack generality because they are limited to strict grid size and structures. They also , sometimes involve the use of adjustable case-dependant constants and are restricted to simple geometry[27, 52]. It is

the purpose of this work to develop the multi-scale model as class of hybrid RANS/LES models to be used in high-speed flows and mixing problems. The multi-scale model is easy to implement for any two-equation model by defining a grid length scale, a turbulent length scale, and a filter function. The eddy viscosity is smoothly varied based on the ratio of the turbulent length scale to the cell size. Therefore there is no sharp transition between RANS and LES and no restriction on where the transition should occur for reasonably varying cell size. This allows the use of any grid resolution with the finer grids simply capable of resolving more turbulent eddies. Because of the smooth nature of the model, we are able to use non-uniform grid and expect smooth solutions at the refinement interface. In the supersonic jet and crossflow interaction problem this will be especially useful when using three-dimensional (3D) grids that are only fine in the plume region and in regions where complex flow phenomena occur.

The response to the multi-scale model alone is, however, limited, in cases where the vortical structures are small and scattered thus requiring expensive grids in order to resolve the flow field accurately. Statistical information related to turbulent fluctuations are collected from multi-scale simulations to estimate an effective turbulent Schmidt number, which is shown to be highly varying in space. Accordingly, an adaptive turbulent Schmidt number approach is proposed, by allowing the resolved field to adaptively influence the value of turbulent Schmidt number in the multi-scale turbulence model. The proposed model estimates a time-averaged turbulent Schmidt number adapted to the computed flowfield, instead of the constant value common to the eddy-viscosity-based Navier-Stokes models. Ther model will be analyzed and improved based on its application in jet and crossflow interaction simulations.

The second problem, is the incompressible liquid plug propagation and rupture, which has applications in flow of mucus in respitory patients. A numerical simulation of a liquid plug in an infinite tube is conducted using an Eulerian-Lagrangian approach and the continuous interface method. A reconstruction scheme is developed to allow topological changes during plug rupture by altering the connectivity information of the interface mesh. Results prior to the rupture are in reasonable agreement with the study of Fujioka et al[53] in which a Lagrangian method is used. For unity non dimensional pressure drop and a Laplace number of 1000 , rupture time is shown to be delayed as the initial precursor film thickness increases and rupture is not expected for thicknesses larger than 0.10 of tube radius. During the plug rupture process, a sudden increase of mechanical stresses on the tube wall is recorded, which can cause tissue damage. The peak values of those stresses increase as the initial precursor film thickness is reduced. After rupture, the peaks in mechanical stresses decrease in magnitude as the plug vanishes and the flow approaches a fully developed behavior. Increasing initial pressure drop is shown to linearly increase maximum variations in wall pressure and shear stress. Decreasing the pressure drop and increasing the Laplace number appear to delay rupture because it takes longer for a fluid with large inertial forces to respond to the small pressure drop.

1.2 Motivation

Supersonic jet and crossflow interaction analysis is needed to understand the physics behind supersonic combustion occurring in SCRAMJET engines. Because the residence time of the flow in the combustor is often on the order of chemical time scales, it is of

utmost importance for the fuel and oxidizer to be mixed quickly. It is necessary to gain better understanding of the effect of different injection configuration and combustor geometries on the injection process in order to achieve desirable designs for scramjet engines. Non-reactive injection of Sonic Ethylene in Mach 2 stream of air crossflow is the primary investigation in this study. The problem, despite simple boundary conditions, requires special treatment, which is usually difficult and computationally expensive, to obtain accurate mixing results. The flow field is three-dimensional with multiple shock structures that interact with the boundary layer and recirculation zones to contribute to the overall dynamics of mixing. Simulation of the turbulent mixing in the jet calls for turbulent treatments that are practical but of higher fidelity than those used in industry. This study is focused on the development and implementation of turbulence modeling that specifically targets accurate simulation of turbulent mixing.

In practical SCRAMJET engines where the injection of liquid jet is considered, multiphase flow modeling becomes important. Gas-liquid interaction in such an environment, however, becomes highly complex, since interfacial phenomena are coupled with those resulting from turbulent mixing and shockwave discontinuities. The simulation of liquid fuel injection into SCRAMJET engines is beyond the scope of this thesis. In this effort, however, we investigate plug flow and rupture in a tube as a simple multiphase flow problem of gas-liquid interaction.

Human lung airways are coated with a thin liquid, which under certain diseases can become thick and unstable. Unstable film can create a liquid plug that occludes the airway. This process is called airway closure; the liquid plug blocks airways and reduces gas exchange, and enhances airway collapsibility. The simulation of incompressible plug

propagation and rupture in an infinite tube can aid in understanding how the mechanical stresses form on the airway. It can also assist in quantifying and locating the peak stresses in the tube, and the effects of pressure drop and fluid properties on the magnitude of those stresses. We use an explicit interface tracking method, to track the gas/liquid interface defining the plug. The method, with the aid a newly developed reconstruction algorithm, can capture important flow information before and after rupture occurs. A dynamically adaptive grid is used to capture higher-resolution properties near the interface incorporating the effects of surface tension and interfacial dynamics on the flow.

1.3 The SCRAMJET Engine

A SCRAMJET is an air-breathing jet engine that relies for propulsion on the compressing or ramming effect on air taken into the engine inlet at supersonic speeds, normally when the aircraft is traveling at speeds above Mach 4. The term is derived from "supersonic combustion ramjet."[54] The Ramjet, an earlier and related invention attributed to Rene Lorin of France in 1913[55], is remarkable in its conceptual simplicity. Lacking moving parts, it is capable of extending the operation beyond the flight speed at which the gas turbine engine becomes inefficient. The Ramjet does not, however, operate from takeoff, and its performance is low at subsonic speeds because the air dynamic pressure is not sufficient to raise the cycle pressure to an efficient operational value.

At high supersonic flight speeds, rotating machinery such as compressors are no longer needed to increase the pressure. This can be done by geometrical changes in area within the inlet and diffuser leading to combustion chamber[12]. Engines without core

rotating machinery can operate with higher maximum temperature, as the limit imposed by turbine presence is eliminated. The Ramjet cycle, with subsonic air speed at the combustion chamber, becomes more efficient. As the speed increases further, the shock associated with subsonic combustion leads to both significant pressure losses and temperature increase. Those losses lead to incomplete recombination-reaction resulting in considerable energy loss. It becomes more efficient to maintain the flow at supersonic speed throughout the engine with heat addition in supersonic flow. Figure 1-1 shows estimated specific impulses for several cycles as the Mach number increases. Rocket specific impulse is included for comparison[56].

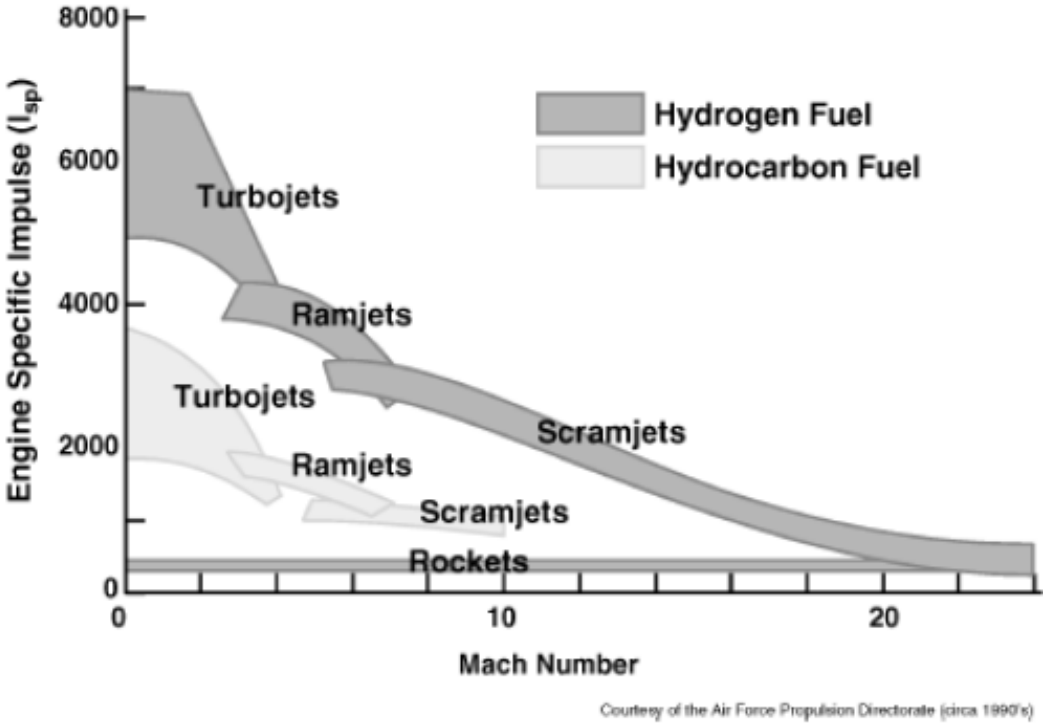

Figure 1-1 Specific Impulses for Several Engine Cycles[56]

1.3.1 SCRAMJET Engine Components

The propulsion system consists of five major engine and two vehicle components:

the internal inlet, isolator, combustor, internal nozzle, and fuel supply subsystem, and the craft's forebody, essential for air induction, and aftbody, which is a critical part of the nozzle. Figure 1-2 illustrates these components[57].

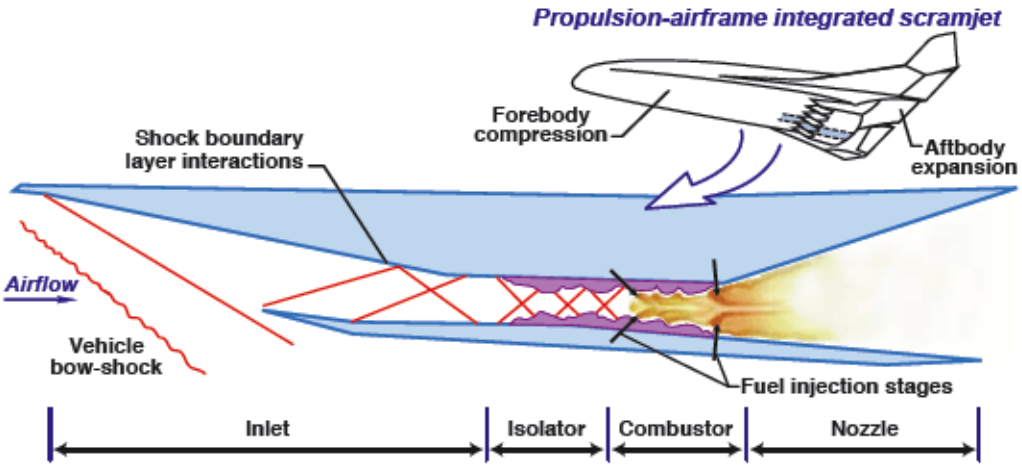

Figure 1-2 Diagram of a SCRAMJET engine, highlighting major components[57]

High-speed air is inducted and compressed, first by the vehicle's forebody then further by the internal inlet. For vehicles flying at supersonic speeds, without the need for rotating machinery, this compression is sufficient for processing by the engine's other components. The Mach number is decreased with an increase in pressure and temperature as the air is passed through the shock waves at the forebody and the inlet. Before entering the combustion chamber, air is passed through the isolator. This stage allows for gradual pressure adjustment before the combustion chamber. A pre-combustion shock is formed in the isolator due to boundary-layer separation driven by the combustor pressure rise. This allows the combustor to achieve the required heat release and pressure. It also helps prevent *unstart;* a condition that occurs when the internal inlet prevents supersonic airflow from entering the combustion chamber, eventually leading to engine shutdown. In the combustion chamber, efficient fuel-air mixing occurs, leading to chemical reaction

and expansion through the nozzle. The air is also further expanded by the aftbody. The design of the nozzle affects the efficiency of the engine greatly because complex phenomena including flow chemistry and three dimensional non-uniform conditions occur as the potential energy generated by the combustor is converted to kinetic energy[58].

1.3.2 SCRAMJET Advantages and Challenges

A major difference between Ramjet and SCRAMJET engines is the latter does not require a physical throat after the combustion chamber because the flow is supersonic throughout the process. Even when the engine functions in a ramjet mode, the Mach number increases by means of a thermal throat[12].

Table 1-1 compares relevant parameters of a SCRAMJET and a ramjet for Mach 12 flight. At Mach 12 flight speed, at an attitude of 40 km with hydrogen as fuel, the stagnation pressure recovery is 38 times larger in the case of supersonic combustion. This is because there is no terminal normal shock in SCRAMJET engine. Also the temperatures at the entrance of the combustion chamber are very large, causing dissociation to occur, which leads to heat released due to the chemical reaction occurring at the nozzle. Because Ramjets require a physical throat, the nozzle in this case would need to be prohibitively long and heavy. A true SCRAMJET has no throat except when it operates in dual mode SCRAMJET (involves both subsonic and supersonic combustion operation); it has a thermal throat that results when the flow is slowed through heat release. Finally, the static pressure is considerably lower in the case of SCRAMJET, which reduces structural loads and results in lighter more efficient systems[10, 12]

Table 1-1 A comparison of several relevant parameters between subsonic and supersonic combustion based ramjets during Mach 12 flight[10, 12]

Combustion chamber entrance	Super-sonic	Sub-sonic	Combustion chamber exit	Super-sonic	Sub-sonic
Ratio of burner entrance to capture area	0.023	0.023	Ratio of exit area to Capture area	0.061	0.024
Stagnation-pressure recovery	0.5	0.013	Ratio nozzle throat to capture area	0.061	0.015
Pressure (atm)	2.7	75	Pressure (atm)	2.7	75
Temperature (K)	1250	4500	Temperature (K)	2650	4200
Mach number	4.9	0.33	Mach number	3.3	0.38

The SCRAMJET idea, despite conceptual simplicity, faces many technological challenges. One is fuel-air mixing with air residence time on the order of milliseconds. Efforts to accelerate mixing result in an increase in losses in momentum and overall efficiency. The problem is also compounded when liquid fuels are used, because additional processes including multiphase dynamics are involved. Injecting fuel into a crossflow can be used as a unit problem to understand the process of turbulent mixing and will be the major focus of this study.

Other challenges include flame stability, which becomes a key issue at such high speeds. Flame holders must be included causing large gradients of temperature and composition. Also, the operation of the SCRAMJET requires a considerable amount of cooling for both engine and vehicle components[12]. Usually the fuel is used for cooling, however, under certain conditions it may not have the cooling capacity and additional

cooling maybe required. Beyond Mach 10 for example, hydrocarbon fuels will not satisfy the requirement and cryogenic hydrogen will become the fuel of choice[59].

1.4 Mixing and Structure of Supersonic Jet and Crossflow

The fluid residence time in a SCRAMJET engine is on the order of milliseconds. Mixing, therefore, becomes the determining factor in a complex ensemble of phenomena leading to heat release and thrust generation. The mixing involves turbulent 3D flows with large velocity gradients causing subsonic regions in a generally supersonic flow. Shock waves that interact with boundary layers are also present. Generally, chemical and thermal processes cannot be uncoupled from practical design of SCRAMJET engines. It is, however, of great importance to understand the mixing process separately using cold injection of gas fuel at large angles into supersonic crossflow. Many injection configurations could be considered including sonic or supersonic injections, liquid jets or dual-phase injection with varying orifice shapes, sizes and momentum ratios. In this study we focus on 90 and 30 degree injection of sonic ethylene into supersonic air crossflow.

The structure of an underexpanded jet in supersonic crossflow is shown in the 3D schematic in Figure 1-3(a) from Portz and Segal[60] and a cross section near the injector in Figure 1-3 (b) from Gruber et al[8]. The flow field involves shock and viscous interactions that improve mixing while increasing losses. The injected fuel plume forms a barrel shock which acts as a barrier to the incoming supersonic flow. This blockage causes a large encompassing bow shock behind the barrel shock. This bow shock works on separating the boundary layer and forms recirculation zones in front of the jet. The

side vortices are spilled and carried axially downstream to aid in the process of mixing. Downstream, the injectant angle decreases relative to the supersonic crossflow and mixing continues with the aid of the spilled side vortices[12]. In practical flows, the thickness of the boundary layer resulting from the incoming flow passing through many engine components can increase significantly. This affects the position and strength of the bow shock. Also, heat release may have an effect on the flow by helping to form subsonic regions downstream of the jet[10]

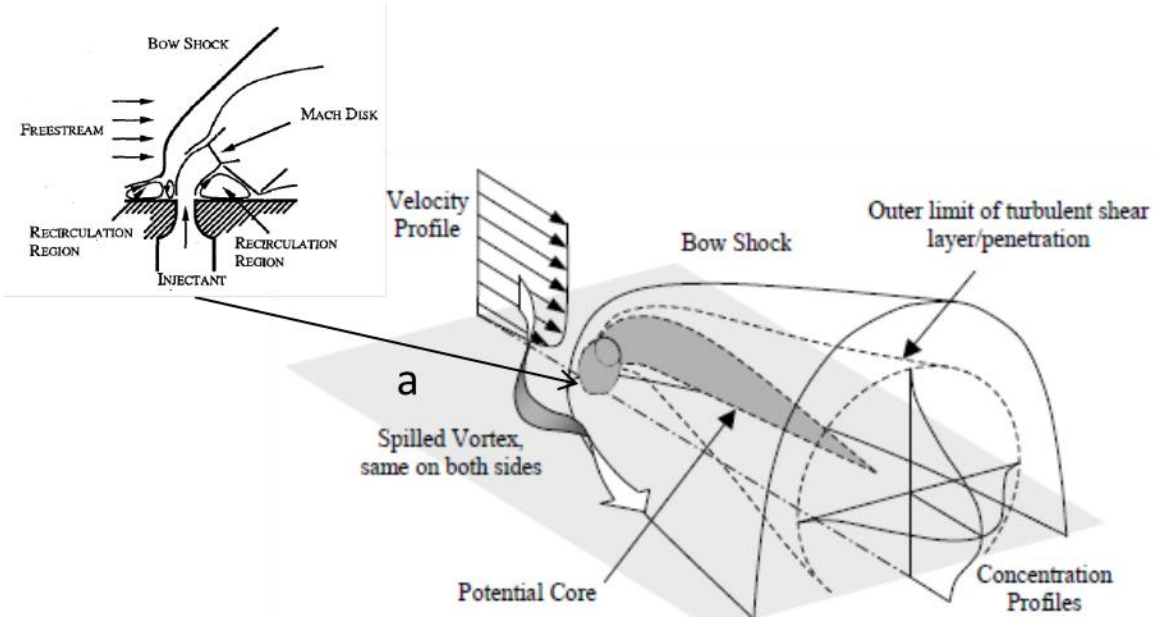

Figure 1-3 Model of transverse underexpanded jet in a supersonic crossflow (a)Full 3D schematic from Portz and Segal[60] (b) cross section schematic near injector from Gruber et al [8]

In 2009, Viti et al [17] did a detailed numerical study of the features of jet and crossflow interaction including the inner structure of the barrel shock. They related compressible features such as the barrel and the bow shock to the complex vortical structure in the flow. The high-pressure region ahead of the injector was shown to have localized pressure maximum and minima. These local peaks in pressure are generated by the presence of two counter-rotating vortices that impinge on the surface; the pressure

peaks corresponding to local stagnation conditions and the pressure troughs to the vortical flow moving away from the surface.

The low-pressure region aft of the injector was found to be created primarily by the reflection of the barrel shock on the solid surface of the wall. This reflection creates a concave indent in the leeward side of the barrel shock that promotes the lowering of the local pressure. The footprint of the low-pressure region on the wall with its two prominent lobes extending far downstream was correlated with the 3D concave channel that the shock reflection creates in the back side of the barrel shock. Figure 1-4 from Viti et al[17] shows the indented barrel shock with recirculation regions in normal sonic air injection into Mach 4 crossflow.

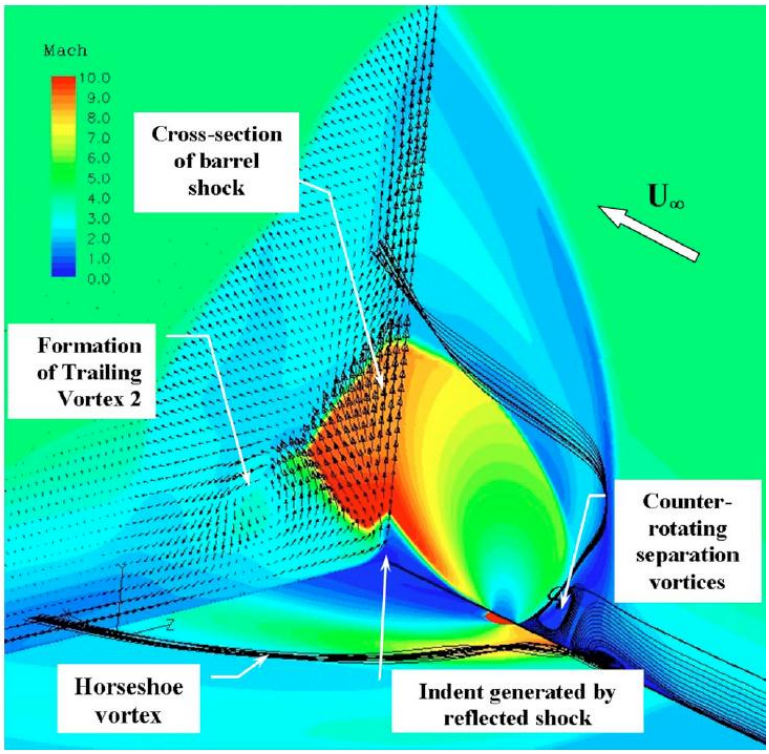

Figure 1-4 Indented Barrel shock with recirculation regions in normal sonic air injection into Mach 4 crossflow from Viti et al [17]

1.5 Experimental Studies of Supersonic Jet and Crossflow

Most of the early experimental measurements used optical techniques to visualize wind tunnel experiments of jet and crossflow. These experiments allowed the researchers to understand the basic flow features associated with supersonic jet and crossflow. Andrepoulos and Rodi[61] authored an extensive review of the experimental work in injection studies up to 1984. More recent studies utilized laser-tracking technology in addition to optical techniques to glean more information from the wind tunnel tests. Table 1-2 lists a selective summary of the experimental studies of jet and crossflow in the more recent literature. McDaniel and Graves[62]conduced one of the earliest laser induced fluorescence (LIF) to quantitatively measure concentrations in constant area duct and backward facing step of jet in a Mach 2 crossflow. Mckmillin et al[63] took temperature measurements in reactive and non-reactive supersonic cross flow using NO for Planar laser induced fluorescence measurements (PLIF). Smith and Mungal[5] also took PLIF concentration measurements for subsonic jet and crossflow at Re=8400-41500 allowing CFD comparison at lower Reynolds numbers. Santiago et al [13] used laser Doppler velocimetry to measure mean velocity components and some Reynolds stresses in Mach 1.6 crossflow with a momentum ratio of 1.7. They provided mean velocity and Mach number contours as well as dimensionless turbulence kinetic energy on the midline plane. Pressure-sensitive paint was used to conduct average wall pressure measurements by Everett et al [14] with Mach 1.6 crossflow at momentum ratios of 1.2 to 2.2 showing increasing pressure with higher momentum ratios. With pressure-sensitive paint being new at the time, only 20 images were averaged temporally to provide average pressure. The temporal resolutions are considered inadequate in a highly turbulent field; however,

spatial resolution was higher at 85 $\mu m/pixel$ or about 47 pixels per injector diameter.

Table 1-2 Selective summary of experimental studies of jet and crossflow interaction

Year	Study	Technique	Details
1988	McDaniel and Graves[62]	Laser-Induced fluorescence (LIF)	Quantitative 3D non-reactive concentration measurements in constant area duct and rearward facing step in Mach 2 crossflow
1993	Mckmillin et al[63]	NO-PLIF	Temperature measurements in reactive and non-reactive supersonic crossflow at q=1.49,1.94
1997	Santiago and Dutton[13]	Laser-Doppler velocimetry (LDV)	Mean velocity and Reynolds stresses in Mach 1.6 , q=1.7 normal injection
1997	Gruber et al [51]	Rayleigh/Mie scattering	Temporally correlated images for Air/helium Mach 1.98 crossflow for circular and elliptical orifices
1998	Everett et al [14]	Pressure sensitive paint (PSP)	Wall pressure measurements in Mach 1.6 crossflow , q-=1.2 to 2.2
1998	Smith and Mungal [5]	PLIF	Quantitative concentration measurements for subsonic jet and crossflow at Re=8400-41500
2000	VanLerberghe et al[50]	Shadowgraph/ PLIF	Temporally resolved shadowgraph/PLIF images used to process probability density functions for mixing Mach 1.6 , q=1.7 normal injection
2006	Ben-Yakar et al[64]	Schlieren/OH-PLIF	Schlieren/OH-PLIF images for Mach 10 , q=1.4 hydrogen and ethylene including combustion
2006	Maddalena [21]	Hot film probe	Measured concentration of helium crossflow in Mach 4 air with and without aero-ramps
2010	Lin et al [16]	Raman scattering/NO-PLIF	Quantitative concentrations at various axial locations for sonic ethylene injection into Mach 2 air crossflow
2011	Crafton et al [15]	Pressure-sensitive paint (PSP)	Wall pressure measurements at a 1000Hz sampling rate of for sonic ethylene injection into Mach 2 air crossflow

Gruber et al[51] used temporally correlated Rayleigh/Mie scattering images to examine vortex structures in a Mach 1.98 crossflow with circular and elliptical injectors using air and helium as fuel . They showed larger near-field convection velocities for helium, with the elliptical orifice causing axis switching and a weaker bow shock

VanLerberghe et al[50] also took temporally resolved shadowgraph images along with laser-induced fluorescence to process the images for probability density functions (PDF) to study the mixing process. The study showed significant mixing in the wake region downstream of the barrel shock. They also showed coherent packets of fuel transported in the shear layer between the jet and crossflow. Figure 1-5 shows sample images taken by VanLerberghe et al[50] at the midline plane. Significant unsteadiness and large turbulent structures are reported near the barrel shock where the concentration variance is the highest. Downstream, high unsteadiness is witnessed only near the shear layer between the jet and the free stream crossflow.

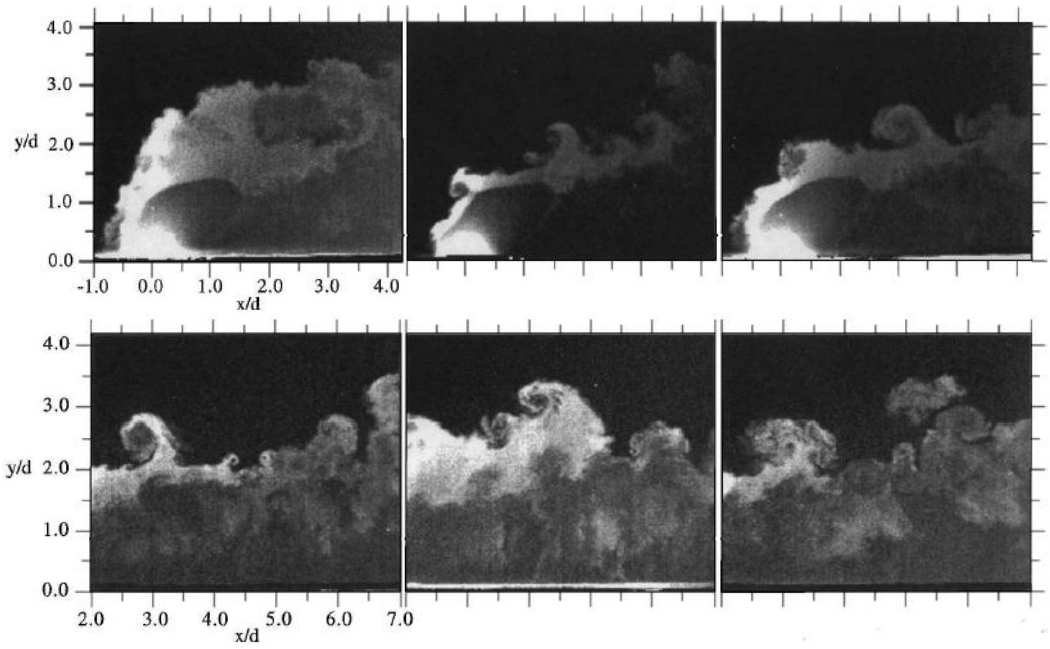

Figure 1-5 Temporally-resolved shadowgraphs of Mach 1.6, q=1.7 Air/Air jet and crossflow by VanLerberghe et al[50]

Combustible injection of both ethylene and hydrogen in Mach 10 crossflow were experimentally investigated by Ben-Yakar et al[64]. They showed much deeper penetration for Ethylene at the same momentum ratio. Auto-ignition occurred in homogenously mixed regions after the fuel has been thoroughly mixed.

In this effort, we focus on the experiments of Lin et al [16, 65]. They used ethylene as fuel injected at sonic speed in Mach 2 crossflow. The experiments were conducted at the continuous-flow supersonic tunnel at Wright-Patterson Air Force Base in Ohio. The tunnel has a constant test cross section of 131 X 152 mm. The injectors were circular with the diameters varied at 1/16, 3/16, and 5/16 of an inch. Momentum ratios of 0.5, 1.0 and 1.5 were used at either normal or inclined (30 degree) injection. Raman scattering[66] was used to collect quantitative instantaneous injector concentration data that was used to calculate time-averaged mole fraction at transverse planes at various axial locations. This comprehensive set of data is the major source for experiments used for comparison in this thesis.

Pressure-sensitive paint was also used at the wall for some of the normal injection cases[15]. Those measurements were done at 1000 Hz temporal resolution, much higher than conventional pressure-sensitive paint. In this thesis we also use these measurements for comparison.

While the mentioned experimental efforts often provide valuable database for understanding the flow physics and CFD comparison, they are costly to perform and reliable measurements are often difficult to obtain. For practical design purposes, experiments may become impossible due to larger engines and/or the number of design iterations required. This has forced an increased reliance on computational studies to augment database of supersonic jet and crossflow, and to become the essential tool in future SCRAMJET design purposes.

1.6 Scaling Efforts for Supersonic Jet and Crossflow

Many efforts for simple correlation and/or analytical solutions can be found in the literature, mostly to evaluate simple parameters such as penetration height to give a good indication of mixing. The first approximate analytical solution based on control volume analysis was done by Schetz and Billig [67] only for limited cases of either no boundary layer effects or very thick boundary layer. The method was then improved to include all injection cases based on a similar analysis dubbed as JETPEN[68]. The method is based on modification to jet penetration into quiescent air to include effects of crossflow. Effects of mixing, shear, heat transfer and axial momentum transfer are neglected. The drag approximation is based on either Newtonian drag or the isentropic assumption. The results show the dependence of Mach disk height (as a measure of penetration height) on the injectant Mach number and momentum ratio as follows,

$$\frac{y}{D_i} = M_i^{\frac{1}{4}} q^{\frac{1}{2}} \qquad \textbf{1.1}$$

where D_i, is the injectant diameter. M_i is the injectant Mach number and q is the momentum ratio defined as,

$$q = \frac{\rho_i u_i^2}{\rho_\infty u_\infty^2} \qquad \textbf{1.2}$$

The JETPEN method was further refined with different treatment to account for inclined injection angles. Also, turbulent entrainment of mainstream fluid into the plume was modeled after the Mach disk[69]. The entrainment model is based on an experimental correlation for subsonic injection [70] that is extended to include high-speed flows. The entrainment results are a crude average value per x/D location. This average value is associated with the plume trajectory calculated by JETPEN. JETPEN penetration heights had a relatively reasonable agreement with experimental Raman

scattering of Ethylene injection by Lin et al [16, 65], however, major discrepancies in plume size and location were found especially further downstream.

Other correlations of penetration heights were purely experimental and included dependence on boundary layer thickness, δ. one example is the correlation from McClinton[11] for sonic injection,

$$\frac{y}{D_i} = 4.2\left[q^{0.3} + \left(\frac{\delta}{D_i}\right)^{0.0574} + \left(\frac{x}{D_i}\right)^{0.143}\right] \qquad \textbf{1.3}$$

There were however major variation in the experimental correlations presented in the literature[12]. Other correlated experimental results include those of Rogers[71] and Hersch et al[72]. Portz and Segal also produced a more recent correlation that included dependence on the molecular weight ratio of jet and air[60].

The mentioned scaling efforts are useful to understand trends in jet and crossflow interaction and can help with initial crude design for injectors. They do not, however, provide detailed information about specific geometries or flow conditions. Computational fluid dynamics (CFD), on the other hand, can compute detailed point by points flow variables to be used for specific design objective and deeper understanding of the flow physics.

1.7 Computational Approaches for Jet and Crossflow

Efforts using computational fluid dynamics can give a great deal of insight into the composition and mechanism of supersonic jet and crossflow interaction because detailed flow information is available at every time step. There are, however, many modeling challenges that occur due to complex 3D structures, recirculation zones,

shocks, and generally unsteady turbulent flow that should be modeled correctly.

Table 1-3 Selective summary of computational studies of jet and crossflow

Year	Study	Technique	Details
1999	Tam et al[19]	RANS: different models	Simulated Gruber et al[51] experiments with 3 RANS models. Penetration heights over predicted by 27%
2000	Chochua et al[3]	RANS: $k-\epsilon$	Study of subsonic turbulent jet and crossflow reveals deficiency in the amount of mixing when compared to the experiment
2005	Palekar et al[73]	RANS: $k-\omega$	Simulated Gruber et al[51] experiment with a finer 4.5 million cell grid and obtained better penetration height match
2006	Maddalena[21]	RANS: $k-\omega$	Mach 4 helium/air crossflow with/without aero-ramps. Computation deviated from experimental concentration measurements
2009	Viti et al [17]	RANS: $k-\omega$	Sonic injection into Mach 4 crossflow. Compared favorably with experimental wall pressure measurements, and qualitatively with shock locations
1996	Jones and Wile [2]	LES: coarse mesh	Subsonic simulation of jet in crossflow at Re=19000, three different sub-grid models on coarse mesh (not adequate for LES). No significant difference between the sub-grid models
1999	Yuan et al[74]	LES: lower Re	Subsonic simulation of jet in crossflow at Re=1050, 2100 to discuss flow physics and vortical structures
2010	Kawai and Lele[18]	LES: Lower Re	LES simulation of experiment with Re 1/6th of experiment. Flow physics and unsteadiness discussed
2010	Boles et al[27]	Hybrid: RANS/LES blend	Used NC state hybrid RANS/LES model to simulate Lin et al [16]experiments, very good match to experimental concentration obtained
2011	Peterson and Candler [52]	Hybrid: DES	Used DES method to simulate Lin et al[16] experiments. Comparison to experimental concentrations superior to RANS
2009	Keislter [75]	RANS: Adaptive Sc_t	RANS with adaptive Sc_t showed limited improvement over RANS alone for Lin et al [16] injection cases

Table 1-3 lists a summary of selective computational studies from the literature that

vary in turbulent treatment; including RANS, LES, and hybrid RANS/LES models. The industry standard in simulation of turbulent flow is dependent heavily on Reynolds-averaged Navier-Stokes (RANS) based approaches, particularly two-equation models such as $k-\epsilon$ [76] These models have shown some limited success in modeling the mechanics of supersonic jet and crossflow interaction. Tam et al.[19] used RANS-based methods with Menter SST[77], Menter BSL[77], and Wilcox *k*-ω[78] turbulence models to simulate the experiments of Gruber et al. [8, 9, 51]. It was claimed that the Wilcox *k*-ω model performed the best of all three; however, in all the models tested the fuel penetration height was over-predicted by up to 27%. Figure 1-6 shows non-dimensional axial location versus non-dimensional penetration height for the three turbulent models versus the experiment reported by Tam et al[19]. All three models over-predict the height by about equal amounts implying less sensitivity to the RANS turbulence model chosen.

Palekar et al. [73] obtained better correlations with penetration heights with a 4.7 million cell grid using the commercial CFD code GASP. The Wilcox k-ω turbulence model was also utilized for turbulence closure. Coarser grids did not sufficiently resolve the flow, and span-wise fuel penetration significantly deviated from the experiment. Maddalena et al. [21] used the k-ω Wilcox turbulence model to simulate an aeroramp injection scheme as well as transverse injection of sonic helium into air. Total pressure loss was shown to be greater than that of a normal injection configuration with the computational results not correlating well with the experiment.

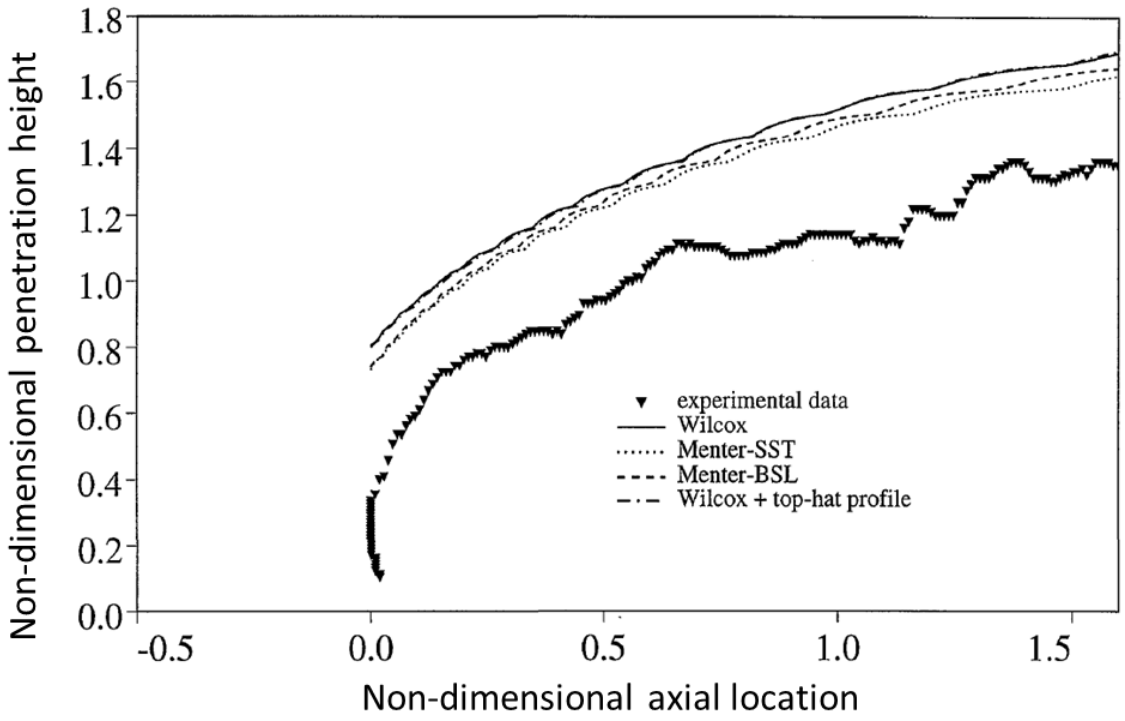

Figure 1-6 Penetration heights compared to the experiment for 3 turbulent models from Tam et al[19]

As stated by many researchers[22-24], there are some obvious limitations to RANS models when applied to unsteady problems because they tend to be overly dissipative (predicting higher eddy viscosity and damping the unsteady motion of the fluid). The jet and crossflow interaction problem usually involves large-scale unsteady turbulent structures, density gradients, and shock/boundary-layer interactions, as evidenced by experimental findings [8, 9, 51]. These phenomena are difficult to capture correctly with standard RANS approaches and may benefit from methods capable of resolving turbulent structures such as Direct Numerical Simulation (DNS) or Large Eddy Simulation (LES). LES is capable of capturing the large-scale turbulent structures, and while not as computationally expensive as DNS, it is currently impractical for use in the supersonic jet and crossflow interaction problem because a prohibitively large number of grid points must be used to resolve the boundary-layer. The number of grid points

required for wall-resolved LES simulations scales with $Re^{9/5}$[28]This would require one billion grid points for a $Re = 100{,}000$ typical for supersonic crossflow simulations.

LES models have been used on coarser meshes with the argument that required LES grid is not important. Jones and Wile [2]conducted a subsonic jet and crossflow simulation of a Re=19,000 using three different LES sub-grid models on a 78,000 point grid (not-adequate by LES standards). Due to the coarse grid, sub-grid models' results showed insignificant differences. The authors claimed a reasonable comparison to the experiment for mean velocity profiles, however, the results were not compared to a RANS solution at a similar resolution, and no proven advantage to the use of such method was presented.

Lower-Re LES simulations can help provide information about the flow structure and physics of jet and crossflow interaction. Yuan et al [74] conducted a subsonic simulation of jet in crossflow using Re of 1050 and 2100. The study discussed shocks and vortical structures associated with the flow. Recently, Kawai and Lele[18] conducted an LES of sonic injection into a supersonic crossflow based on the experiment of Santiago and Dutton[13], and showed key physics of the jet mixing in supersonic crossflow, such as clockwise and counterclockwise rotating strong longitudinal vortices forming a pair of U-shaped counter-rotating vortices. To reduce the expense of the computations, the Reynolds number was lowered by a factor of six, relative to the experiment[13] but the boundary-layer thickness upstream of jet injection is matched.

Due to the RANS models' limitations and the impracticality of LES, hybrid RANS/LES methods rose to provide the best compromise between the two. The concept is to use RANS models near the wall (where LES would require very fine grids) and LES

is used in the rest of the domain. These methods provide the robustness and reliability of RANS solution near the wall, combined with the capability of resolving large eddies in the main flow. Boles et al [27]used the NC State hybrid RANS/LES model in which they explicitly blended divided the domain into RANS and LES regions connected by a blending function that lies in the log-layer region of the boundary-layer. They simulated Gruber et al.[8, 9, 51] air and helium injection cases as well as an ethylene injection case conducted at Air Force Research Laboratory (AFRL) and reported by Lin et al.[16, 65]. In all cases, time-averaged hybrid results were superior to RANS quantitatively and qualitatively when compared to experimental injectant distribution. Figure 1-7 shows time-averaged mole fraction comparison of RANS, hybrid RANS/LES and experimental distribution at 3 axial locations for the normal ethylene injection case of Lin et al[16]at q=0.5. The hybrid RANS/LES, unlike RANS, provides very good match to the experimental results.

The NC State hybrid RANS/LES model, however, lacks generality due to the need of blending function calibration for each case. Also, because the blending function has to lie within the boundary-layer, finer grid is required near the wall, although not as fine that required by LES. The method is also restricted to structured type grids, thus injector solution had to be imposed on the bottom wall, rather than simulated (due to injector geometry). The simulation grid limitation also required the use of a smaller domain and artificial turbulence for the inflow boundary

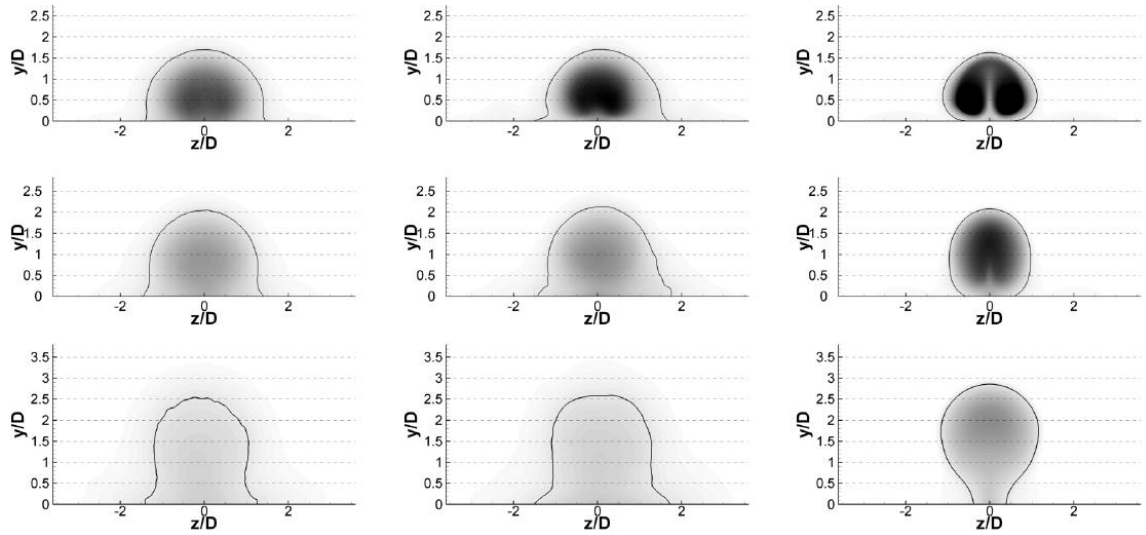

Figure 1-7 Experimental, RANS and Hybrid RANS/LES concentration comparison from Boles et al[27]

Peterson and Candler[52]were able to successfully simulate the crossflow experiments of Lin et al [16]using detached eddy simulation (DES) [24] based on the Spalart-Allmaras one-equation turbulence model[79]. They also obtained very good match to the experimental time-averaged concentration for normal injection case. The DES method, a class of the hybrid methods, uses a single RANS formulation and transition to LES is based on grid spacing. The method sometimes resulted in the LES mode turned on in the boundary-layer, in areas where it cannot effectively resolve the turbulent length scale[20]. Also DES faces a potential for log-layer mismatch in turbulence quantities due to transition from RANS to LES. This occurs when the inner log-layer produced by RANS does not match the outer log-layer produced by LES [80-82] . This phenomenon is caused by mismatch of turbulent energy and Reynolds shear stress at the LES/RANS interface. Log-layer mismatch can result in an under-prediction of the friction coefficient by as much as 15-20 %[82]. While some of these problems

were alleviated later by variations of the DES method[20, 82], DES still requires carful grid generation to properly handle the RANS/LES juncture and avoid abrupt transition. Production of such grids is sometimes difficult for complex geometry and/or internal flows. Peterson and Candler [52]were able to include the geometry of the injector of the domain; however, they had to use a special hexahedral grid generator to carefully generate a smooth grid capable of handling DES. They also had to limit their domain size and use synthetic turbulence at the boundary.

It is desirable to capitalize on the advantages of the hybrid methods in the simulation of jet and crossflow without domain size limitations, grid restrictions, or adjustable constants. This would allow these methods to be used in practical CFD codes with standard grid generation techniques and computational capabilities. In the literature, there are filter-based approaches, which limit the eddy viscosity in the RANS model, thus allowing resolution of turbulent structures where the grid resolution allows. These models face little restriction on where the transition between RANS/LES should occur for reasonably varying cell size. Johansen et al[83] introduced the filter based model (FBM) where the eddy viscosity was reduce based on the ratio of the grid size and the turbulent length scale. The filter based model was tested with 2D subsonic simulation of flow over square where it showed superior results over RANS and was also used by Tseng and Shyy [135] with both 2D and 3D subsonic simulations of cavitation flow. Nichols and Nelson [22, 84]also developed a filter based approach that they called multi-scale hybrid RANS/LES. Their model used a smooth filter function method and was tested with several subsonic problems including flow over a cylinder, NACA 0015 airfoil and square cavity. It was also tested with essentially 2D supersonic shear flow where it showed

superior results over the DES method due to the smooth filter function allowing the transition between RANS and LES to occur without abrupt discontinuous solutions[84]. In chapter 2, the concepts of the filter based approaches will be used to develop a model capable of handling supersonic jet and crossflow interaction

The turbulent Schmidt number is a measure of turbulent mass diffusion versus turbulent momentum diffusion and it is usually specified as a constant number both in RANS and LES sub-grid models. In LES, the effect of the turbulent Schmidt number specification is usually minimal because large-scale turbulent structures are resolved without the need for modeling turbulent mass diffusion. For normal injection in supersonic flow cases of Lin et al[16, 65], Hassan et al.[29](also detailed in chapter 3) and Boles et al.[27] derived estimates for the turbulent Schmidt number, based on the resolved field, which were not constant with strong variations throughout the flow.

There have been many efforts in the RANS community to calculate, rather than specify, the turbulent Prandtl and Schmidt numbers, starting as early as 1975.[85] Methods based on the mixing length used a two equation model to calculate turbulent diffusivity in conjunction with k-ε.[86, 87] In general, results from these methods showed an improvement over k-ε alone in low-temperature, high-Mach number cases. Guo et al.[88] used a genetic algorithm to obtain model constants for a diffusion vector transport equation used in addition to k-ε. The results showed some improvement over a baseline k-ε model for a jet and crossflow application. CRAFT Tech developed a variable Prandtl(Pr_t) and Schmidt(Sc_t) number approach based largely on earlier efforts[86, 87] with added compressibility correction. The model showed improvements over a constant Pr_t/Sc_t in a range of classical validation cases.[89, 90] Keistler[75] used

a reacting model with variable Pr_t/Sc_t method designed for high-speed flows and based on CRAFT tech efforts[89, 90] to simulate Lin et al.[65] mixing case. He compared his results to those obtained by hybrid RANS/LES method of Boles et al.[27] While the variables approach showed some limited improvement over RANS in predicting fuel concentration levels. It fell short of the hybrid RANS/LES method in predicting jet shape mainly due to inability to produce large-scale turbulent structures.

To the author's knowledge, there have been limited or no efforts in the literature to combine hybrid RANS/LES type approaches with variable turbulent Schmidt number methods. This is desirable because it would improve the modeled portion of the turbulence thus allowing coarser grids to be used with hybrid RANS/LES methods. In chapter 2, such model will be developed to calculate the turbulent Schmidt number based on the resolved field.

1.8 Mixing of Liquid Jets

The issues of jet penetration and mixing apply when liquid jets (fuels) are injected instead of gas in SCRAMJET engines. There are clear advantages in using liquid fuels in comparison to gaseous-based systems, particularly when liquid-hydrocarbon fuels are used in small hypersonic vehicles limited to Mach 8[12]. The energy density in these liquid-hydrocarbons is higher than gaseous fuels such as hydrogen; however, they require higher energy densities to initiate exothermic reaction[91]. Aspects of combustion characteristics of various fuels are reviewed by Segal and Shyy[91], Marchand et al[92], and Yang and Zarko[93].

The interaction between the liquid jet and the supersonic airstream is dominated by

the instabilities that develop on the surface of the liquid column, resulting in jet breakup, vaporization and mixing[94, 95]. Before the jet is completely atomized for vaporization, it is broken up into irregularly shaped clumps of liquid. Kush and Schetz[96] identified specific regimes for jet penetration depending on the momentum ratios For high momentum ratios, the jet penetrates for several injection diameters undisturbed for several injection diameters. With lower ratios, the jet remains in a narrow layer close to the injection wall with random shape disintegration before it is finally vaporized. The breakup regime is dominated by aerodynamic forces in the initial stage but, as the waviness of the jet surface increases and large structures are formed, the breakup is dominated by liquid turbulence and inertial forces leading to jet disintegration[97].

Simulation of such injections involve coupling of multi-phase flow with turbulent and high-speed dynamics. This difficult problem is beyond the scope of this thesis. The computational capabilities we use for this work are limited to simulations of multiphase flows without turbulence modeling or discontinuities (low Reynolds number flows)[46, 48].To demonstrate some of those capabilities we solve the problem of flow and rupture of liquid plug in a tube. This problem has application in mucous dynamics in human lung airways[98] and will be discussed in detail in section 1.9

1.9 Plug Flow and Rupture Problem

Lung airways are coated with a thin liquid, which under certain diseases can become thick and unstable. Unstable film can create a liquid plug that occludes the airway. This process is called airway closure; the liquid plug blocks airways and reduces gas exchange, and enhances airway collapsibility. Also, the mechanical stresses induced by

the plug propagation can cause pulmonary epithelial cells to be damaged[53, 99]. Figure 1-8 from Tavana et al [99] represents a typical response of the microfluidic airway to repeated propagation of liquid plugs. Green and red fluorescence represent live and dead human pulmonary epithelial cells stained with dyes (study used live human cells attached to thin polyester membrane representing the airway). Many of the studies on liquid plug propagation in a channel utilize the Lagrangian interface tracking method focusing only on the liquid phase.

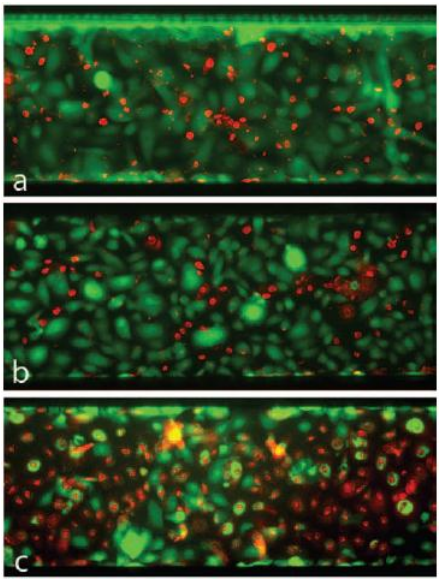

Figure 1-8 Live-dead staining of human pulmonary epithelial cells after 10(a),50(b), and 100(c) plug propagation events from Tavana et al [99]

Bilek et al. [100] investigated lung epithelial cell damage in a model of airway reopening, consisting of a semi-infinite bubble propagating in a narrow fluid-filled channel lined with pulmonary epithelial cells. They showed that cell damage increased with decreasing reopening velocity, and that the presence of a pulmonary surfactant prevented this injury. Using a single-fluid Lagrangian model, they demonstrated that as the air finger propagates over the cells lining the channel, walls experience different

types of mechanical stresses such as shear stress and pressure. They concluded that the steep pressure gradient near the finger front was the most likely cause of the observed cellular damage. Kay et al. [101] showed that cell damage was directly correlated with the pressure gradient, not the duration of stress exposure (period for a pressure wave to pass over a cell). Repeated reopening and closure was shown to damage the cell layer, even under conditions that would not lead to extensive damage from a single reopening event.

Studies by Bilek et al. [100] and Kay et al. [101] focused on the cell injury caused by air-finger replacement in liquid filled airways equivalent to the rear half of a long liquid plug. Huh et al. [98] investigated mechanical injury of primary human small airway epithelial cells (SAECs) caused by propagation and rupture of liquid plugs. The micro-fluidic channel was lined with SAECs and a thin liquid film. Exposure of the SAECs to physiological fluid mechanical stresses associated with surfactant-deficient airway reopening led to significant cellular damage whose severity was elevated with increasing frequency of plug propagation and rupture. Furthermore, plug rupture imposed a higher risk of cellular injury than plug propagation alone. Additional experimental and theoretical studies on plug propagation in flexible micro-channels by Zheng et al. [102] indicate higher risk of injury for greater flexibility, which is a feature of airways in emphysema, for example.

Howell et al. [103] modeled the propagation of a liquid plug through a compliant channel in the limit of Stokes flow and small capillary number. They obtained expressions for the pressure drop across the plug and the trailing film thickness as functions of the elastic properties of the channel, the capillary number, and the precursor

film thickness. Their study showed that rupture (or reopening) is more likely to occur in a compliant channel coated with pre-existing thicker film. They also showed that increasing longitudinal wall tension decreases the likelihood of rupture and that there is a critical pressure drop above which rupture occurs. Waters and Grotberg [104] considered the effect of soluble surfactant on the plug propagation through a single tube, and found that surfactant activity increases the trailing film thickness and the pressure drop across the plug needed to move it at a prescribed velocity.

Fujioka and Grotberg [105, 106] used a finite-volume method for a single-fluid Lagrangian formulation and considered the effects of inertia and surfactant. If the channel is wider than the plug length, the trailing film thickness is less than that of a semi-infinite bubble at the same Reynolds number (*Re*). The front meniscus develops a capillary wave whose amplitude increases with *Re*, causing large variations in wall shear stresses and pressures, which can lead to a detrimental effect on the cells lining the airways. When surfactant is present, it accumulates on the front meniscus interface as it is swept from the precursor film. The surfactant concentration is at maximum somewhere in the front meniscus, and a surface tension gradient opposes the flow out of the film region. In this region, the surface velocity almost vanishes, and this results in the precursor film thickness near the meniscus being larger than the leading film. Because of an increase in the minimum film thickness, there is a reduction in the peaks of wall pressure and shear stress. However, in the thicker film region, the drag forces are actually larger than the surfactant free case. Therefore, the pressure drop across the plug increases as the result of the increasing surfactant concentration.

Suresh and Grotberg [107] and Zheng et al.[108] considered the effect of gravity on

the steady or quasi-steady motion of a liquid plug in a two-dimensional liquid-lined channel oriented at an angle α with respect to gravity, and found that the pre-bifurcation asymmetry of the plug increased with the plug length (L_p), capillary number (Ca) Re, but decreased with the Bond number (Bo). Fujioka et al. [53] and Uzgoren et al. [48] investigated unsteady liquid plug propagation numerically. They considered the propagation of a liquid plug within a rigid axisymmetric tube coated by a thin liquid film with and without surfactant. The magnitudes of the wall pressure and wall shear stress are greatest in the front meniscus region, and they increase with a thinner precursor film. If the trailing film is thicker (thinner) than the precursor film, the plug volume decreases (increases) as it propagates. When the plug length (L_P) becomes short, the Marangoni stress increases the hydrodynamic viscous friction and causes L_P to plateau. During the period of L_P plateau, since the meniscus surface curvature near the wall becomes strong, the pressure gradients and shear stress within the transition regions increase. The stability of the motion of a liquid plug is investigated by Campana et al. [109].

Fujioka et al. [53] investigated the propagation of a liquid plug based on the Lagrangian method, which works well until its rupture. At rupture, the break-up of the plug creates difficulties for Lagragian approaches during the re-gridding process. Furthermore, when the precursor film becomes sufficiently thin, the liquid plug shrinks and the air fingers become closer to each other ultimately leading to rupture. As reported in [98], this scenario may lead to excessive stresses that damage pulmonary epithelial cells. Erneux and Davis [110] studied the critical film thickness at which the rupture of thin films occur. They have found that the critical thickness is directly related to the molecular forces and surface tension.

1.10 Multiphase Flow Methods

The computational techniques for treating the moving interface are usually categorized into Lagrangian methods [39, 40, 53] that modify the grid to match the interface location, Eulerian methods[34, 37, 111, 112] that extract the interface location with the help of scalar function on a stationary grid, and Eulerian-Lagrangian methods[43, 46, 48] that utilize a separate set of grid representing interface (Lagrangian) that move freely on a background grid (Eulerian). Once the interface is known, various models are used to impose discontinuous flow properties across the interface, taking into account surface tension forces. These models either use a continuous interface method; using one set of equations and smearing the flow properties across the interface[43, 48, 113, 114], or sharp interface methods that impose conditions directly by solving two sets of equations [37, 115-118].

In this effort we use the Eulerian-Lagrangian method and the continuous interface method in conjunction with adaptive grid to increase resolution near the interface [46, 48]. Figure 1-9 (a) and(b) show sample of the Lagrangian interface grid used as line segments in 2D and triangular grid in 3D.

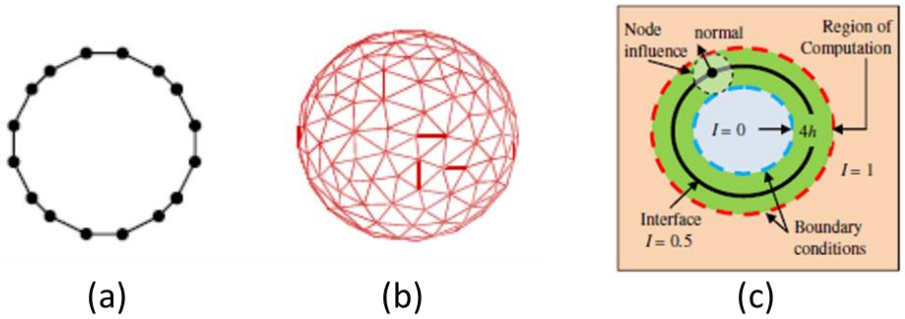

Figure 1-9 Interface representation by marker points (a) line segments in 2D (b) triangular elements in 3D (c) indicator function used to smear properties across the interface with values varying from 0 to 1[48]

The indicator function shown in Figure 1-9(c) is used to smear properties across the

interface in a continuous matter.

In order to simulate rupture dynamics for plug flow and propagation study, a reconstruction algorithm allowing topological change should be implemented. In chapter 5, the reconstruction algorithm along with detailed information about the numerical models and methodology will be discussed.

1.11 Objectives and Proposed Models

1.11.1 Jet and Crossflow Interaction

As discussed in section 1.7 due to the limitations of the RANS models and the impracticality of LES, hybrid RANS/LES models provide the best compromise between the two. The available hybrid models proved capabilities in successfully simulating highly unsteady jet and crossflow problems[27, 52], however, they lack generality due to domain size and geometry restriction, grid size and type limitations, or the need for a case-based adjustable constants. In the case of DES, they sometimes also face difficulties achieving smooth transition between RANS and LES. Our **first** modeling objective is to develop a model with the following characteristics

- Can be used to accurately simulate supersonic jet and crossflow interaction and in general, problems involving high speed mixing and unsteadiness
- Should be able to resolve turbulent structures similar to hybrid RANS/LES but be more practical in terms of grid size , generality, and the ability to deal with complex geometries.
- Achieves smooth transition between RANS and LES in reasonably varying grid

size.

In this effort we propose the use of multi-scale turbulence modeling [83, 84] based on the concepts of Johansen et al[83]'s filter based model. The multi-scale model is easy to implement for any two-equation model (In this study we select Menter SST[119]) by defining a grid length scale , a turbulent length scale, and a filter function. The eddy viscosity is smoothly varied based on the ratio of the turbulent length scale to the cell size. Therefore there is no sharp transition between RANS and LES and no restriction on where the transition should occur for reasonably varying cell size. This allows the use of any grid resolution with the finer grids simply capable of resolving more turbulent eddies. Because of the smooth nature of the model, we are able to use non-uniform grid and expect smooth solutions at the refinement interface. In the supersonic jet and crossflow interaction problem this will be especially useful when using three-dimensional (3D) grids that are only fine in the plume region and in regions where complex flow phenomena occur. The model is introduced in chapter 2 and results are shown and analyzed in chapter 3.

In section 1.6, the importance and sensitivity of the turbulent Schmidt number was discussed. It was mentioned that the assumption of a constant turbulent Schmidt number in the RANS assumption is inadequate[27, 29]. While there have been efforts to calculate rather than specify the turbulent Schmidt number using RANS-type formulation, to the author's knowledge, there has been no efforts in the literature to use an adaptive turbulent Schmidt number approach based on the resolved information in hybrid RANS/LES. Such a method would improve the turbulent mixing prediction of the modeled (sub-filter) portion of the flow, thus allowing the use of coarser grids in hybrid

RANS/LES approaches. Our **second** modeling objective is to develop a turbulent Schmidt number approach based on the resolved statistics in hybrid RANS/LES models. The model should have the following characteristics:

- Does not require specification of turbulent Schmidt number , Sc_t
- Can improve estimates for sub-filter mixing for coarser grids used with the multi-scale model
- Relies on actual flow for estimation without any correlation based on experiment or ad-hoc transport equations.

In chapter 2, we propose an extension to the multi-scale model allowing for the calculation of the turbulent Schmidt number. The method we propose does not utilize transport equations with ad hoc constants. The value of the turbulent Schmidt number in the sub-filter RANS model is adaptively changed based on the resolved turbulent field. At every time step, the average turbulent Schmidt number based on the ratio of the resolved mass and momentum eddy viscosity is calculated. This value is used in the mass transport equation instead of the specified constant value. The method assumes that Sc_t is the same in all turbulent scales, and in chapter 4, we evaluate this assumption with the Lin et al.[29] mixing case.

In **addition** to the modeling objectives, we would like to analyze the response and sensitivity of the jet and crossflow interaction problem to the proposed models; including effect of grid resolution and different injection configurations. Based on the analysis it is our objective to understand the advantages and limitations of our modeling approaches for simulation of supersonic crossflow.

1.11.2 Plug Propagation and Rupture

In section 1.9, the importance of plug propagation and rupture and its relationship to flow in lung airways is demonstrated. It is desirable to simulate this process to understand the behavior of mechanical stresses on the airway walls before and after plug rupture. This following are the objectives required for such simulation:

- Develop a reconstruction algorithm within the multi-phase flow solver to allow for rupture to be simulated.
- Validate the pre-rupture results against available data from the literature.
- Analyze dynamics of peak wall mechanical stresses location and time in relation to plug rupture.
- Analyze the effect of parameters such as: liquid film thickness, pressure drop, and surface tension forces on the magnitude and location of mechanical stresses as well as their effect on delaying plug rupture.

In chapter 5, we further extend a Eulerian-Lagrangian technique reported earlier [48] to handle topological changes during the plug rupture to investigate stresses at the airway walls. Specifically, in order to handle topological changes of fluid-fluid interfaces, we have developed a reconstruction scheme based on altering connectivity information detailed in the computational procedure section5.2. Comparison with the previous Lagrangian model, up to the rupture, and the flow field and associated stress characteristics during and after rupture will be discussed.

Chapter 2.
Governing Equations and Numerical Methods

2.1 Governing Equations

2.1.1 Instantanous Balance Equations

Instantaneous Navier-Stokes conservation equations for a chemically reacting mixture without body forces and external heating are given in Einstein notation as[120]:

$$\frac{\partial \rho}{\partial t} + \frac{\partial \rho u_i}{\partial x_i} = 0 \qquad \textbf{2.1}$$

$$\frac{\partial \rho Y_m}{\partial t} + \frac{\partial \rho u_i Y_m}{\partial x_i} = \frac{\partial}{\partial x_i}\left(\rho V_{m,j} Y_m\right) + \overline{\dot{\omega}_m}\ , \qquad m = 1, .., NS \qquad \textbf{2.2}$$

$$\frac{\partial \rho u_i}{\partial t} + \frac{\partial \rho u_i u_j}{\partial x_j} = -\frac{\partial p}{\partial x_i} + \frac{\partial \tau_{ij}}{\partial x_j} \qquad \textbf{2.3}$$

$$\frac{\partial}{\partial t}(\rho H - p) + \frac{\partial}{\partial x_j}\left(\rho u_j H\right) = \frac{\partial}{\partial x_j}(u_j \tau_{ij} - q_j) \qquad \textbf{2.4}$$

where Y_m, and is mass fraction of species m, $V_{m,j}$ is diffusion velocity for species m, and $\dot{\omega}_m$ is the chemical source term

For a Newtonian fluid, the viscous stress tensor is given by:

$$\tau_{ij} = \mu\left(\frac{\partial u_i}{\partial x_j} + \frac{\partial u_j}{\partial x_i}\right) - \frac{2}{3}\mu\frac{\partial u_k}{\partial x_k}\delta_{ij} \qquad \textbf{2.5}$$

where the bulk viscosity is neglected. In Equation 2.6, the species diffusion velocities are given by Fick's Law as:

$$V_{m,j}Y_m = -D_m \frac{\partial Y_m}{\partial x_j} \quad \textbf{2.6}$$

Note that in Equation 2.4, the heat flux vector contains both the Fourier's law component and the component due to diffusion of species with different enthalpies:

$$q_j = -\lambda \frac{\partial T}{\partial x_j} + \rho \sum_{m=1}^{NS} h_k D_k \frac{\partial Y_m}{\partial x_j} \quad \textbf{2.7}$$

2.1.2 Equation of State

Assuming each species behaves as a thermally perfect gas, Dalton's law is used to determine mixture pressure:

$$p = \sum_{m=1}^{NS} \rho_m R_m T \quad \textbf{2.8}$$

Note that an equation of state that supports thermally imperfect species could be used, however, it was not required for this effort. A more general equation of state that has been widely used in combustion problems was developed by Hirschfelder et al.[121, 122]

Equation 2.8 relates mixture pressure to mixture temperature which is not readily available from the solution of the balance equations. Temperature is instead obtained via the internal energy of the mixture:

$$e = \sum_{m=1}^{NS} Y_m e_m \quad \textbf{2.9}$$

where the internal energy of each species is evaluated as:

$$e_m = \int_{T_{ref}}^{T} c_{P_m}(\tau) d\tau - R_m T \qquad \textbf{2.10}$$

The species specific heats, c_{P_m}, are provided as 4th degree polynomials in terms of temperature. The polynomial coefficients can be obtained from references such as JANAF tables [123]

For each species, transport properties (laminar viscosity, μ, thermal conductivity, λ, and species diffusivity, D) are obtained via CHEMKIN transport library[124] in the form of 4th order polynomial fits as a function of temperature.

2.1.3 Averaged and Filtered Navier-Stokes Equations

The instantaneous balance equations 2.1-2.4 govern both laminar and turbulent flow regimes. However, turbulent flows exhibit flow structures covering a wide range of time and length scales.[125] Resolving all these scale numerically using direct numerical simulation (DNS) remains extremely costly for virtually all engineering problems. However, for most engineering purposes, the main interest is the description of the mean flow field, which is the common aim for all RANS-based turbulence models. RANS methods solve for the Favre averaged quantities, separating them from their turbulent fluctuations. In problems where there is interest in resolving large-scale turbulent structures, large eddy simulation (LES) is often used. LES solves a filtered version of the balance equations separating large-scale and sub-grid fluid dynamics.

For RANS formulation, each variable is decomposed into its density-weighted ensemble average[126] and its instantaneous deviation from the averaged value as:

$$\phi = \widetilde{\phi} + \phi'' , \widetilde{\phi} = \frac{\overline{\rho\phi}}{\bar{\rho}} \quad \textbf{2.11}$$

Favre averaging has the standard ensemble average properties as well:

$$\widetilde{\widetilde{\phi}} = \widetilde{\phi} , \widetilde{\phi''} = 0 \quad \textbf{2.12}$$

LES simulation models require filtering the balance equations into resolvable scale components and sub-grid scale (SGS) components. For a generic property A:

$$A = \breve{A} + A' \quad \textbf{2.13}$$

where $\breve{A}$ is the filtered component of the property. A generic spatial filter is of the form[127]

$$\breve{A}_\iota(x_i, t) = \int\int\int G(x_i - \xi_i, \Delta) A_i(\xi_i, \Delta) d^3\xi_i \quad \textbf{2.14}$$

The filter function is normalized as follows:

$$\int\int\int G(x_i - \xi_i, \Delta)\, d^3\xi_i = 1 \quad \textbf{2.15}$$

where $, \Delta,$ a spatial filter usually based on cell size allowing the filter operation to have properties similar to the averaging:

$$\breve{\breve{A}} = \breve{A} , \breve{A}' = 0 \quad \textbf{2.16}$$

Comparing equations 2.11 and2.12 with 2.13 2.16, we realize that the averaging and filtering operations exhibit identical definitions and properties. When applying either operation to the instantaneous balance equations we obtain equations of identical form for filtered or averaged quantities. We will use these equations interchangeably with the Favre average notation, however, they could also be written with the filter notation. The filtered/average form of the balance equations is:

Mass

$$\frac{\partial \bar{\rho}}{\partial t} + \frac{\partial \bar{\rho} \widetilde{u_\iota}}{\partial x_i} = 0 \qquad \textbf{2.17}$$

Momentum

$$\frac{\partial \bar{\rho} \widetilde{u_\iota}}{\partial t} + \frac{\partial \bar{\rho} \widetilde{u_\iota} \widetilde{u_\jmath}}{\partial x_i} = -\frac{\partial \bar{p}}{\partial x_i} + \frac{\partial}{\partial x_j}(\tau_{ij} - \overline{\rho u_\iota'' u_\jmath''}) \qquad \textbf{2.18}$$

The shear stress term for a Newtonian fluid is written as:

$$\tau_{ij} = \mu \left(\frac{\partial \widetilde{u_\iota}}{\partial x_j} + \frac{\partial \widetilde{u_\jmath}}{\partial x_i} - \frac{2}{3} \frac{\partial \widetilde{u_k}}{\partial x_k} \delta_{ij} \right) \qquad \textbf{2.19}$$

where fluctuations in dynamic viscosity are ignored

Species Mass Fraction

$$\frac{\partial \bar{\rho} \widetilde{Y_m}}{\partial t} + \frac{\partial \bar{\rho} \widetilde{u_\iota} \widetilde{Y_m}}{\partial x_i} = \frac{\partial}{\partial x_i} \left(-D_m \frac{\partial \widetilde{Y_m}}{\partial x_j} + \bar{\rho} \widetilde{u''_\jmath Y''_m} \right) + \overline{\dot{\omega}_m} \ , \qquad \textbf{2.20}$$

$$m = 1, .., NS$$

Energy

$$\frac{\partial}{\partial t}\left(\bar{\rho}\widetilde{H} - \bar{p}\right) + \frac{\partial}{\partial x_j}\left(\bar{\rho}\widetilde{u}_j \widetilde{H}\right) = -\frac{\partial}{\partial x_j}\left(q_j + \right.$$

$$\left.\overline{\rho u''_\jmath h''}\right) + \frac{\partial}{\partial x_j}\left[\tilde{u}_j\left(\tau_{ij} - \overline{\rho u_\iota'' u_\jmath''}\right)\right] + \frac{\partial}{\partial x_j}\left[\overline{u_\iota'' \tau_{\iota\jmath}} - \right. \qquad \textbf{2.21}$$

$$\left.\overline{\rho u''_\jmath \left(\frac{1}{2} u_\iota'' u_\iota''\right)}\right]$$

2.1.4 Turbulence Closure

Boussinesq's eddy viscosity hypothesis, in analogy to molecular transport, relates turbulent flux of momentum to mean velocity gradient and turbulent kinetic energy by introducing the concept of eddy viscosity, μ_t, as:

$$R_{ij} = -\overline{\rho u_i'' u_j''} = \mu_t \left(\frac{\partial \tilde{u}_i}{\partial x_j} + \frac{\partial \tilde{u}_j}{\partial x_i} - \frac{2}{3} \frac{\partial \tilde{u}_k}{\partial x_k} \delta_{ij} \right) - \frac{2}{3} \bar{\rho} k \delta_{ij} \qquad \textbf{2.22}$$

where *k* is turbulent kinetic energy:

$$\bar{\rho} k = \frac{1}{2} \overline{\rho u_i'' u_i''} \qquad \textbf{2.23}$$

While the molecular viscosity is a fluid property, the eddy (or turbulent) viscosity varies with the turbulent flow characteristics. On dimensional grounds, the kinematic eddy viscosity is:

$$\nu_t = \frac{\mu_t}{\rho} = l \; x \; u \qquad \textbf{2.24}$$

where *l* and *u* are the characteristic length and velocity scales of the turbulent fluctuations. The role of the turbulence model is then to model these two scales. The turbulent species flux is related to the first moments similar to molecular diffusion as:

$$\bar{\rho} \widetilde{u_j'' Y_m''} = \frac{\mu_t}{Sc_t} \frac{\partial \widetilde{Y_m}}{\partial x_j} \qquad \textbf{2.25}$$

Finally the unclosed terms in the energy equation are modeled as [128]

$$\bar{\rho} \widetilde{u_j'' h'} = \frac{\mu_t}{Pr_t} \frac{\partial \tilde{h}}{\partial x_j} \quad \widetilde{u_i} \qquad \textbf{2.26}$$

and

$$\overline{u_i'' \tau_{ij}} - \overline{\rho u_j'' \left(\frac{1}{2} u_i'' u_i'' \right)} = \left(\mu + \frac{\mu_t}{Pr_t} \right) \frac{\partial k}{\partial x_j} \qquad \textbf{2.27}$$

2.2 Turbulence Modeling

Since the instantaneous flow properties can be represented as the sum of a mean and fluctuating part or a resolved and sub-grid part (Eqs. 2.11,2.12 and 2.13-2.16),the

resulting governing equations contain fluctuation correlation terms that cannot be readily evaluated with the knowledge of the mean quantities. With the concept of the eddy viscosity, these quantities can be calculated once the eddy viscosity is estimated as a field variable. Detailed approaches to turbulent closure are an exhaustive subject and can be explored elsewhere.[125, 127, 129, 130] Amongst the most popular methods are the Reynolds/Favre averaged Navier-Stokes (RANS) model and the Large Eddy Simulation (LES)[25, 26, 131]

The most widely used RANS models solve two additional transport equations to calculate the eddy viscosity.[127] The two equations provide information of the time and length scales, which are then linked to the eddy viscosity via dimensional assessment. Derivation of these equations and relations are aided by numerous scaling arguments and empirical observations. Strictly speaking, only the small turbulent scales in the inertial and Kolmogorov ranges can be assumed universal and the larger scales will depend on the problem geometry.[125] LES models take advantage of this property of turbulent flows by attempting to numerically resolve the larger, geometry dependent scales while modeling the rest with sub-grid models (SGS). The SGS models in LES have the advantage of incorporating the information from the resolved scales and hence pose less or no empirical dependence. While LES methods offer increased accuracy in some cases, the also introduce a significant increase in computational cost compared to RANS models. The additional cost is due to the need of finer, 3D grids and a fine temporal resolution. In supersonic flows, wall grids needed for LES become prohibitively expensive and often times, they are not fully resolved[27, 132].

Due to the substantial computational cost of LES, RANS models remain widely used

for most engineering turbulent flows. For supersonic jet and crossflow interaction, large-scale turbulent structures are present making LES an attractive choice. However due to the prohibitively expensive boundary-layer grid, this option becomes unfeasible. This gave rise to hybrid RANS/LES methods[24, 27, 28, 74, 127]. In most hybrid RANS/LES methods, RANS like equations are solved near the wall , while LES-type equations are solved in areas where large-scale turbulent structures are present[27, 132, 133]. This class of methods attempts to take advantage of the RANS efficiency near the wall, and LES capabilities elsewhere.

2.2.1 RANS: Menter-SST

Two of the most widely used RANS turbulence models are $k-\epsilon$[76] and $k-\omega$[134], where k is the turbulent kinetic energy, ϵ is the dissipation rate and ω is defined as the dissipation rate per turbulent kinetic energy. The latter model offers improved accuracy near solid walls in the presence of adverse pressure gradients but displays strong sensitivity to free stream values[135]. Menter's shear stress transport (SST)[77] uses the $k-\omega$ near solid walls and transitions to $k-\epsilon$ away from the walls with the help of a blending function, hence combining the strength of both models. SST also incorporates an empirical dampening function for the eddy viscosity near the walls to mimic the suppression of turbulence. Due to the demonstrated enhancements[77] offered by the model without additional computational cost, SST was used as the base RANS model in the current study. Details of the model are given below.

Kinematic Eddy Viscosity

In the $k-\epsilon$[76] model, transport equations for the turbulent kinetic energy and its

dissipation rate are solved. The turbulent length and velocity scales in Equation2.24 are then related to k and ϵ as:

$$u = k^{\frac{1}{2}}, \qquad l = \frac{C_\mu k^{\frac{3}{2}}}{\epsilon} \tag{2.28}$$

where $C_\mu = 0.09$ is the dissipation rate constant. The dissipation rate is defined as:

$$\epsilon = \nu_t \overline{\frac{\partial u''_\iota}{\partial x_j} \frac{\partial u''_\iota}{\partial x_j}} \tag{2.29}$$

The kinematic eddy viscosity is defined as:

$$\nu_t = \frac{C_\mu k^2}{\epsilon} \tag{2.30}$$

In the $k - \omega$[134] model, instead of ϵ, a transport equation is solved for turbulent dissipation per turbulent kinetic energy defined as:

$$\omega = \frac{\epsilon}{C_\mu k} \tag{2.31}$$

hence, the eddy viscosity becomes:

$$\nu_t = \frac{k}{\omega} \tag{2.32}$$

In Menter's SST model [77], the ϵ equation is cast in terms of ω. The $k - \epsilon$ and $k - \omega$ models are blended based on nearest wall distance. The eddy viscosity in SST is expressed as:

$$\nu_t = \frac{a_1 k}{max(a_1 \omega, \Omega F_2)} \tag{2.33}$$

where Ω is the absolute value of vorticity, a_1=0.31 and the blending function, F_2 is given as:

$$F_2 = \tanh(arg_2^2) \quad \textbf{2.34}$$

$$arg_2 = \max\left(2\frac{\sqrt{\mathrm{k}}}{0.09\omega \mathrm{y}}, \frac{500\nu_{\mathrm{t}}}{\mathrm{y}^2\omega}\right) \quad \textbf{2.35}$$

where y is the normal distance to the nearest wall. Near the wall turbulent fluctuations are locally damped and the turbulent Reynolds number, $k^2/\epsilon\nu$, approaches zero. The SST model incorporates this effect via the empirically derived damping as shown in Equation2.33.

Turbulent Quantities Transport Equations

Exact equations for the turbulent kinetic energy, k, and its dissipation rate, ϵ or ω, can be derived[125] based on the instantaneous and averaged momentum equations,2.2 and 2.18, and the definitions given in Equations 2.23,2.292.31. However both introduce additional unclosed terms. Utilizing the gradient transport hypothesis and the turbulent Prandtl number, Pr_t, the diffusion term is modeled and the following form of the k equation is obtained:

$$\frac{\partial}{\partial t}(\bar{\rho}k) + \tilde{u}_l\frac{\partial}{\partial x_l}(\bar{\rho}k) = R_{ij}\frac{\partial \tilde{u}_l}{\partial x_l} - C_\mu\bar{\rho}\omega k + \frac{\partial}{\partial x_j}\left[\left(\mu + \frac{\mu_t}{Pr_t}\right)\frac{\partial k}{\partial x_j}\right] \quad \textbf{2.36}$$

where R_{ij} is given in Equation 2.22 and is proportional to the eddy viscosity. The exact equation for ω, however, is not as useful starting point since several other fluctuation correlations and higher order moments are introduced. Hence an entirely empirical form is used. In SST formulation, ω and ϵ equations are combined into a common form with a blending function which ensures a smooth switch based on the distance to the wall:

$$\frac{\partial}{\partial t}(\bar{\rho}\omega) + \tilde{u}_l \frac{\partial}{\partial x_l}(\bar{\rho}\omega) = \frac{\gamma}{\nu_t} R_{ij} \frac{\partial \tilde{u}_l}{\partial x_l} - \beta \bar{\rho}\omega^2 + \frac{\partial}{\partial x_j}\left[(\mu + \mu_t \sigma_\omega)\frac{\partial \omega}{\partial x_j}\right] + \frac{2(1-F_1)\bar{\rho}\sigma_{\omega 2}}{\omega} \frac{\partial k}{\partial x_j}\frac{\partial \omega}{\partial x_j} \quad \textbf{2.37}$$

where

$$F_1 = tanh(arg_1^4)$$

$$arg_1 = min\left(max\left(\frac{\sqrt{\mathrm{k}}}{0.09\omega \mathrm{y}}, \frac{500\nu}{\mathrm{y}^2\omega}\right), \frac{4\bar{\rho}\sigma_{\omega 2}k}{CD_{k\omega}\, y^2}\right) \quad \textbf{2.38}$$

$$CD_{k\omega} = max\left(\frac{2\bar{\rho}\sigma_{\omega 2}}{\omega}\frac{\partial k}{\partial x_j}\frac{\partial \omega}{\partial x_j}, 10^{-20}\right)$$

The last term in the ω transport equation is called the cross diffusion term. It arises due to the blending between $k-\epsilon$ and $k-\omega$ and does not appear in the standard $k-\omega$ model. F_1 is unity at the wall and the cross diffusion term vanishes resulting in pure $k-\omega$ model. The $k-\epsilon$ and $k-\omega$ constants[129, 136] are also blended as:

$$\phi = F_1\phi_{k\omega} + (1-F_1)\phi_{k\epsilon} \quad \textbf{2.39}$$

where $\phi_{k\omega}$ are:

$$\sigma_{k1} = 0.85, \qquad \sigma_{\omega 1} = 0.5, \qquad \beta_1 = 0.075, \qquad C_\mu = 0.09$$

$$\kappa = 0.41, \qquad \gamma_1 = \frac{\beta_1}{C_\mu} - \sigma_{\omega 1}\kappa^2/\sqrt{C_\mu} \quad \textbf{2.40}$$

and $\phi_{k\epsilon}$ are:

$$\sigma_{k2} = 1.0, \qquad \sigma_{\omega 2} = 0.856,$$
$$\beta_2 = 0.0828, \qquad C_\mu = 0.09$$
$$\kappa = 0.41, \qquad \gamma_1 = \frac{\beta_2}{C_\mu} - \sigma_{\omega 2}\kappa^2/\sqrt{C_\mu} \qquad \textbf{2.41}$$

2.2.2 LES: Smagorinsky Lilly Model

Most simply, in LES, the large-scale eddies are computed, and eddies smaller than the SGS eddies are modeled. This is done, similar to RANS, by introducing an eddy viscosity to the filtered Navier Stokes equations (Eqs.2.17, 2.21). Because larger fluctuations are calculated directly and SGS fluctuations are modeled, cells and time steps can be much larger than DNS, but smaller than those of RANS. The standard Smagorinsky model relates turbulent stresses to the magnitude of strain rate to define the eddy viscosity as [25, 26]:

$$\mu_{t_{SGS}} = \rho(\mathrm{C_s}\Delta)^2 \mathrm{S} \qquad \textbf{2.42}$$

where S is the strain rate magnitude defined as ,

$$S = \sqrt{S_{ij}S_{ij}} \qquad \textbf{2.43}$$
$$S_{ij} = \left(\frac{\partial \tilde{u}_i}{\partial x_j} + \frac{\partial \tilde{u}_j}{\partial x_i} - \frac{2}{3}\frac{\partial \tilde{u}_k}{\partial x_k}\delta_{ij}\right)$$

where $\mathrm{C_s} = 0.1 \sim 0.2$ is a constant and Δ is a length scale related to cell size. In LES simulations once the eddy viscosity is defined, it is related to Reynolds stresses and the sub-grid heat flux in a manner similar to the RANS approach:

$$R_{ij} = -\overline{\rho u_i'' u_j''} = \mu_t \left(\frac{\partial \tilde{u}_i}{\partial x_j} + \frac{\partial \tilde{u}_j}{\partial x_i} - \frac{2}{3} \frac{\partial \tilde{u}_k}{\partial x_k} \delta_{ij} \right) \quad \textbf{2.44}$$

$$\bar{\rho} \widetilde{u''_j Y''_m} = \frac{\mu_t}{Sc_t} \frac{\partial \widetilde{Y_m}}{\partial x_j} \quad \textbf{2.45}$$

$$\bar{\rho} \widetilde{u''_j h'} = \frac{\mu_t}{Pr_t} \frac{\partial \tilde{h}}{\partial x_j} \quad \widetilde{u_i} \quad \textbf{2.46}$$

It should be noted that the modeling of R_{ij} in equation 2.44 does not contain the isotropic turbulence term that is in equation2.18. This is because in LES formulation the turbulent kinetic energy, k, is not modeled, and dynamics resulting from isotropic turbulence is assumed to be contained within the filtered strain rate of velocity. In addition, modeling of the term in equation 2.21 is usually neglected altogether in LES.

2.2.3 Hybrid RANS/LES: NC State Model

In high-speed flows generally and supersonic jet and crossflow specifically, the grid needed to conduct an LES simulation near the wall is prohibitively expensive. Using RANS near the wall and LES elsewhere makes it possible to conduct such simulations, and to obtain detailed information about the large turbulent structures present in the flow. Hybrid RANS/LES approaches rely on the similarity in averaged and filtered balance equations. Boles et al.[27] take advantage of that by using one set of equations throughout the domain, and a blending function to change the value of the eddy viscosity from Menter BSL [119] to Smagorinsky SGS model. The eddy viscosity is defined as:

$$\mu_{t_{NC}} = \rho \left[\Gamma \frac{\mathrm{k}}{\omega} + (1 - \Gamma) \rho (\mathrm{C_s} \Delta)^2 \mathrm{S} \right] \quad \textbf{2.47}$$

where the authors[27, 132, 133]recommend a $\mathrm{C_s}$ value of 0.1 for high-speed flows. The

blending function is based on a ratio of the closest wall distance, d, to a modeled form of the Taylor microscale, λ:

$$\Gamma = \frac{1}{2}\left\{1 - \tanh\left[5\left(\frac{\kappa}{\sqrt{C_\mu}}\eta^2 - 1\right) - \phi_b\right]\right\} \quad \textbf{2.48}$$

Where

$$\eta = \frac{d}{A\lambda} \quad \textbf{2.49}$$

The physical location of the transition point is shifted by adjusting the value of A. The term ϕ_b is set to $\tanh^{-1}(0.98)$ so that the transition from RANS to LES occurs at $\Gamma = 0.99$. The function is set up that $d^+ = A^2$ at the RANS/LES juncture where $\Gamma = 0.5$. The value of d^+ is found using the method described in Edwards et al[137] using the Law of the wall formulation, free stream properties, wall thermal conditions, and estimated boundary-layer thickness.

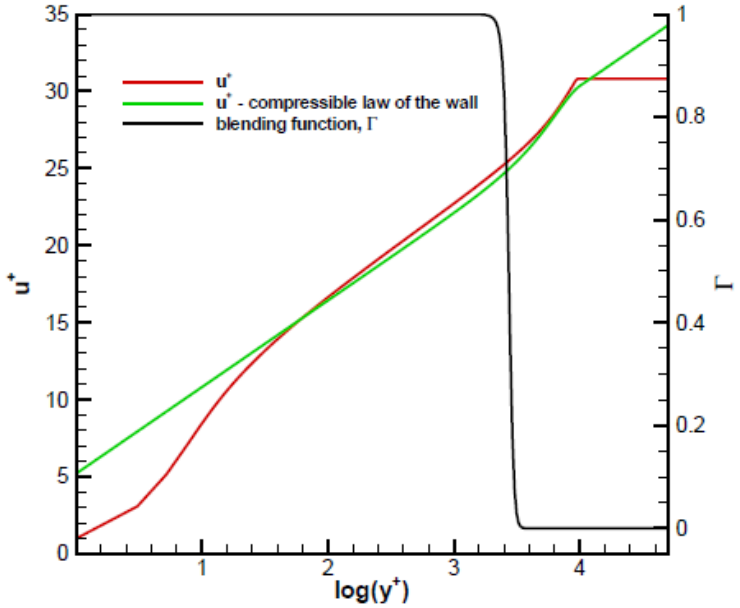

Figure 2-1 NC State blending function and velocity boundary-layer in wall coordinates

The value of A varies from case to case and must be predetermined prior to

running any computations. Figure 2-1 shows the blending function for NC state hybrid RANS/LES along with computed and law of the wall velocities in a compressible boundary-layer.

The use of the NC State model with the supersonic jet and crossflow interaction problem produced superior results over RANS when compared to the experiment[27]. The model however, lacks generality due to the calibration of A in Eq 2.49. Also, because the blending function,Γ, has to lie within the boundary-layer, finer grid is required near the wall, although not as fine as LES requirements[28]. The method was also restricted to structured type grids, thus injector solution had to be imposed on the bottom wall, rather than simulated(due to injector geometry). The simulation grid limitation also required the use of a smaller domain and artificial turbulence for the inflow boundary

2.2.4 Detached Eddy Simulation (DES)

Detached Eddy Simulation (DES) was proposed [24] as a remedy for computations with large separated flows that are wall bounded. These flows can benefit from an LES like computation of the eddies away from the wall (detached) while the wall bounded eddies (attached) are treated with standard RANS methods. The main idea in DES is altering the mixing length ,l , with one that is related to the grid spacing and/or wall distance. Spalart et al[24] conducted the modification to the Spalart-Allmaras RANS equations[79] by replacing the distance to the wall ,d_w, with the DES length scale, $\tilde{l}$, throughout the model formulation,

$$\tilde{l} = \min(d_w, C_{DES}\Delta) \qquad \textbf{2.50}$$

The grid spacing is the maximum cell dimension,

$$\Delta = \max(\Delta_x, \Delta_y, \Delta_z) \quad \textbf{2.51}$$

This formulation works near the wall due to cell anisotropy. $\tilde{l}$ becomes the distance to the wall while away from the wall it becomes related to the grid size. The only experimentally adjustable constant is C_{DES} and it is typically ~ 1. Note that DES allows single variable formulation throughout the domain without the need for an explicit blending function between RANS and LES.

Strelets[138] applied the DES idea to Menter-SST turbulence model, first by defining the turbulence length scale,

$$l_{k-\omega} = k^{\frac{1}{2}}/\beta^*\omega \quad \textbf{2.52}$$

then replacing the length scale in the k transport equation destruction term as follows,

$$D^k_{RANS} = \rho\beta^* k\omega = \frac{\rho k^{\frac{3}{2}}}{l_{k-\omega}} \quad \textbf{2.53}$$

$$D^k_{DES} = \frac{\rho k^{\frac{3}{2}}}{\tilde{l}}$$

The DES length scale in this case is defined as follows,

$$\tilde{l} = min(l_{k-\omega,} C_{DES}\Delta) \quad \textbf{2.54}$$

The DES method effectively increases the destruction term in the RANS equations, thus reducing the modeled turbulent kinetic energy. Boundary-layer grids, however, can trigger LES computation without the proper grid resolution due to parallel grid densities[20, 139]. While variations to the original DES method exist to remedy some issues related to the grid[20, 82], DES still requires carful grid generation to properly handle the RANS/LES juncture and avoid abrupt transition. Production of such grids is

difficult for complex geometry and/or internal flows

2.2.5 Filter Based Approach

The filter based approach relies on reducing the eddy viscosity within the RANS model using a filter function. The filter function is directly related to the grid size and turbulent length scale thus allowing the model to only resolve turbulence where the grid resolution allows. Similar to DES, there is only one set of equations being solved without explicit blending between RANS and LES. The filter based model (FBM) is originally formulated by Johansen et al.[83] to modify the $k-\epsilon$ model by first defining a grid length,L_G, scale and turbulent length scale turbulent length scale,L_T

$$\mathrm{L_G} = \Delta \textbf{ or } \sqrt{dxdydz}$$
$$L_T = k^{3/2}/\epsilon \qquad \textbf{2.55}$$

The grid length scale is either a constant measure, Δ, usually taken as the largest grid size in the domain or varies by cell size in hexahedral grid. Only the constant $\mathrm{L_G}$ was tested by Johansen et al.[83], while the use of the cell-based $\mathrm{L_G}$ was proposed. The filter function is then constructed based on $\mathrm{L_G}$ and $\mathrm{L_T}$:

$$\mathrm{f_{d_{FBM}}} = \min\left(1, \mathrm{C_3}\frac{\mathrm{L_G}}{\mathrm{L_T}}\right) \qquad \textbf{2.56}$$

The eddy viscosity follows,

$$\nu_\mathrm{t} = \mathrm{f_d}\nu_{\mathrm{t_{RANS}}} \qquad \textbf{2.57}$$

where the constant C_3 was set to a value of 1. The constant must must be recalibrated for use with other RANS based models. The filter function ensures that the eddy viscosity does not increase beyond the RANS value and is proportional to the ratio of $\mathrm{L_G}/\mathrm{L_T}$. The

filter based model was tested with 2D subsonic simulation of flow over square. It was also used by Tseng and Shyy[140] with both 2D and 3D simulations of cavitation flow, in all studies only a constant L_G was used.

Nichols and Nelson[84] proposed a method called the multi-scale hybrid RANS/LES approach. Similar to the filter based model, they modified the $k-\epsilon$ formulations by proposing a turbulent and grid length scales

$$L_{G_{NN}} = max(dx, dy, dz)$$
$$L_{T_{NN}} = max\left(6\sqrt{\frac{\nu_{t_{RANS}}}{\Omega}}, \frac{{k_{RANS}}^{3/2}}{\epsilon_{RANS}}\right) \quad \textbf{2.58}$$

They used a smoother filter function to avoid abrupt transition issues between RANS and LES,

$$f_{d_{NN}} = \frac{1}{2}\left\{1 + tanh\left[2\pi\left(\frac{1}{1+\left(\frac{L_T}{2L_G}\right)^{4/3}} - 0.5\right)\right]\right\} \quad \textbf{2.59}$$

Unlike the filter based model, they had a slightly different definition of the eddy viscosity based on an additional eddy viscosity related to LES , $\nu_{t_{LES}}$

$$\nu_t = (1 - f_{d_{NN}})\nu_{t_{RANS}} + f_{d_{NN}}\nu_{t_{LES}}$$
$$\nu_{t_{LES}} = C_{NN}L_G\sqrt{k_{LES}},\ k_{LES} = f_{d_{NN}}k_{RANS} \quad \textbf{2.60}$$

Nichols and Nelson tested the method with several subsonic problems including flow over a cylinder, NACA 0015 airfoil and square cavity. It was also tested with essentially 2D supersonic shear flow where it showed superior results over the DES method due to the smooth filter function allowing the transition between RANS and LES to occur without abrupt discontinuous solutions[84].

2.3 Current Modeling Approach

With the concept of eddy viscosity used in either a standard two-equation RANS approach or the Smagorinsky sub-grid model in LES, both filtered and averaged mass, momentum, and energy equations yield an identical mathematical form (assuming we use the modeling in Equations 2.17-2.21 for all models).By averaging the output variables of each model, the balance equations combined with the averaging procedure, become a single mathematical formulation in which we input an eddy viscosity and output averaged quantities. This formulation is valid for averaged, filtered and instantaneous equations as long as the correct eddy viscosity value is provided.

Employing concepts from the filter based approach in section 2.2.5, we propose the multi-scale model for use in supersonic jet and crossflow interaction. We assume the input eddy viscosity is a continuous function that varies from the RANS value to zero depending on the ratio of the grid size, L_G, to a locally defined turbulence length scale, L_T. The model should allow smooth transition from RANS to LES to DNS with the grid size and local turbulent length scales being the determining factors of which model to use. When employing this approach, there should not be limitations on grid size or geometry because the transition between the models can occur anywhere in the computational domain.

The concept is introduced already in the filter based model developed by Johansen et al.[83] however, it should be extended for use of high-speed flows, specifically the supersonic jet and crossflow interaction. To extend the filter based model for our current use, the following is proposed

- The turbulence length scale L_T is reformulated for used with Menter-SST

turbulence model which shows better performance for wall bounded flows than $k-\epsilon$

- The constant of proportionality, C_4 , is calibrated by relation to LES and DES models
- The turbulent grid length scale is cell based , formulated for unstructured grids, to allow maximum use of grid resolution locally and allow varying grid sizes within the computational domain.
- A filter function similar to that of Nichols and Nelson[84] is used for smooth transition between RANS and LES

To improve the multi-scale model's performance in jet and crossflow interaction simulation, we propose the use of the adaptive turbulent Schmidt number extension. Turbulent fluctuations are collected from the multi-scale simulation to estimate a resolved turbulent Schmidt number, which is adapted and used in the RANS formulation instead of the constant value. The model improves turbulent mixing predictions and allows multi-scale simulations with coarser grids. Details of the model will be discussed in subsequent sections.

2.3.1 Multi-scale Turbulent Treatment

Model Formulation

To extend the filter-based model (FBM) developed by Johansen et al.[83] for use with the Menter's SST[77] turbulence model, we define the turbulent length scale based on Menter-SST formulation in section2.2.1,

$$L_T = \frac{\sqrt{k}}{C_4 \max(\omega, \frac{SF_2}{a_1})} \qquad \textbf{2.61}$$

where C_4 is added to the definition of the turbulent length scale similar to C_3 in Eq2.57 as

a proportionality factor relating the reduction of the eddy viscosity to the turbulent length scale. The constant, C_4, must be calibrated for use the Menter-SST turbulent model. In a manner similar to the method used by Johansen et al.[83] one can relate C_4 to the Smagorinsky constant in the LES limit. First we set the eddy viscosity (away from the wall) equal to its Smagorinsky counterpart,

$$f_d \nu_{t_{RANS}} = C_4 L_G \sqrt{k} = (C_s L_G)^2 S \qquad \textbf{2.62}$$

Assuming equilibrium between turbulence production and dissipation in the LES limit, one can approximate the LES limit production is $0.3kS$, while dissipation is $\nu_t S^2$

$$\nu_t S^2 = 0.3kS$$

$$\sqrt{k} = \sqrt{\frac{\nu_t S}{0.3}} = \frac{C_4 L_G S}{0.3} \qquad \textbf{2.63}$$

$$C_4 = C_s \sqrt{0.3} = 0.0548 \qquad \textbf{2.64}$$

The value of *Cs* varies, but in this approach we use the value of 0.1 as recommended by Boles et al[27, 132, 133]for this particular case.

The multi-scale approach can also be related to DES by looking at the dynamics in the Menter SST- DES model in Eqs.2.52-2.54 .If the selection of the DES length scale is conducted every time step (as opposed to only at the beginning of the simulation), then in areas of fine grid the destruction of k will increase, decreasing the eddy viscosity, which will in turn, resolve more turbulence length scales. $\tilde{l}$ will keep on decreasing until it drops below the value of $C_{DES}\Delta$ at that time the length scale in the original menter SST equations will be used and the eddy viscosity will be increased again until it reaches $C_{DES}\Delta$. So in effect the method tries to find the value of ν_t that will cause the menter SST

k-ω transport equations to produce a turbulence length scale such that,

$$\tilde{l} = k^{\frac{1}{2}}/(\beta^{*}\omega) = C_{DES}\Delta \qquad \textbf{2.65}$$

This is equivalent to a multi-scale approach with a filter function that stops reducing the eddy viscosity at the same ratio of turbulence length scale to grid size. This can be formulated for the Johansen [83]FBM as follows: For the Menter-SST turbulence model,

$$f_{d_{DES}} = \min\left(1, \frac{C_{DES}\Delta\beta^{*}\omega}{k^{1/2}}\right) \qquad \textbf{2.66}$$

Strelets[138] used the experiments of Comte-Bellot and Corsin [141] to calibrate C_{DES}. The experiments were of homogeneous isotropic turbulence. Strelets reported two values of C_{DES}; $C_{DES_{k-\omega}}$for the $k-\omega$ portion of Menter SST and $C_{DES_{k-\epsilon}}$for the $k-\epsilon$ portion. Strelets suggested blending the two values using Menter SST blending function. For simplicity, however, we know that the LES regime will almost always lie in the $k-\epsilon$ portion of the domain (because RANS is applied near the wall) so the value of $C_{DES_{k-\epsilon}}$ is the most reasonable, and it is 0.61. $C_{DES}\beta^{*} = 0.0549$ is comparable to the value chosen for C4=0.0548.

The grid length scale used in this effort is cell-based; each cell has its own grid length scale, L_G. The use of a cell-based grid length scale allows the use of non-uniform grids without sacrificing the amount of turbulence being resolved. In this study, for example, the fine grid used in the baseline case contains coarse cells with grid length scale that is 75 times larger than finer cells near the injector area. The grid length scale is compatible with LOCI-CHEM framework which uses general type unstructured mesh, and is defined as,

$$L_G = 2\,max\left|\vec{X}_{center} - \vec{X}_{face}\right| \qquad \textbf{2.67}$$

Where $\vec{X}_{center}$ and $\vec{X}_{face}$ are the position vectors for the center of the cell and each face center the cell contains respectively. The distance between the two vectors is calculated for each face for the cell considered then the maximum distance is chosen and multiplied by 2. L_G is therefore the maximum possible distance between two face centers in a cell. It is a conservative measure to ensure robust computation with oddly shaped cells.

Choice of Filter

The filter function used in this effort is based on the work of Nichols and Nelson[84]. Due to their smooth function, transition between RANS and LES occurred smoothly with superior results to DES [84]. Their definition of the eddy viscosity is, however, different than the one used in FBM. Before using their filter function, it must be reformulated with the same definition used by FBM. Comparing Eq2.57 to Eq.2.64, one can re-write Eq.2.64 in terms of Nichols and Nelson's filter , $\mathbf{f_{d_{NN}}}$ as follows,

$$\nu_{t_{NN}} = \nu_{t_{RANS}} f_{d_{NN}} + (1 - f_{d_{NN}}) C_4 L_G \sqrt{f_{d_{NN}} k} \qquad \textbf{2.68}$$

We can further manipulate Eq.2.71 to be in the same form of Eq.2.57for direct comparison with FBM,

$$\nu_{t_{MS}} = \nu_{t_{RANS}} f_{d_{NN}}{}^{*} \qquad \textbf{2.69}$$

Where the effective function, $f_{d_{NN}}{}^{*}$, is rewritten as,

$$f_{d_{NN}}{}^{*} = f_{d_{MS}} + \frac{L_G}{L_T}(1 - f_{d_{MS}})\sqrt{f_{d_{MS}}} \qquad \textbf{2.70}$$

Filter Function Role and Solution Dynamics

The filter functions, $f_{d_{FBM}}$, $f_{d_{NN}}$, and $f_{d_{NN}}{}^{*}$,are plotted in Figure 2-2 versus

L_T/L_G. The filter value is near unity where L_T/L_G is smaller than one so that the model renders standard RANS in grid areas that cannot resolve further turbulent structure. The filter also approaches zero as L_T/L_G goes to infinity and turbulence modeling is no longer needed. The filter functions are intended to be general and capable of handling a wide range of grid resolutions and flow conditions.

Therefore, in order to evaluate the filter functions in Figure 2-2 we must first understand their dynamic role in progressing the solution in regions varying in grid size and turbulence intensity. In all the following cases we assume that we start applying the multi-scale approach to a converged RANS solution:

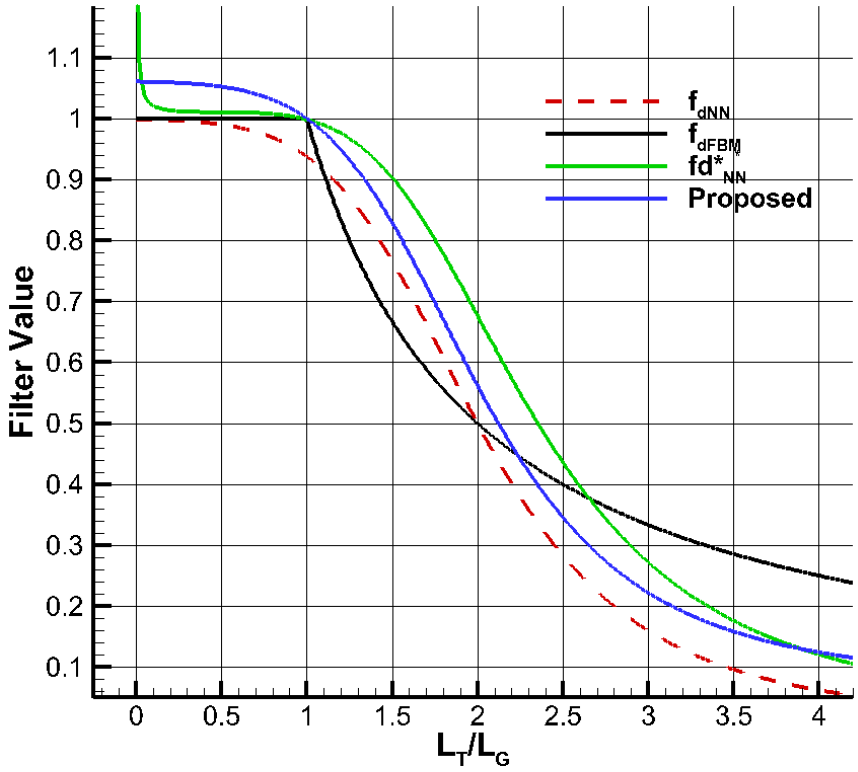

Figure 2-2 Filter functions for FBM, multi-scale models and proposed filter

1. Flow is approaching laminar, $L_T/L_G \sim \infty$: In this case the grid size can handle the flow and the filter function should approach zero. Reducing ν_t will not cause any production of turbulent structures. Because the eddy viscosity is used again in the

k transport equation. It will be recursively reduced without a stop because L_T/L_G will not reach unity.

2. Flow is turbulent but grid is capable of resolving all turbulent scales, $L_T/L_G > 1$: In this case the flow is initially free of turbulent structures because of the original RANS solution. *fd* will be less than 1, and as ν_t decreases more vortical structures are formed, and the RANS equations act as a subgrid model for the unresolved part of the grid. This in turns decreases ν_{t_RANS} and L_T/L_G which increases the filter function as more scales are resolved. Even after all scales are resolved L_T/L_G remains greater than 1 and *fd* will be less than unity. Lowering the eddy viscosity further will not affect the solution negatively therefore to be successful in this region *fd* should be low enough that it does not reach unity before all scales are resolved.
3. Flow is turbulent but grid is capable of resolving some turbulent length scales, and the unresolved portion is in the dissipation range, $L_T/L_G > 1$ then $L_T/L_G < 1$: This represents the LES limit. The flow is initially free of turbulent structures and vortices are forming while ν_{t_RANS} decreases and *fd* increases until it reaches 1) and that stops any further decrease of ν_t. The value of the filter function near *fd*=1 is very critical as it determines at which value of L_T/L_G the filtering action stops. In the case of FBM, C_4 is calibrated to match the LES limit in this region which should adjust the filtering process accordingly. This however may not be an exact match, as different two-equation models calculate RANS variables differently. If ν_t were to drop further below the LES value the vortical structures will continue to

be produced until the numerical viscosity takes over and stops further eddies from forming. This will be equivalent to the Implicit LES approach.

One way to alleviate this problem is to set a lower limit for the eddy viscosity as follows:

$$\nu_t = \max(\nu_t, \nu_{t_{LES}}) \qquad \textbf{2.71}$$

where $\nu_{t_{LES}}$is calculated using the standard Smagorinsky model in Eq.2.42

4. Flow is turbulent but grid is capable of resolving some turbulent length scales, and the unresolved portion is *not* fully in the dissipation range, L_T/L_G >1 then L_T/L_G <1: This is the hardest region to resolve because it lies between RANS and LES. There is a dependence on the filter function value at *fd*=1 as it determines when to stop the filtering process. In this region, care must be taken so that ν_t is not decreased to the implicit LES limit, and that the two equation model is used as a sub-grid model for the entire process. Increasing L_T/L_G at *fd*=1 would drive the modeling away from the implicit LES limit but would compromise resolving vortical structures at finer, higher quality grid regions. The filter function should be constructed so that there is some compromise, where finer regions may not resolve all possible turbulent length scales, and bad quality cells that are far from regions of interest will end up at the implicit LES limit because of the higher numerical viscosity they possess. When there is a large variation in grid size in this region transfer of turbulent kinetic energy between the resolved and the sub-grid scales may need special attention. Johansen et al.[83] suggest adding an extra term to the k equation containing the gradient of cell size to alleviate this problem.

5. Flow is turbulent but grid is not capable of resolving any turbulent length scales, L_T/L_G <1: This is the RANS limit where the filter value should be very close to 1 so that it does not alter the original RANS eddy viscosity. ν_t and *fd* stay constant because no eddies are produced.

Considering the scenarios mentioned above the filter function should match fd_{-FBM} as much as possible near *fd*=1 so that C_4 is calibrated correctly. *fd* should be very close to 1 in the RANS limit when L_T/L_G <=1with the maximum value being a little above unity to ensure that it will numerically stop reducing ν_t when it is required to do so. The filter should also be smooth for stability reasons.

From the filters in Figure 2-2, $f_{d_{FBM}}$lacks smooth transition and its maximum value is 1. $f_{d_{NN}}{}^{*}$ is smooth but it possess higher filter values near L_T/L_G~1 than those of $f_{d_{FBM}}$ and increases the RANS value by 18% as L_T/L_G approaches zero. $f_{d_{NN}}$ is the best choice of all three but needs higher filter values near L_T/L_G <1. A proposed filter[29] function that is similar to $f_{d_{NN}}$ but shifted up so that L_T/L_G =1 at *fd*=1 is also plotted in Figure 2-2. This filter is implemented by using the Nichol and Nelson's[84] filter shifted as follows,

$$f_{d_{proposed}} = f_{d_{NN}} + 0.0622 \qquad \textbf{2.72}$$

The filter function in Eq.2.72 is used in the current approach along with L_T of FBM and a conservative measure for L_G designed for unstructured grids a summary of the multi-scale model we use in the current effort is provided in Eq.2.73

$$f = \frac{1}{2}\left\{1 + tanh\left[2\pi\left(\frac{1}{1+\left(\frac{L_T}{2L_G}\right)^{\frac{4}{3}}} - 0.5\right)\right]\right\} + 0.0622 \qquad \textbf{2.73}$$

$$L_T = \frac{\sqrt{k}}{C_4 \max(\omega, SF_2/a_1)}$$

$$L_G = 2\,max\left|\vec{X}_{center} - \vec{X}_{face}\right|$$

$$\nu_t = f\nu_{t_{RANS}}$$

2.3.2 Adaptive Turbulent Schmidt Number Extension

The multi-scale approach, similar to other hybrid RANS/LES approaches, when applied to the jet in a cross flow causes turbulent eddies to appear in the solution. When those eddies are used to estimate the turbulent Schmidt number large variations are observed. It is therefore believed that one of the weakest aspects of using a RANS model alone is the assumption of a constant turbulent Schmidt number[27, 29].

The numerical scheme used in this work is only second-order upwind, thus very fine grids are needed for the multi-scale model to resolve considerable scales of turbulence. It is therefore of interest to try to improve the predictions of the sub-filter RANS model which in this case is Menter SST[77]. The purpose of the adaptive turbulent Schmidt number approach is to improve the value of the turbulent Schmidt number in the sub-filter RANS model based on the resolved field. The need and value of this approach will be discussed in subsequent chapters based on supersonic jet and crossflow interaction simulations conducted with the multi-scale model.

In the standard RANS approach the turbulent momentum flux is modeled as follows,

$$-\overline{\rho u_i' u_j'} = \mu_t S_{ij}(\tilde{u}_i) - \frac{2}{3}\overline{\rho k}\delta_{ij} \qquad \textbf{2.74}$$

$$S_{ij}(\tilde{u}_i) = \left(\frac{\partial \tilde{u}_i}{\partial x_j} + \frac{\partial \tilde{u}_j}{\partial x_i} - \frac{2}{3}\frac{\partial \tilde{u}_k}{\partial x_k}\delta_{ij}\right) \qquad \textbf{2.75}$$

Turbulent mass flux for multispecies is modeled as,

$$-\overline{\rho u_i' Y_m'} = \frac{\mu_t}{Sc_t}\frac{\partial \tilde{Y}_m}{\partial x_i} \qquad \textbf{2.76}$$

We can multiply both sides of Eq.2.74 by $S_{ij}(\tilde{u}_i)$ and both sides of Eq2.76 by $\partial \tilde{Y}_m/\partial x_i$ to obtain scalar equations. This process, while mathematically correct, it is not unique. Eqs. 2.74 and 2.73 are tensor equations and lumping the information contained into scalar form can be done in many combinations. We choose the scaling by $S_{ij}(\tilde{u}_i)$ and $\frac{\partial \tilde{Y}_m}{\partial x_i}$ to emphasize their role in the definision of turbulent quantaties. Then we can define mass and momentum eddy viscosities based on turbulent fluctuations,

$$\upsilon_{t,mom} = \frac{\mu_t}{\bar{\rho}} = -\frac{\left(\overline{\rho u_i' u_j'} - \frac{2}{3}\overline{\rho k}\delta_{ij}\right) S_{ij}(\tilde{u}_i)}{\bar{\rho} S_{ij}(\tilde{u}_i) S_{ij}(\tilde{u}_i)} \qquad \textbf{2.77}$$

$$\upsilon_{t,mass} = \frac{\mu_t}{Sc_t \bar{\rho}} = -\frac{(\overline{\rho u_i' Y_m'})}{\bar{\rho}}\frac{\left(\partial \tilde{Y}_m/\partial x_i\right)}{\left(\partial \tilde{Y}_m/\partial x_i\right)\left(\partial \tilde{Y}_m/\partial x_i\right)} \qquad \textbf{2.78}$$

The turbulent Schmidt number can be obtained by dividing the mass and momentum eddy viscosities. When using the multi-scale model approach only fluctuations in the resolved field are calculated directly, while those in the sub-filter field are calculated using the RANS model. To eliminate uncertainties associated with specifications of the turbulent Schmidt number. We defined the resolved turbulent Schmidt number based on resolved quantities as follows,

$$Sc_{t\_Res} = \frac{\frac{\left(\overline{\rho u_i^R u_J^R} - \frac{2}{3}\overline{\rho k_{Res}}\delta_{ij}\right) S_{ij}(\tilde{u}_i)}{\bar{\rho} S_{ij}(\tilde{u}_i) S_{ij}(\tilde{u}_i)}}{\frac{\left(\rho u_i^R Y_m^R\right)}{\bar{\rho}}\frac{(\partial \tilde{Y}_m/\partial x_i)}{(\partial \tilde{Y}_m/\partial x_i)(\partial \tilde{Y}_m/\partial x_i)}} \qquad \textbf{2.79}$$

The use of the resolved turbulent Schmidt number in the RANS model assumes that the ratio of turbulent momentum fluxes and turbulent mass fluxes in the resolved

portion of the flow is the same as in the unresolved portions of the flow. In other words if we split the energy spectrum at a certain wave length equal to the filter function we have equal ratios of mass and momentum turbulent fluxes in the sub-filter and resolved portions. While this seems like a very reasonable assumption, it does require further investigation. The results and cases presented in subsequent chapters could be regarded as validation for this assumption.

The resolved turbulent Schmidt number (Sc_{t_Res}) is calculated at every time step during the simulation and is used in the RANS mass transport equation. The value of the resolved turbulent Schmidt number is theoretically constant at every time step however, because averages are not available a priori, the estimations of the averages improve as the simulation proceeds and Sc_{t_Res} converge to a constant value. Also the application of Sc_{t_Res} into the RANS sub-filter model is not done until after a number of iterations at constant Sc_t , to avoid erroneous values of Sc_{t_Res} at the beginning of the simulation. Also the positivity of the resolved turbulent Schmidt number is maintained by taking the absolute value.

This approach is tested in subsequent chapters and in previous effort [30] and it is found that the effect of the adaptive approach is limited because numerical viscosity was not taken into consideration when calculating sub-filter turbulent diffusion. The following correction is suggested to the Reynolds diffusion term,

$$D_{i_m}^R \approx -\frac{\mu_t + \mu_{\text{num}}}{Sc_t}\frac{\partial \tilde{Y}_m}{\partial x_j} \qquad \textbf{2.80}$$

The numerical viscosity is estimated using the generalized coefficient approach[142, 143] taking the following approximate value

$$\mu_{\text{num}} = \bar{\rho} C_{\text{gs}} L_G^2 |S| \qquad \textbf{2.81}$$

A generalized coefficient, C_{gs}, value of 0.2 is used in this effort as suggested by Mossi et al.[143] for a second order scheme in a compressible fully developed flow. The need and value of the adaptive approach with and without the numerical viscosity correction in Eq2.80 will be discussed in detail in subsequent chapters based on the simulation results.

2.4 Numerical Methodology

2.4.1 Base CFD Code

Loci-Chem[144]CFD code is utilized in the current study. It is based on a rule-based programming framework called Loci[145]. Applications in Loci are written using a collection of rules, each of which is implemented in the form of a C++ class. In addition, the user must create a database of facts describing the known facts of the problem, such as boundary conditions. Once the facts and rules are provided, a query is made to have the system construct a solution. A salient feature of Loci is its ability to automatically determine the scheduling of events in order to produce the answer to the desired query. It also tests the consistency of the inputs to determine whether a solution is possible. Another major advantage of Loci is its automatic handling of domain decomposition and distribution of the problem to multiple processors. Loci-Chem is a density-based finite-volume code operating on unstructured and mixed element types. Evaluation of gradients at cell and face centers leads to second-order-accurate convective and diffusive fluxes. The order of accuracy maybe considered too low for LES type problems, however, the

code provides much needed flexibility and stability with varying geometries and grid quality. For a more comprehensive background on finite-volume and unstructured grid methods, see the text by Blazek[146].

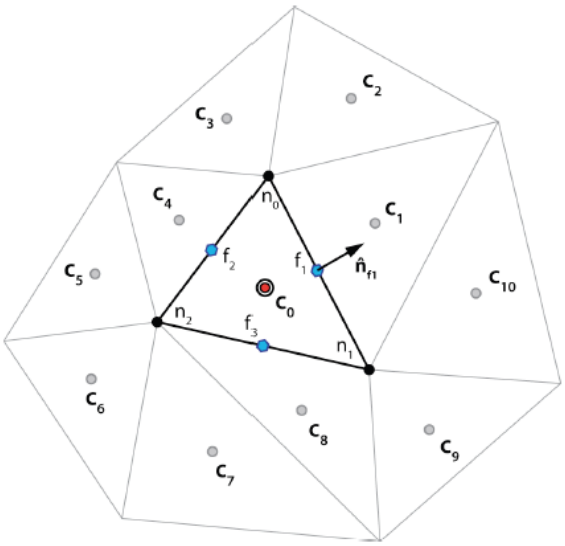

Figure 2-3 Cell-neighbor notation in an unstructured grid

All of the flow variables are stored at cell centers (collocated arrangement). Variations of the primitive variables within the cell are reconstructed as a piece-wise linear function:

$$\Phi_{c_0}^{R}(\vec{x}) + \nabla\Phi_{c_0}.\left(\vec{x} - \vec{x}_{c_0}\right) + 0\left(\left(\vec{x} - \vec{x}_{c_0}\right)^2\right) \qquad \textbf{2.82}$$

where Φ is any primitive variable (see Figure 2-3 for notation). The gradient at cell center c_0 is obtained via minimizing the weighted error (via least squares) between the reconstruction and the face sharing neighbor cell center values:

$$error = \sqrt{\sum_{f}\left(A_f\left(\Phi_{c_0}^{R}(\vec{x}_{nbr}) - \Phi_{nbr}\right)\right)^2} \qquad \textbf{2.83}$$

where *nbr* denotes the face sharing neighbor cell index and A_f is the area of the face.

In the presence of discontinuities, Eq.2.82 is prone to produce non-physical overshoots. Hence the reconstruction is limited as:

$$\Phi_{c_0}^{R}(\vec{x}) + \Psi_{c_0} \nabla\Phi_{c_0}.\left(\vec{x} - \vec{x}_{c_0}\right) \qquad \textbf{2.84}$$

where Ψ_{c_0} is a limiter function. In the current study, the limiter proposed by Venkatakrishnan[147] is used.

For the evaluation of diffusive fluxes, gradients at the face centers are needed. They are obtained via volume weighted average of the neighboring cell centered gradients; $\nabla\Phi_{avg}$, and the component of the gradient along the face normal direction is replaced by the more accurate direct finite differencing. An example for face f_1 in Figure 2-3 is:

$$\nabla\Phi_f = \nabla\Phi_{avg} - \left(\nabla\Phi_{avg}\,.\,\vec{n}_f\right)\vec{n}_f + \frac{\Phi_{c_1} - \Phi_{c_2}}{\left(\vec{x} - \vec{x}_{c_0}\right).\,\vec{n}_f}\,\vec{n}_f \qquad \textbf{2.85}$$

Loci-Chem[144] solves for each flow variable($\rho_1, .., \rho_{NS}, u_i, E, k, .. etc$) in a fully coupled manner with implicit 1st or 2nd order time integration. Generalized Minimal Residual Method (GMRES) algorithm with Jacobi preconditioning is used for the solution of the linear system. Pressure is obtained via the equation of state(ideal gas law). Construction of cell variables on either side of a face is achieved via Eq. 2.84. An approximate Riemann solution for these initial left and right states is obtained via the well-known Roe scheme, extended for multi-species and reacting flows[148]. The SST turbulence model is used as described in section 2.2

2.4.2 Implementation of Current Model

Multi-scale model

Implementation of the multi-scale model into Loci-Chem is done simply by modifying the kinematic eddy viscosity produced by the code at each time-step with the filter function shown in Eq.2.72 as follows,

$$\nu_t = f_{d_{proposed}} \nu_{t_{RANS}} \quad \textbf{2.86}$$

The turbulent length scale,L_T in Eq 2.76 is found using turbulent model information (Menter_SST) for each time step at the cell centers. L_G is calculated as a field variable at the cell centers, only once during the computation (no grid deformation or dynamic adaptation occurs). For each cell the distance between the cell center and each of the faces is calculated using the position vectors. The maximum distance for each cell is chosen to be used in Eq 2.76.

The solution procedure for the multi-scale model is shown in Figure 2-4. The initial condition is a converged RANS solution. Unsteady simulation is conducted with the modification of the eddy viscosity in Eq2.86 which causes a decrease in the eddy viscosity. Eddy viscosity is decreased iteratively as the simulation proceeds in time as shown in the dashed box in Figure 2-4; the filter function reduces the RANS eddy viscosity, which in turns reduces turbulent kinetic energy(TKE), k, because the production of TKE is proportional to the value of the eddy viscosity. Reduction of k causes a reduction of the turbulent length scale, L_T (see definition in 2.76) which causes the filter function to increase thus reducing the eddy viscosity further but at a lower rate. The process in the dashed box continues until the eddy viscosity is considered converged and statistics can be collected. Because of the iterative procedure followed in the reduction of eddy viscosity, initial and boundary conditions of the eddy viscosity are less sensitive to the overall solution, because if the values on the boundary are higher than

needed, the eddy viscosity will continue to decrease to reach the same point. This was also found by Tseng and Shyy[140] when using the filter based model.

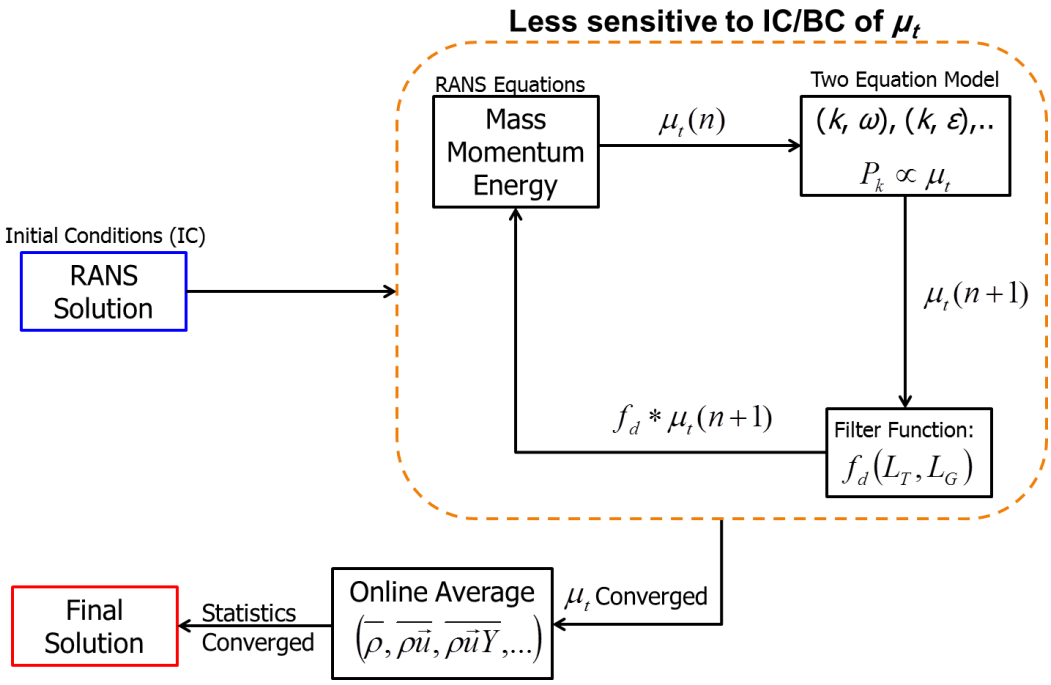

Figure 2-4 Flow chart of the solution procedure using the multi-scale model

Due to the highly unsteady nature of the flow, statistics had to be collected online using an ongoing average approach; up to 20,000 iterations were used before an average was statistically converged.

.The average is collected on line as a function of the previous average value, the new instantaneous value and the iteration number:

$$\bar{\phi}(n) = \frac{1}{n}\phi(n) + \left(1 - \frac{1}{n}\right)\bar{\phi}(n-1) \qquad \textbf{2.87}$$

where ϕ is the instantaneous quantity being averaged and n is the iteration number. The final solution is reached once the average is statistically converged (does not change).

In some instances, the variance was also collected for qualitative comparison with experimental variance. The procedure uses standard definition for the variance with the

mean defined in Eq2.87

$$var\left(\phi(n)\right) = \overline{\phi(n)^2} - \left(\overline{\phi(n)}\right)^2 \qquad \textbf{2.88}$$

Adaptive Turbulent Schmidt Number Approach

The adaptive approach was implemented as an improvement to the multi-scale model based on the results which will be presented in chapter 3. Simulations with the adaptive approach along with detailed discussions of its implications are discussed in chapter 4. To implement the adaptive approach in LOCI-CHEM we use the multi-scale model to construct Sc_{t_Res} in Eq 2.79. Calculation of fluctuation terms, , $\overline{\rho u'_j \phi'}$, is conducted using the following property,

$$\overline{\rho u'_j \phi'} = \overline{\rho u_j \phi} - \overline{\rho u_j}\frac{\overline{\rho\phi}}{\overline{\rho}} \qquad \textbf{2.89}$$

which is valid assuming the flow is not hypersonic and density fluctuations can be neglected. The averages on the right hand side of Eq2.89 are calculated using the averaging procedure in Eq2.87. The averages, however, are not accurate at the beginning of the simulations; therefore the adaptive approach is not started until after a reasonable average is collected. In this effort we run the simulation for 2000 iterations at CFL near unity before modifying the turbulent Schmidt number. Also the value of the turbulent Schmidt number is limited by enforcing positivity (taking the absolute value) to be consistent with the RANS model eddy viscosity and imposing upper and lower limits for the resolved turbulent Schmidt number set at 0.001 and 10000 respectively. The computational procedure used with the adaptive approach is summarized in Figure 2-5.Following the same procedure of the multi-scale solution, ongoing average is collected and used to produce Sc_{t_Res}, after 2000 iterations it is used in the mass transport

equation and the solution is adapted accordingly. The online average of the variables is not affected by the use of Sc_{t_Res} in the mass transport equation and it is collected until statistically converge and a final solution is reached.

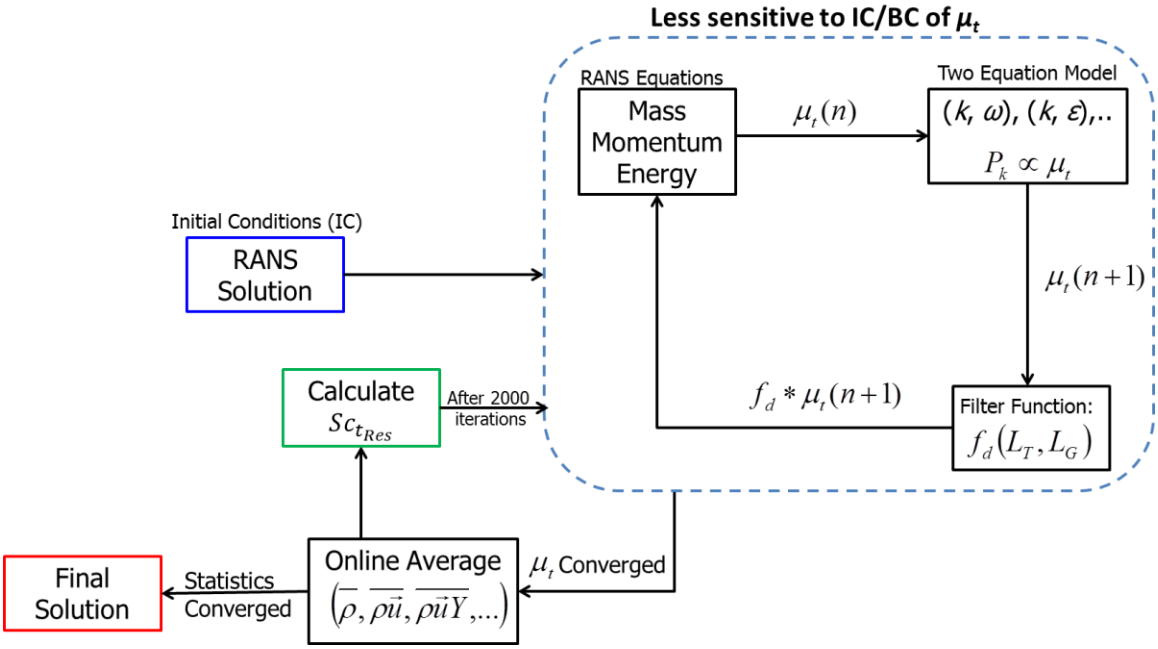

Figure 2-5 Flow chart of the solution procedure using multi-scale model with the adaptive approach

Chapter 3.
Multi-scale Turbulence Modeling for Supersonic Jet and Crossflow

Jet and crossflow interaction simulations can benefit from hybrid approaches where flow near the wall can be solved well with Reynolds-averaged Navier Stokes (RANS) models and large eddy simulation(LES) can be used in the rest of the domain. This work is aimed at assessing the capability of the multi-scale modeling approach, detailed in chapter 2, in solving ethylene normal and inclined injection into supersonic crossflow. This approach allows for wide variation in grid size, geometry and flow regimes because it smoothly varies the eddy viscosity to resolve turbulent structures consistent with the grid. Predictions of the time averaged fuel concentration from the multi-scale model were improved over Reynolds-averaged Navier-Stokes simulations when compared to experimental measurements. The Reynolds-averaged Navier-Stokes approach predicts velocity and pressure fields similar to that of the multi-scale and experimental pressure-sensitive paint measurements. It is therefore believed that the effect of turbulent mass diffusivity is limited to fuel mixing and does not affect the flow field overall.

3.1 Experimental Setup

Lin et al[16, 65] performed an ethylene injection experiment in Mach 2 air at the continuous flow supersonic tunnel at Wright Patterson Air Force Base, Ohio[8, 149]. The

experimental conditions are detailed in Table 3-1.The injector had a circular port and was placed in the bottom wall of the test section. The injectors were circular with a diameter of 3/16 of an inch (the diameter used in this study) and were placed 5.9 inches downstream of the constant test area. The constant test area is 131 mm by 152 mm with three-sided optical access Figure 3-1 shows a schematic of the injectors used in the simulation of this study at 90 and 30 degree angles from the constant test area.

Table 3-1 Experimental conditions for cases considered

Parameters	*Values*
P_0 (freestream)	244 KPa
T_0 (freestream)	300 K
M (freestream)	2
Diameter	4.8 mm(3/16 in)
momentum ratio, q	0.5,1.0,1.5
Injectant angle(θ)	90°,30°

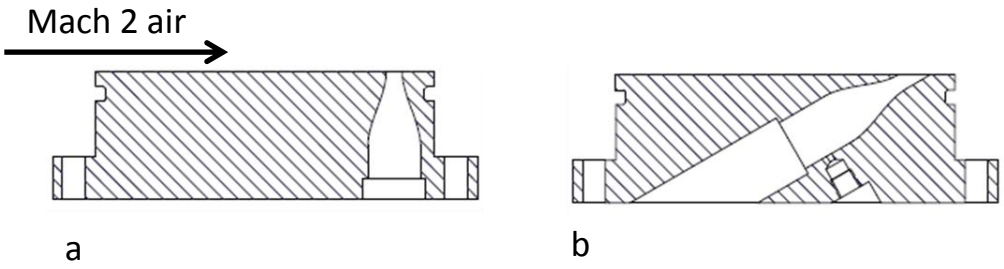

Figure 3-1 Injector shape and placement for (a) normal injection and (b) inclined injection

The Raman scattering technique was used to collect quantitative concentration data at various *x/D* locations. This technique is allows high resolution measurements without the need for seeding the flow[16]. Raman scattering measurements were then used to calculate the mixture fraction, Z, as follows,

$$Z = \frac{sY_f - Y_o + Y_{oo}}{sY_{ff} + Y_{oo}} \quad \textbf{3.1}$$

where Y_f is the local mass fraction of the fuel, Y_o is the local mass fraction of the oxidizer, Y_{oo} is the mass fraction of the oxidizer in the oxidizer stream, Y_{ff} is the mass fraction of the fuel in the fuel stream, and s is defined as

$$s = \frac{X_o M_o}{X_f M_f} \quad \textbf{3.2}$$

where X_o, and X_f are the mole fractions of the oxidizer and fuel at stoichiometric conditions. M_o and M_f are molecular weights of the oxidizer and fuel respectively. For air and ethylene M_o/M_f is 1.02 and mass fractions are practically the same as mole fractions for the purpose of this work.

3.2 Computational Parameters

The base fluid solver, Loci-Chem[144, 145],discussed in chapter 2 was used with the parameters detailed in Table 3-2. For RANS simulations Menter-SST[77] was used in turbulence modeling with no chemical reactions. Three species were used in the composition of the fluid; oxygen, nitrogen and ethylene, the air stream consisting of 22% oxygen and 78% nitrogen. The fuel stream is entirely composed of ethylene. All transport properties (density, viscosity and heat conduction) are a function of temperature and a Chemkin[124] transport model was used to produce 4th order polynomials for their lookup.

The flow and turbulence equations are coupled using a Newton iteration method with the implicit linear solver iterated using generalized minimal residual method (GMRES) provided by PETSc library[150]. Time integration is second order with spatial accuracy

also second order. While higher order spatial fluxes especially those centered for convection terms are desirable in LES simulations, they were not available in this code. The fluxes used here are based on Roe's flux difference splitting[151] , which handles complex geometries with general type unstructured grids without robustness/stability problems often encountered with higher order fluxes. The fluxes were limited with Venkatakrishnan's[147] unstructured limiter with $k_l = 10$. For RANS simulations, local time stepping was used to accelerate convergence[144].

Table 3-2 Loci-Chem Computational Parameters

Parameter	*Loci-Chem Setting*
Convective flux	Second order upwind
Time accuracy	Second order
Chemistry	3 species no reactions (O_2,N_2, C_2H_4)
Transport and diffusion	Chemkin
Base Turbulence Model	Menter SST
Linear Solver	PETSc
Limiter	Venkatakrishnan, K_l=10

Accurate time marching was used in the multi-scale simulation (implementation details in chapter 2) with a constant time step corresponding to CFL ~ 1. In order to start collecting averages for a multi-scale simulation, convergence is first determined holistically using probes at various flow locations that are evaluated for consistent fluctuation frequency and magnitude. There are however no unique criteria for values of frequency and magnitude selected to specifically signal convergence due to the unsteady nature of the flow. Once it is decided to start collecting the average, 20,000 iterations are

averaged (using ongoing average in Eq 2.87) or until the average no longer changes. Figure 3-2 shows a sample pressure probe located at inside the boundary-layer at y/D=0.25 and z/D=0.25 and 5 diameters upstream of the jet when the flow is considered statistically converged.

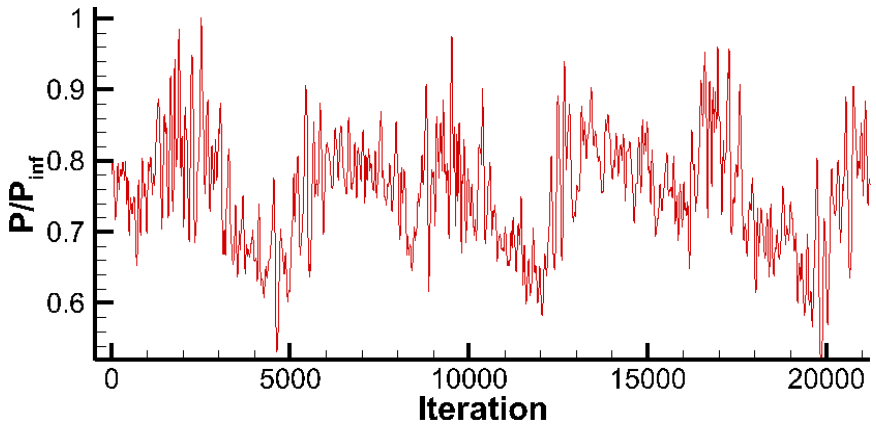

Figure 3-2 Pressure probe data at x/D=5, y/D=0.25 and z/D=0.25 for 30 degree injection. Flow is considered statistically converged and iterations are used to collect average

The computational domain for the jet in crossflow extends about 30 diameters upstream and 30 diameters downstream with cross section matching the experimental geometry. The inflow boundary condition did not include any artificial turbulence or unsteady boundary conditions. It was however interpolated from an output of a separate RANS simulation of the nozzle that matches experimental nozzle geometry to ensure the correct thickness of boundary-layer for the incoming flow.

The boundary conditions are setup in LOCI-CHEM framework. *inflow(prescribed),* is used with a file containing the output date for the nozzle simulation. The outflow boundary condition is *supersonic outflow* condition which also allows subsonic flow near the wall. The wall boundary condition is *walllaw* which automatically switches between law of the wall and viscous wall depending on the value of y^+. The boundary condition *viscouswall* was also used with finer grids where y+ was of the order ~10 and no law of

the wall was needed. *IsentropicInflow* was used at the inflow of the injector to prescribe total pressure and temperature of pressurized ethylene bottle used in the experiment. Figure 3-3 shows the computational domain and boundary conditions for the jet and crossflow interaction problem and the nozzle. The total length of the domain is 187 injector diameters with the jet and crossflow domain being 60 diameters long.

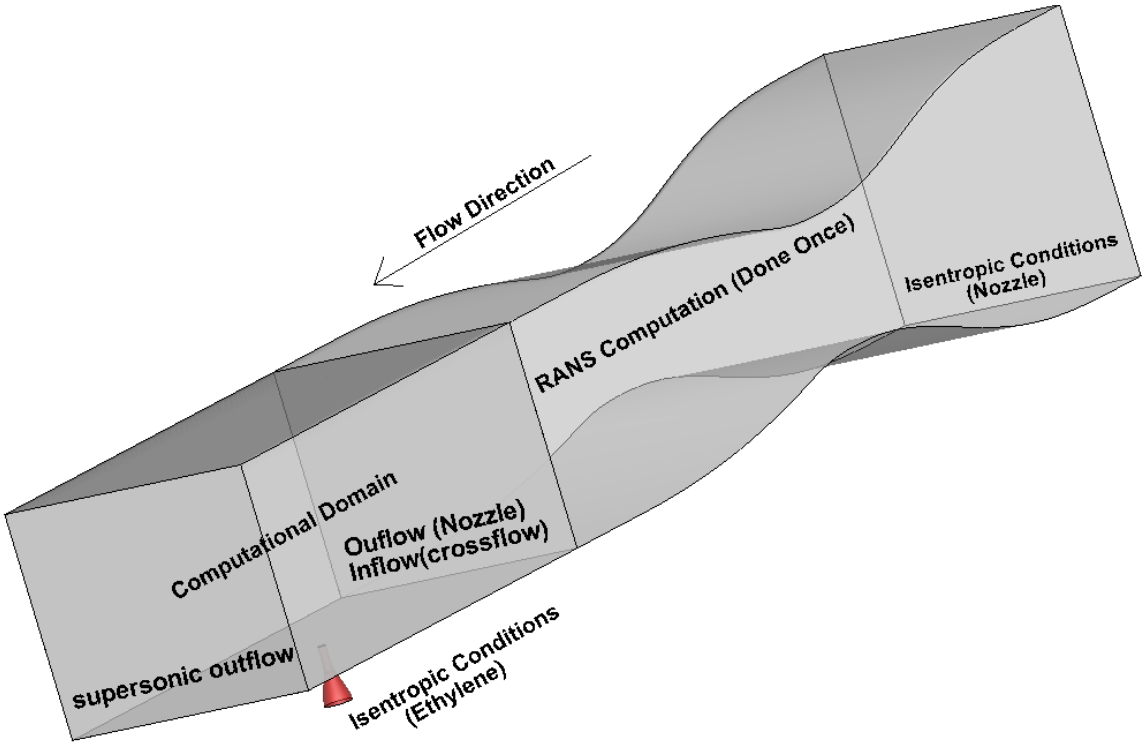

Figure 3-3 Computational domain and boundary conditions for jet and crossflow interaction and nozzle simulations

3.3 Nozzle Simulation

A hexahedral grid is used for the nozzle simulation with a total of 830,000 cells. A boundary-layer grid is used for all walls with the bottom wall boundary-layer grid matching that of the jet and crossflow domain to minimize interpolation errors.

Figure 3-4 shows the outflow boundary grid with line plots of axial velocity and

turbulence kinetic energy at the center of the domain near the bottom wall. It can be seen that the boundary-layer entering the jet and crossflow domain is already about a diameter thick with the velocity reaching 99% of free stream at z/D=1.01.

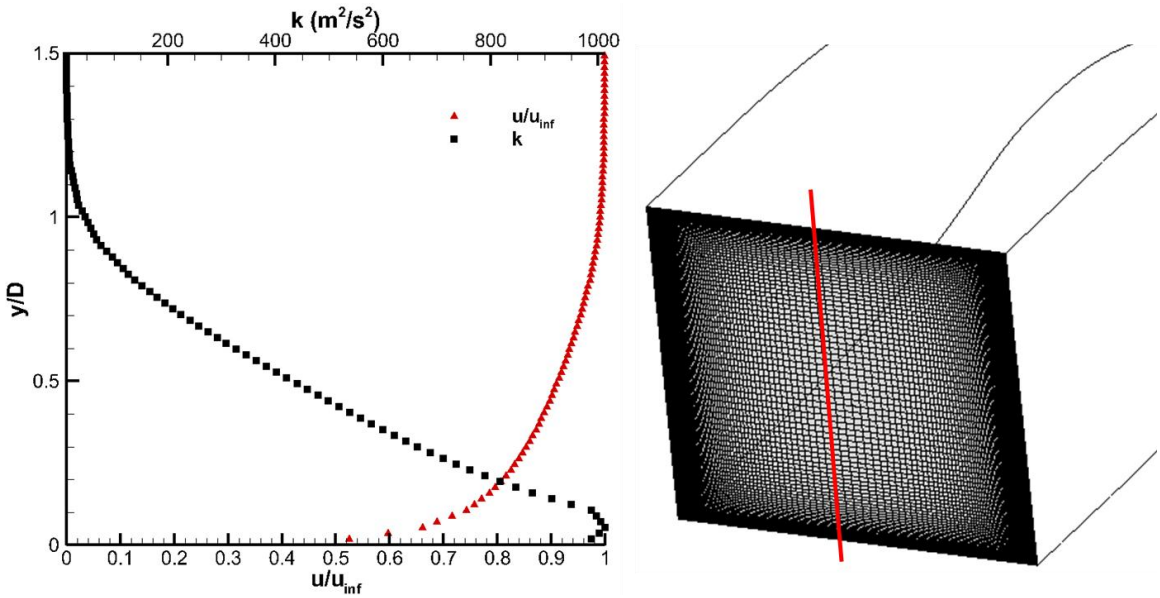

Figure 3-4 Nozzle simulation(right): outflow boundary-layer axial velocity and turbulence kinetic energy, grid distribution for outflow boundary(left)

3.4 Sonic Injection Cases

The baseline case used for sonic injection is the ethylene normal injection case with a momentum ratio, q=0.5. First, a RANS simulation is conducted with a 600,000 cell symmetric grid using different turbulent Schmidt numbers. Multi-scale simulations are then performed with 3 grids; 7 million, 17million, and 27 million cells.

The 17 million cell grid is also used to conduct a MILES simulation[152] to evaluate the effect for normal injection at q=0.5 to evaluate the effect of numerical viscosity.

Three other configurations are tested along with the baseline case; normal injection with q=1.5, inclined injection (30^o) with q=1.0, and inclined injection (30^o) with q=0.5.

The normal injection with q=1.5 is conducted with the 17 million cell grid used with the baseline case. Inclined injections (30^o) simulations are conducted using RANS model on a 7 million cell grid and multi-scale simulations are done on a 29 million cell grid.

Table 3-3 Sonic injection cases considered for multi-scale model testing

Case	Configuration	Grid Size (~ cells)	Turbulence	Notes
1,2,3	**90^o, q=0.5**	600,000	RANS	Sc_t=0.9,0.4,0.1
4		17 Million	RANS	Sc_t=0.7
5		7 Million	Multi-scale	Sc_t=0.7
6		17 Million	Multi-scale	Sc_t=0.7
7		27 Million	Multi-scale	Sc_t=0.7
8		7 Million	MILES	Sc_t=0.7
9	**90^o, q=1.5**	17 Million	RANS	Sc_t=0.7
10		17 Million	Multi-scale	Sc_t=0.7
11	**30^o, q=1.0**	7.3 Million	RANS	Sc_t=0.7
12		29 Million	Multi-scale	Sc_t=0.7
13	**30^o, q=0.5**	7.3 Million	RANS	Sc_t=0.7
14		29 Million	Multi-scale	Sc_t=0.7

Results are always compared to experimental mole fraction contours at *x/D=5* and *x/D=25*. They are also compared at *x/D=10* when experimental measurements are available Comparisons with PSP[15] wall pressure measurements are made with normal injection of q=0.5 and q=1.5 for both RANS and multi-scale. Other analysis of turbulent fluctuations and resolved eddy viscosities is provided by analyzing the resolved field of

the 17 million grid for normal injection, q=0.5.

3.4.1 Baseline Case: 90^{o}, q=0.5 [Cases 1-8]

RANS simulations were conducted using a 600,000 cell unstructured mesh with hexahedral cells with a center-plane symmetry boundary condition. This grid density was suitable because the solution reached grid independence and larger grids showed similar results. For the multi-scale simulations three different grids were used with mixed hexahedral domains as shown in Figure 3-5

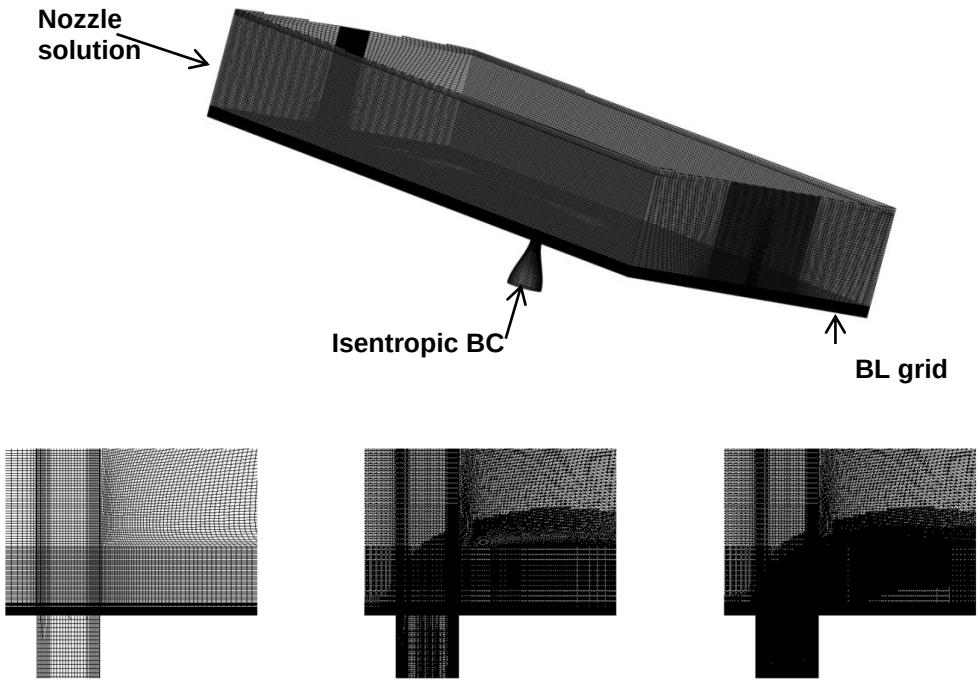

Figure 3-5 Grid distribution and boundary conditions for normal injection (top). Center plane cut: coarse, intermediate and fine grids in order

A coarse grid contains about 7 million cells with the jet region and boundary-layer at a finer resolution. Loci-Chem RefMesh tool was used to refine the grids starting from the coarse grid. Intermediate grid was refined from the coarse grid based on the filter function and ethylene mole fraction and contains about 17 million cells. A fine grid

was refined from the intermediate grid and contains 27 million cells. All three grids had a boundary-layer resolution starting at y^+ ~10

Flow Features of Jet and Crossflow Interaction (Intermediate Grid)

The multi-scale model produced flow features that are consistent with experimental and computational studies discussed in chapter 1 (ie [8, 17, 27, 52]). Mean values for pressure iso-surface, velocity streamlines, and midline ethylene concentration at the midline plane are shown in Figure 3-7. The bow shock separates the boundary-layer causing recirculation zones. A pair of spilled vortices is produced, and moves axially due to a bend in pressure between the bow shock and the foot print of the barrel shock on the boundary-layer. One of the pair is shown in Figure 3-7 by velocity streamlines. The vortex is blended back into the jet further downstream causing increased mixing as shown by the ethylene mole fraction downstream.

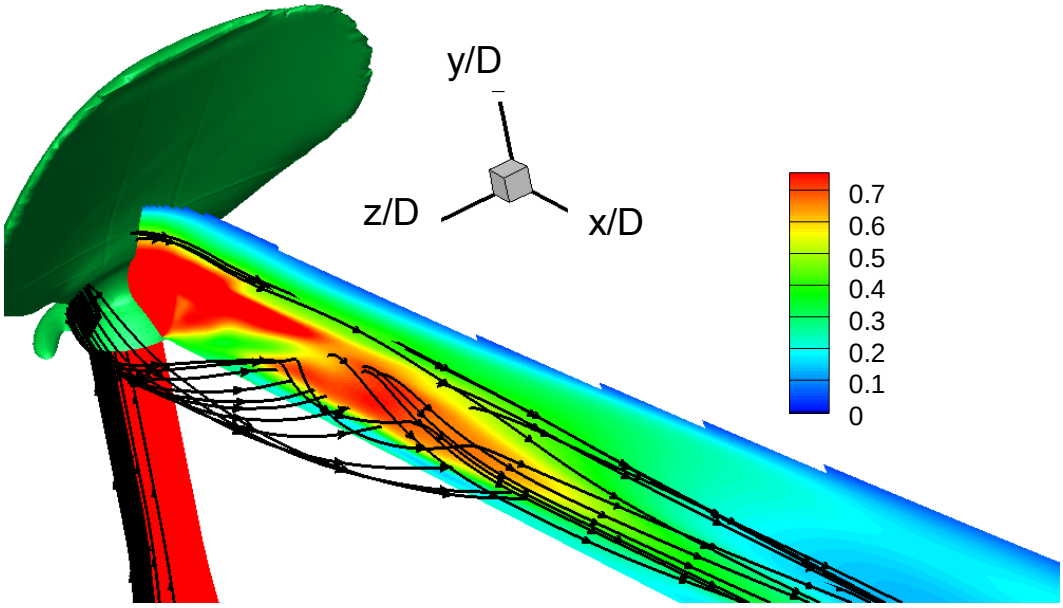

Figure 3-6 Pressure iso-surface (bow shock), midline average ethylene mole fraction (midline plane), and selected streamlines showing spilled vortex (baseline case, intermediate grid)

A snapshot of the Mach number is plotted in Figure 3-7 along with the profile of

the jet. The jet is bent quickly to conform to the crossflow angle and the height is increased in a linear manner beyond x/D=5. Mach numbers show the barrel shock that forms due to the fuel plume expansion beyond injection orifice.

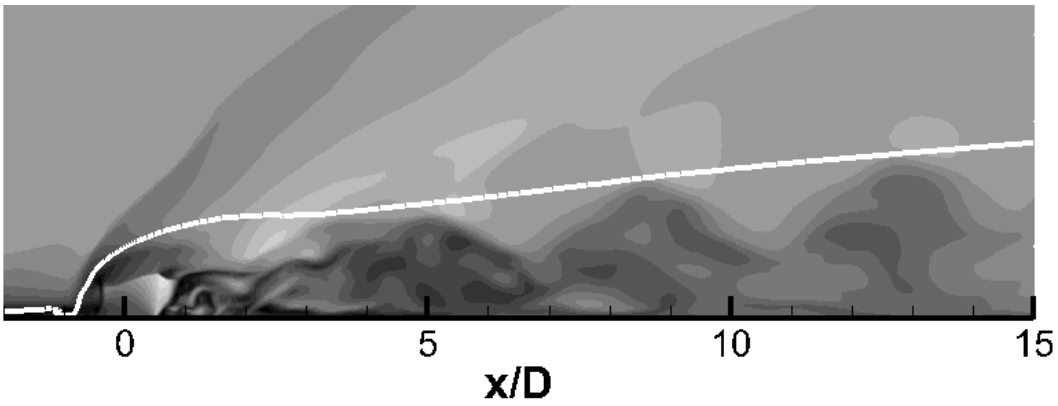

Figure 3-7 Snapshot of Mach number on the midline plane showing the barrel shock. White line outlines the jet profile at ethylene mole fraction of 0.05 (baseline, intermediate grid)

RANS Solution with various turbulent Schmidt numbers

RANS simulations without multi-scale modeling showed results that were of a different fuel structure than of the experiment consistent with the findings of other researchers[27, 132] who conducted the same simulation with various turbulence models and grid resolutions. In this effort, we used the Menter SST turbulence model with 3 different turbulent Schmidt numbers. The turbulent Schmidt number directly affects turbulent mixing in RANS with lower values corresponding to higher mixing. Jet and crossflow interaction simulations were shown to be very sensitive to their values[153].

Figure 3-8 shows the results for three different Sc_t (0.9, 0.4, and 0.1) as well as experimental measurements[16, 65]. For commonly used Sc_t(0.4-0.9), results similar to other researchers[27, 132] were observed. Near field at x/D= 5, the fuel is detached from the wall with an inverse heart shape. There is a large concentration of fuel in two kidney shaped vortices in the center. Then at x/D=10 the fuel shifts from the wall and high

concentration of fuel is lifted upward leading to high penetration heights and complete detachment at x/D= 25. When Sc_t is dramatically decreased to match the fuel concentration of the experiment better results are obtained (Sc_t=0.1). Compared to Sc_t= 0.4 , for Sc_t= 0.4 there is a decrease in the fuel concentration at x/D= 5 however the two kidney vortices are still present and the fuel structure is still similar to Sc_t= 0.9 for both x/D= 10 and x/D= 25. When Sc_t= 0.1, the fuel concentration is of roughly the same values as the experiment. At x/D= 5, the fuel core does not show the fuel rich vortex pair, however the structure still resembles an inverse heart shape and the penetration height is over-predicted. At x/D= 10 the fuel core is attached to the wall similar to the experiment however it is more elongated with penetration height and width larger than the experiment. At x/D= 25 the fuel core is very large and dispersed showing similarities to the experiment but with larger cross sectional area.

From the results it is evident that the RANS approach with typical values of Sc_t (0.4 - 0.9) is inadequate and shows poor correlation with the experimental measurements. It is possible to lower Sc_t to match experimental fuel concentration, but the results still show different fuel structure with penetration height mismatch. In this case, the use of a constant Sc_t is inadequate because the results are very sensitive to its value with only a very low Sc_t(outside common range) needed to obtain similar fuel concentrations. Even with Sc_t set to 0.1, there is a mismatch in fuel structure between computation and experiment.

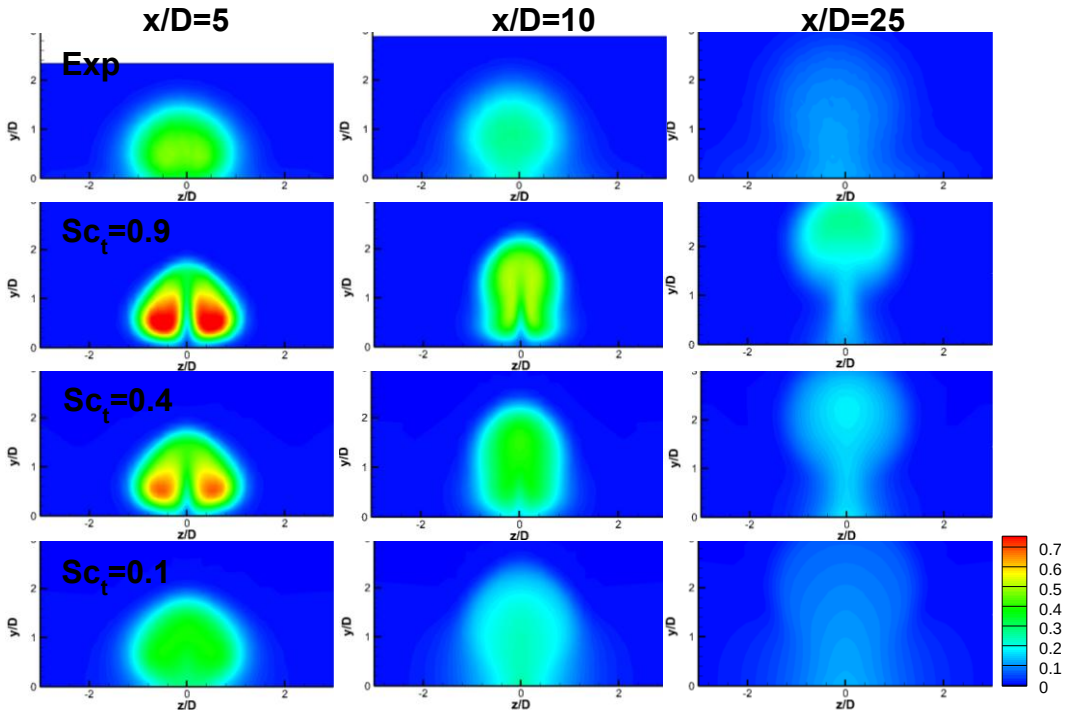

Figure 3-8 Average ethylene mole fraction results for RANS with different turbulent Schmidt numbers comparison with experiment. (baseline case)

Simulations with the multi-scale model

The instantaneous NOPLIF images from the experiment show large segregation between the jet and crossflow. Looking at sample images at x/D=5 and x/D=25 in Figure 3-9, the flow does not show the degree of mixing of the average mole fraction shown in Figure 3-8. Instead the mixed nature of the average contour plots is due to the large degree of unsteadiness witnessed in the flow field. The mean values are therefore misleading and looking at the variance is important to understand the flow field.

Simulations with the multi-scale model were conducted using a turbulent Schmidt number of 0.7 in the sub-filter RANS model.. Mean and variance of fuel concentrations are plotted on the center plane for the intermediate grid in Figure 3-10.They are qualitatively compared to the experimental NO PLIF images. The means for the RANS at

Sc_t= 0.1 and multi-scale are comparable to the experiment. Due to low Sc_t, the RANS computation appears more mixed than both experiment and the multi-scale result with almost homogenous concentration of fuel beyond the plume.

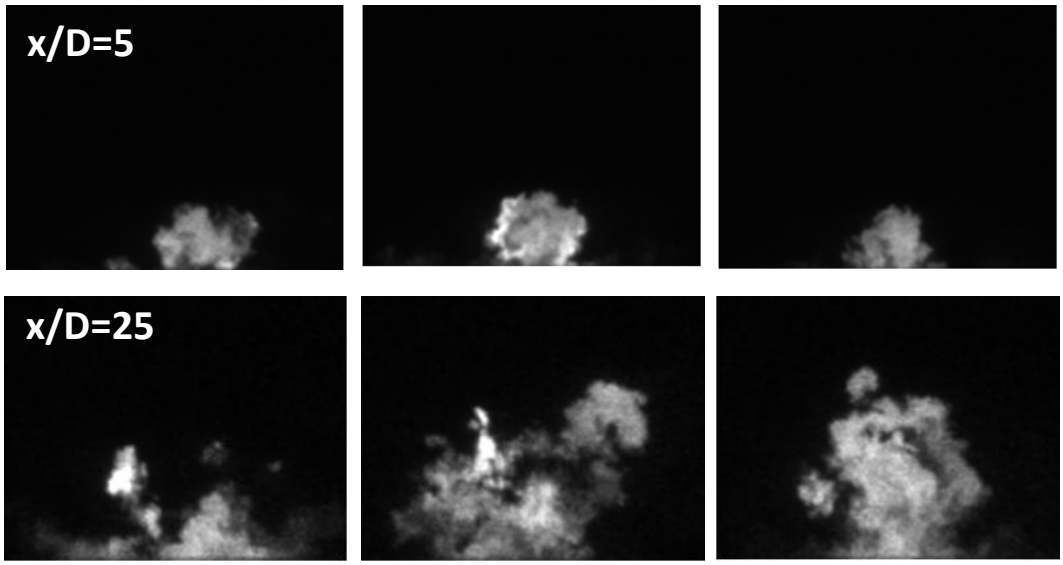

Figure 3-9 Sample NOPLIF images for the baseline case for x/D=5 (top) and x/D=25 (bottom)

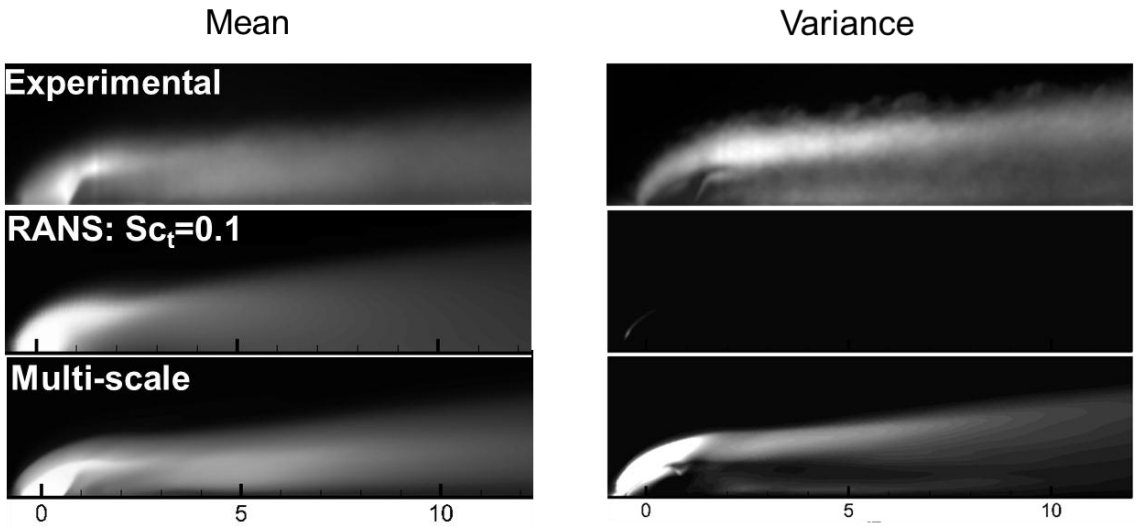

Figure 3-10 mean and variance of fuel concentration for RANS, multi-scale and experimental NO PLIF images(baseline case)

The multi-scale result shows regions of high concentration downstream of the

plume consistent with the experiment. There is a thin layer of low variance near the wall of the multi-scale results due to the RANS model being activated near the wall. The RANS variance is essentially zero with integrated variance that is 44000 times less than multi-scale (multi-scale integral variance is 0.79 while RANS is 1.6e-5). The multi-scale variance contours display similar character to the experimental NOPLIF images variance. This shows that the mean alone is not enough to represent the problem because of substantial difference with RANS solution.

Instantaneous ethylene mole fraction contours show more detailed structures of the highly turbulent field as the grid is refined.

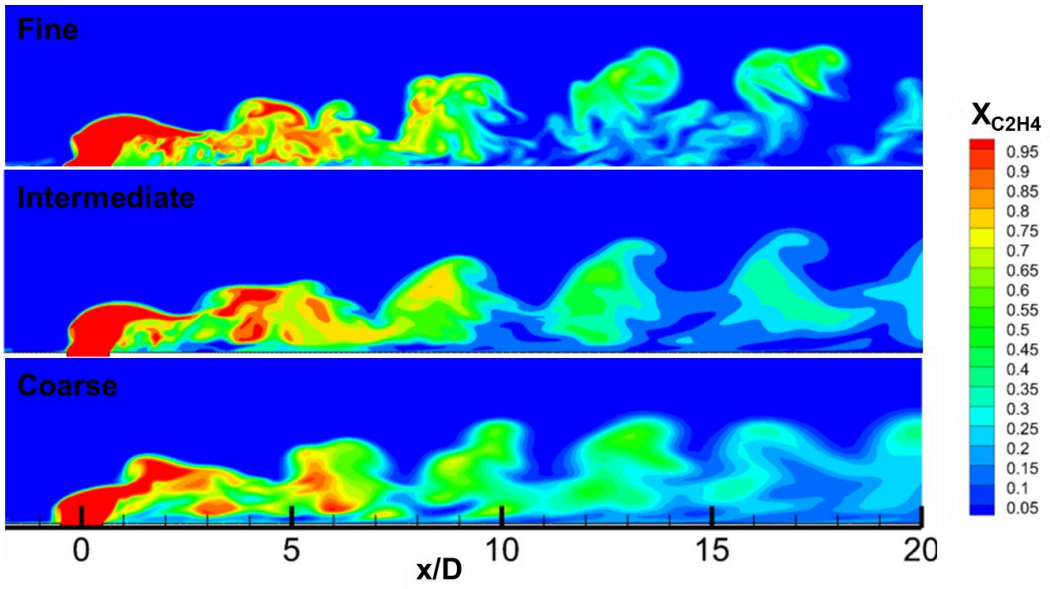

Figure 3-11 Instantaneous snapshots of ethylene mole fraction contours for coarse, intermediate, and fine grids(baseline case)

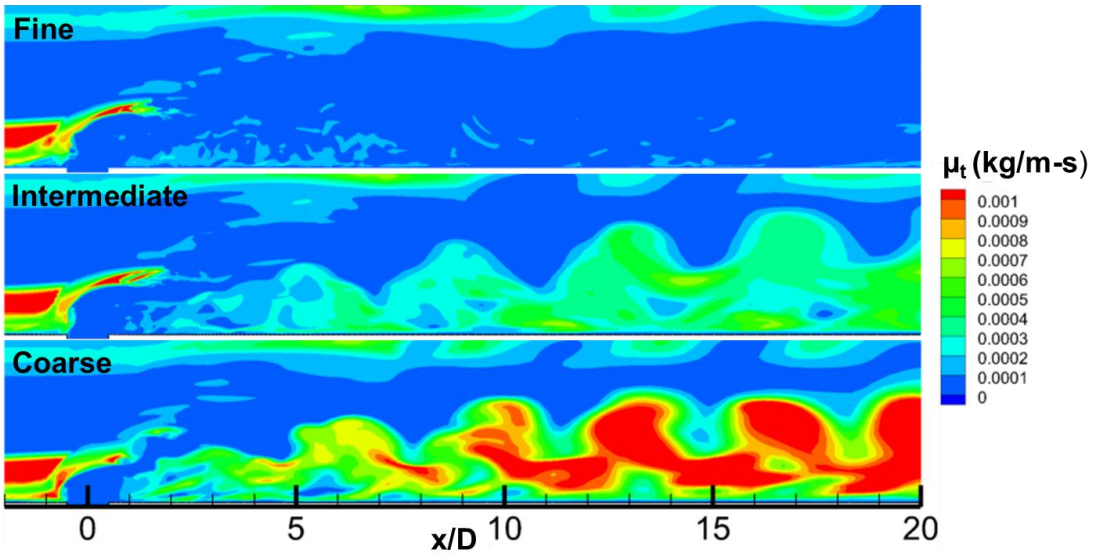

Figure 3-12 Instantaneous snapshots of eddy viscosity contours for coarse, intermediate, and fine grids(baseline case)

Figure 3-11 shows that there are smaller and more refined fuel structures in the intermediate grid simulation than in the coarse grid simulation. The fine grid shows even more turbulent structures near the tip of the fuel plume where it breaks violently into smaller eddies. Figure 3-12 shows the instantaneous (modeled) eddy viscosity contours for all three grids. As the grid gets finer the modeled eddy viscosity becomes lower with the coarse grid showing eddy viscosities up to an order of magnitude higher than that of the fine grid.

Figure 3-13 shows time-averaged ethylene mole fractions collected from the multi-scale simulation. For x/D= 5, the penetration height is well predicted for all three grids. As the grid is refined the shape of the fuel cross section becomes more flat shifting away from the heart-shaped RANS results with more interaction with the wall boundary-layer. The coarse grid simulation shows a kidney-shaped plume with two high fuel concentration vortices at the center similar to the RANS solution except that they are closer together and of less intensity. This may show a crossover between RANS and

multi-scale modeling since the grid is not highly refined. Intermediate and fine grids show less concentration of the fuel center with the shape becoming more representative of the experimental results. The fuel core center is however still over-predicted in the finest grid level. This may mean we need finer grid or higher order flux functions. For $x/D=$ 10, there is an over-prediction of the penetration height similar to the RANS solution but improving as the grid refined. The solution resembles the experimental results as the grid is refined and the fuel core center becomes less concentrated. The shape of the fuel core also becomes more circular and closer to the wall. For $x/D=$ 25, there is also an improvement with the fuel core becoming attached to the wall resembling the experiment as the grid is refined. From the results it is evident that when more turbulent structures are numerically resolved the solution improves. This would point to inadequate modeling of mass transport and mixing in the RANS approach, which is not solved by simply reducing the turbulent Schmidt number as shown in the last section.

It is desirable to compare the experimental concentrations to the computational results using a single quantitative measure (per x/D). The mean values in Figure 3-13 do not contain all the important information since the flow is shown (both experimentally and computationally) to have high variance therefore, using a single mean value per axial location may prove to be misleading. Comparing maximum height and width can be used to show on average the extent of the fuel profile, however, definitions of penetration involve arbitrary cut off values. In this study we compare centers of penetration in the y direction (height) and in the z direction (width). Because the flow is considered symmetric around the y axis, we find the center of the fuel cross section only for positive z/D values in each axial location. The integration is performed as follows,

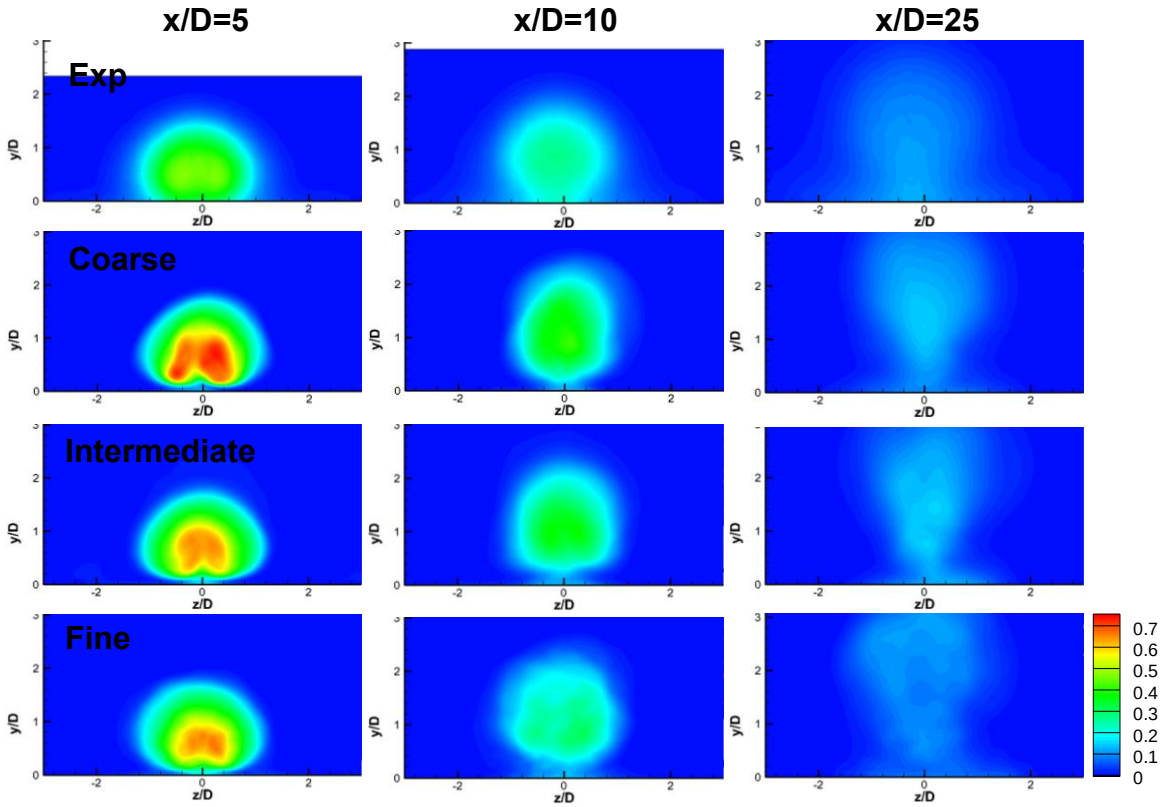

Figure 3-13 Average ethylene mole fraction results for grid refinement study(baseline case)

$$[y_{height}, z_{width}] = \frac{\int X_{C2H4} r(y,z) dA_{half}}{\int X_{C2H4} dA_{half}} \qquad \textbf{3.3}$$

Where A_{half} is the area constrained in x/D=constant, y/D>0, and z/D>0.

Figure 3-14 (a) shows centers of penetration height for experimental, RANS, and multi-scale models. The discrepancy between all models is less than 0.2 injection diameters. For x/D=5, RANS is closer to the experimental results than the multi-scale model, under-predicting the height only by 0.05 diameters. At x/D=10 RANS over-predicts the height by 0.06 diameters while the multi-scale models are closer within 0.03 diameters of the experimental results. Further downstream RANS continues to over-predict the experiment by about 0.2 diameters, while multi-scale models are lower and

closer to the experimental measurements. The penetration height centers are largely dependent on flow convection especially near the injector. RANS appears to predict the average convection correctly, therefore it performs well in the near field and continues to over-predict further downstream as diffusion starts to play a larger role in predicting jet penetration height. The multi-scale model improves diffusion prediction and results become closer to the experiment downstream with the finer grid predicting the lower penetration height and showing the least over-prediction at x/D=25. Overall because convection forces are predicted well by all models no large discrepancies are shown in any of the models for penetration height centers.

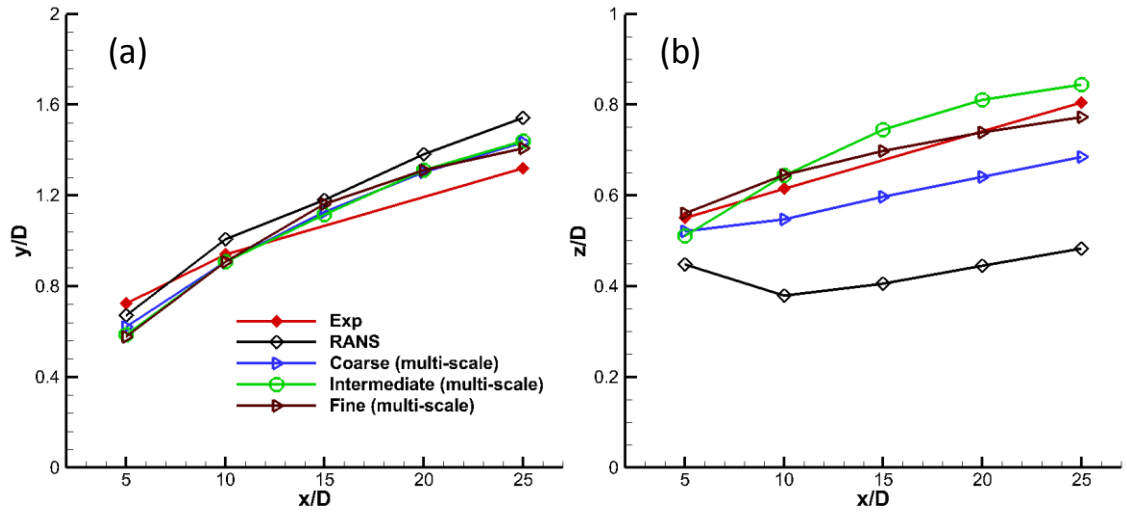

Figure 3-14 Centers for fuel penetration((a) height, (b)widths) for experiment, RANS, and multi-scale models (baseline case)

Figure 3-14(b) shows the penetration width centers for experimental, RANS, and multi-scale models. RANS results under-predict the width at x/D=5 by 0.1diamaters, at x/D=10 by 0.2 diameters, and at x/D=25 by 0.35 diameters. This shows RANS limitation

in predicting the experimental diffusion especially downstream where diffusion becomes the dominant factor in determining the penetration width. Multi-scale model produces points closer to the experimental results as the grid is refined. All three grids are closer to the experimental results than RANS. The fine grid is within 0.03 diameters from the experiment at all x/D locations. Overall because penetration width is more dependent on diffusion, RANS shows large discrepancies when compared to the experiment while multi-scale model shows more consistent results.

Pressure and velocity on intermediate grid

Pressure and axial velocity were very similar in the RANS computations using the 0.6 million cell symmetric grid with no injector geometry and the multi-scale computations using the intermediate grid and full injector geometry.

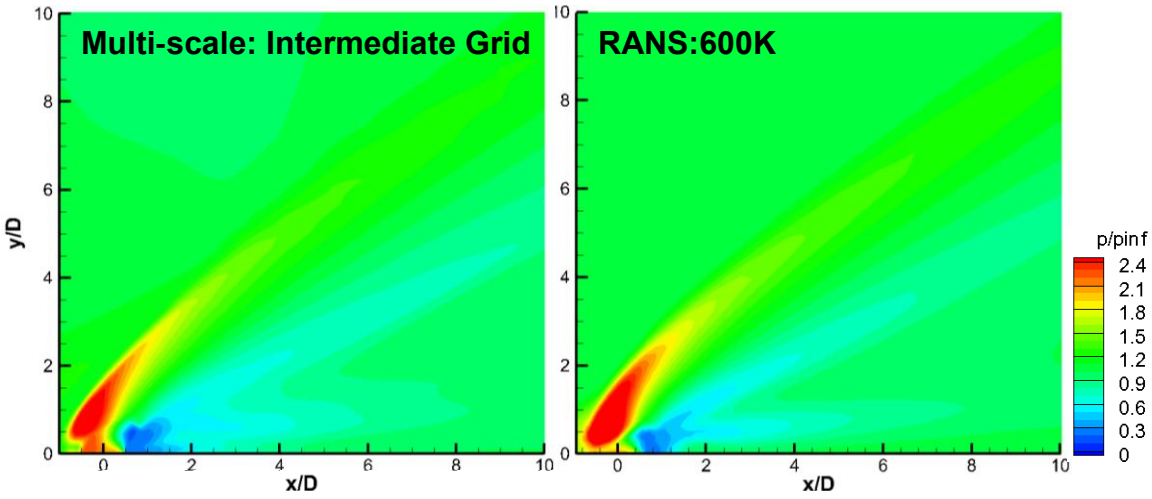

Figure 3-15 Pressure on the center plane. Comparison between RANS and multi-scale computation(baseline case)

Figure 3-15 shows pressure fields at the center plane for both RANS and multi-scale computations. Similar shocks and flow structures are seen in both contours with the RANS computation showing features that are less sharp due to the significantly coarser grid. Figure 3-16 displays axial velocity for RANS and multi-scale computations.

Contours show similar trends with the multi-scale model showing sharper features.

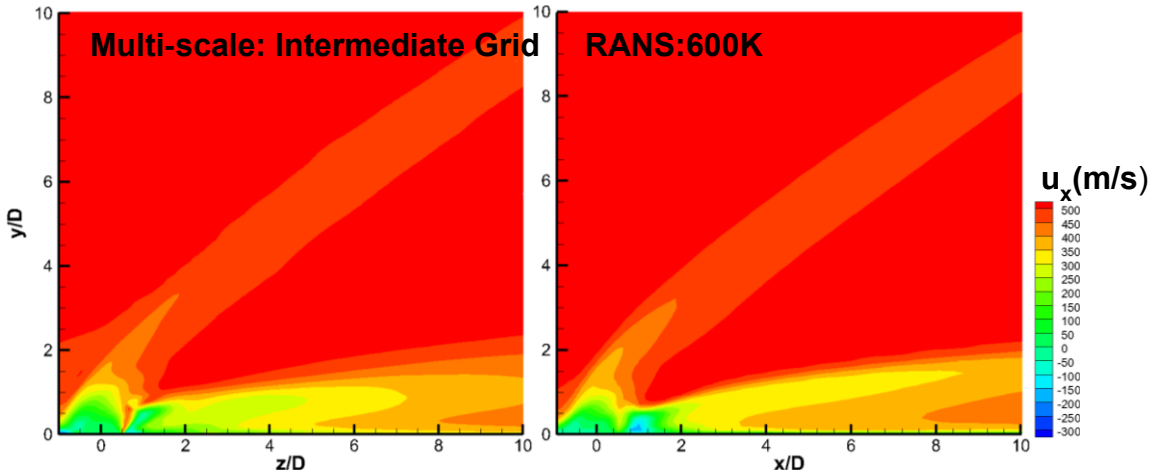

Figure 3-16 Axial velocity on center plane. Comparison between RANS and multi-scale(baseline case)

Figure 3-17 shows pressure contours for the intermediate grid on the bottom wall for RANS and multi-scale computations and compares it with experimental PSP[15]. Both RANS and multi-scale compare well with experimental results. Pressure in the shockwave upstream of the injector is slightly over-predicted by RANS however shock location is in good agreement with the experiment. The wake behind the injector is predicted well with both RANS and multi-scale except for few disturbances in pressure in the RANS solution around *x/D*=2. Overall multi-scale results show sharper features than RANS due to higher resolution of the grid. Figure 3-18 shows line a plot on the center line of the wall at $z/D = 0$.

The pressure drop upstream of the injector is sharper in the multi-scale and RANS solutions than the PSP measurements. The pressure in the wake region is in good agreement with the experiment in both RANS and multi-scale computations. The RANS computation shows a small pressure pump upstream of the injector that is not present in either experiment or multi-scale results. This pressure jump signals over-prediction of boundary-layer separation.

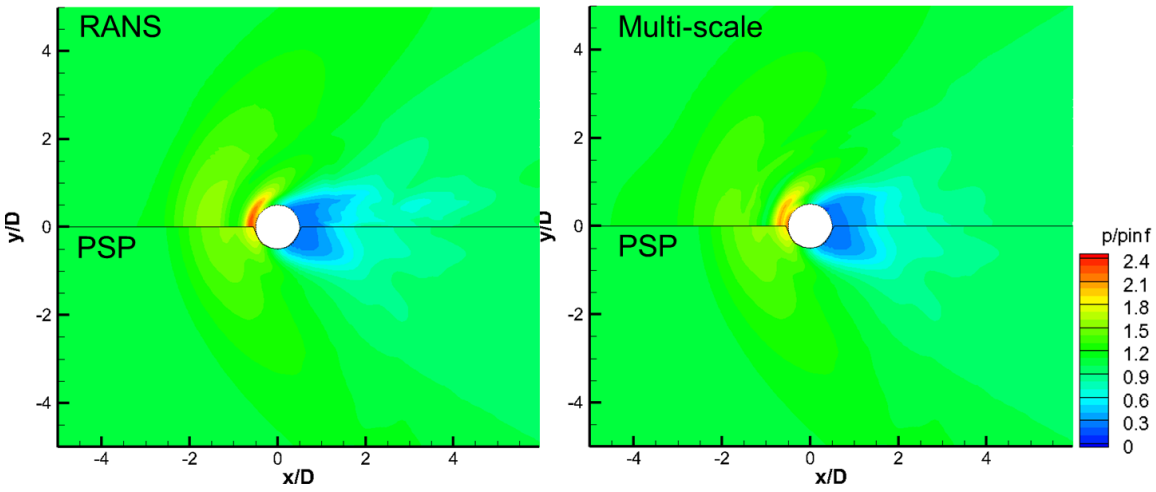

Figure 3-17 Contours of P/P_∞ on bottom wall. RANS and multi-scale predictions compared to PSP (baseline case)

It should be noted that the PSP measurements were accurate to 1000 Hz[15] , corresponding to a time step of 0.1ms. The time step used in multi-scale simulations is 0.1μs. The PSP measurements are therefore expected to exhibit less sharp features. No additional wall functions were used in the intermediate grid because y^+ was of order 1. The wall pressure results are overall similar in RANS and multi-scale and they both resemble the experiment relatively well.

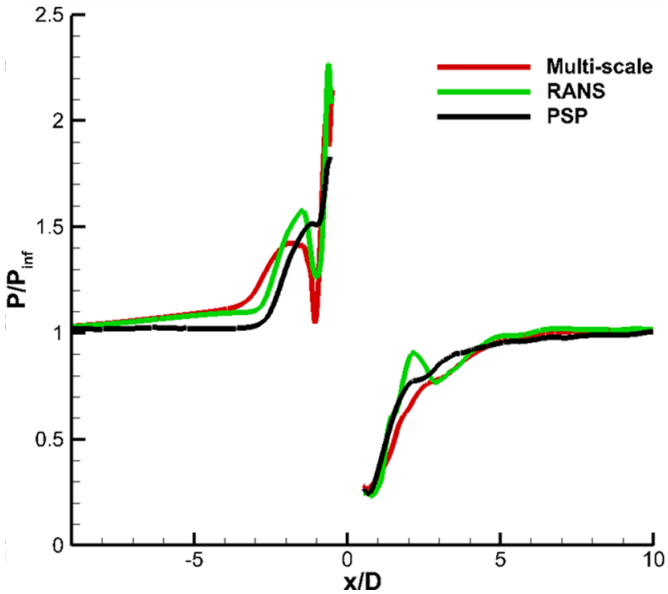

Figure 3-18 P/P_∞ on the surface at z/D=0(baseline case)

Analysis of resolved turbulence for intermediate grid

For the intermediate grid, turbulent statistics were collected to estimate turbulence kinetic energy, mass and momentum eddy viscosities, and turbulent Schmidt number based on actual fluctuations of the resolved field. The procedure used here is the one detailed in Boles et al.[27] and briefly explained below.

Assuming the flow speed is not hypersonic fluctuations in density can be neglected and a flux of a variable ϕ'may be expressed as,

$$\overline{\rho u'_j \phi'} = \overline{\rho u_j \phi} - \overline{\rho u_j} \frac{\overline{\rho \phi}}{\bar{\rho}} \qquad \textbf{3.4}$$

where the over bars are time averages. This would allow us to calculate estimates for fluctuation variables such as, $\overline{\rho u'_j \phi'}$, by collecting the terms on the right hand side during the simulation.

For turbulent mass transport, the value above may be corrected with a gradient-diffusion assumption,

$$-\overline{\rho u'_i Y'} = \bar{\rho} \nu_{t,mass} \frac{\partial \tilde{Y}_m}{\partial x_i} \qquad \textbf{3.5}$$

where a Favre-averaged variable $\tilde{\phi}$ is defined as,

$$\tilde{\phi} = \frac{\overline{\rho \phi}}{\bar{\rho}} \qquad \textbf{3.6}$$

In general, separate eddy viscosities $\upsilon_{t,mass,j}$ could be estimated for each component of the gradient vector. The validity of the gradient-diffusion assumption requires that $\overline{\rho u'_j Y'}$ be well correlated with the gradient in mole faction. Boles has verified that this is the case for the mixing region downstream of the injection at least for the y and z directions[132]. As RANS model will typically use an isotropic eddy viscosity, an effective

isotropic eddy viscosity associated with mass transport can be determined by taking an L_2 norm of the turbulent diffusion velocity vector,

$$\upsilon_{t,mass,Res} \approx -\frac{\overline{\overline{\rho u_i' Y'}}}{\bar{\rho}} \frac{\left(\partial \tilde{Y}/\partial x_i\right)}{\left(\partial \tilde{Y}/\partial x_i\right)\left(\partial \tilde{Y}/\partial x_i\right)} \quad \textbf{3.7}$$

Similarly, one can define isotropic eddy viscosity associated with momentum transports as follows:

$$\upsilon_{t,mom,Res} \approx -\frac{\left(\overline{\rho u_i' u_j'} - \frac{2}{3}\overline{\rho k_{Res}}\delta_{ij}\right) S_{ij}(\tilde{u}_i)}{\bar{\rho} S_{ij}(\tilde{u}_i) S_{ij}(\tilde{u}_i)} \quad \textbf{3.8}$$

$$S_{ij}(\tilde{u}_i) = \frac{\partial \tilde{u}_i}{\partial x_j} + \frac{\partial \tilde{u}_j}{\partial x_i} - \frac{2}{3}\frac{\partial \tilde{u}_k}{\partial x_k}$$

where $\overline{\rho k_{Res}}$ is defined as,

$$\overline{\rho k_{Res}} = \frac{1}{2}\left(\overline{\rho u_k u_k} - \overline{\rho u_k}\frac{\overline{\rho u_k}}{\overline{\rho}}\right) \quad \textbf{3.9}$$

Effective turbulent Schmidt numbers may then be calculated by taking ratios of the isotropic eddy viscosities,

$$Sc_{t,Res} = \frac{\upsilon_{t,mom,Res}}{\upsilon_{t,mass,Res}} \quad \textbf{3.10}$$

We can estimate resolved turbulence kinetic energy, $K_{Res,}$ and turbulence kinetic energy ratio, $K_{Ratio,}$ as follows,

$$K_{Res} = \frac{\overline{\rho k_{Res}}}{\overline{\rho}}$$

$$K_{Ratio} = \frac{\overline{k_{RANS}}}{K_{Res} + \overline{k_{RANS}}} \quad \textbf{3.11}$$

where $\overline{k_{RANS}}$ is the average turbulence kinetic energy predicted by the sub-filter RANS model

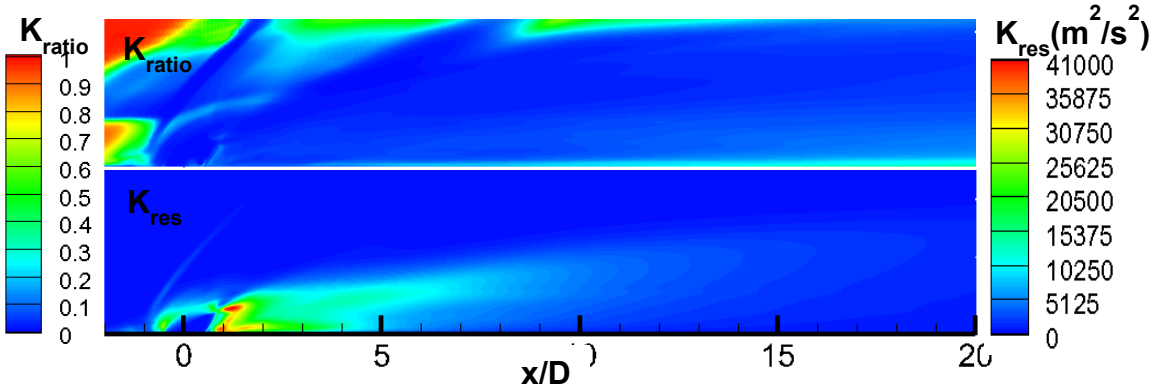

Figure 3-19 Turbulence kinetic energy (K_{Res}, bottom) and ratio of unresolved turbulence kinetic energy to total turbulence kinetic energy (K_{Ratio}, top) (baseline case)

Figure 3-19 shows contours of turbulence kinetic energy $K_{Res,}$ and K_{Ratio} at the center plane. K_{Res} displays a highly concentrated source just downstream of the barrel shock then diffuses quickly into the jet. At this location about 10 to 20 % of the total turbulence kinetic energy is modeled. The plot generally demonstrated that simulation with multi-scale turbulence model with the intermediate grid was able to resolve most of the turbulent structures. Both K_{Res} and K_{Ratio} show a smooth behavior and no sign of abrupt transition between models near the wall or near the plume area.

It should be noted the total turbulent kinetic energy used in Figure 3-19 does not include effects of numerical viscosity. Numerical viscosity may contribute to a large portion of the total viscosity in the simulation. In this effort a standard second order upwind scheme is used for the convective terms. This scheme is usually more dissipative than other schemes used in the LES community[27, 52]. One way to separate the effects of the numerical viscosity caused by the grid and the numerical scheme is to simply set the eddy viscosity to zero, thus using no turbulence model. This method is equivalent to conducting an LES simulation with the sub-grid model implicitly defined as the numerical viscosity providing an upper limit to the turbulent oscillations in the solution

for a particular grid and numerical scheme. This method was first named Monotone Integrated LES (MILES) by Boris[152] and an extensive analysis can be found in the book by Grinstein et al.[154]

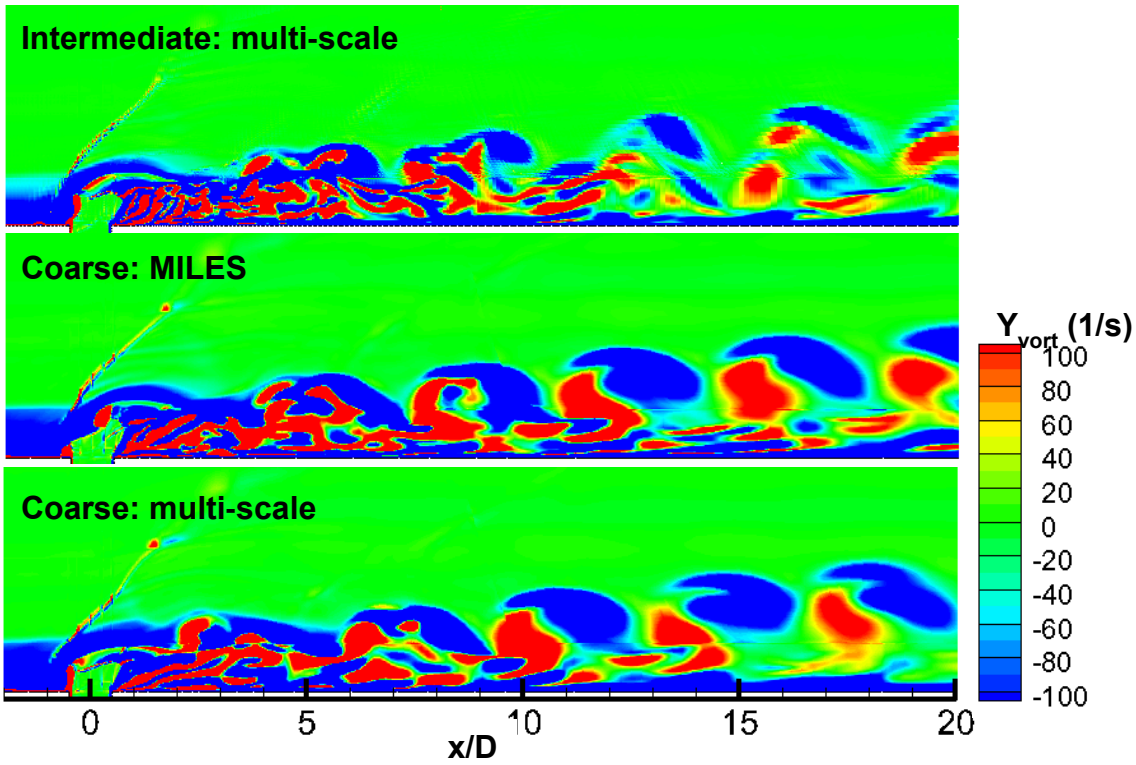

Figure 3-20 Instantaneous *y* vorticity snapshots on the center plane for multi-scale (intermediate grid on top and coarse grid on the bottom) and MILES (coarse) approaches. Maximum and minimum limited to 100, -100

Figure 3-20 shows the y vorticity on the center plane for coarse, intermediate grids as well as the MILES approach of zero eddy viscosity for the coarse grid. This figure gives a qualitative assessment for the numerical viscosity. The vortices in the MILES solution are sized in between coarse and intermediate, but closer in size to the coarse grids. This indicates that the eddy viscosity in the intermediate grid is less than the numerical viscosity in the coarse grid. We could also say that the numerical viscosity is not orders of magnitude larger than the eddy viscosity in the coarse grid because the MILES solution displays smaller vortices than those seen in coarse grid results. The effect of

numerical viscosity is therefore significant, especially for coarser grids. Very fine grids and/or high-order fluxes should be used to obtained adequate results.

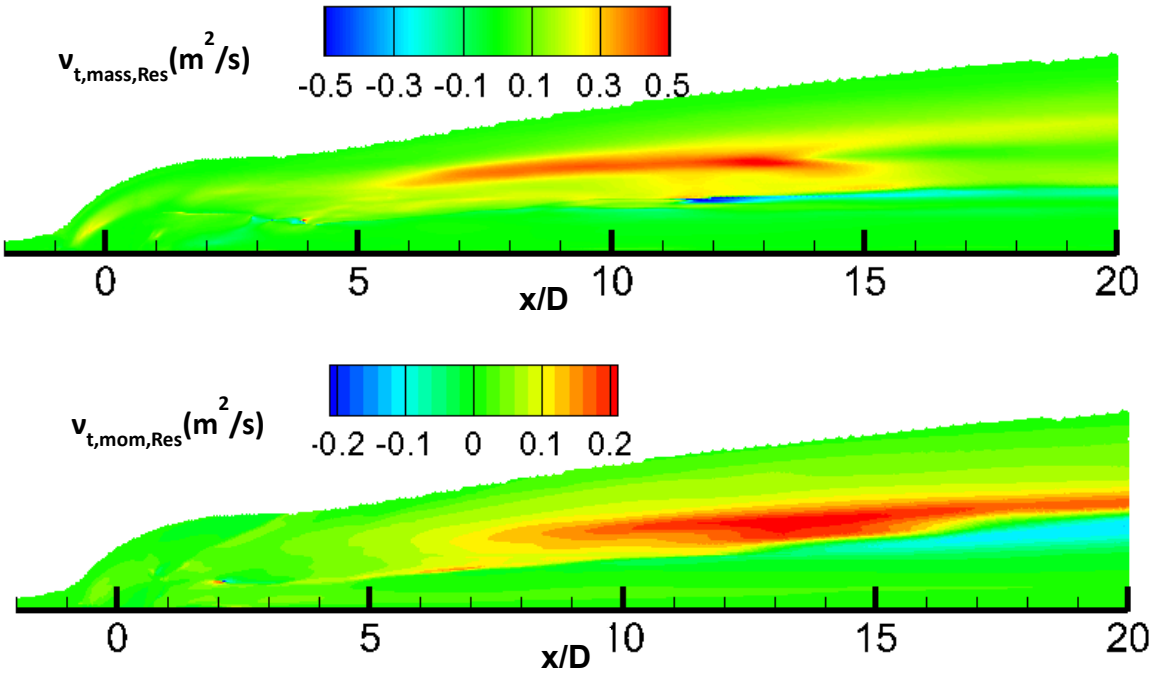

Figure 3-21 Mass and momentum eddy viscosities based on resolved field at the center plane (baseline case)

Figure 3-21 shows mass and momentum eddy viscosities estimated by Eqs. 3.7 and3.8. Higher values of mass eddy viscosities are found in the center of the jet between x/D = 7 and x/D = 15. This is the area where the jet widens and mass is diffused outwards. Momentum eddy viscosity shows a similar trend with high momentum fluxes in the center/upper region of the jet between x/D=10 and x/D =20. Thin layers of negative momentum eddy viscosity exist below high concentration regions similar to the mass eddy viscosity. There is however a narrow region of negative mass and momentum eddy viscosities, which would translate into mass/momentum being drawn into regions of higher fuel mass/momentum concentration. While this is physically possible, it is

unlikely because the thin region is probably the result of errors in the estimation method due to the assumption of isotropy.

Figure 3-22 shows mass and momentum eddy viscosities and effective turbulent Schmidt number computed by Eqs 3.7, 3.8, and 3.10 for x/D= 5. At the center of the jet cross section, there is a high concentration of mass and momentum eddy viscosities due to an increase of turbulent fluctuations in this region. It should be mentioned that this is the same region where the multi-scale model over-predicts the fuel concentration. Therefore, finer grid or higher order fluxes maybe needed to resolve more turbulence. It is clearly observed that overall the magnitude of turbulent Schmidt number is in the lower end of its typical modeled values. It also varies depending on the location with a non-uniform distribution. There are regions of negative values due to the mass and momentum eddy viscosities having opposite signs. Recalling the effects of constant turbulent Schmidt number on RANS simulations and non-uniform turbulent Schmidt number distribution on the plane obtained by current multi-scale simulations, an adaptive turbulent Schmidt number should be considered[30]

3.4.2 Non-Baseline [Cases 9-14]

For the baseline case studied above, overall, there is a significant improvement when using the multi-scale model over RANS. When comparing a typical RANS simulation with Sct=0.7 to a multi-scale simulation with the same turbulent Schmidt number on the intermediate grid, we observe fuel structures and concentrations of more resemblance to the experiment in both width and penetration heights.

Figure 3-23 shows this overall result comparing the fuel mass fractions between

RANS and multi-scale. The next logical step is to test the multi-scale model with different injection configurations to understand the mechanism at which it improves mixing predictability.

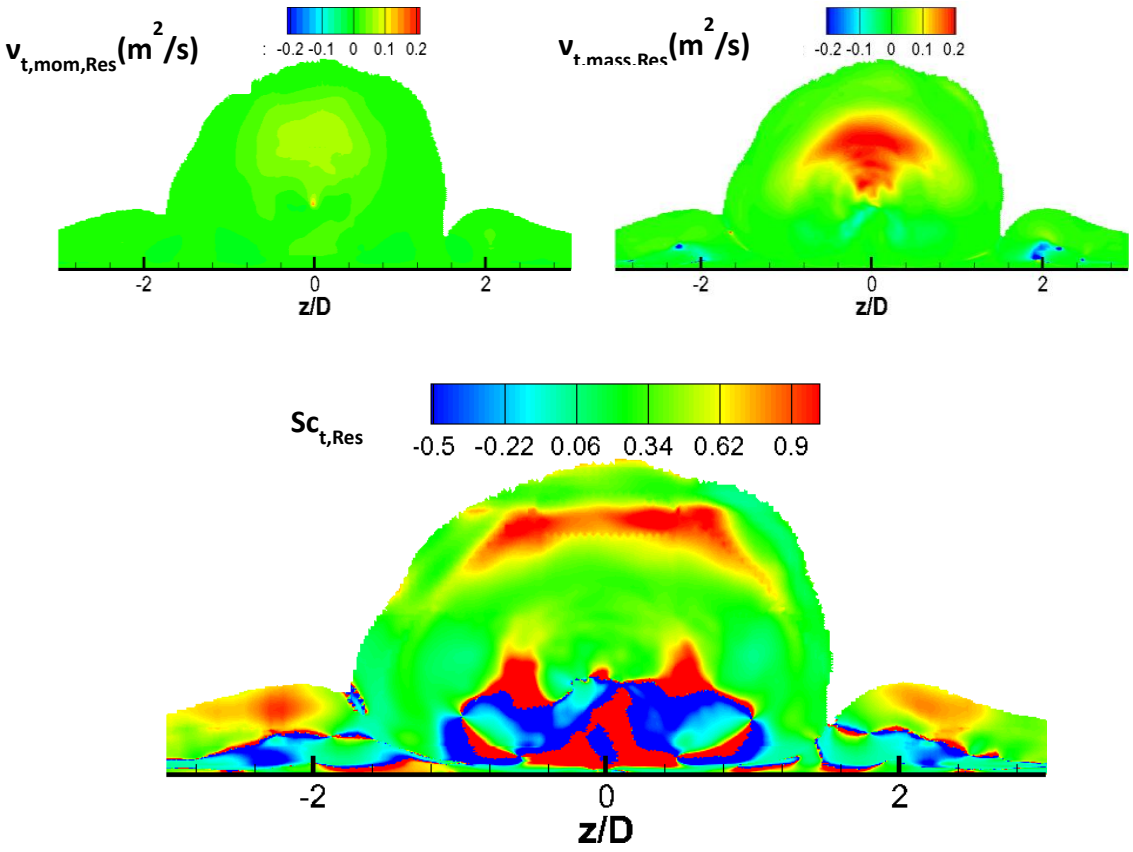

Figure 3-22 Mass and momentum eddy viscosities as well as effective turbulent Schmidt number based on resolved field for *x/D*= 5 intermediate grid (baseline case)

Three other injection configurations are tested with both multi-scale and RANS models; normal injection with momentum ratio q= 1.5, and inclined injection (30^o) with momentum ratios q=0.5 and q=1.0.The normal injection with a momentum ratio q=1.5 is conducted in RANS and multi-scale using the same intermediate grid used for the baseline case (17million cells). The inclined cases are conducted on a 7.3 million grid for RANS and 29 million for multi-scale. Both grids include full geometry of the injector and

a finer boundary-layer grid near the bottom wall.

The inclined injection grid layout and center plane cuts are displayed in Figure 3-24. The grids were refined to have more cells near the wall boundary-layer and the expected jet location. A $y^+ \sim 10$ is maintained for both RANS and multi-scale. The multi-scale grid is designed with 29 million cells to have a similar grid size to the fine grid for normal injection.

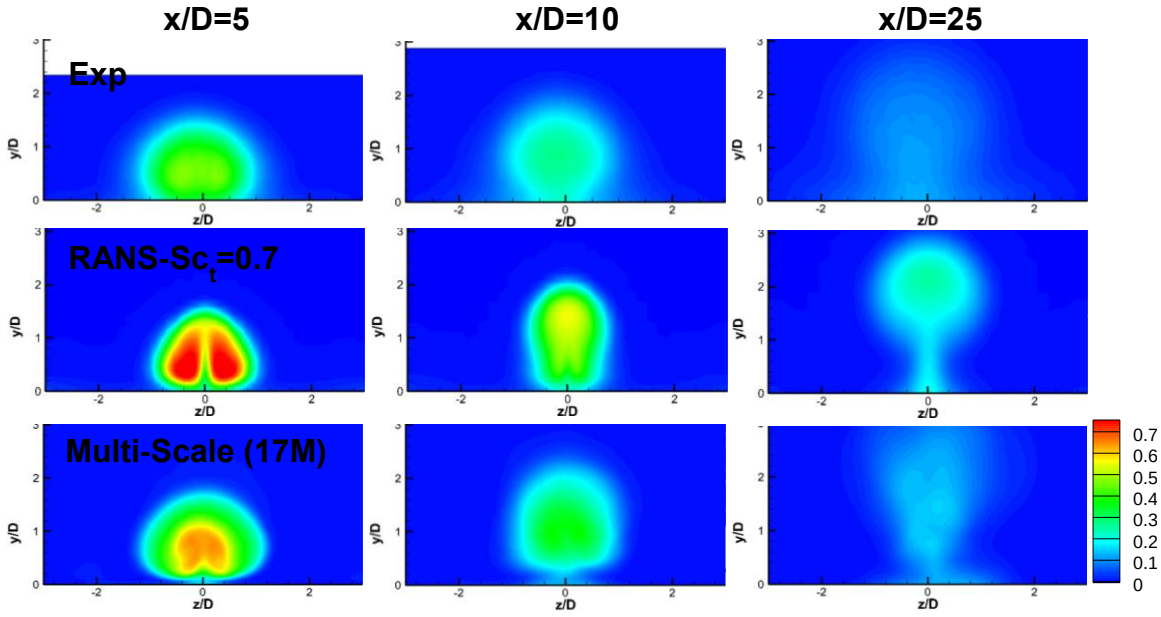

Figure 3-23 Baseline ethylene mole fractions comparison, intermediate grid (baseline case)

The high momentum case (q=1.5) was run on the intermediate grid using RANS and multi-scale models. Figure 3-25 shows mole fraction contours for both models and experimental results at x/D = 5 and x/D = 25. Overall the penetration heights and widths are predicted well by the computations. At x/D = 5 the RANS and multi-scale results are similar with square like inverse u-shaped fuel core that is different from experimental arc like structure.

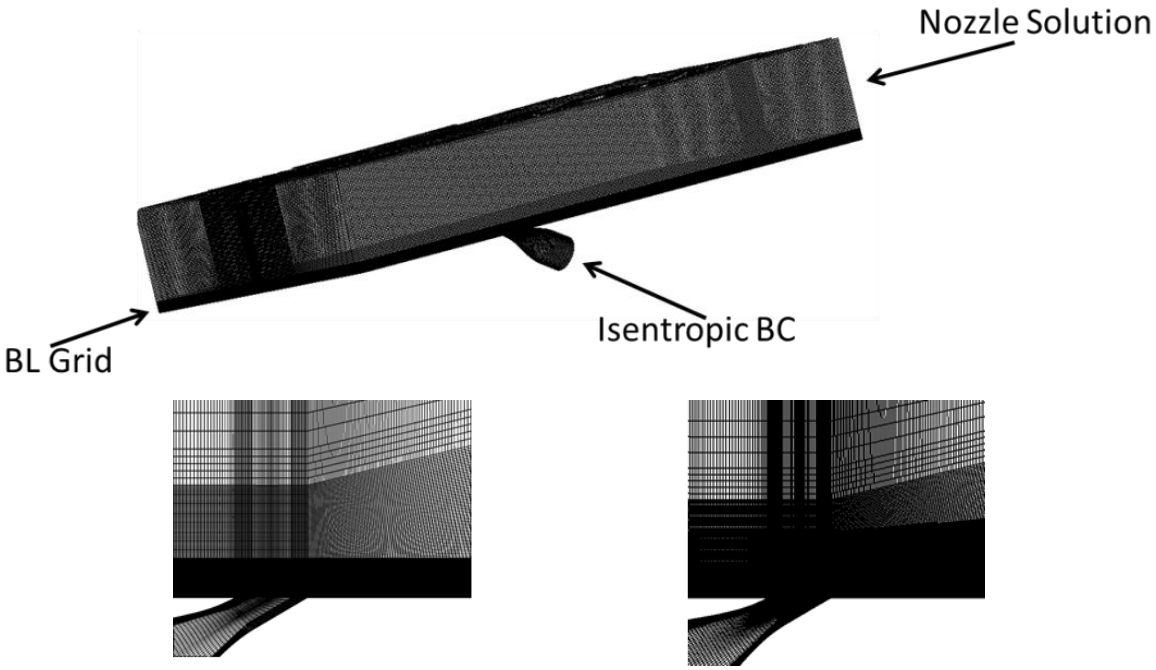

Figure 3-24 Grid distribution and boundary conditions for inclined injection (top). Center plane cut: RANS and multi-scale grids in order(bottom)

Normal injection, q=1.5 results

The fuel concentrations are over-predicted in the u-shaped core but they are of lower concentration when the multi-scale model is used. It is evident that finer grids are needed to resolve more turbulent structures to accurately represent the mixing in the case of multi-scale. At x/D = 25 the penetration heights are slightly over-predicted in RANS computation. The penetration width is under-predicted with the thinning of the fuel core and higher fuel concentration. The multi-scale model compares better with the experiment in terms of penetration height and width. The fuel shape is in better agreement with the experiment, however, it is still slightly over-predicted.

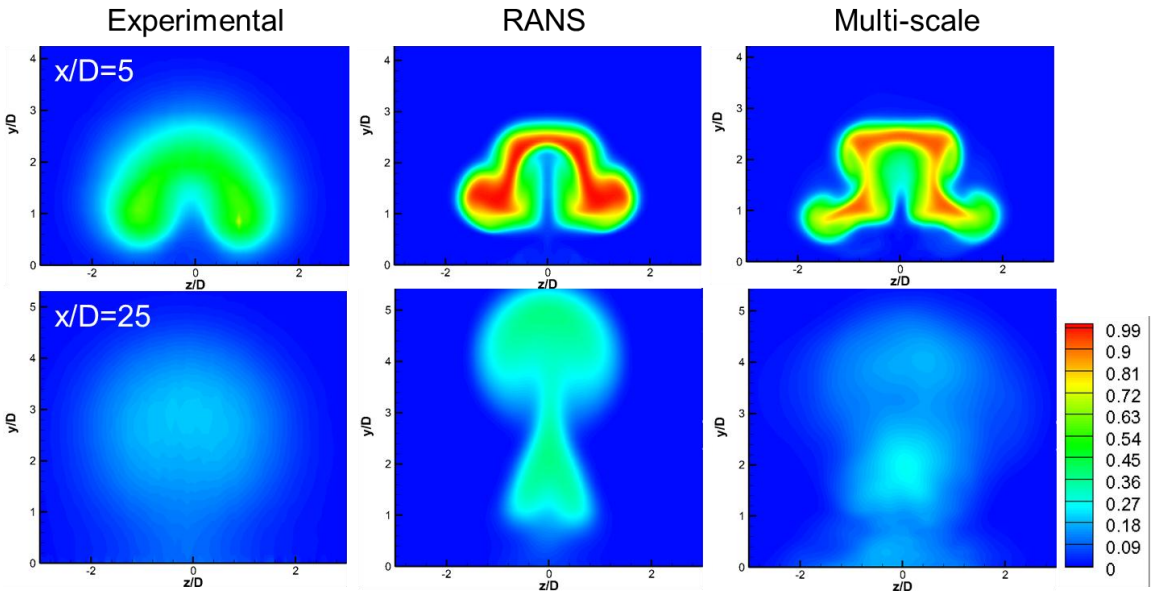

Figure 3-25 Average ethylene mole fractions comparison, RANS and multi-scale (90^o, q=1.5)

One notable difference between the q= 0.5 and q= 1.5 cases is that the near field fuel structures are similar between RANS and multi-scale in the case of q=1.5. This is because the high momentum fuel jet is less prone to large-scale turbulent breakup than the low momentum one. Therefore, it takes longer for large-scale turbulent fluctuations to appear. The main reason the fuel cores are still over-predicted in the near field is that in the sub-filter level (RANS model), turbulent mass diffusivity is under-predicted and a Sc_t lower than 0.7 may result in more accurate predictions in both RANS and multi-scale computations.

Inclined injection, q=1.0 and q=0.5 results

For the 30 degree injection q=1.0 case, fuel mole fractions are quantitatively compared to the available experimental Raman scattering results at 2 different *x/D* locations in Figure 3-26.

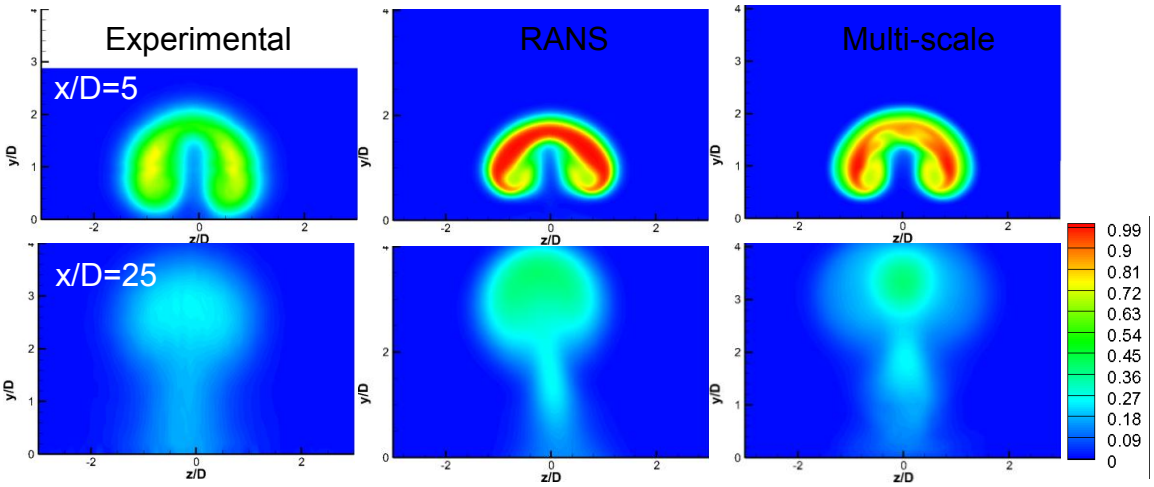

Figure 3-26 Average ethylene mole fractions comparison, RANS and multi-scale (30^o, q=1.0)

The concentration of the horse-shoe vortex is over-predicted by RANS at *x/D=5*, however, the overall shape of the fuel core including widths and heights are well predicted. With the use of the multi-scale model, the horse-shoe vortex is of lower fuel concentration. At *x/D=25*, penetration height is slightly over-predicted by RANS and multi-scale and penetration width is under-predicted by RANS. The multi-scale model improves penetration width prediction and produces concentrations closer to that of the experiment. Overall, the fuel core shapes were well predicted by both RANS and multi-scale unlike the normal injection cases.

For the 30 degree injection, q=0.5, fuel mole fractions are quantitatively compared to the available experimental Raman scattering results at 3 different *x/D* locations in Figure 3-27. The fuel concentration is over-predicted at *x/D*=5 by RANS which shows a single horse-shoe vortex of concentration higher than 70% and taking up the entirety of the cross section. The multi-scale results show two weaker kidney shaped vortices that are larger than those in the experiment but smaller and weaker than the RANS results. The experimental concentrations at *x/D*=5 are still much weaker than multi-scale even

though the latter is conducted with nearly 30 million cells. At *x/D*=10, fuel concentration is over-predicted by both RANS and multi-scale however results are closer to the experiment with the multi-scale approach.

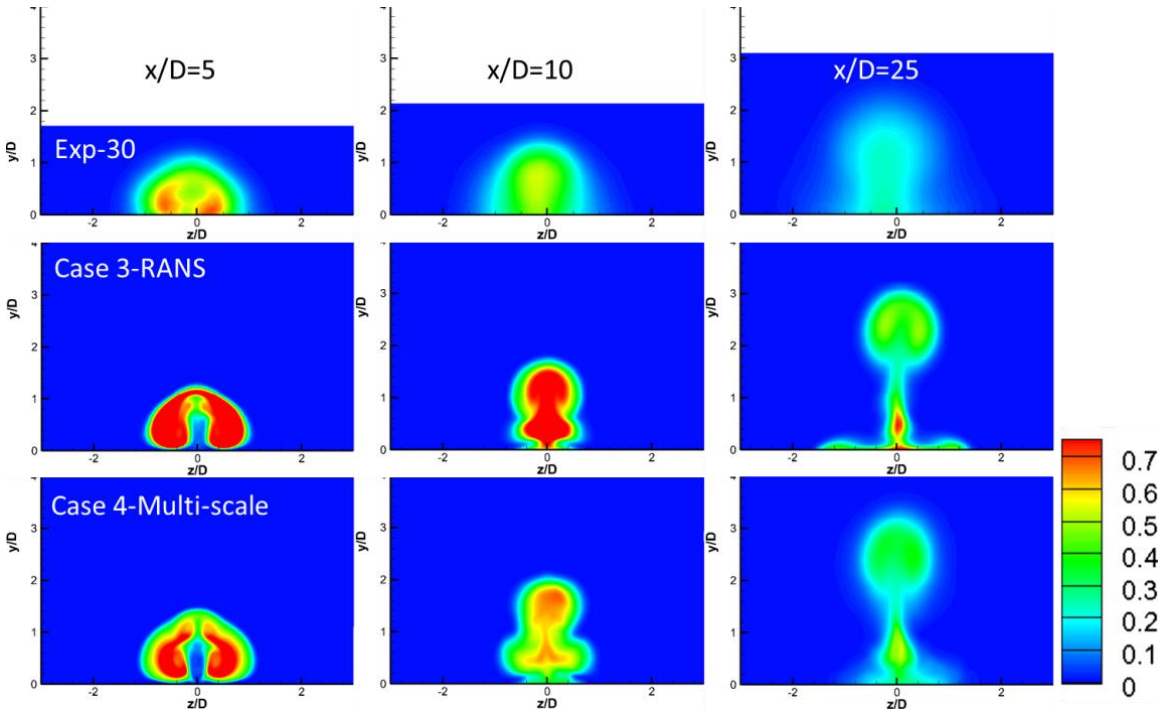

Figure 3-27 Average mole fraction predictions for RANS and multi-scale compared to experimental Raman scattering at 3 different axial locations. (30^o,q=0.5)

There is also a bend in the numerical measurements in both RANS and multi-scale near y/D=1 that is not present in experimental results. Penetration heights are also slightly over-predicted with both RANS and multi-scale, which corresponds to jet growth faster than that witnessed in the experiment.

At *x/D*=25 the predictions of both RANS and multi-scale show a balloon like structure that is more mixed in the case of multi-scale. The results, however, are different from the experiment which shows a single-width column attached to the wall. The penetration height is over-predicted due to higher jet growth. Overall, the multi-scale model did not improve the results significantly over RANS especially when looking at

results with the 90 degree injection in Figure 3-23 in which the multi-scale model resulted in significant improvement over RANS.

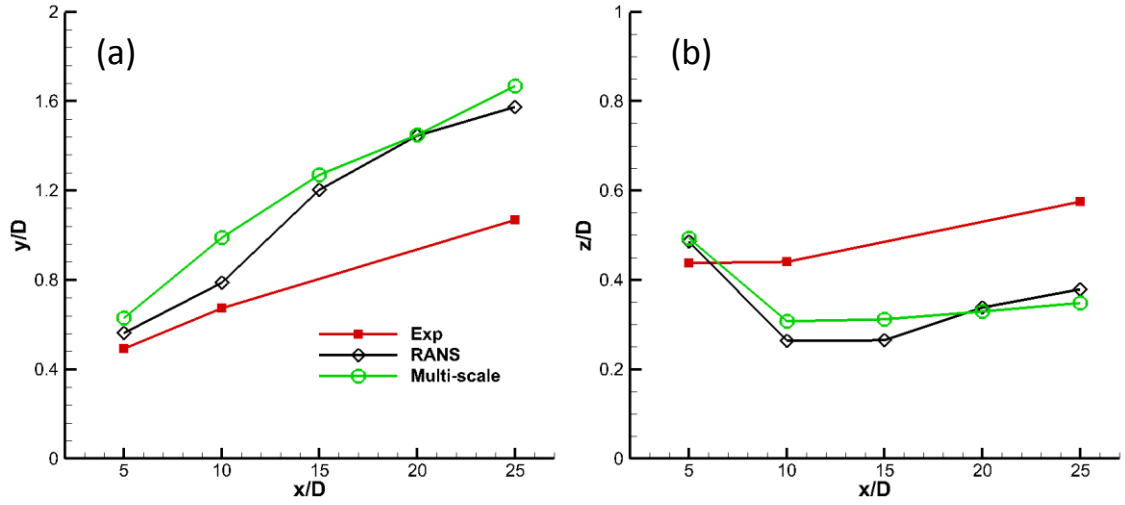

Figure 3-28 Centers for fuel penetration((a) height, (b)widths) for experiment, RANS, and multi-scale models (30^o,q=0.5)

Figure 3-28(a) shows penetration heights centers for the inclined injection (30^o, q=0.5). The heights are over-predicted by up to 0.35 diameters at x/D=25. Both RANS and multi-scale models over-predict the heights with the discrepancy increasing further downstream. In Figure 3-28(b) width centers are plotted versus experimental results. Penetration widths are under-predicted by up to 0.25 diameters at x/D=25. Overall both RANS and multi-scale fail to predict the penetration heights and widths except at x/D=5 where they come within 0.05 diameters of the experimental results. This shows the diffusion of the jet is not predicted correctly even with the multi-scale model with 29 million cells.

3.5 Assessment of Multi-scale Model Performance

The main mechanism that provides the multi-scale model an advantage over RANS is resolving of turbulent structures. When the grid is refined and turbulent structures are larger, the multi-scale model is able to perform well. However, with smaller turbulent structures, even when the grid is refined, the improvement can be limited.

Injection configurations in the jet and crossflow interaction problem produce different vortical structures. Figure 3-29 shows snapshots of the instantaneous *y* vorticity in the center plane for different injection configurations. In the baseline case, with the intermediate grid, vortical structures are large and chaotic. Starting from the Mach disk, they are produced both in the boundary-layer and throughout the jet. The entire flow consists of negative and positive vorticity wrapped around each other to carry the fuel. This is due to combination of normal injection angle with the low momentum of the jet. The normal injection ensures strong interaction between the jet and the crossflow while low jet momentum allows the fuel plume to break up quickly into large chaotic vortices.

For the normal injection at a high momentum ratio (q=1.5), the interaction is strong between jet and crossflow however, the fuel plume does not start to break up intensely until around *x/D=8*, which is why the results at x/D=5 are similar between RANS and multi-scale except for a small reduction of fuel concentration. After the large vortical structures break up, the multi-scale model is able to show improvements beyond *x/D=8* and far field at *x/D=25* multi-scale is able to produce fuel concentration and shape of more resemblance to the experiment.

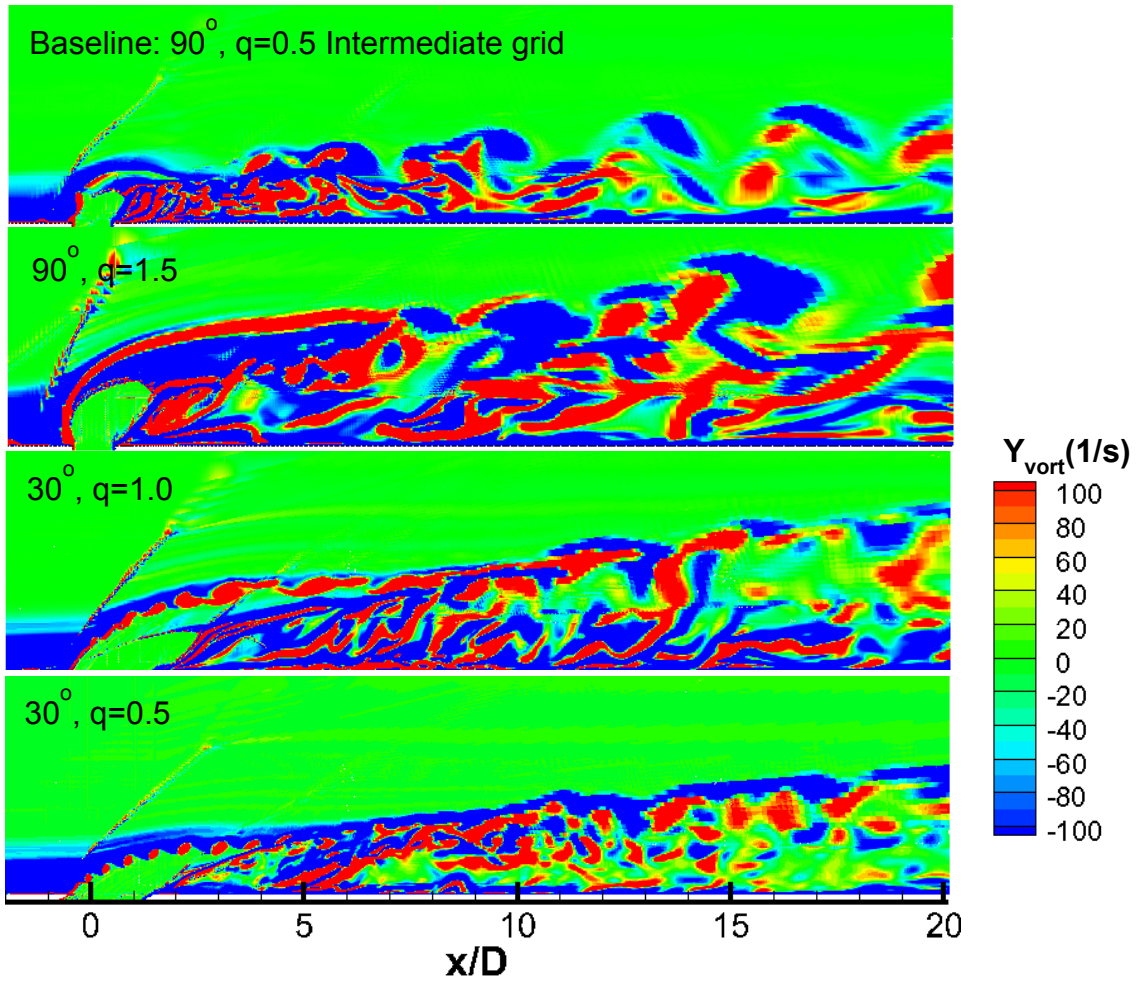

Figure 3-29 Vorticity in the y plane (out of the paper) for different injection configurations on the center plane Maximum and minimum limited to 100, -100

In the inclined cases the interaction between jet and crossflow are milder causing overall smaller vortices. For q=1.0 both RANS and multi-scale predicted reasonable fuel core shapes compared to the experiment with the multi-scale causing a reduction in fuel concentration in agreement with the experiment. The jet momentum was large enough to lift the jet away from the boundary-layer and to reduce chaotic interactions thus allowing RANS to perform reasonably well along with the multi-scale. The fuel concentrations were still over-predicted by the multi-scale model because the 30 degree injection is milder thus producing smaller turbulent structures that require higher resolution to resolve.

The most challenging case is that of inclined injection at q=0.5. The voritcal structures were scattered and small because of the mild interaction and also the momentum of the jet was small that turbulent mixing is significant. The jet was also narrower, and closer to the wall therefore, even finer grid was needed to resolve the boundary-layer. With 29 million cells, both multi-scale and RANS predicted different fuel structures and concentrations than that of the experiment.

It should be noted that the overall cost of the multi-scale model is comparable to RANS for the same grid resolution since the multi-scale model does not impose extra computational time except that involved with collecting and averaging unsteady solutions. The number of grid points required for the multi-scale model is, however, larger than the RANS counterpart and resolution of turbulent structures is dependent on the grid size. If the grid is too coarse the solution approaches the RANS model. As the grid is refined more turbulent structures are resolved and turbulent diffusion and mixing is predicted accurately. The RANS models, however, does not produce significant unsteadiness even with larger grids. The number of grid points required for the multi-scale model to resolve sufficient amounts of turbulent structures varies by case due to the turbulent length scale present in the solution. In cases where the turbulent length scale is smaller such as the 30^{o}, q=0.5 case, the multi-scale model and the RANS solution are similar because finer grids are needed to resolve smaller turbulent structures. To improve the efficiency of the multi-scale model higher order convective fluxes can be used to resolve more turbulent structures and reduce the effect of the numerical viscosity or an improvement of the sub-filter mixing model should be proposed. The latter is proposed in the next chapter in the form of an adaptive turbulent Schmidt number.

3.6 Summary

The multi-scale model was successfully tested with different configurations and grids for the jet and crossflow interaction causing an improvement over RANS results when compared to experiment, to some extent, for all injection configurations. The mechanism at which the multi-scale model works is resolving more turbulent structures in the solution, those turbulent structures may give more accurate average predictions than those predicted by RANS.

The fuel distribution, which is significantly dependent on turbulent mixing, was the most affected/improved when switching to multi-scale. For the baseline case, results were consistent with other researchers' studies of the same case in which hybrid RANS/LES methods improved predictions in a similar fashion[27, 52]. The major conclusions to be drawn with the use of the multi-scale model specifically are outlined below:

- RANS model does not produce significant unsteadiness which is important because the mean of fuel concentration is not correlated with the instantaneous results which contain large variance from the mean.
- Mixing, especially with the baseline case, was the most sensitive to the use of the multi-scale model, showing overall different behavior than RANS and producing average concentration profiles closer to the experiment. Penetration widths which are more dependent on diffusion were significantly improved by switching to multi-scale. When resolved structures were used to estimate a resolved Sc_t, they showed a non-constant behavior unlike the constant assumption in RANS.

- RANS was able to capture other important flow variables such as velocity and pressure fields reasonably well leading in most cases to a reasonable prediction of penetration heights.
- Different configurations responded differently to the use of the multi-scale model. With the cases of aggressive interaction, yielding larger turbulent structures, experiencing the most improvement. For cases where the interaction resulted in a milder segregation between the jet and crossflow or the momentum of the jet caused a delay in plume breakup, the vortical structures were small and scattered and the multi-scale model's improvement was limited even with very fine grids

To increase resolved turbulent structures, we must minimize the amount of numerical viscosity, which could be done by refining the grid considerably, using only uniform grid, or using higher-order fluxes. The use of high-order convective fluxes would aid in the reduction of the number of grid points, however, it may cause stability and grid limitations. The other option is to improve sub-filter mixing which is done in the next chapter by introducing the adaptive turbulent Schmidt number approach.

Chapter 4.
Adaptive Turbulent Schmidt Number in Turbulence Modeling

As shown in chapter 3, the multi-scale turbulence approach is useful in predicting mean flows in jet and crossflow interaction problems containing complex turbulent structures that are otherwise unattainable using standard RANS models. Using the multi-scale turbulence approach, turbulent mass diffusion in the resolved field showed variations not correlated with the eddy viscosity. This chapter aims to modify the multi-scale turbulence approach to allow the resolved field to adaptively influence the value of turbulent Schmidt number in the RANS sub-filter model within the jet and crossflow interaction problem. The proposed model estimates a time-averaged resolved turbulent Schmidt number that is used in place of the constant value common to RANS. This approach is assessed by grid refinement study in which different amounts of turbulence are resolved. Fuel concentration predictions show an improvement when compared with experimental measurements versus the multi-scale model without the adaptive approach

4.1 Implications of The Adaptive Approach

The use of the estimated Sc_{t_Res} instead of the constant value in the RANS sub-filter model provides an estimate for sub-filter diffusion based on the actual fluctuations of the case considered. The adaptive approach does not rely on any previous correlations or ad-hoc numbers thus eliminating uncertainty associated with specifying an Sc_t. Additionally the estimated Sc_{t_Res} is a field variable that varies spatially throughout the domain consistent with the behavior of resolved turbulent Schmidt number estimated in the previous chapter.

As shown in chapter 3(and in chapter 2), it is possible to estimate the turbulent Schmidt number based on the resolved field using the following formulation,

$$Sc_{t\_Res} = \frac{\frac{\left(\overline{\rho u_i^R u_J^R} - \frac{2}{3}\overline{\rho k_{Res}}\delta_{ij}\right)S_{ij}(\tilde{u}_i)}{\bar{\rho} S_{ij}(\tilde{u}_i) S_{ij}(\tilde{u}_i)}}{\frac{\left(\overline{\rho u_i^R Y_m^R}\right)}{\bar{\rho}} \frac{(\partial \tilde{Y}_m/\partial x_i)}{(\partial \tilde{Y}_m/\partial x_i)(\partial \tilde{Y}_m/\partial x_i)}} \qquad \textbf{4.1}$$

There are two types of terms on the right hand side of Eq.4.1; fluctuation terms and gradient terms. The gradient terms, $S_{ij}(\tilde{u}_i)$ and $\partial \tilde{Y}_m/\partial x_i$, are evaluated using the derivatives of average variables such as $\tilde{u}_i$ and $\tilde{Y}_m$. As long as the averages of those variables are evaluated accurately the gradient terms should be considered accurate. The challenge is the average variables are not converged until the end of the simulation and we therefore use an estimate of their values that improves as the simulation proceeds. To minimize the estimation error we only start to employ the adaptive turbulent Schmidt number approach after a number of iterations (in this study we use 2000).

The fluctuation terms such as $\overline{\rho u_i^R u_j^R}$ and $\overline{\rho k_{Res}}$ are evaluated using the general expression

$$\overline{\rho u^R{}_J \phi^R} = \overline{\rho u_J \phi} - \overline{\rho u_J}\frac{\overline{\rho \phi}}{\bar{\rho}} \qquad \textbf{4.2}$$

Where the terms on the right hand side of Eq 4.2 would suffer from the same estimation errors encountered with the gradient terms. Additionally we must note that the use of the fluctuation variables $\overline{\rho u^R{}_J \phi^R}$ in place of $\overline{\rho u'{}_J \phi'}$ is another approximation that assumes that each iteration of the simulation generates a truly instantaneous field. *In other words, we assume that the turbulent mixing in the sub-filter field is correlated with the resolved mixing in the simulation*. This is the main assumption of the model and it directly leads to limited range of spatial and time resolution in which the adaptive

approach is applicable.

For example, if the grid is too coarse the evaluation of the fluctuation terms are not accurate because there is not enough resolved structures to evaluate for the mixing. If on the other hand the grid is very fine, we will collect good estimations for the resolved mixing, however, the need for accurate sub-filter turbulent Schmidt number may not be needed because the simulation is already resolved. *So the ideal problem for the adaptive turbulent Schmidt number approach is one that when applying the multi-scale model, resolved turbulent structures are present in the simulation and are representative of those in the sub-filter field but at the same time grid resolution is not too fine that sub-filter turbulent mixing is not important.* One way to check for consistent fluctuations (whether the grid is fine enough) is to check for degree of symmetry in the Sc_t contours for a symmetric problem. We use this method to evaluate the quality of the adaptive approach for jet and crossflow interaction cases.

In addition to grid size limitations associated with the adaptive turbulent Schmidt number approach, the scalar assumption of a turbulent Schmidt number is still assumed implying isotropy which is not always true leading to estimated Sc_t that is sometimes negative. Positivity is enforced with an absolute value function to prevent instabilities with the RANS model. Table 4-1 outlines advantages and challenges of the adaptive approach.

In order to evaluate the adaptive approach, it is tested first with the baseline case with two different grid resolutions to evaluate its sensitivity to grid refinement. Then it is used with the 30^o, q=0.5 injection configuration that was shown in chapter 3 to be most challenging to evaluate with the multi-scale model alone.

Table 4-1 Advantages and limitations of the adaptive approach

Advantages	*Limitations*
Does not require specification of Sct	Averages are not fully converged when estimated
Can estimate sub-filter mixing for multi-scale coarser grids	Limited only to use with multi-scale model or LES type approaches
Relies on the actual flow for estimation without any correlation/previous data	Limited to a range of grid resolution
	Many simplifying assumptions including isotropy cause unphysical Sct predictions

4.2 Baseline Case: 90^o,q=0.5 [Cases 15-19]

The adaptive approach is applied to the multi-scale model and the results are compared to the multi-scale model alone for two different grid resolutions. Based on the results, an adjustment to account for numerical viscosity is added to improve the performance of the adaptive approach. The Details of the numerical viscosity correction are discussed later in the chapter. After evaluation with the baseline case, the model is tested with the 30^o, q=0.5 case that suffered the most with the multi-scale alone. Table 4-2 details the baseline cases considered in order to evaluate the adaptive approach.

Table 4-2 Baseline injection cases considered for adaptive approach

Case	*Configuration*	*Grid resolution*	*Turbulence treatment*	Sc_t	μ_{num} *correction*
Chapter 3					
5		Grid 1 / 7 Million	Multi-scale-SST	0.7	No
6		Grid 2 /17 Million	Multi-scale-SST	0.7	No
8		Grid 1 / 7 Million	MILES (no model)	N/A	N/A
Chapter 4	Baseline				
15	(90o,q=0.5)	600,000	RANS-SST	0.7	No
16		Grid 1 / 7 Million	Multi-scale-SST	Adaptive	No
17		Grid 2 /17 Million	Multi-scale-SST	Adaptive	No
18		Grid 1 / 7 Million	Multi-scale-SST	Adaptive	Yes
19		Grid 2 /17 Million	Multi-scale-SST	Adaptive	Yes

4.2.1 Adaptive Sc_t multi-scale and comparison to constant Sc_t multi-scale and RANS results

The adaptive Sc_t multi-scale approach explained earlier is implemented and tested with both grid 1 and grid 2. To be consistent, it is compared to RANS solution with Sc_t= 0.7 and earlier multi-scale solutions with Sc_t= 0.7. It should be noted that in chapter 3, RANS results were very sensitive to the value of Sc_t and comparable levels of fuel mole fractions were obtained by drastically lowering its value. When running the simulation, a constant Sc_t of 0.7 is used for the first 2000 iterations while an average is collected for the adaptive resolved Sc_t. With numerical experiments, the resolved Sc_t was independent of the initial constant value used in the first 2000 iterations.

The resolved turbulent Schmidt number contours for grid 1 and grid 2 are shown

in Figure 4-1.Those contours are an indication of the mixing in the resolved field of each grid. The range is limited from 0 to 1 because larger values imply negligible turbulent mass diffusivity. Also these values are irrelevant in areas that do not contain fuel. Overall features of the distribution of the turbulent Schmidt number are similar in grid 1 and grid2.

Distributions in grid 1 however, are not fully symmetric, and symmetry improves when the grid is refined. This shows that for grid 2, the resolved field is strong enough to overcome errors induced by approximate averaging procedures. Symmetry and similarity between the two grids are better in the near field region where the grid is finer than the rest of the domain. In the far field where the grid is coarser and less resolved mixing occurs, the results seem to be less symmetric and more differences are observed between grid 1 and grid 2. This is simply because of weaker resolved mixing which results in more data noise.

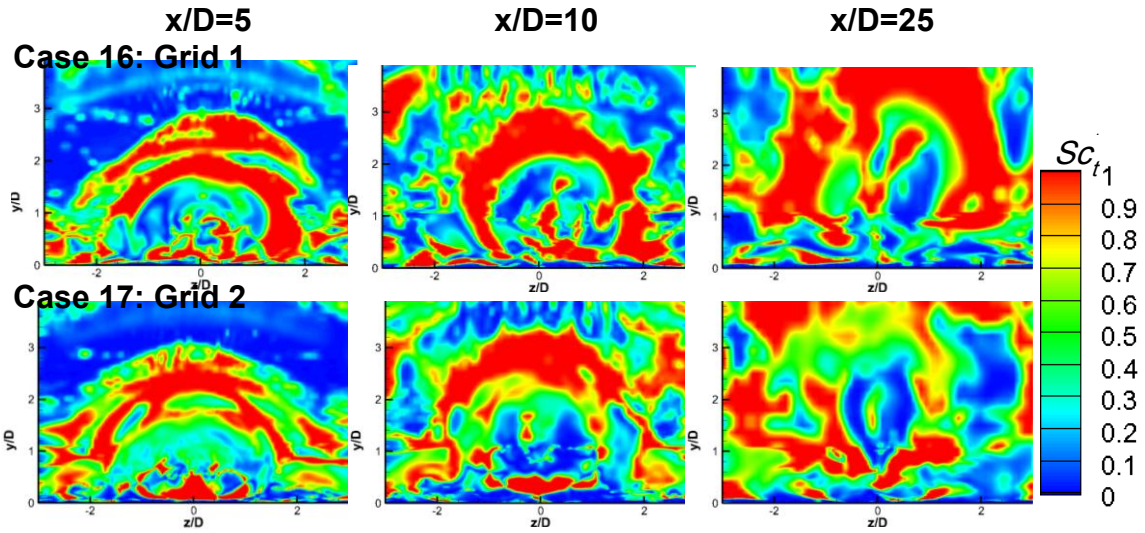

Figure 4-1 Adaptive turbulent Schmidt number contours for grid 1(top) and 2 (bottom) at different x/D locations (baseline case)

Fuel mole fraction results are displayed for experimental, RANS, multi-scale, and

multi-scale with adaptive Sc_t approaches. The results are shown at two axial locations x/D= 5 and x/D= 25 in Figure 4-2 and Figure 4-3 respectively. At x/D= 5, RANS results show two kidney vortices that are largely unmixed. When the multi-scale approach is used these two vortices are reduced in size and appear closer to each other in grid 1. In grid 2 these two vortices merge into one mixed core in the center similar to findings in the experimental measurements. The concentration of the fuel core is still over-predicted in both grid 1 and grid 2. When applying the adaptive Sc_t extension, results were largely unchanged. In the grid 1 the kidney vortices were closer and formed a single core. The contour also shows slightly larger attachment to the wall. For grid 2, only a slight reduction in core fuel concentration is observed. Overall, although insignificant, the results were closer to the experimental measurements.

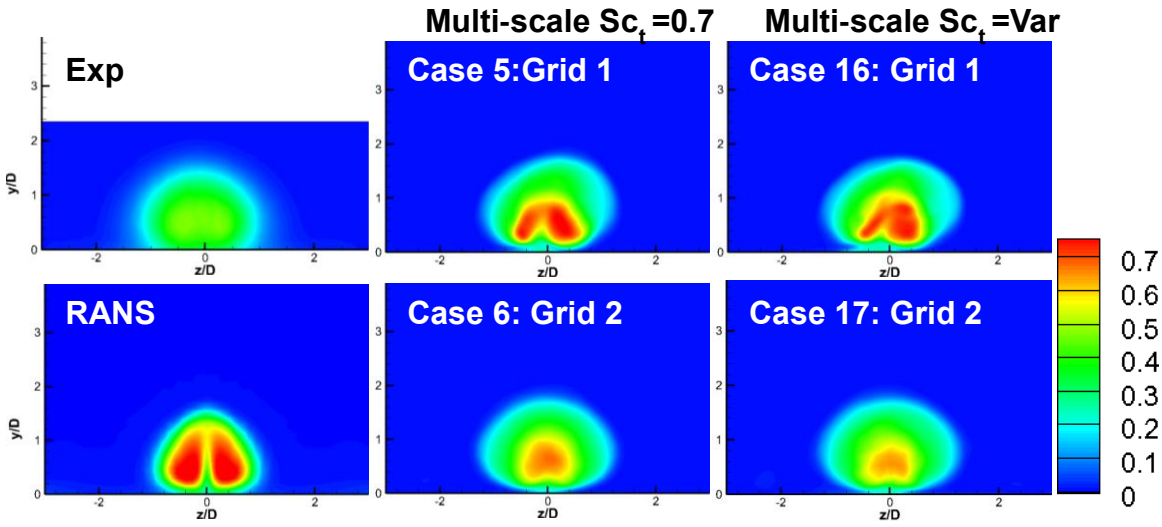

Figure 4-2 Fuel mole fraction contours at x/D= 5 for experimental and different numerical approaches. In multi-scale simulations grid 1 results are on top and grid 2 on the bottom

At x/D= 25, the RANS results show a lifted circular core that is attached to the wall through a slender neck of fuel. Multi-scale results at grid 1 show a more diffuse core with the fuel neck occurring closer to the wall. At grid 2, the results compare better to the

experiment and show no fuel neck and a more diffuse fuel core. In all cases, there is a slight over-prediction in the fuel penetration height. With the adaptive approach extension, grid 1 results were more diffuse and necking occurred closer to the wall than the constant Sc_t multi-scale. There was however, necking at the top of the fuel core on the left side that is asymmetric and is not predicted by the experiment. With grid 2, results improved slightly in resembling the experiment when using the adaptive Sc_t extension for grid 2.

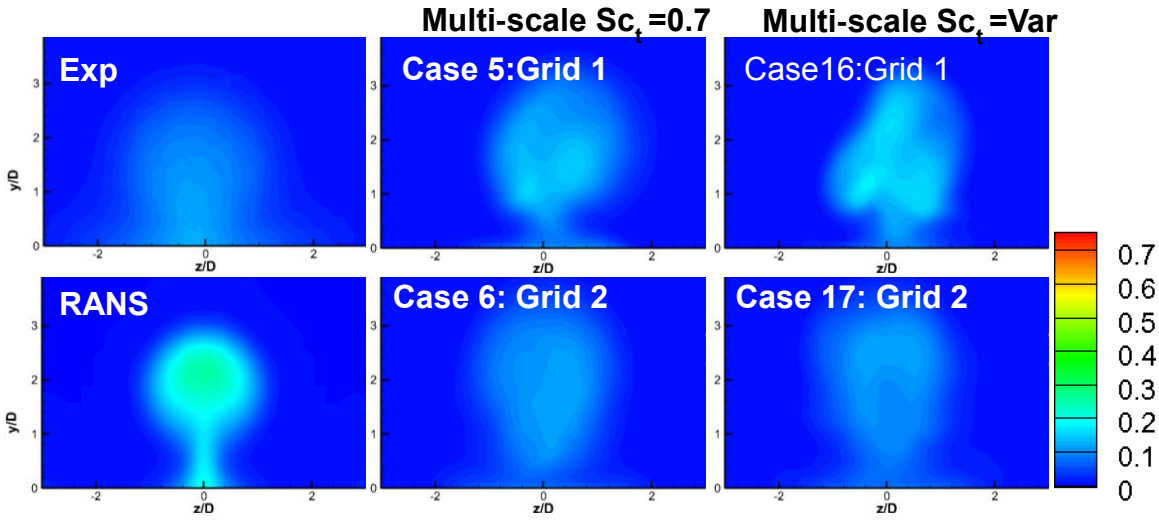

Figure 4-3 Fuel mole fraction contours at x/D= 25 for experimental and different numerical approaches. In multi-scale simulations grid 1 results are on top and grid 2 on the bottom

4.2.2 Effect of Numerical Viscosity on Turbulent Diffusivity

In the LES community, it is often argued that high-order-low-dissipation schemes are needed for an accurate LES simulation. This is because the error caused by the scheme often produces numerical viscosity that is on the order of eddy viscosity provided by the sub-grid model. In multi-scale modeling, numerical viscosity also plays an important role preventing the model from resolving smaller turbulent structures. In this effort, standard

second order upwinding is used to model convective terms in the momentum equation leading to relatively high numerical dissipation. Therefore, finer grids are needed to produce the same size turbulent structures that are found in other researchers' results for the same problem[27, 52].

For multi-scale modeling, the amount of turbulent mass diffusivity is determined by the Reynolds diffusion term in the mass transport equation, namely, $D_{i_m}^R \approx -\frac{\mu_t}{Sc_t}\frac{\partial \tilde{Y}_m}{\partial x_j}$. This term is directly proportional to the value of the momentum eddy viscosity (μ_t). In RANS modeling, this is acceptable because the value of the eddy viscosity is much larger than the numerical one. In multi-scale modeling, however the resolved eddy size is determined by the sum of all three viscosities. Dissipation in the momentum equation caused by the laminar, numerical and eddy viscosities determine the size of the resolved turbulent structures present in the solution. For example by not accounting for numerical diffusivity, the fuel diffuses in the sub-filter within eddies much smaller than those present in the solution (determined by the eddy viscosity alone). This causes limited turbulent mass diffusion in the overall solution.

One way to separate the effects of the numerical viscosity caused by the grid and the numerical scheme is to simply set the eddy viscosity to zero thus using no turbulence model. This method is equivalent to conducting an LES simulation with the sub-grid model implicitly defined as the numerical viscosity providing an upper limit to the turbulent oscillations in the solution for a particular grid and numerical scheme. This method was first named Monotone Integrated LES (MILES) by Boris[152] and an extensive analysis can be found in the book by Grinstein et al.[154].

Figure 4-4 (repeated from Figure 3-20) shows the y vorticity on the center plane

for grid 1, and grid 2 (without adaptive Sc_t approach) as well as the MILES approach (zero eddy viscosity) for grid 1.

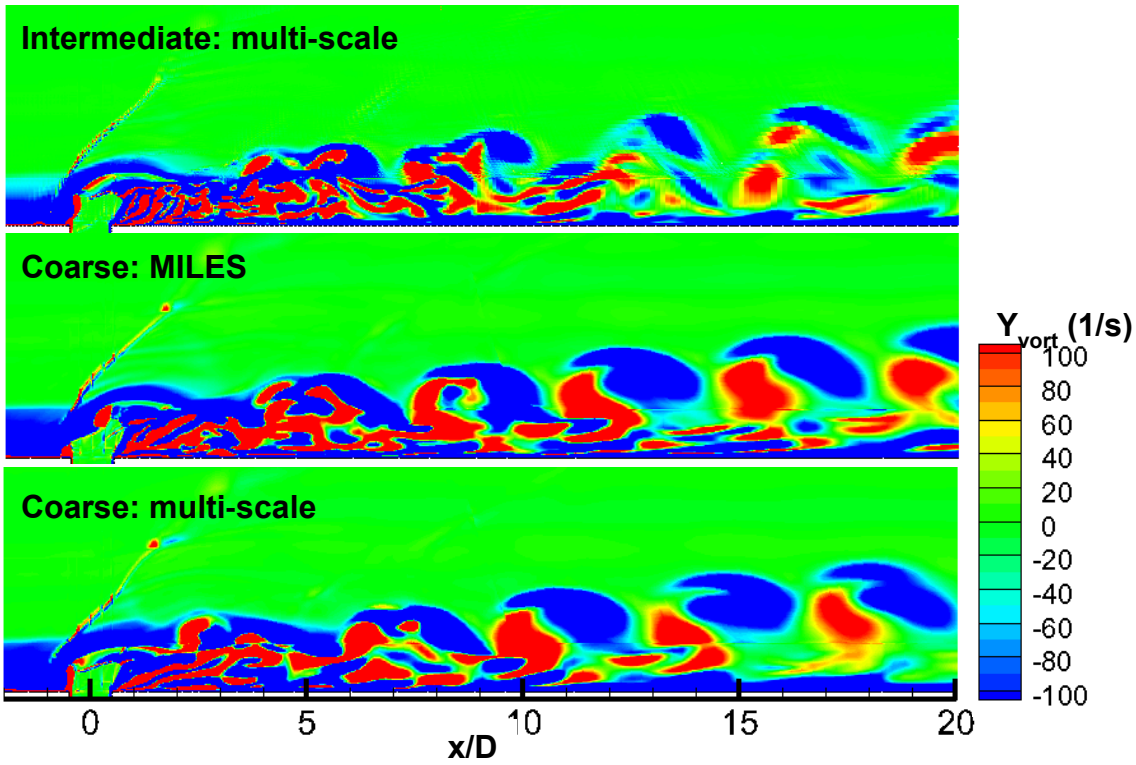

Figure 4-4 (repeated from 3-16) Instantaneous *y* vorticity snapshots on the center plane for multi-scale (grid 2 on top and grid 1 on the bottom) and MILES (grid1) approaches. Maximum and minimum limited to 100, -100

This figure gives a qualitative assessment for the numerical viscosity. The vortices in the MILES solution are sized in between grid 1 and grid 2, but closer in size to the grid 1. This indicates that the eddy viscosity in grid 2 is less than the numerical viscosity in grid 1. We could also say that the numerical viscosity is not orders of magnitude larger than the eddy viscosity in grid 1 because the MILES solution displays smaller vortices than those seen in grid 1 results.

Fuel mole fractions' contours for multi-scale grid 1and grid 2 and grid 1 MILES solution are displayed in Figure 4-5. It is seen that fuel in the MILES solution is much less diffusive than grid 1 and has about the same diffusivity as grid 2. This observation is in line with effect of the numerical viscosity on turbulent diffusion. Even though

numerical viscosity has caused larger vortices in the MILES solution (slightly smaller than grid 1), the fuel was not dispersed in the same manner. In fact, fuel dispersion in the coarse MILES solution is comparable to grid 2.

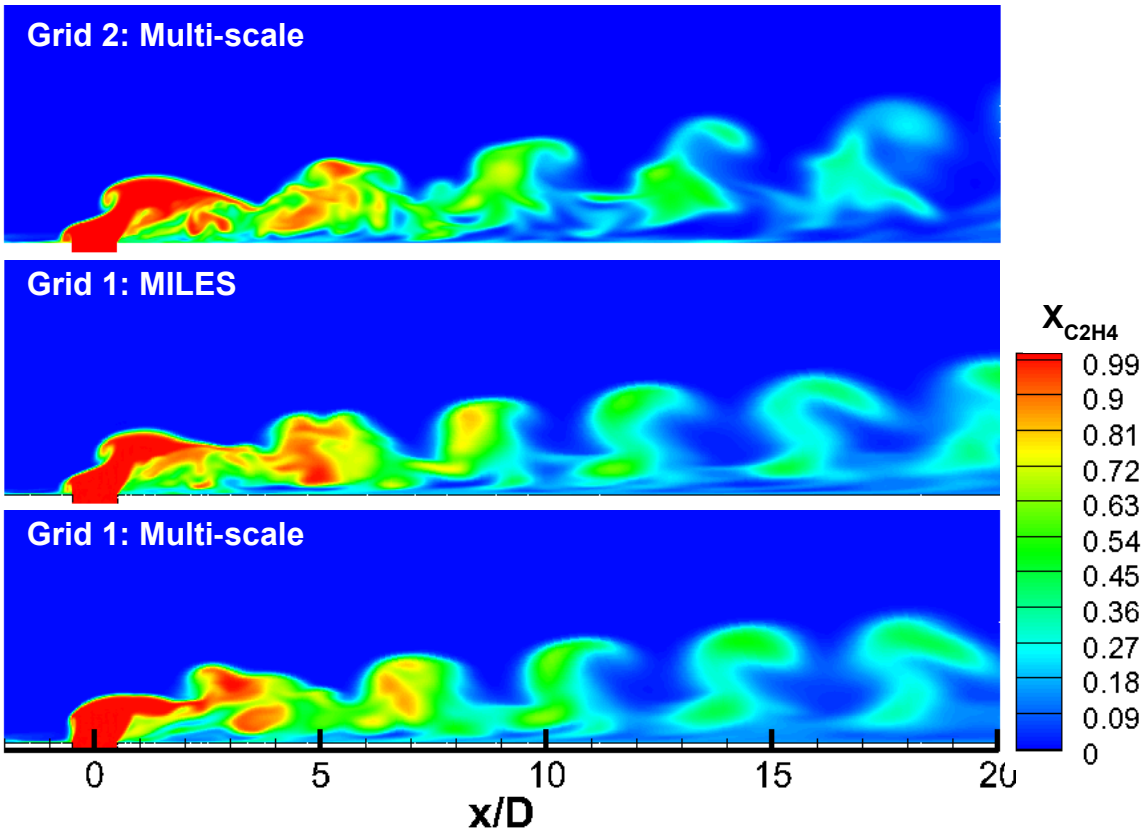

Figure 4-5 Instantaneous fuel mole fraction snapshots on the center plane for multi-scale (grid 2 on top and grid 1 on the bottom) and MILES (grid1) approaches (baseline case)

To include the effect of numerical viscosity one must modify the Reynolds diffusion term as follows

$$D_{i_m}^R \approx -\frac{\mu_t + \mu_{\text{num}}}{Sc_t}\frac{\partial \tilde{Y}_m}{\partial x_j} \qquad \textbf{4.3}$$

It is difficult to calculate the numerical viscosity without a solution of higher order convection scheme which is not available and would make the computation impractical. One way to crudely estimate the numerical viscosity is to use the generalized Smagorinsky coefficients[142, 143] and estimate it as follows,

$$\mu_{\text{num}} = \bar{\rho} C_{\text{gs}} L_G^2 |S| \qquad 4.4$$

The generalized coefficient, C_{gs}, value suggested by Mossi et al.[143] for a second order scheme in a compressible fully developed flow case is 0.2. This value is not universal and should be refined further for this particular case but we will use it here as a rough estimate for numerical viscosity.

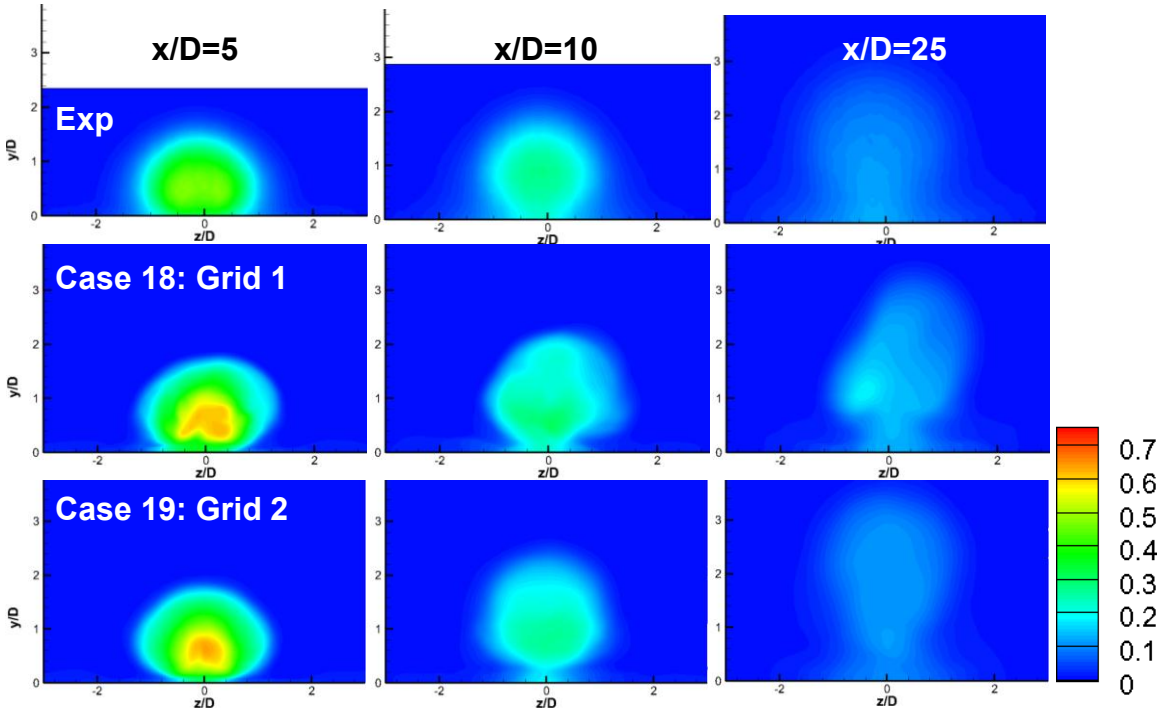

Figure 4-6 Fuel mole fraction predictions for the multi-scale adaptive Sc_t approach with numerical viscosity correction. Experimental measurements on the top, grid 1 in the middle and grid 2 on the bottom

When the numerical viscosity is taken into account fuel mole fraction are calculated for grid 1 and grid 2. The results are shown in Figure 4-6. Both the mixing and the fuel structure are in good agreement with the experiment. Grid 1 results have improved significantly especially in the near field showing more attachment to the wall and higher overall mixing consistent with the experiment. Grid 2 showed slight improvement over standard multi-scale at x/D= 5 and better resemblance of the experiment at x/D= 25. This is because near field grid resolution is so fine that diffusion

within the sub-filter field becomes unimportant. Coarser grid in the far field, however, allows sub-filter turbulent mass diffusion to play a larger role.

4.2.3 Adaptive Turbulent Schmidt Number Effect on Solution and Mixing

The difficulty in predicting experimental fuel distribution lies largely in the near field. Specifically, at $x/D = 5$, fuel core concentrations were over-predicted at varying degrees by all methods used in both this and previous chapter. It was also over-predicted by others using hybrid RANS/LES[27]. This is mainly because near the fuel plum and the barrel shock, there is a high degree of unsteadiness that must be captured correctly. This unsteadiness works in mixing the fuel on the average sense in the near field region. Figure 4-7 shows average mole fraction iso-surfaces for cases 5(multi-scale alone-7 Mil), 6(multi-scale alone-17 Mil) and 18(Adaptive approach with numerical viscosity correction) as well as streamlines and bow shock pressure iso-surface for case 6. The fuel coming from the center of the injector is projected along the top of the jet and is diffused conventionally as it travels downstream. Most of the unsteady mixing takes place in fuel carried by the horse-shoe vortices which are originated from the edges of the injector. Those vortices are generated behind the injector in the area between the bow shock and its footprint on the boundary-layer. Due to strong unsteadiness at the fuel plume near the barrel shock, the horse-shoe vortices lose their strength on the average sense and diffuse with the main flow. The unsteady mixing process is stronger as we refine the grid causing the horse-shoe vortices to diffuse faster.

Average fuel mole fractions are displayed as iso-surfaces in Figure 4-7 and as color contours on the center plane in Figure 4-8 for cases 5(multi-scale alone-7 Mil), 6(multi-

scale alone-17 Mil) and 18(Adaptive approach with numerical viscosity correction) . As the grid is refined, fuel rich iso-surfaces become shorter as indicated in Figure 4-7 and the fuel vortex following the plume in Figure 4-8 becomes less intense due to unsteady mixing. It is the goal of this effort to model this mixing process in the near field using the adaptive Sc_t approach. It is therefore logical to use Sc_t based on the resolved field resulting in more mass diffusion in highly resolved regions. We can compare the fuel structure of case 18, which uses the adaptive Sc_t multi-scale approach with the numerical viscosity correction, to case 6 which is a simple refinement over case 5 using standard constant Sc_t multi-scale approach. In case 18, the fuel vortex is less intense and the fuel rich iso-surface is shorter resembling the mixing dynamics of the finer grid in case 6.

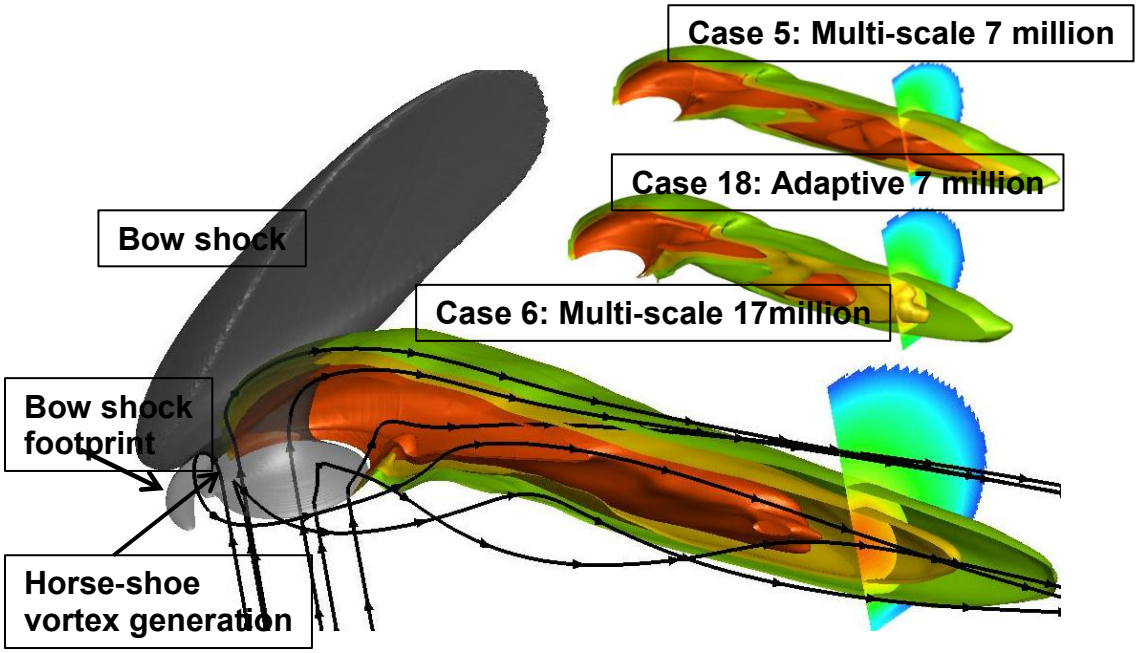

Figure 4-7 Average bow shock pressure iso-surface and fuel streamlines for case 6. Average fuel mole fractions iso-surfaces for cases 5, 18, and 6.

Figure 4-9 displays average pressure contours on the center plane for cases 6 and 18. The pressure contours are similar showing the bow the barrel shock near the injector. It is evident that the adaptive Sct multi-scale approach had no adverse effects on the

pressure field. Similarly, Figure 4-10 shows axial velocity for the same two cases that have similar features.

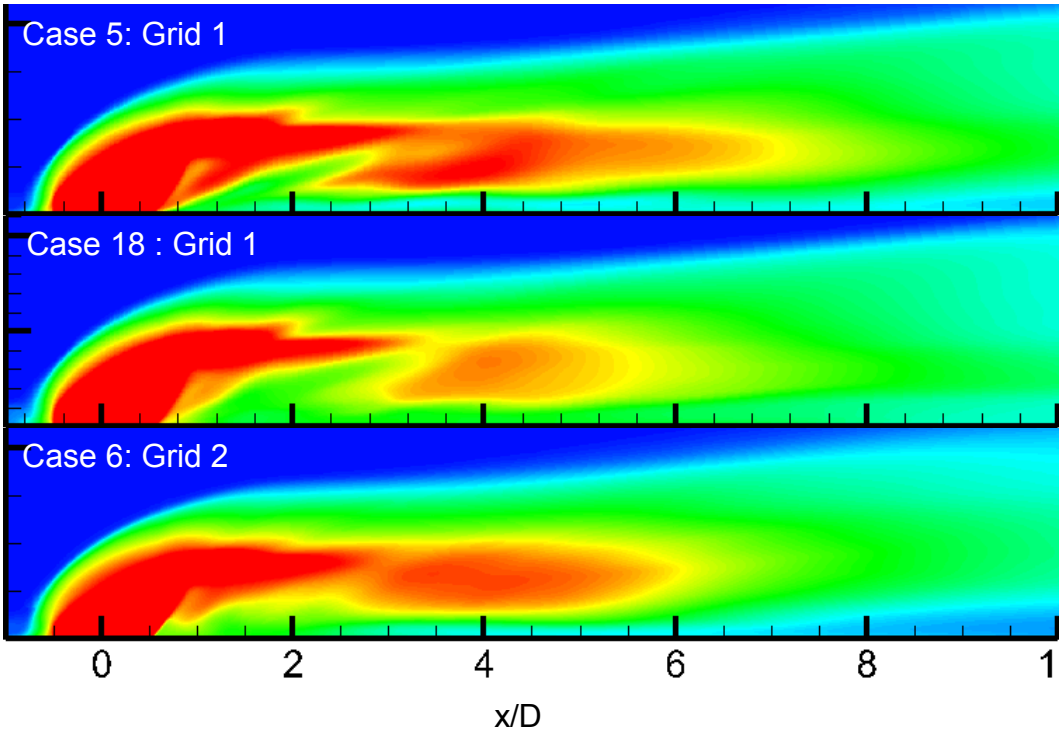

Figure 4-8 Average fuel mole fractions at center plane for cases 5, 18, and 6..

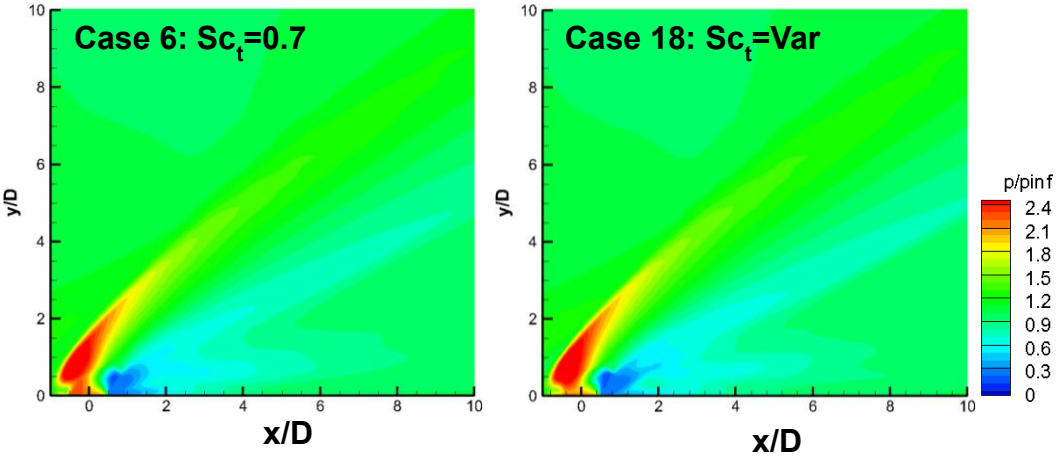

Figure 4-9 Center plane pressure contours for cases 6 and 18. Injector is located at x/D= 0

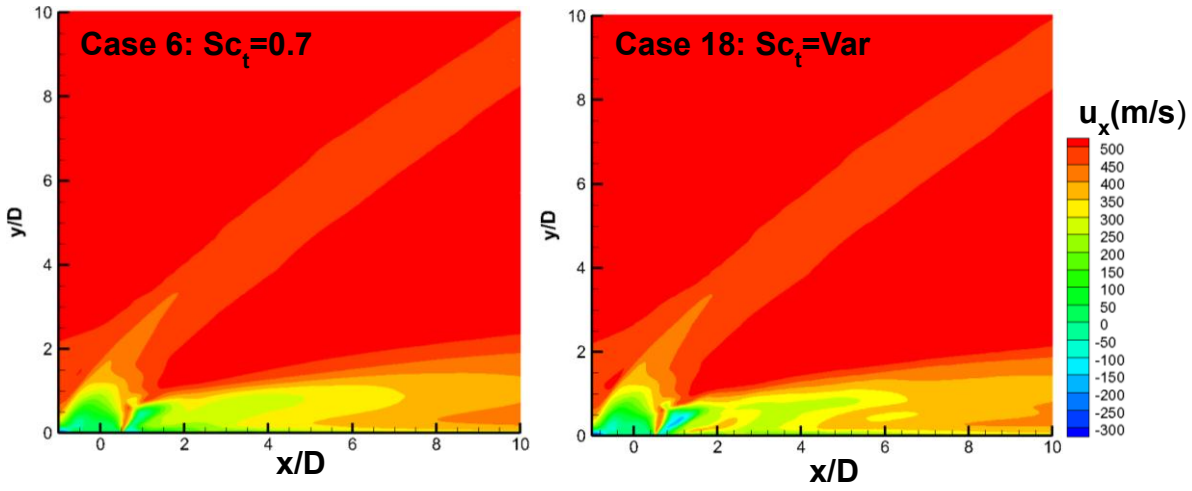

Figure 4-10 Center plane axial velocity contours for cases 6 and 18. Injector is located at x/D= 0

4.3 Inclined Case : 30^o, q=0.5

The 30^o, q=0.5 case was the one with the least improvement over RANS in chapter 4.It is considered a good candidate for the adaptive approach because most of the turbulent mixing is carried by smaller vortices that are harder to resolve. Therefore the modeled portion of the flow has a significant effect on the overall turbulent diffusion. The case was run with the adaptive approach including the numerical viscosity correction using 29 million cell grid originally used with the multi-scale model in chapter 3. Also the RANS results from chapter 3 are included for comparison.

To evaluate the capability of RANS, multi-scale, and adaptive approaches, first the average fuel mole fraction on the center plane of the injector is collected and shown in grey scale in Figure 4-11 to compare with the mean intensity of processed PLIF images obtained experimentally by Lin et al.[16, 65] It should be noted that the mean intensity images do not have scaling information, therefore, no scale is displayed.

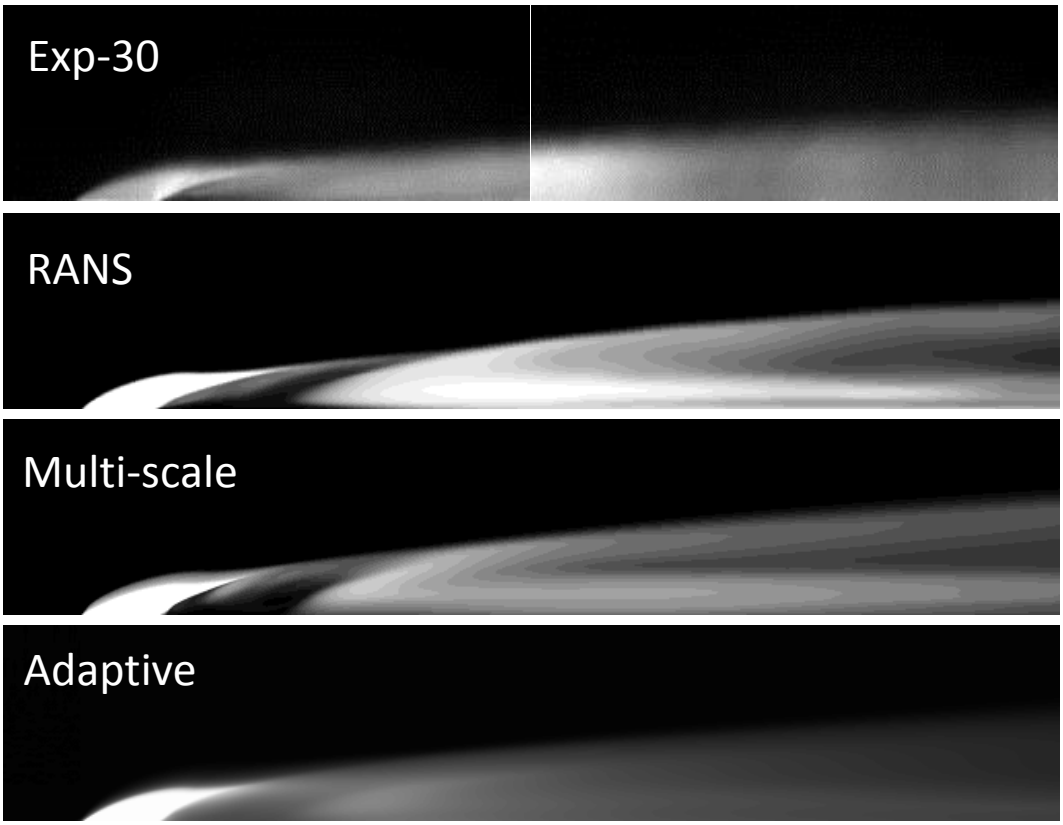

Figure 4-11 Mean intensity of PLIF images (2 separate images taken) compared to fuel mole fraction contours in grey scale of RANS ,multi-scale, and adaptive models(30^o,q=0.5).

Despite different grid resolutions, the multi-scale and RANS results have similar jet structure. The intensity of fuel concentration is lower in the case of multi-scale than RANS due to higher degree of mixing. Experimental results show significantly higher turbulent mixing with slower jet growth than either RANS or multi-scale. Below the fuel plume there is a fuel lean pocket that is more pronounced in the RANS and multi-scale results than the experiment because fuel is able to diffuse there with the higher turbulent mixing. In the far field there is also a slender fuel lean pocket in the center of the jet in RANS and multi-scale that is not present in experimental mean PLIF images. Overall multi-scale results are slightly more mixed than RANS while still not significantly closer to the experiment. With the adaptive approach, similar to the experiment, fuel lean pocket

under the plume is smeared due to high turbulent mixing. The jet growth and penetration heights are well predicted with the jet only slightly larger than the experiment. Fuel concentration in the far field is also slightly under-predicted with the adaptive approach. Overall the adaptive results are very good compared to the experiment and are a significant improvement over RANS and multi-scale alone.

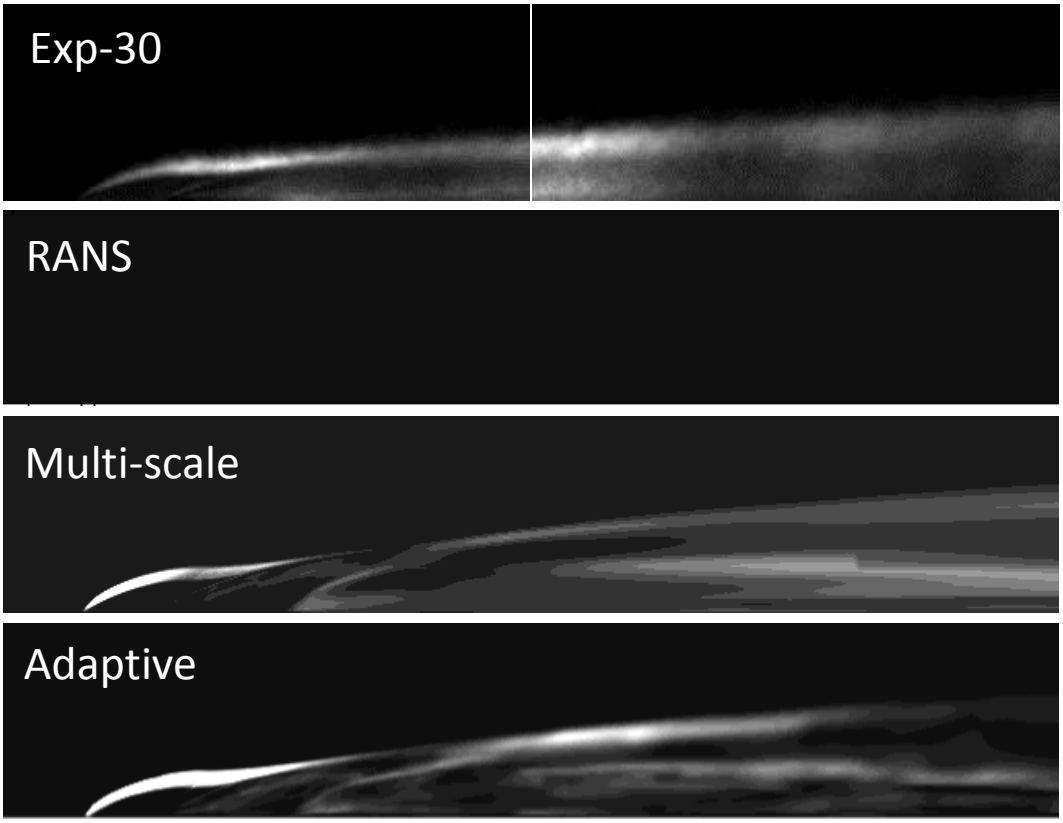

Figure 4-12 Variance of intensity of PLIF images(2 separate images taken) compared to fuel mole fraction variance contours in grey scale of RANS , multi-scale, and adaptive models(30^o,q=0.5).

In order to qualitatively check the resolved turbulent fluctuations in multi-scale models, the variance of the fuel mole fraction is compared to the variance of the intensity of the PLIF images. The results of the comparison are plotted in greyscale in Figure 4-12. Scaling information is not shown because it is not present with the experimental results. Naturally, the RANS results show an insignificant variance because no variance is

captured as the high eddy viscosity dampens turbulent structures. The multi-scale variance shows some similarity to the experiment especially near the jet exit. The integrated value of the RANS variance is 5.5e-5 while multi-scale and adaptive approach variances are 0.54 and 0.33 respectively. The multi-scale integrated variance is 10000 times larger than RANS. The integral value of the adaptive approach variance is slightly lower than the multi-scale because the reduction of turbulent Schmidt number introduces damping to the turbulent structures in the flow.

The adaptive approach displays the same variance characteristics as those obtained from PLIF images. Following the upper jet boundary there is a higher variance region that decreases and increases in intensity. The entire length of the upper jet boundary is well captured by the simulation and is in much better agreement than the multi-scale results alone. The inside of the jet shows lower variance in the fuel plume and the fuel lean pocket is in agreement with the experiment. There is some deviation in variance in the far field below the jet boundary. Those disagreements are far less obvious than those shown with the multi-scale alone. Overall the variance obtained using the adaptive approach is superior to those obtained without it when compared to the experiment.

Experimental Raman scattering fuel concentration results are compared to the adaptive approach at 3 axial locations. Fuel concentration is slightly over-predicted at x/D=5 with the overall structure of the fuel core similar to that of the experiment. Penetration height and width are well predicted. At $x/D=10$, fuel concentration is well predicted with similar structure however penetration height is slightly over-predicted. There is no bend in the numerical results unlike multi-scale alone. At x/D=25, the predictions of the adaptive approach are of similar structure to the experimental

measurements, however, penetration height is over-predicted and higher concentration fuel core is thinner in the center. There is no balloon like structure unlike multi-scale alone.

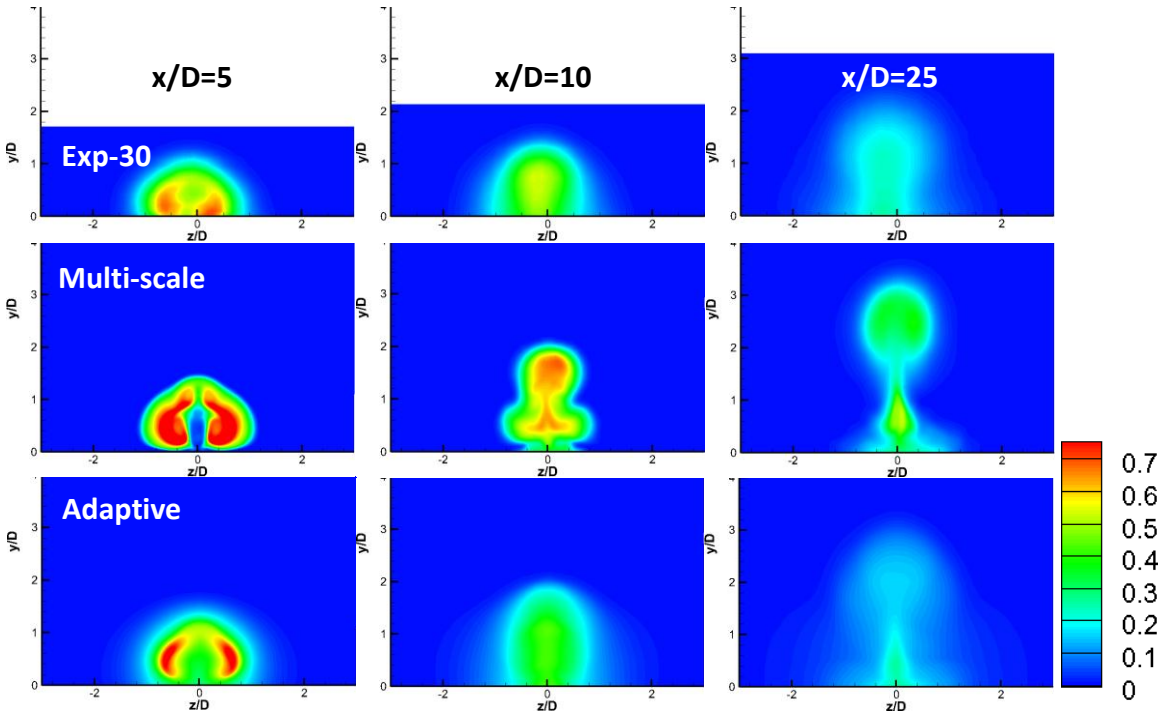

Figure 4-13 Fuel mole fraction predictions for multi-scale with/without the adaptive approach compared to experimental Raman scattering at 3 different axial locations(30^o,q=0.5).

Figure 4-14(a) shows penetration heights centers for the inclined injection (30^o, q=0.5). Both RANS and multi-scale models over-predict the heights with the discrepancy increasing further downstream as shown in chapter 3. The adaptive approach extension improves the prediction considerably with the experimental profile well predicted within 0.1 diameters. In Figure 4-14(b) width centers are plotted versus experimental results. Both RANS and multi-scale alone fail to predict widths except at x/D=5 where they come within 0.05. The adaptive approach shows excellent correlation with the experiment at all x/D locations where the width is predicted within 0.03 diameters of the experimental results. This shows the turbulent mass diffusion is more correlated with the experiment

and plays a major role in fuel concentration predictions

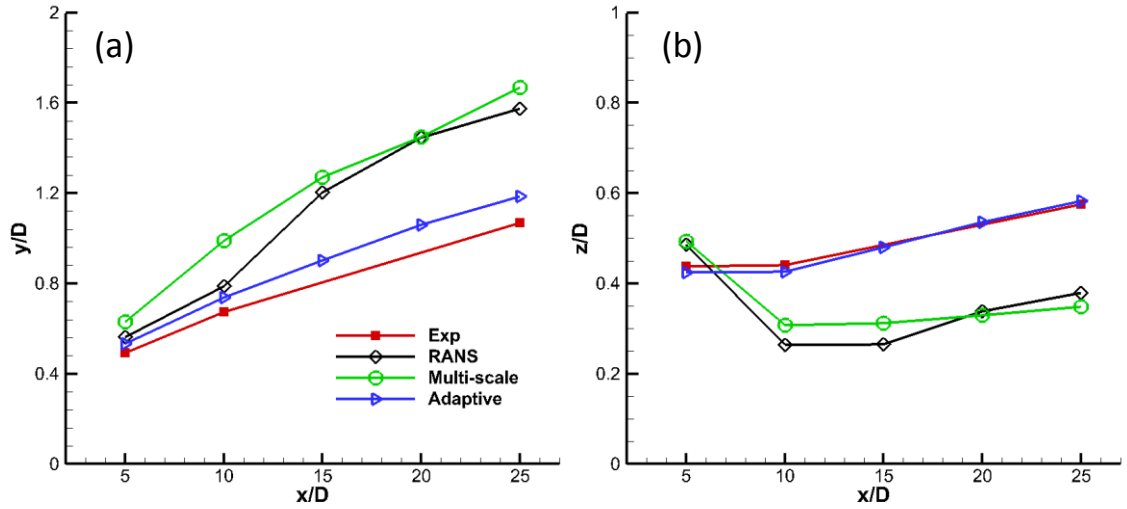

Figure 4-14 Centers for fuel penetration((a) height, (b)widths) for experiment, RANS, and multi-scale with and without the adaptive approach (30^o,q=0.5)

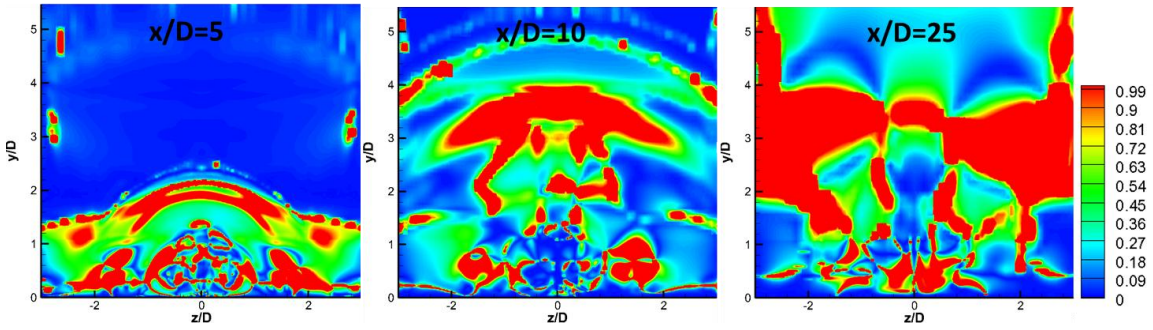

Figure 4-15 Adaptive turbulent Schmidt number contours for at different x/D locations(30^o,q=0.5).

Adaptive turbulent Schmidt number contours for 3 axial locations are plotted in Figure 4-15. In most areas of interest the value of turbulent Schmidt number is less than 0.7. There are areas however with high values of Sc_t corresponding to low turbulent diffusion. Overall, the value of Sc_t varies dramatically throughout the flow. There is symmetry around z/D=0 in Sc_t contours which is a sign that good quality fluctuations have been collected from the flow field[30]. Symmetry is more apparent in the near field,

however, at x/D=25 there is still overall symmetry in Sc_t contours.

4.4 Summary

An adaptive Schmidt number extension to the multi-scale model was developed and implemented for the baseline and inclined cases. As the simulation proceeds, average resolved turbulent mass and momentum viscosities are calculated and a turbulent Schmidt number is defined based on their ratio. When applied directly into the RANS sub-filter model, the solution showed fuel structure closer to the experimental measurements however, changes over the constant approach were not significant. When the numerical viscosity is taken into account to calculate turbulent mass diffusivity, the solution improves significantly to be in a good agreement with experimental measurements. Turbulent Schmidt number contours showed more symmetry as the grid was refined because resolved data becomes more dominant than noise resulting from the averaging procedure. This shows that the approach should be used only on grids producing adequate level of resolved turbulent fluctuations. A grid too fine, however, would not benefit much from the adaptive approach, since most of the mass diffusion will be occurring in the resolved field. Because of the use of highly dissipative second order upwind for the convection terms, better estimates for the numerical viscosity should be obtained.

In chapter 3, for the 30^o q=0.5 case, improvement with the multi-scale alone over RANS results was limited. When the adaptive approach is employed, the results improve significantly. Mean and variance fuel concentration predictions compare favorably with experimental measurements and are far superior to either RANS or multi-scale alone.

Chapter 5.
Propagation and Rupture of Incompressible Liquid Plug in a Tube

An introduction to the liquid plug propagation and rupture problem and its application in lung airways was given in chapter 1. In this chapter, a numerical simulation of a liquid plug in an infinite tube is conducted using an Eulerian-Lagrangian approach and the continuous interface method. A reconstruction scheme is developed to allow topological changes during plug rupture by altering the connectivity information of the interface mesh. Results prior to the rupture are in reasonable agreement with the study of Fujioka et al. in which a Lagrangian method is used. For unity non dimensional pressure drop and a Laplace number of 1000 , rupture time is shown to be delayed as the initial precursor film thickness increases and rupture is not expected for thicknesses larger than 0.10 of tube radius. During the plug rupture process, a sudden increase of mechanical stresses on the tube wall is recorded, which can cause tissue damage. The peak values of those stresses increase as the initial precursor film thickness is reduced. After rupture, the peaks in mechanical stresses decrease in magnitude as the plug vanishes and the flow approaches a fully developed behavior. Increasing initial pressure drop is shown to linearly increase maximum variations in wall pressure and shear stress. Decreasing the pressure drop and increasing the Laplace number appear to delay rupture because it takes longer for a fluid with large inertial forces to respond to the small pressure drop.

5.1 Model Description

Figure 5-1 shows a schematic of the computational model. A liquid plug propagates in a straight circular tube of radius R^*. The problem is assumed to be axisymmetric so that only (r, z) components are considered. The tube domain of $0<r^*<R^*$ and $-6R^*<(z^*-z_P^*)<6R^*$, is considered, where z_P^* is the middle of both tips. It is noted that the dimensional quantities are denoted by *. After non-dimensionalization, the * is removed. The pressure difference between left and right air-bubbles drives the liquid plug with a constant surface tension. The liquid plug length, L_P, non-dimensionalized by the tube radius, is the distance between air bubble tips. The liquid film thickness for the front air bubble is denoted as h_2 whereas the trailing film thickness is denoted as h_1. They are also non-dimensionalized by the tube radius. The no-slip boundary condition is applied at the tube wall. Constant uniform air pressures of P_1^* and P_2^* are prescribed in cross-sections at z = $-6R^*$ and $6R^*$ respectively, while zero velocity condition is applied for the liquid film in the same cross-sections at = $-6R^*$ and $6R^*$.

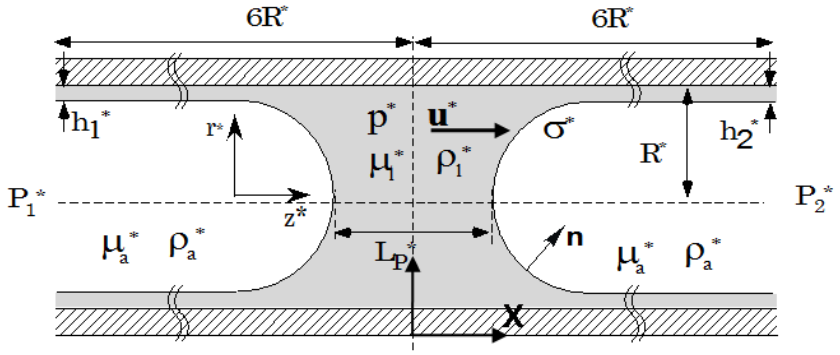

Figure 5-1 Computational setup and the boundary conditions, x axis attached to plug center before rupture and to the wall afterwards. Plug moves to the right

The dimensionless form of the Navier-Stokes equations and the continuity equation is:

$$\lambda\rho\left\{\left[\frac{\partial \mathbf{u}}{\partial t}\right]_{(r,z)} + (\mathbf{u}.\nabla)\mathbf{u}\right\} = -\nabla p + \nabla.[\mu\nabla\mathbf{u} + \mu(\nabla\mathbf{u})^T] + \mathbf{F_s} \qquad \textbf{5.1}$$

$$\nabla.\mathbf{u} = 0 \qquad \textbf{5.2}$$

where $\mathbf{u}=\mathbf{u}^*/(\sigma^*/\mu_l^*)$ is the dimensionless fluid velocity vector, μ_l^* is the liquid viscosity, σ^* is surface tension of the air-liquid interface; $p=p^*/(\sigma^*/R^*)$ is the dimensionless pressure, R^* is the tube radius; $t=t^*/(\mu_l^* R^*/\sigma^*)$ is the time; $z=z^*/R^*$ and $r=r^*/R^*$. ρ and μ are the dimensionless density and the viscosity scaled by liquid ρ_l and μ_l respectively With the density and viscosity of the gas kept constant, *ρ=1.3e-3 and μ=4e-4* for the baseline case. A key dimensionless parameter $\lambda= \rho_l{}^* \sigma^* R^*/\mu_l^{*2}$, is the Laplace number ($\lambda^{-1/2}$ is often called the Ohnesorge number). It involves the fluid properties and the tube diameter, and serves to characterize the plug and associated fluid dynamics. The body force term, $\mathbf{F}_s$, in the present context is used to represent surface tension, and will be discussed further.

To compare with the previous study of Fujioka et al.[53], which focused on the plug dynamics prior to the rupture, the same initial condition is employed. At t=0, a stationery liquid plug of length L_{P0} begins to move due to a constant driving pressure force. Since the velocity is initially set to zero in the entire domain, the pressure in each air phase should be uniform so that the initial driving pressure is $\Delta P=P_1-P_2$. The initial plug shape is approximated by a hemi-sphere of radius 1-h_2 for front and rear menisci, the length between both meniscus tips L_{P0}, and a uniform film thickness of h_2 on both sides of the plug.

5.2 Computational Procedure

The marker-based immersed boundary method employs Eulerian and Lagrangian

variables in order to perform the interfacial flow computations. The Eulerian quantities are solved on a fixed background grid in the computational frame, whereas the Lagrangian quantities arise due to the marker points defined on the interface which can move freely. A single fluid formulation for all fluid phases is made possible by smearing the properties across the interface.

Here the computational frame is set to follow the coordinate with the plug velocity **U**=(U,0), which is the average of both tip velocities. After rupture, the computational frame is fixed to the wall and the plug is allowed to move within it. From this point forward, discussion and results will be presented in terms of x instead of z because it is more convenient to represent an infinite tube. The x-coordinate in this frame,(x, r), is defined as follows:

$$x = \begin{cases} z - z_p & t \le t_{rupture} \\ z - z_{p,rupture} & t > t_{rupture} \end{cases} \qquad \textbf{5.3}$$

where z_p is the z position of the center of the plug and $z_{p,rupture}$ is z_p at the moment of rupture. $t_{rupture}$ is the time at which rupture occurs. This definition guarantees the plug is located in the center of the computational domain until $t_{rupture}$ after which it is free to move.

The time derivative term in Eq.5.1 is redefined in terms of the computational node point(x, r)

$$\begin{aligned} \lambda\rho\left\{\left[\frac{\partial \mathbf{u}}{\partial t}\right]_{(x,r)} + [(\mathbf{u}-\mathbf{U}).\nabla]\mathbf{u}\right\} &= -\nabla p + \\ \nabla.[\mu\nabla\mathbf{u} + \mu(\nabla\mathbf{u})^T] + \mathbf{F_s}\ , t \le t_{rupture} & \\ \lambda\rho\left\{\left[\frac{\partial \mathbf{u}}{\partial t}\right]_{(x,r)} + [\mathbf{u}.\nabla]\mathbf{u}\right\} &= -\nabla p + \\ \nabla.[\mu\nabla\mathbf{u} + \mu(\nabla\mathbf{u})^T] + \mathbf{F_s}\ , t > t_{rupture} & \end{aligned} \qquad \textbf{5.4}$$

The source term in Eq.5.4, $\mathbf{F_s}$, represents the condition at the interfaces due to surface

tension.

5.2.1 Surface Tension Treatment

The surface tension effect in volumetric form, $\mathbf{F_s}$, in Eq.5.4, involves curvature, (κ), surface normal, $(\mathbf{n})$, and the Dirac delta function, $\delta\left(\frac{\mathbf{x}-\mathbf{X}}{\Delta x}\right)$, as given in Eq.5.5

$$\mathbf{F_s} = \int Ca^{-1}\kappa\mathbf{n}\delta\left(\frac{\mathbf{x}-\mathbf{X}}{\Delta x}\right)dS \qquad \mathbf{5.5}$$

For curvature and other computations related to geometry, marker points placed on the interface are utilized. These marker points, represented in the Lagrangian framework with **X**, are free to move in response to the flow field computed on the background grid, which is represented in the Eulerian framework with **x**. The Magnitude of the position vectors **x** and **X** is normalized by the cell size, Δx. The marker locations for the surface grid are computed using a simple advection scheme via Eq.5.6 where the marker velocities are interpolated from the Eulerian grid.

$$\frac{\partial \mathbf{X}}{\partial t} = \mathbf{u}(\mathbf{X}) \qquad \mathbf{5.6}$$

The interpolation of the velocity field is performed with the help of a discrete form of the Dirac delta function, $\delta\left(\frac{\mathbf{x}-\mathbf{X}}{\Delta \mathrm{x}}\right)$, given in Eq.5.7

$$\delta\left(\mathbf{r} = \frac{\mathbf{x}-\mathbf{X}}{\Delta \mathrm{x}}\right) = \begin{cases} \frac{1}{8}\left(5 - 2|\mathbf{r}| - \sqrt{-7 + 12|\mathbf{r}| - 4|\mathbf{r}|^2}\right) & 1 \le |\mathbf{r}| \le 2 \\ \frac{1}{8}\left(3 - 2|\mathbf{r}| - \sqrt{1 + 4|\mathbf{r}| - 4|\mathbf{r}|^2}\right) & 0 \le |\mathbf{r}| \le 1 \\ 0 & |\mathbf{r}| > 1 \end{cases} \qquad \mathbf{5.7}$$

This approximation, which is also utilized in calculating the surface tension term in Eq.5.5, ensures that mass and momentum are conserved for any conversion between the background grid (Eulerian) and markers points (Lagrangian) as shown by Peskin et al. [113] and Shyy et al.[32]

As the markers advance to new positions with time, they can be unevenly distributed on the interface leading to larger computational errors. To maintain desirable numerical accuracy, the markers are rearranged by addition/deletion based on the background grid with no more than two markers in each computational cell.[45].

5.2.2 Interface Reconstruction Scheme

Reconstruction of the interface due to rupture is triggered numerically when the plug length decreases to a critical value, $L_{P,critical}$, that is in the order of the smallest grid size. In reality, the critical length is several orders of magnitude smaller and is related to the molecular forces. Furthermore, as is well known, the rupture dynamics (the detailed break-up process) can't be faithfully simulated entirely in the context of the continuum formulation. Since we don't consider any molecular aspects of the model, our treatment is, necessarily, phenomenological in nature. The current study focuses on the fluid physics immediately before and after the rupture. The computational results reported below do have adequate resolutions in the pre- and post-rupture instants.

The reconstruction scheme involves altering of the interface data, primarily marker connectivity, to accommodate the rupture. The minimum distance between the marker points on left and right bubbles is tracked. When this distance reduces to a value less than the critical length, $L_{P,critical}$, corresponding markers are removed.

To compute the distance between two bodies, a list based algorithm identifies the markers to be used and a length-based coordinate mapping procedure is utilized to exclude markers not participating in topology change. In 2D, the coordinates are translated into 1D form by computing the length of the interface along its path.

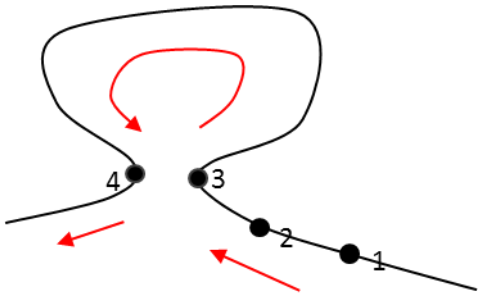

Figure 5-2 Identification of necking, a possible cause for topological change

In, Figure 5-2 the markers tagged with 1 and 2 can be excluded during the binary search for marker point tagged with 3 because the coordinate mapping identifies those as neighboring markers. On the other hand, the marker 4 is included in the search as the mapping will not qualify it as a neighbor of marker 3. Once the distance between markers 3 and 4 becomes less than the critical distance, two markers are removed to allow topological change. Overall, the triggers for the reconstruction algorithm are as follows:

- Distance between markers in physical space should be smaller than the critical length.
- Distance between markers in surface coordinates should be larger than four computational cell lengths guaranteeing that the neighboring markers are excluded.
- Distance between the corresponding markers should decrease in time.

The third criterion utilizes marker velocities and is embedded into the reconstruction

algorithm as a final check. The reconstruction scheme developed, involves the following steps:

- Markers flagged are removed. When the removed markers create a block (of markers), they are still represented by a single temporary element during this stage.
- Calculate the center and the average velocity of temporary elements.
- Check the distance between all other temporary elements.
- If the distance is less than the critical length, the connectivity information between the corresponding elements will be updated.

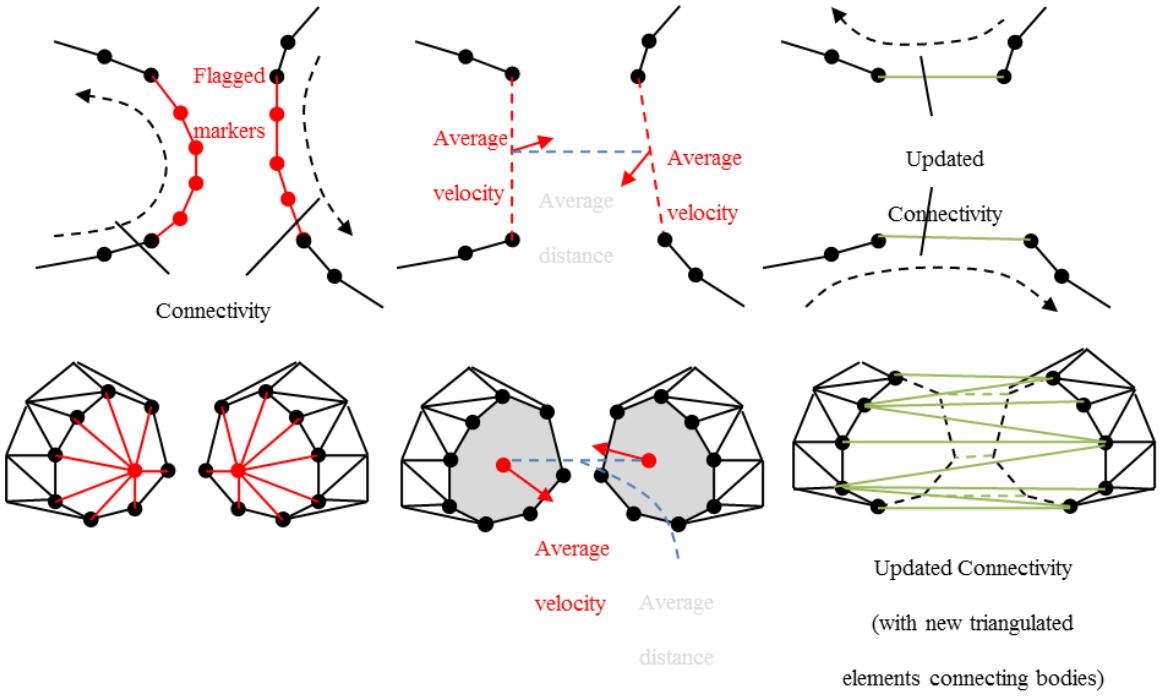

Figure 5-3 Summary of the reconstruction algorithm in 2D and 3D

The connectivity update involves the following steps:

- A marker on the first temporary element is selected. Another marker on the other temporary element is selected based on its proximity to the initially selected marker.
- The nodes of the first element are ordered in counter clockwise direction, while the nodes of the second element are ordered in the clockwise direction.
- Following the ordered list of markers on temporary elements, create edges between the corresponding markers. The normal direction of the newly created elements is chosen in a way that they follow the normal direction of all the neighboring elements.

The markers which lose the connectivity information due to marker removal procedure in Figure 5-4 are connected to each other to accommodate topological change.

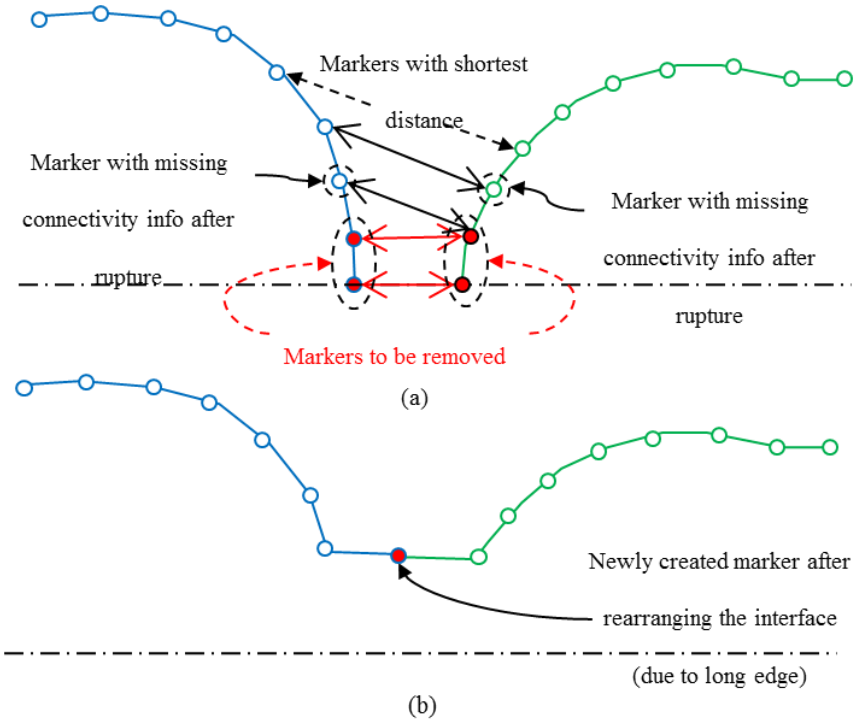

Figure 5-4 Reconstruction scheme. (a) Two interfaces come close so that the distance for red markers are less than critical length, (b) forming a single interface by updating the connectivity information

It should be noted that because the closest nodes are chosen for reconstruction in the finest region of the grid, that mass conservation errors are kept to a minimum. In addition, the newly formed segments are reconstructed in a conservative manner such that there is always the same amount of fluid in each phase before and after marker addition/deletion. This procedure and validations are discussed in detail in [46, 48]

5.2.3 Local Refinement of Eulerian Grid

The described marker-based method solves a single set of equations for all the constituents, which brings rapid variations to flow variables and material properties around the interface. Resolving the whole domain to the desired length scale may result in unnecessary resolutions at regions far from the interface. In this study, an isotropically adaptive Cartesian grid is employed for solution of the flow governing equation.

The grid is initialized in a uniform structure which has prescribed number of cells in each coordinate direction. The cell that needs to be refined is split into four smaller and equal cells. This procedure brings additional levels of grid in which new coordinates in computational space is assigned to the level that cells reside. To ensure a smooth variation in grid cell-size for quality and simplicity, cells sharing a face are not allowed to differ by more than one level of refinement. The implementation details are described in [48]. All the cells cut by the interface are flagged for refinement. In addition to those cells, their neighboring cells (up to five layers) are also flagged for refinement to ensure the uniformity for proper smearing via discrete Dirac delta function. This process of flagging and splitting cells is carried out recursively until the prescribed grid resolution around the interface is obtained. Figure 5-5 illustrates this refinement process.

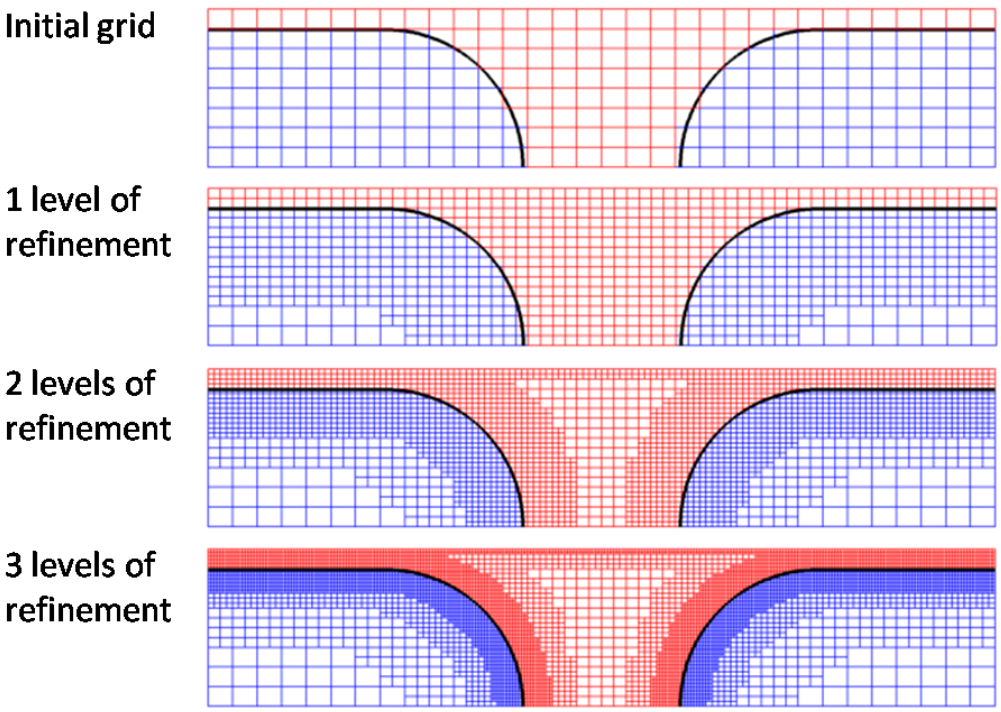

Figure 5-5 Geometry based grid refinement around the interface at various resolutions

In addition to interface-based grid adaptation, computational cells away from the interface are refined or coarsened based on the flow solution. The present implementation uses a phase-based vorticity criterion to determine critical cells for refinement or coarsening. A statistical mean and a variation are computed for each phase. For the present study, the liquid phase is the main focus and consequently only cells containing liquid phase are considered for solution refinement. When the vorticity in a computational cell deviates from the mean by a value more than the specified variation, it is marked to be refined. On the other hand, computational cells with vorticity within 10% of the mean can be coarsened if four adjacent cells are found.

5.2.4 Adaptive Time Stepping

It should be noted that the numerical simulation of the rupture dynamics requires

a numerical scheme that allows adaptive time stepping, especially to be able to capture the sudden changes in flow field in regard to shear stress and pressure. The present simulation adjusts the time step based on surface tension and the velocity field to restrict marker movement to a single cell per time step. During the liquid rupture process, the time step can decrease by about a factor of 10.

5.3 Results and Discussion

The two-fluid formulation presented above is utilized to investigate liquid rupture dynamics. The fluid physics associated with the velocity field, pressure and shear stress variations under various flow conditions, defined by the Laplace number (λ), initial plug length (L_{p0}), and initial precursor film thickness (h_2). The results will be compared to those of Fujioka et al. [53], which, uses the Lagrangian method and considers only the flow characteristics prior to the moment of rupture. The main components of the current computational framework has been previously utilized by Uzgoren et al. [48] and validated against steady plug propagation results in [105]. The present methodology can handle the topological change of the object, and the computation has been conducted to investigate the post-rupture dynamics. To ease the reading of the results, prior to rupture, the moving frame fixing to the center of the plug is used so that the results can be directly compared to those of Fujioka et al. [53]. After rupture, the stationary frame anchored by the wall is adopted, and the rupture plug is allowed to move within the reference frame.

5.3.1 Pre-Rupture Dynamics

First, the effect of initial precursor film thickness on plug length is studied to

assess the current approach with that of the single fluid formulation by Fujioka et al[53]. The initial plug length and the non-dimensional pressure drop across the plug,ΔP, are taken as 1 at .$\lambda = 1000$ Five cases are chosen based on the precursor film thickness, h_2, by setting it to 0.05, 0.07, 0.09, 0.10, and 0.13.

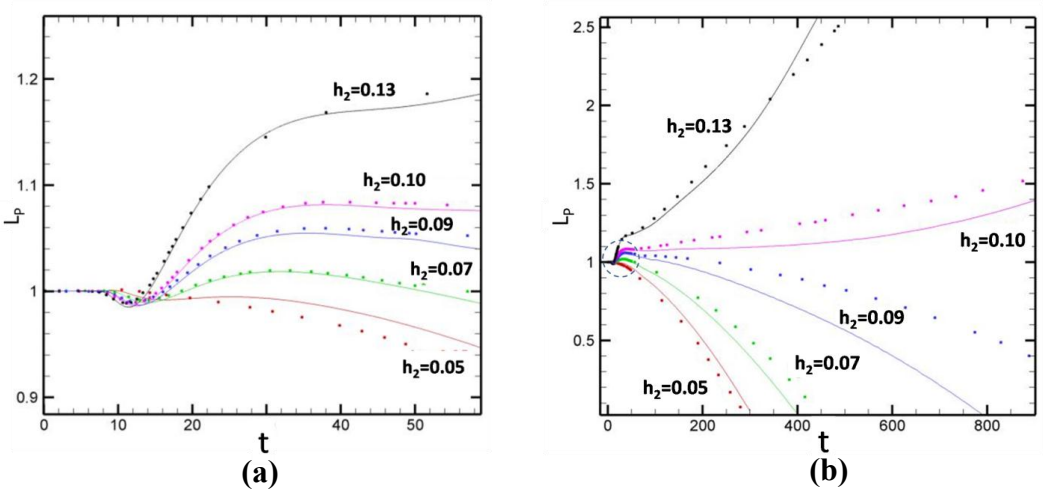

Figure 5-6 Plug length variation in time for various initial precursor film thickness values. Solid lines represent present study while dots represent study of [53]. (b) shows a more confined time domain to show details

Figure 5-6 (a) and (b) show the time dependent variation of plug length at various initial precursor thicknesses, for 0 < t < 900 and 0 < t < 60 for magnified view, respectively. In the present study, the pressure drop is prescribed between the far left and right boundaries. At the initial stages of the simulation, the pressure drop is the primary force driving the liquid plug at an axial speed, u_z^*which, as shown in the non-dimensionalization procedure, can be represented by the local capillary number, $Ca = u_z^*/(\sigma^*/\mu^*)$. The time history of the capillary number is presented in Figure 5-7 (a) for 0 < t <900 and magnified view in Figure 5-7 (b).

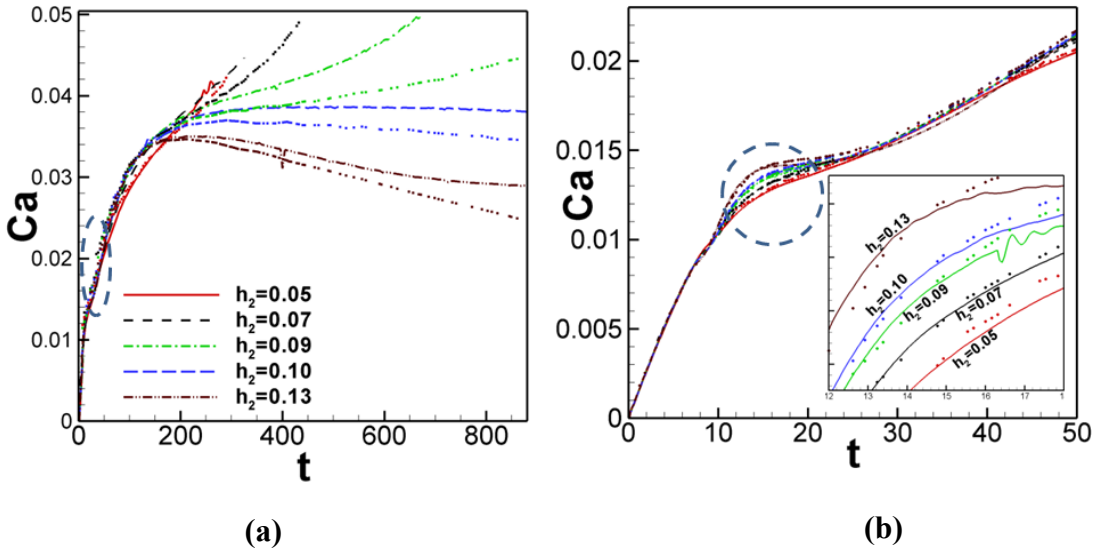

Figure 5-7 Course of plug speed, defined as the capillary number, in time for various initial precursor film thickness values. Solid lines represent present study while dots represent study of [53]. (b) shows progressively zoomed in views of the plot in (a)

The interplay between the precursor thickness, h_2, and the trailing film thickness, h_1, influences the plug length as a result of the mass balance in the liquid phase. During the initial stage of the movement, the plug propagation speed, or *Ca*, increases at a near constant rate for all cases presented. The plug length also remains the same until t = 8, then the plug propagation speed starts to vary. In Figure 5-6 (b), a similar variation is observed as the plug length decreases first, and then increases between t=10 and 20. The change in plug length can be interpreted as mass addition and removal, suggesting that as the plug widens, the precursor film thickness, h_2 becomes first larger than the trialing thickness, h_1 and then as the plug becomes narrower, h_2 becomes thinner that h_1. Figure 5-6 (b) also shows that the variation in plug length appears earlier and faster for cases with larger initial precursor thicknesses. Consistent with the finding of Fujioka and

Grotberg [105], the change in trailing film thickness is influenced mainly by the capillary number. As a result, when the plug length is at minimum in the early stages, *Ca* increases faster with larger precursor thicknesses. The overall trends seen in Figure 5-6 (a) and Figure 5-7(b) show that the liquid plug rupture is not expected with a precursor thickness 0.10 and higher. This behavior is reversed for $h_2 = 0.09$ and smaller provided that the rupture occurs at the same critical length. Accordingly, the rupture times are expected to be as follows: $t_R \approx 280$ for $h_2 = 0.05$; $t_R \approx 430$ for $h_2 = 0.07$; $t_R > 1000$ for $h_2 = 0.09$. As the initial precursor thickness becomes larger, the rupture is further delayed.

Figure 5-6 indicates that if $h_2 < 0.10$ rupture occurs. The above discussion is in agreement with single fluid formulation of Fujioka et al. [53] which ignores the fluid motion associated with the gas phase. The difference between the two studies becomes more visible for $h_2 = 0.09$ and $h_2 = 0.10$, for which the dynamics of the liquid plug becomes very sensitive to the critical precursor thickness. In the single fluid formulation the air pressure condition is directly applied at the liquid interface as constant pressure, whereas, in this study, it is applied at the far left and right domain boundary (-6*R** and -6*R**, respectively). Even though this value is small, the pressure variation within the gas phase as high as 0.5% in ΔP at the meniscus tips of both gas bubbles. As the pressure drop at the bubble tips are different for the single- and two-fluid formulations by Fujioka et al. [53] and the present study, respectively, the two simulations are expected to show some differences. The differences between the two studies become more visible with larger initial h_2 values (hence stronger multiphase effects near the wall), and as time progress (due to the unsteady accumulation of the pressure difference between the two

studies). In Figure 5-7 (a), the capillary number (the fluid velocity) continues to increase with $h_2 \leq 0.09$, whereas it shows a decrease with $h_2 \geq 0.10$ after t > 100. The decrease with $h_2 = 0.10$ is very slow, and approaches the steady state case presented in [105] with a steady Ca number at 0.0385 and a steady L_p of 1.15. This is in contrast with the reporting of Fujiokat et al. [53] where the unsteady solution did not approach the steady case of [105]. This was accounted to the difference in L_p between the steady state case of [105] and the unsteady one of [53] (presented with dots in Figure 5-6). Fujioka et al. [53] reported that as the plug length becomes larger than the steady plug length of 1.15, a constant *Ca* can't be maintained. While qualitatively similar trends can be observed in Figure 5-6 and Figure 5-7 between the present simulations and those of Fujiokat et al. [53], the mass transfer between the plug and the film and the dynamics in the gas phase result in observable differences and may suggest a larger L_p limit. Figure 5-6 and Figure 5-7, one sees that for $h_2 = 0.09$ or lower, the plug moves faster while reducing L_p (for t>40) indicating that the plug is losing mass. These figures suggest that the decrease rate in the plug length is inversely related to the initial precursor film thickness (which is initially set equal to the trailing film thickness h_1) for this range of Laplace number, pressure drop, and precursor film thicknesses.

Figure 5-8 shows (a) pressure distribution and wall shear stress along the wall for h_2 = 0.05 and h_2 = 0.09. The snapshots are taken at times when the plug length, L_p, becomes 0.3 as was done by Fujioka et al. [53]. Substantial variations in both wall pressure and wall shear stress are observed around $0.6 \leq x \leq 1.0$ which is around the minimum thickness at the front meniscus region. The minimum peak for pressure ($P_w = -3.3$) occurs at $x = 0.66$ for $h = 0.09$, whereas its absolute value is slightly increased($P_w =$

$-3.5)$ at $x = 0.72$ for $h = 0.05$. This suggests that the wall pressure increases for smaller initial precursor film thicknesses.

In Figure 5-8 (a), the wall shear stresses have both negative and positive peaks around the front meniscus region, $0.5 \leq x \leq 0.8$, as a result of a direction change in velocity field this region. The positive peak for $h_2 = 0.05$, at $\tau_w = 0.52$, is higher than the positive peak for $h_2 = 0.09$,, at $\tau_w = 0.38$. The negative peak for both precursor film thicknesses is the same at $\tau_w = -0.57$. Figure 5-8 (a) shows the present solutions with those reported in Ref. [53], showing good agreement between the two studies.

5.3.2 Rupture Dynamics

Snapshots of flow fields highlighting pressure contours at various instants of time are presented in Figure 5-9, for precursor thickness h_2 of 0.06, the rupture occurs at t = 321 when plug length, L_P reaches the critical length of 0.1. After the plug ruptures, the newly formed neck between air fingers takes its expected course when it moves away from the centerline.

The maximum magnitude of wall pressure and shear stress occur at the region of minimum film thickness after rupture. This is shown in Figure 5-10 for h_2=0.06 where wall shear stress shows two peaks in opposite directions resulting from the movement of the ruptured liquid-gas interface. The wall pressure exhibits a minimum near where the minimum wall shear stress is located. To offer more details, Figure 5-10 and Figure 5-11 show the velocity vectors along with pressure contours around the location of the peaks before and after rupture respectively. It can be observed that the mentioned extreme conditions occur at the right finger of the plug where the thickness is at minimum.

Liquid flow through the narrow portion of the film creates a highly localized region of pressure drop which shows as a global minimum.

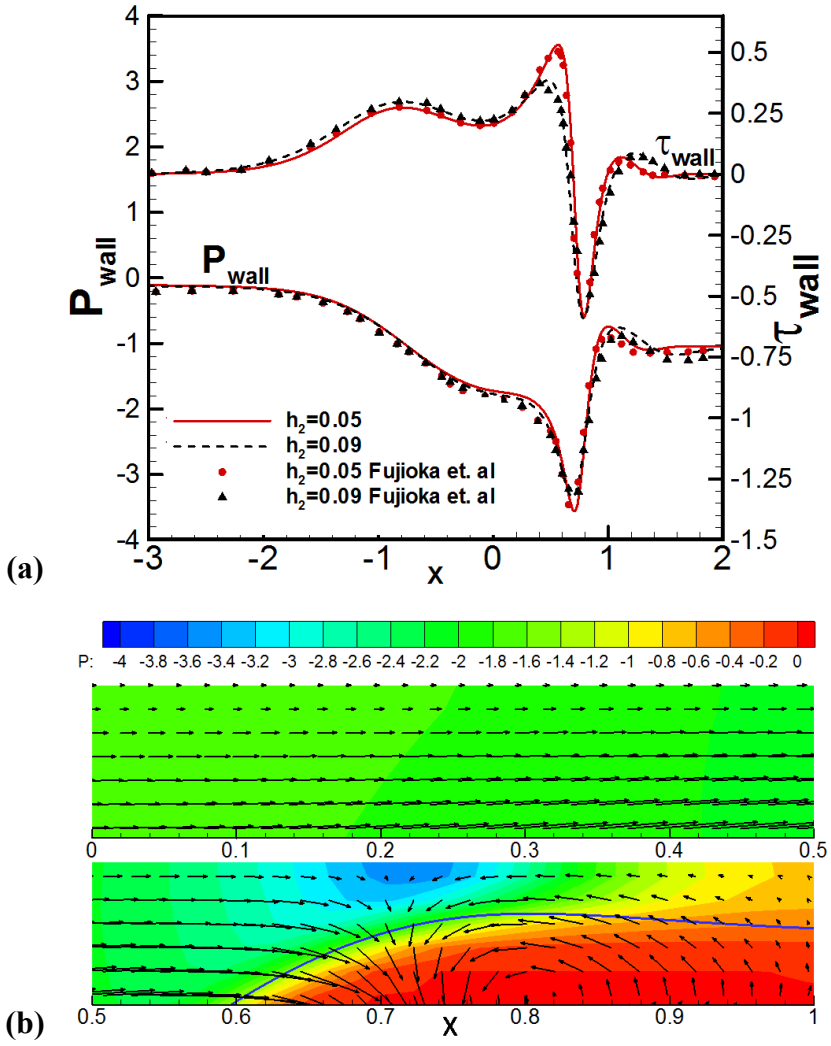

Figure 5-8 (a)Pressure and shear stress variation at the airway walls before plug rupture when Lp = 0.3, ΔP = 1, and λ = 1000. Solid lines represent present study while dots represent study of [53] (b) Pressure contours and velocity vectors near the wall corresponding to

As the interface is pulled towards the low pressure region, its curvature there becomes large to accommodate the larger pressure drop across the phase boundary . A recirculation zone is observed following the interface corner due to the surface tension force interaction with the pressure force. The flow reversal explains the opposite

directions in wall shear stress.Once the plug is ruptured, there is a sudden increase in the amount of fluid pushed through the narrow area at the minimum film thickness (to conserve the mass lost by rupture). Fluid accelerates causing a larger pressure drop in this area which, in return, pulls the interface and increases its curvature and surface tension force.

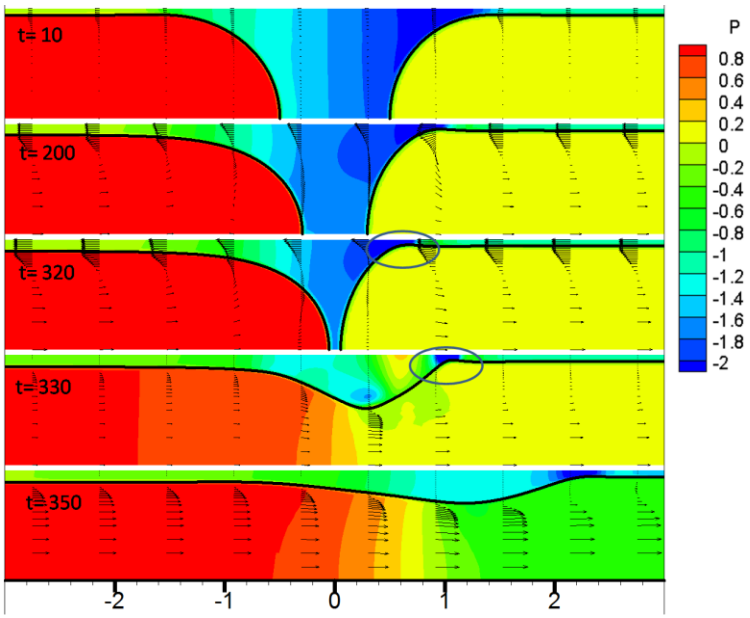

Figure 5-9 Snapshots of pressure contours before and after rupture. h_2 = 0.06, ΔP = 1, and λ = 1000.

The dual increase in pressure and surface tension forces causes larger mechanical stresses. This is shown in Figure 5-9 and Figure 5-10 where there is an increase in mechanical stresses, velocity, pressure drop, and interface curvature at t=330 (after rupture) compared to t=320 (before rupture). The same behavior during the rupture occurs in other cases at different times. For case with h_2 = 0.05, rupture is initiated at t = 286 .Rupture happens at t = 376 when h_2 is 0.07,

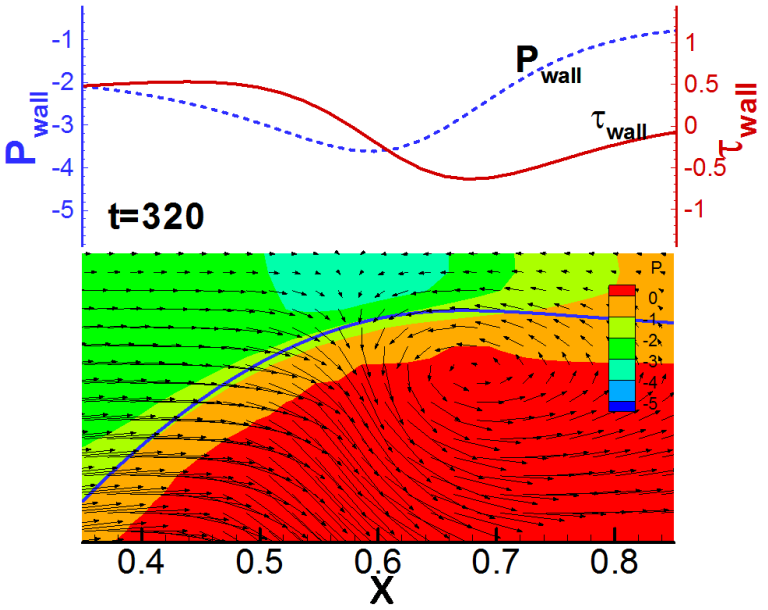

Figure 5-10 Pressure contours, velocity vectors and wall pressure and wall shear stress prior to rupture for h_2=0.06. View is zoomed at the location of minimum film thickness

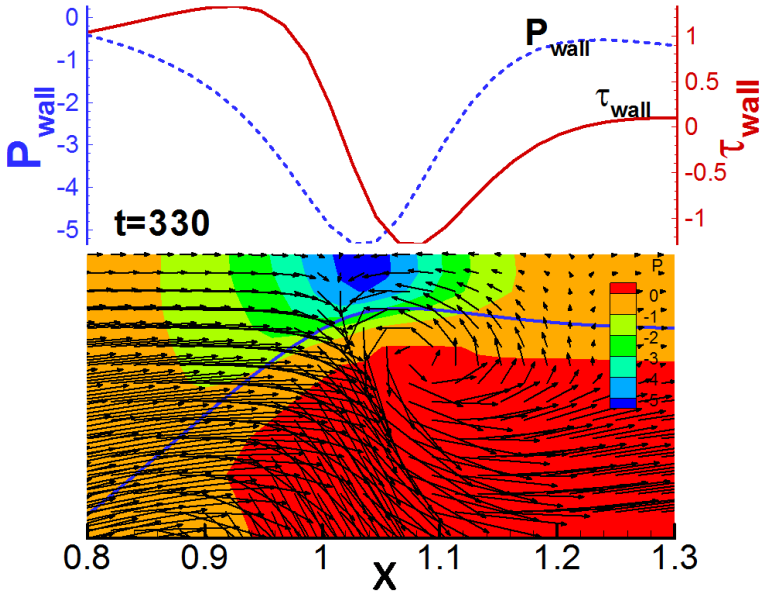

Figure 5-11 Pressure contours, velocity vectors and wall pressure and wall shear stress after rupture for h_2=0.06. View is zoomed at the location of minimum film thickness.

whereas it is delayed to t = 482 with h_2 = 0.08 in. Figure 5-12 shows pressure contour snapshots before and after rupture for h_2 = 0.08 and h_2 = 0.05. After the reopening of the

tube, the pressure distribution along the streamwise direction changes, eventually becoming linear (namely, approaching a fully developed flow profile) once the effects of rupture diminish. Correspondingly, the liquid flow slows down quickly leading to a sharp change in the wall shear stresses. This is illustrated in Figure 5-13 for h_2 of 0.06 (other film thicknesses show similar behaviors and are omitted). The dash line shows the wall stresses before rupture. Furthermore, the next recorded time step for pressure and shear stress at the airway walls illustrate that the pressure and shear stress build up at the location where the liquid plug was located. The wall pressure and shear stress show a large variation when compared to their values before the rupture. The x-coordinate in Figure 5-13 is stationary with its origin fixed at the plug center at the instant of rupture.

The variations of maximum and minimum wall shear stresses in time are presented in Figure 5-14. The figure shows sudden build-up of wall shear stresses right after the liquid plug rupture, followed by quick decays. The peak values of wall shear stresses are higher than the values prior to the rupture, and they take finite time to achieve their values after rupture The variations become larger with smaller initial precursor film thickness values for both pressure and shear stress at the airway walls. The differences in maximum and minimum values of wall shear stress and pressure are plotted in Figure 5-15. The maximum difference in wall shear stress is observed for h_2=0.05 to be 2.7 and decreases slightly for larger h_2 to be 2.3 for h_2=0.08. Similarly the maximum difference in wall pressure is observed for h_2=0.05 to be 6.1 and 4.8 for h_2=0.08.

It should be noted that the pressure and shear stress in Figure 5-13 propagate as a wave in the positive x-direction following the plug motion to the right. This is illustrated for the h=0.06 case in Figure 5-16 where the location of the tip of the ruptured plug(defined

as the lowest point on the interface) is plotted along with the location of the maximum shear stress. The similarity in the slopes of the two curves indicates that the shear stress wave propagate at about the same speed as the ruptured plug.

Crackles are sounds heard by a stethoscope during a medical examination and categorized into fine and coarse crackles. Fine crackles are characterized by discontinuous, interrupted explosive sounds that are loud and high in pitch [155] .

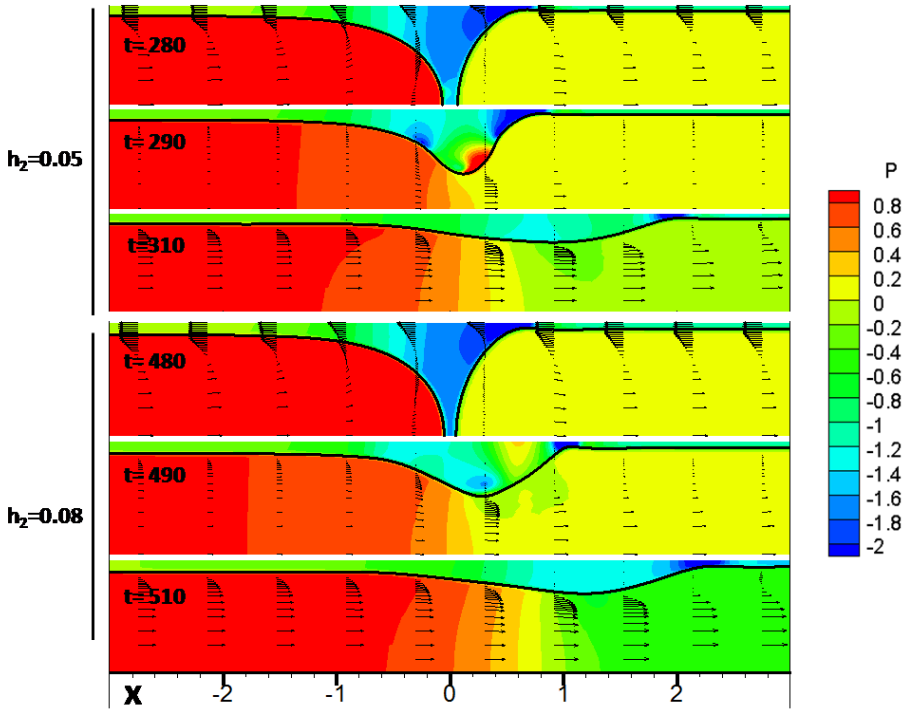

Figure 5-12 Snapshots of pressure contours before and after rupture. h_2 = 0.05,0.08, ΔP = 1, and λ = 1000.

The sound of crackles can be a sign of several diseases including Pneumonia, Asthma and Interstitial Pulmonary Fibrosis[155].There are two possible causes of crackles known by researchers; closures/reopening of airways (i.e. plug rupture) and the collapse of airways due to abnormalities [156]. The acoustic wave form associated with crackles is shown to have discontinuous sudden peaks [155] similar in behavior to the pressure/shear stress waves in Figure 5-13

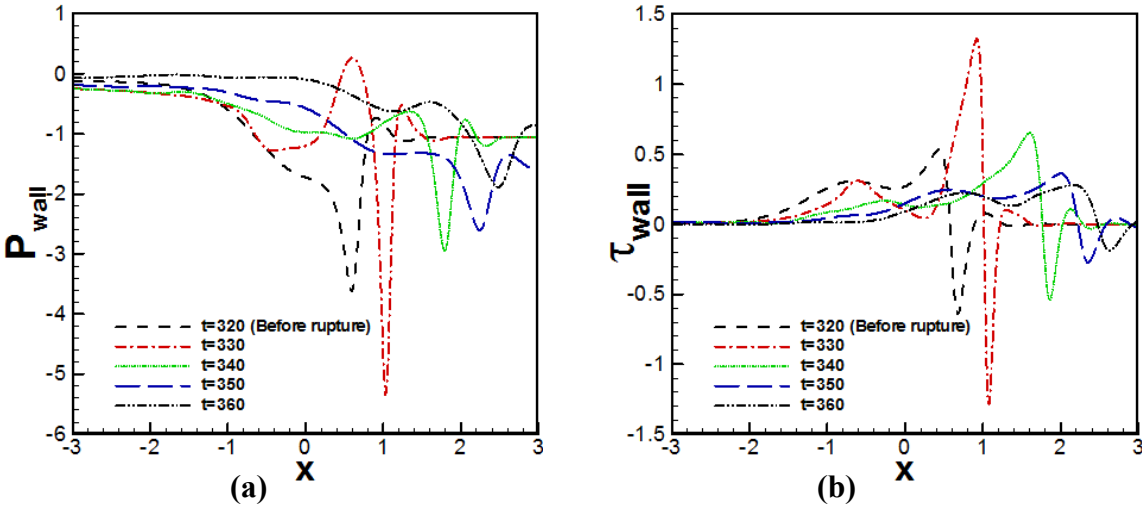

Figure 5-13 Pressure and shear stresses at the airway walls before and after the rupture. h_2 = 0.06, ΔP = 1, and λ = 1000.

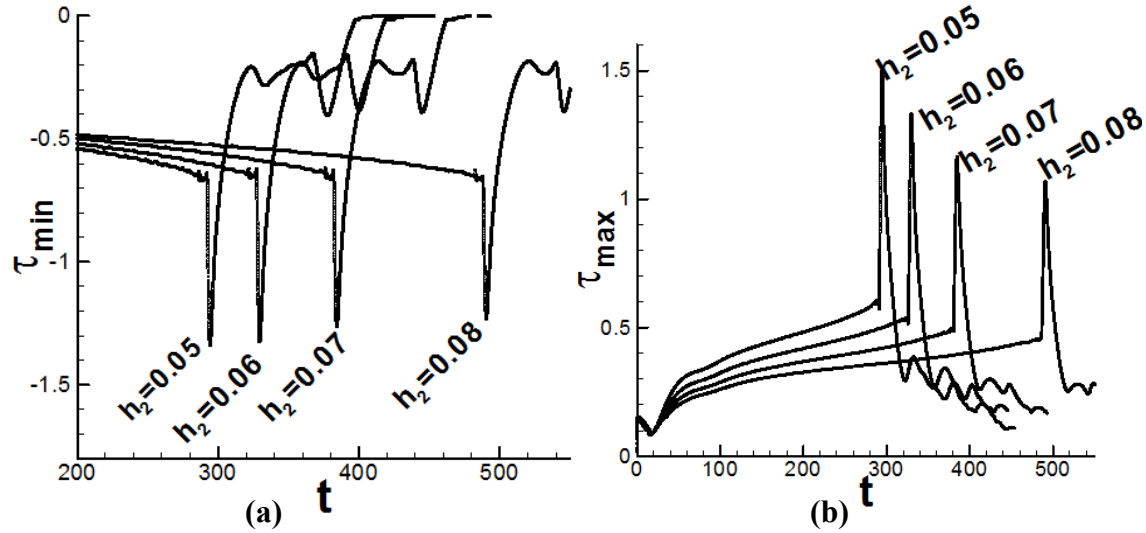

Figure 5-14 Variation of minimum and maximum wall shear stress in time. ΔP=1 and λ=1000

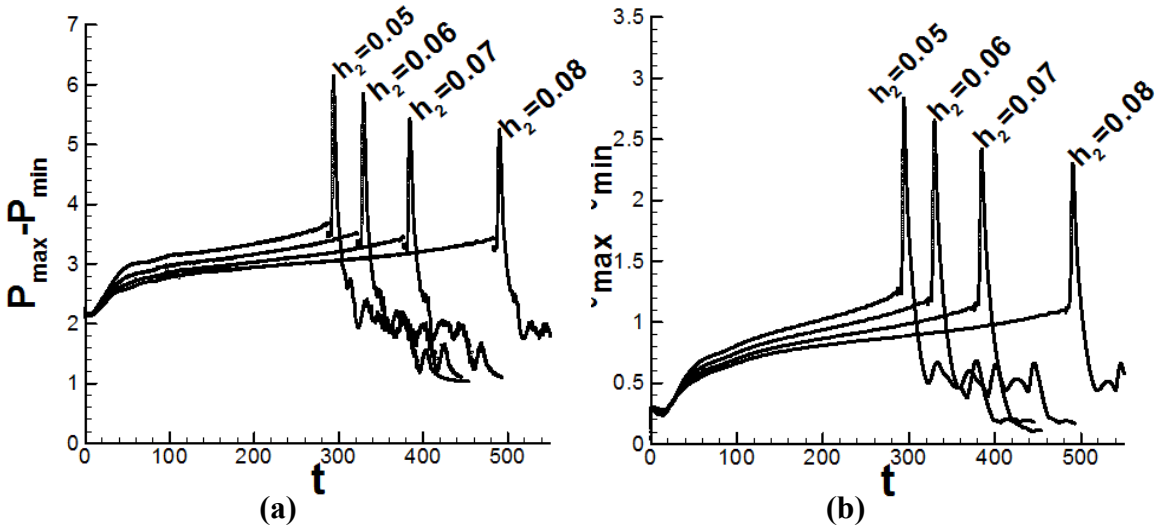

Figure 5-15 Maximum minimum difference in wall pressure(a) and wall shear stress(b) in time. ΔP=1 and λ=1000

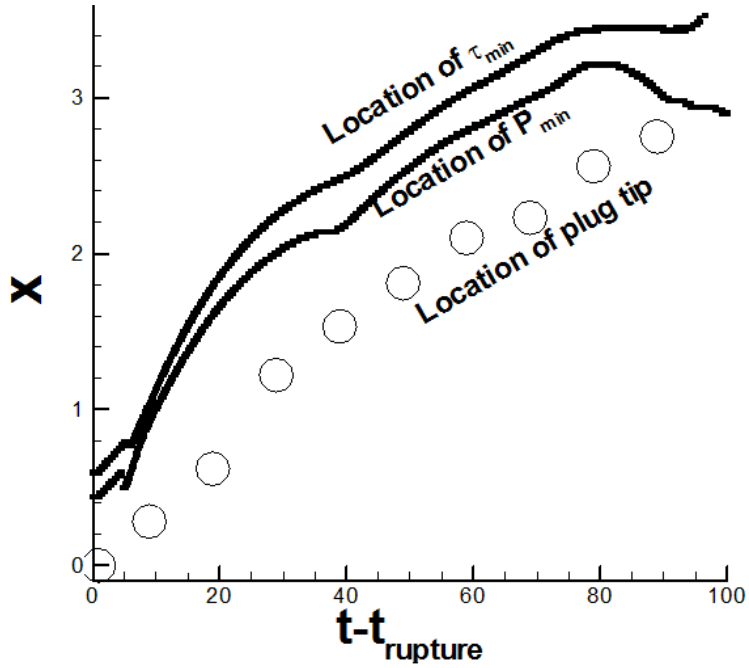

Figure 5-16 Location of maximum wall shear stress and minimum wall pressure versus ruptured plug. ΔP=1 and λ=1000

around the time of plug rupture. This suggested link between plug rupture and crackles is in agreement with findings of Munakata et al. [157] which shows, experimentally in

canine lungs, that the most probable cause for fine crackles is opening and closing of airways rather than abnormal airway collapsibility. Naturally, more rigorous investigation is needed to establish a direct link with quantitative relationships.

5.3.3 Effects of Pressure Drop and Laplace number

The effects of the initial pressure drop, ΔP, and the Laplace number, λ, on rupture dynamics are investigated by conducting a parametric study. The pressure drop controls the speed of the plug, and the Laplace number accounts for the fluid properties and tube diameter combinations; they both can influence the rupture and fluid dynamics. Using the case with h_2=0.05 as a baseline (keeping initial film thickness constant), ΔP is varied keeping all the other non dimensional parameters constant. Similarly, with ΔP held constant, the Laplace number, λ, is varied to investigate its effect on plug rupture. The cases are summarized in Table 5-1.

Cases 2-6 are studied together with the baseline case to separate the effect of ΔP and cases 7-10 with the baseline are used to study variations in λ. Focusing on the magnitude of wall mechanical stresses, the maximum variations in wall pressure, P_{max}-$P_{min,}$ and shear stress,$\tau_{max} - \tau_{min,}$ are used to characterize the effects of the parameters. The time at which rupture occurs is also studied because of its direct relation to rupture frequency in lung airways.

Figure 5-17, 18, 19 are related to parametric change of initial pressure drop, while Figure 5-20, 21 are related to change of the Laplace numbe. Figure 5-17 and Figure 5-20 show variation of P_{max}-$P_{min,}$ and shear stress, τ_{max}-τ_{min} in time. The rupture time is subtracted from the time axis to show when the peaks occur in reference to rupture. In

Figure 5-17 (a), the maximum peaks in P_{max}-P_{min} increase in magnitude as ΔP increases. Figure 5-17 (b) also shows a similar behavior for τ_{max}-τ_{min} , with the wall shear stress gradually increasing before rupture in the cases of ΔP =2,3. Figure 5-19 shows the peaks in P_{max}-$P_{min,}$ and, $\tau_{max} - \tau_{min}$versusΔP. A curve fit shows the relationship is largely linear, and consequently linear increase in mechanical stresses in response to pressure build up. The rupture time is plotted versus ΔP in Figure 5-18, there is a rapid delay in rupture with small pressure drop with a region of no rupture at very small pressure drops (verified by case 2 in which rupture never initiates). As ΔP is increased rupture occurs sooner but appears to reach a plateau of minimum rupture time for very largeΔP.

Table 5-1 Summary of cases run for parametric study

Case	ΔP	λ
Baseline	1	1000
2	1/5	1000
3	1/2	1000
4	2/3	1000
5	2	1000
6	3	1000
7	1	200
8	1	500
9	1	2000
10	1	5000

The maximum variations in wall pressure and shear stress are plotted with respect

to rupture time in Figure 5-20 for Cases 7-10. There is a largely linear increase in the peaks for pressure, as verified in Figure 5-21(b), however, the magnitude of the wall shear stress is mainly unaffected. The reason for the increase of the wall pressure is that increasing the Laplace number, $\lambda = \rho_l^* \sigma^* R^* / \mu_l^{*2}$, is achieved by increasing the liquid density which directly affects the wall pressure. There are no significant changes to the flow field (not shown) or the plug shape when λ is varied. Figure 5-21(a) shows a linear increase in rupture time when increasing λ. This is because as the Laplace number increases inertia of the liquid increases with respect to the viscosity and it takes longer for the liquid plug to become thinner and to respond to pressure drop.

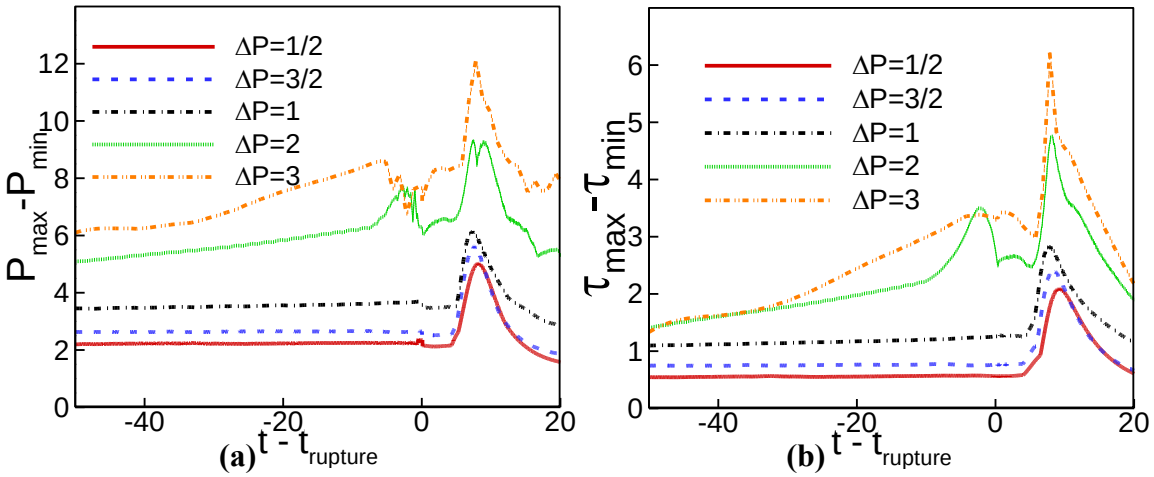

Figure 5-17 Maximum variations in wall pressure(a) and shear stress(b) varying initial pressure drop. λ=1000 and h_2=0.05

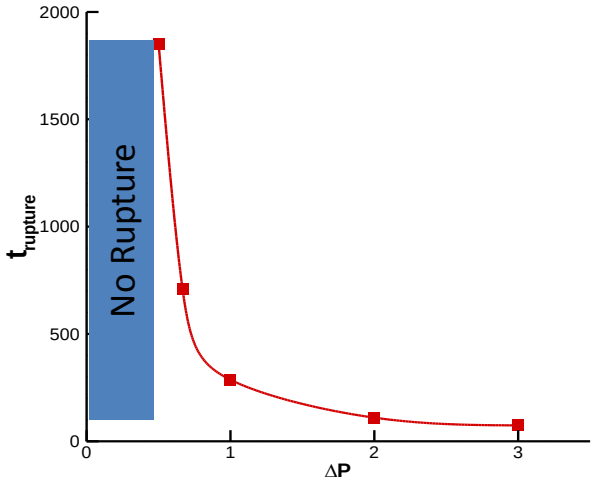

Figure 5-18 Rupture time versus initial pressure drop (data connected using spline). λ=1000 and h_2=0.05

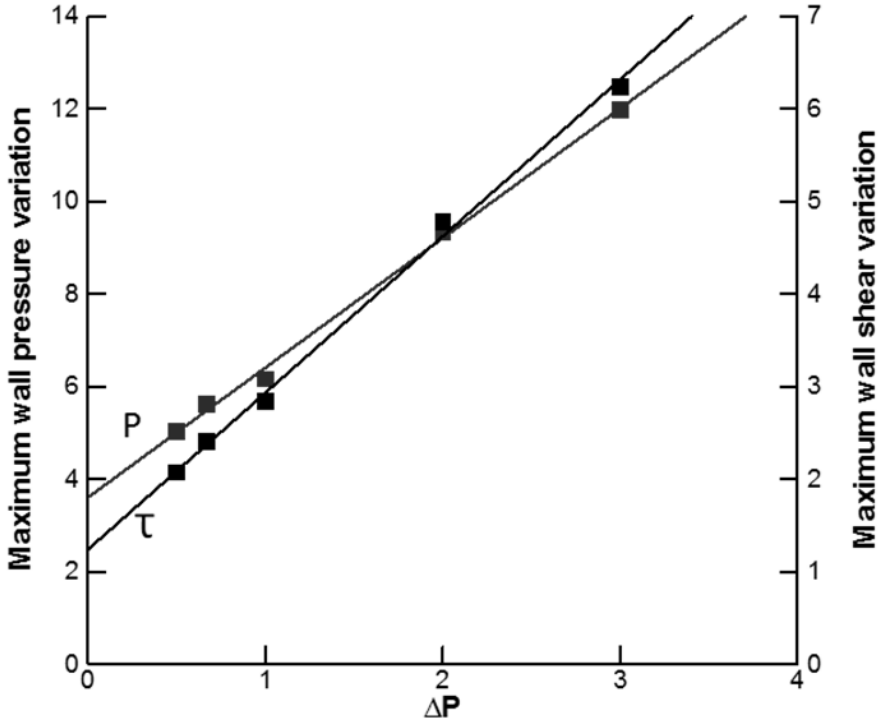

Figure 5-19 . Maximum wall pressure and shear stress variations versus initial pressure drop. λ=1000 and h_2=0.05

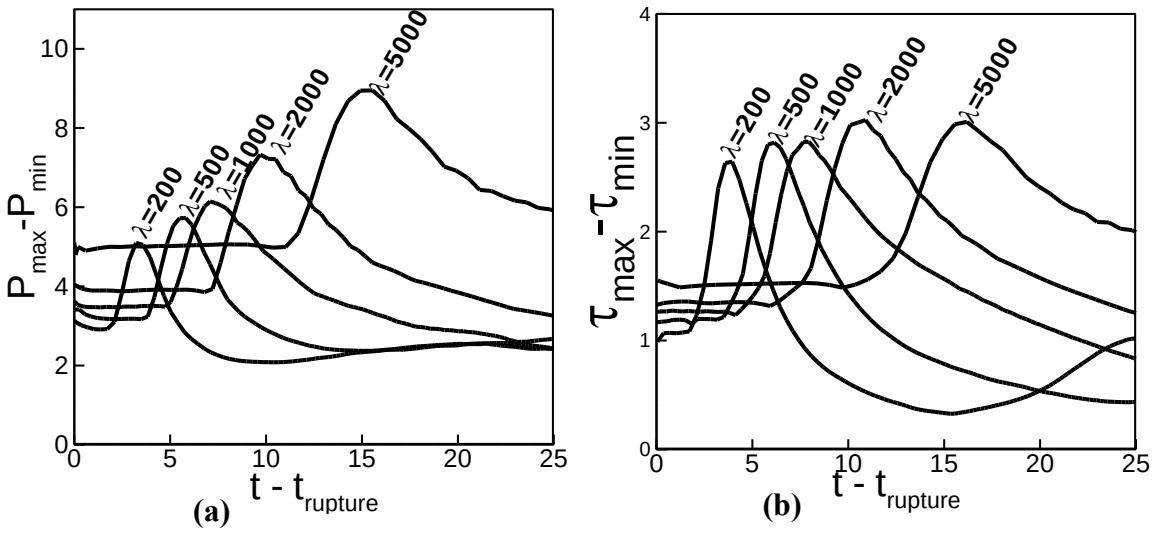

Figure 5-20 . Maximum variations in wall pressure (a) and shear stress(b) varying Laplace number. ΔP=1 and h_2=0.05

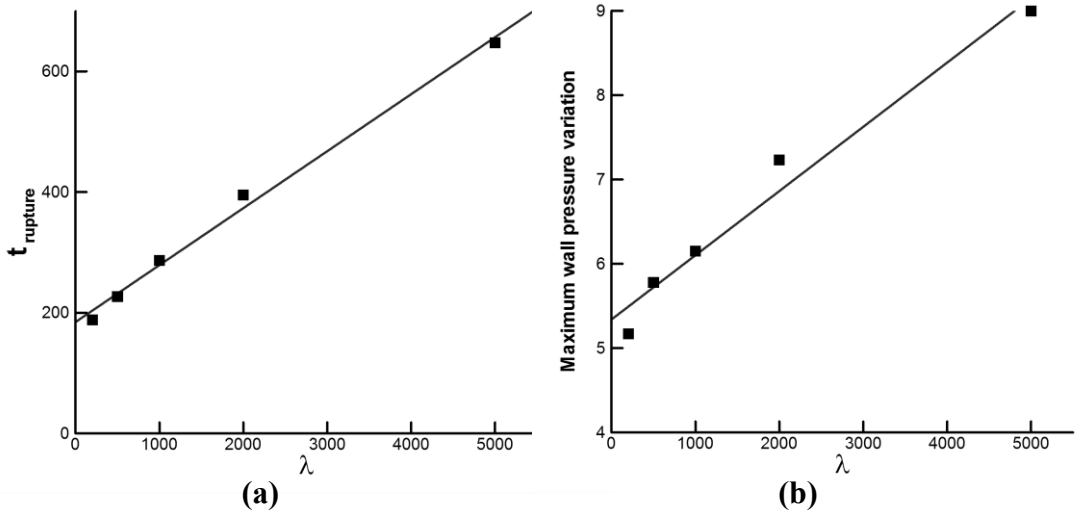

Figure 5-21 . (a) . Rupture time versus Laplace number. ΔP=1 and h_2=0.05 (b) . Maximum wall pressure variations versus Laplace number. ΔP=1 and h_2=0.05

5.4 Summary

This chapter aims to investigate the dynamics of liquid plug rupture using a novel numerical approach that utilizes a Cartesian grid based incompressible Navier-Stokes

solver with grid adaptation capability. Interface tracking is marker based using the continuous interface method for all constituents to easily allow for large deformations. A new surface reconstruction algorithm triggered by the critical length is developed to allow for plug rupture. The algorithm developed is verified against another numerical study on liquid plug propagation by Fujioka et al. [53] The study employs a single fluid formulation on a Lagrangian framework and is limited to simulation prior to rupture. The presented numerical approach ameliorates this limitation and investigates the dynamics of the liquid rupture for various initial precursor film thickness values. The results have shown the following:

- There is an overall agreement when compared to the study of Fujioka et al. [53] prior to rupture. The plug length, velocity, wall pressure and shear stress are in good agreement. Discrepancies between the two studies are probably due to different boundary condition implementation and different numerical approach.
- The liquid plug rupture causes a sudden build up in the mechanical stresses at the airway walls, which can cause damage to the tissues. The magnitude of these stresses reaches its peak at a finite time after the rupture occurs. After reaching the peak values they decrease in magnitude and follow the ruptured plug as it vanishes. The sudden peaks in mechanical stresses suggest a link between plug rupture and crackles that should be further investigated by comparing the acoustics.
- The post rupture flow field shows a low pressure region near the wall at the right finger of the plug. This low pressure region exhibits a global minimum and increases the interface curvature as it is pulled towards it. After rupture, assuming steady flow of air, a fully developed behavior is observed.

Parametric variation shows that the peak values increase when the initial precursor film thickness decreases with a constant Laplace number of 1000 and a unity non-dimensional pressure drop. With a constant initial film thickness and Laplace number, there is a linear relation between initial pressure drop and maximum wall mechanical stresses. For high initial pressure drop, there is an increase in wall shear prior to rupture due to small thickness, h_2, region created by the interface shape. Higher initial pressure also resulted in earlier plug rupture. With the pressure drop and the initial film thickness held constant, increasing the Laplace number causes a delay in rupture due to an increase in inertial effects

Chapter 6.
Concluding Remarks

6.1 Summary and Conclusions

This dissertation addresses model development and applications of two distinct multi-fluid interaction problems; the supersonic jet and crossflow, motivated by SCRAMJET fuel mixing, and liquid plug propagation and rupture, motivated by dynamics of lung airway mucus treatment. Supersonic jet and crossflow calls for accurate representation of turbulent mixing along with interactions of shock and surrounding flow. A multi-scale model and an adaptive turbulent Schmidt number approach are developed and assessed. The multi-scale model was developed and modified based on earlier filter based approaches [83, 84] that adjust the value of the eddy viscosity in a RANS model thus allowing it to vary based on the grid size compared to the main turbulence length scale. Due to the reduction of the eddy viscosity, resolved unsteady structures appear in the solution similar to hybrid RANS/LES methods[27, 52]. The value of the constant,C_4, used in the definition of the turbulent length scale (Eq.2.64) is related to the Smagorinsky constant,C_s, in the LES limit (Eq.2.64). The value of the constant was further verified by comparison to the DES constant ,C_{DES}, used in Menter SST-based DES approach (2.66) based on experimental calibrations[138, 141] A filter function was developed based on earlier filters [83, 84] to be smooth near unity for stable transition from RANS. Also it does not allow the filter value to increase beyond one thus

preventing over-damping the flow beyond the RANS solution. The concept of a resolved turbulent Schmidt number is introduced in Eq. 2.79 based on statistical information related to turbulent fluctuations. RANS definitions of turbulent mass and momentum diffusions are combined with fluctuation correlations extracted from the solution (Eqs.2.77and 2.78) to estimate an effective turbulent Schmidt number that represents the resolved mixing dynamics. The number produced with this method is used in the sub-filter RANS model to improve predictions of turbulent mixing beyond the use of a constant value.

The multi-scale model was successfully tested with different configurations and grids for the jet and crossflow interaction causing an improvement over RANS results when compared to experiment, to some extent, for all injection configurations. The mechanism at which the multi-scale model works is resolving more turbulent structures in the solution, those turbulent structures may give more accurate average predictions than those predicted by RANS.

The fuel distribution, which is significantly dependent on turbulent mixing, was the most affected/improved when switching to multi-scale. For the baseline case (90^o, q=0.5), results were consistent with other researchers' studies of the same case in which hybrid RANS/LES methods improved predictions in a similar fashion[27, 52]. The major conclusions to be drawn with the use of the multi-scale model specifically are outlined below:

- RANS model does not produce significant unsteadiness which is important because the mean of fuel concentration is not correlated with the instantaneous results which contain large variance from the mean.

- Mixing, presented in averaged fuel concentrations, especially with the baseline case, was the most sensitive to the use of the multi-scale model (as evidenced in Figure 3-23) showing overall different behavior than RANS and producing average results comparing well with the experiment. This was also evident when resolved structures were used to estimate a resolved turbulent Schmidt number of non-constant behavior (Figure 3-22).
- RANS, however, was able to capture other important flow variables such as velocity and pressure fields reasonably well(Figure 3-16, 3-17, 3-18) leading in most cases to a reasonable prediction of penetration heights.
- Different injection configurations (injection angle and momentum ratio) responded differently to the use of the multi-scale model as shown in Figure 3-22,and 3-25 to 3-27. The cases with aggressive jet and crossflow interaction, yielded larger vortical structures and experienced the most improvement (Figure 3-22). For cases where the interaction resulted in a milder segregation between the jet and crossflow or the momentum of the jet caused a delay in plume breakup, the vortical structures were smaller and more scattered and the multi-scale model's improvement was limited even with very fine grids This was most evident for the 30^{o}, q=0.5 case simulated with a 29 million cell grid (Figure 3-27, 3-29)
- To increase resolved turbulent structures, it is desirable to reduce the amount of numerical viscosity which could be done by refining the grid, or using higher order numerical fluxes to increase spatial accuracy. The use of high-order

convective fluxes would aid in the reduction of the number of grid points, however, it may cause stability problems and grid limitations that may sacrifice the code capabilities with complex geometries and practical applications The other option is to improve sub-filter mixing which is done by introducing the adaptive turbulent Schmidt number approach.

The adaptive Schmidt number extension to the multi-scale model was successfully developed and implemented for the baseline (90^o, q=0.5) and inclined (30^o, q=0.5) cases. As the simulation proceeds, average resolved turbulent mass and momentum viscosities are calculated and a turbulent Schmidt number is defined based on their ratio.

Turbulent Schmidt number contours showed more symmetry with finer gird regions and as the grid was refined (Figure 4-1) because resolved data become more dominant than noise resulting from the averaging procedure. This shows that the approach should be used only on grids producing adequate levels of resolved turbulent fluctuations. A grid too fine, however, would not benefit much from the adaptive approach, since most of the mass diffusion will be occurring in the resolved field.

When applied directly into the RANS sub-filter model, the solution showed fuel structure closer to the experimental measurements however, changes over the constant approach were not significant as evidenced by the baseline case results (Figure 4-2 and 4-3). The numerical viscosity caused a gap between the eddy size predicted by the model's eddy viscosity and the actual eddy size present in the solution (Figure 4-4). The eddy size predicted by the model's eddy viscosity is smaller causing sub-filter turbulent mixing to be under-predicted. The effect of the numerical viscosity is accounted for by including a

numerical viscosity term in the Reynolds diffusion (Eq 4.3). The estimate of the numerical viscosity is based on the use of generalized Smagorinsky coefficients[142, 143]. When the numerical viscosity is taken into account to calculate turbulent mass diffusivity, the solution for the baseline case improves significantly to be in a good agreement with experimental measurements (Figure 4-6).

Average fuel concentration contours were used to evaluate the effect of the adaptive approach on mixing. This was done by comparing the use of the adaptive approach with the coarse grid versus simply refining the grid without using the adaptive approach (Figure 4-7 and 4-8). The adaptive approach was able to produce results comparable to those obtained by refining the grid without altering the velocity and/or the pressure fields (Figures 4-9 and 4-10)

For the 30^{o} q=0.5 case, improvement with the multi-scale alone over RANS results was limited. Smaller scattered vortices required more accurate sub-filter model of the turbulent mixing to avoid prohibitively expensive simulations. When the adaptive approach is employed, the results improve significantly. Mean and variance fuel concentration predictions compare favorably with experimental measurements and are superior to either RANS or multi-scale without adaptive Schmidt number (Figure 4-12 to 4-14).

For the liquid plug propagation and rupture study, simulations are conducted using a novel numerical approach that utilizes a Cartesian grid based incompressible Navier-Stokes solver with grid adaptation capability. Interface tracking is marker based using the continuous interface method for all constituents to easily allow for large deformations [46, 48, 158]. A new surface reconstruction algorithm triggered by the critical length is

developed to allow for plug rupture (Figures 5-2, 5-3, 5-4). The algorithm developed is verified against another numerical study on liquid plug propagation by Fujioka et al. [53] which employs a single fluid formulation on a Lagrangian framework and is limited to simulation prior to rupture. The presented numerical approach ameliorates this limitation and investigates the dynamics of the liquid rupture for various initial precursor film thickness values. The results have shown the following:

- There is an overall agreement when compared to the study of Fujioka et al. [53] prior to rupture(Figure 5-6 , 5-7, 5-8). The plug length, velocity, wall pressure and shear stress are in good agreement. Discrepancies between the two studies are probably due to different boundary condition implementation and different numerical approach.
- The liquid plug rupture causes a sudden build up in the mechanical stresses at the airway walls, which can cause damage to the tissues. The magnitude of these stresses reaches its peak at a finite time after the rupture occurs. After reaching the peak values they decrease in magnitude and follow the ruptured plug as it vanishes (Figure 5-13). The sudden peaks in mechanical stresses suggest a link between plug rupture and crackles that should be further investigated by comparing the acoustics.
- The post rupture flow field shows a low pressure region near the wall at the right finger of the plug. This low pressure region exhibits a global minimum and increases the interface curvature as it is pulled towards it. After rupture, assuming steady flow of air, a fully developed behavior is observed.

Parametric variations shows that the peak values increase when the initial precursor film thickness decreases with a constant Laplace number of 1000 and a unity non-dimensional pressure drop (Figure 5-14, 5-15). With a constant initial film thickness

and Laplace number, there is a linear relation between initial pressure drop and maximum wall mechanical stresses (Figure 5-19). For high initial pressure drop, there is an increase in wall shear prior to rupture due to small thickness, h_2, region created by the interface shape (Figure 5-17). Higher initial pressure also resulted in earlier plug rupture (Figure 5-18). With the pressure drop and the initial film thickness held constant, increasing the Laplace number causes a delay in rupture due to an increase in inertial effects (Figure 5-21)

6.2 Future Work

6.2.1 Jet and Crossflow Interaction

It has been mentioned through this dissertation that the calculation of convective fluxes constituted a limiting factor to the capabilities of the multi-scale model. Numerical viscosity was found to be at least on the order of the calculated eddy viscosity with the coarser grids thus requiring extremely fine grid resolutions to obtain adequate solutions. The numerical viscosity also limited the use of the adaptive Schmidt number approach requiring a numerical viscosity correction in order for the adaptive approach to be effective. The numerical viscosity correction involved the use of a correlated constant to estimate the effects of numerical viscosity (Eq.4.4). The addition of higher-order fluxes to the computation is therefore critical to the performance of the turbulence treatments introduced in this work. One of the major advantages of the multi-scale model is smooth filtering of the eddy viscosity thus allowing the use of complex geometry and

unstructured grids. Applying higher-order fluxes, however, usually introduces instabilities and grid limitations. A good alternative to explore for future work is discontinuous Galarkin methods which allow higher order fluxes without restriction on the grid stencil for easy application into unstructured grids[159, 160]. Other extensions to the efforts in this dissertation include:

- Further analysis of the of the multi-scale model including implications on shock and boundary-layer interactions including the ability to predict separation should be considered. A numerical simulation of the impinging shock wave on boundary-layer can be conducted and compared to the DNS data of Pirozzoli and Grasso[161]. This would serve to increase confidence in the multi-scale model for use in complex problems including combusting fuel injection in SCRAMJET engines.
- Transfer and conservation of turbulent kinetic energy across turbulence models and between the resolved and sub-filter portions of the flow should be carefully analyzed. This would serve to verify the models' capabilities in predicting turbulent quantities without modeled stress depletion (MSD) commonly encountered in DES methods [20] Such a study could use resolved experimental data for supersonic flow past a blunt annular sting [162] and results of other models including DES and LNS (using same computational framework) for comparison. This would in turn shed the light on whether synthetic turbulence/recycling techniques [27, 153] are needed to sustain turbulent fluctuations.

- The adaptive turbulent Schmidt number approach introduced the resolved Sc_t as a scalar. This can be extended to a tensor definition to be used in the RANS momentum transport equations which are solved in all three dimensions. This can be done dividing Eq .2.77 by 2.78 thus obtaining a tonsorial equation with directionality preserved.
- .The adaptive approach can be extended to turbulent Prandtl number, Pr_t, which is also specified as a constant in RANS formulations. This should help in heat transfer problems where there is high sensitivity to Pr_t

There other applications that can benefit from the multi-scale and the adaptive approach in the immediate future. Those include combusting supersonic flows which suffer from turbulent Schmidt number sensitivity. Those flows can be solved using the current computational framework which already allows for chemical reactions and was validated in numerous applications[163, 164]

6.2.2 Plug Propagation and Rupture

For the plug flow propagation and rupture study, finer grids should be considered to reveal smaller features such as secondary droplets occurring during rupture. Such study would require extending the current computational framework to include parallel capabilities which is already taking place[165]. With high-resolution computations available, the inclusion of van der Waals forces could be critical to accurately capture details of topology changes[110]. A model based on close proximity between interfaces such as that used by Uzgoren et al [48] can be used to calculate the van der Waals potential function for inclusion as a forcing term in Eq.5.1

Bibliography

1. **Karagozian, A.R., L. Cortelezzi, and A. Soldati, *Manipulation and Control of Jets in Crossflow*, ed. C.I.C.f.M. Sciences. 2003: Springer.**
2. **Jones, W.P. and M. Wile, *Large-Eddy Simulation of a Plane Jet in a Cross-Flow.* international Journal for Heat and Fluid Flow, 1996. 17(3): p. 296-306.**
3. **Chochua, G., W. Shyy, S. Thakur, A. Brankovic, J. Lienau, L. Porter, and D. Lischinsky, *A Computational and Experimental Investigation of Turbulent Jet and Crossflow Interaction.* Numerical Heat Transfer Part A: Applications, 2000. 38(6): p. 57-572.**
4. **Hahn, S. and H. Choi, *Unsteady Simulation of Jets in a Cross Flow.* Journal of Computational Physics, 1996. 134(2): p. 342-356.**
5. **Smith, S.H. and M.G. Mungal, *Mixing, Structure and Scaling of the Jet in Crossflow.* Journal of Fluid Mechanics, 1998. 357: p. 83-122.**
6. **Shyy, W., S.M. Correa, and M.E. Braaten, *Computation of Flow in a Gas Turbine Combustor.* Combustion Science and Technology, 1988. 58: p. 97-117.**
7. **Fearn, R. and R.P. Weston, *Vorticity Associated with a Jet in a Cross Flow.* AIAA Journal, 1974. 12(12): p. 1666-1670.**
8. **Gruber, M.R., Nejad, A S., J. C. Dutton, *An Experimental Investigation of Transverse Injection from Circular and Elliptical Nozzles into Supersonic Crossflow.* Wright Lab Technical Report, 1996. WL-TR-96-2102.**
9. **Gruber, M.R., A.S. Nejad, T.H. Chen, and J.C. Dutton, *Compressibility Effects in Supersonic Transverse Injection Flowfields.* Physics of Fluids, 1997. 9(5): p. 1448-1461.**
10. **Ferri, A., *Mixing Controlled Supersonic Combustion.* Annual Review of Fluid Mechanics, 1973. 5: p. 307-338.**
11. **McClinton, C.R., *Effect of Ratio of Wall Boundary-Layer Thickness to Jet Diameter on Mixing of a Normal Hydrogen Jet in a Supersonic Stream.* 1974. NASA TM X-3030.**
12. **Segal, C., *The Scramjet Engine Processes and Characteristics*. 2009, New York: Cambridge University Press.**
13. **Santiago, J.G. and J.C. Dutton, *Velocity Measurements of a Jet Injected into a Supersonic Crossflow.* Journal of Propulsion and Power, 1997. 13(2): p. 264-273.**
14. **Everett, D.E., M.A. Woodmansee, J.C. Dutton, and M.J. Morris, *Wall Pressure Measurements for a Sonic Jet Injected Transversely into a Supersonic Crossflow.* Journal of Propulsion and Power, 1998. 14(6): p. 861-868.**

15. **Crafton, J., A. Forlines, S. Palluconi, M. Hsu, C. Carter, and M. Gruber, *Investigation of Transverse Jet Injections in a Supersonic Crossflow Using Fast Responding Pressure-Sensitive Paint.* AIAA journal, 2011. Submitted.**
16. **Lin, k.-C., M. Ryan, C. Carter, M. Gruber, and C. Raffoul, *Raman Scattering Measurements of Gaseous Ethylene Jets in Mach 2 Supersonic Crossflow.* Journal of propulsion and power 2010. 26: p. 503-513.**
17. **Viti, V., R. Neel, and J.A. Schetz, *Detailed Flow Physics of the Supersonic Jet Interaction Flow Field.* Physics of Fluids, 2009. 21(046101-1).**
18. **Kawai, S. and S.K. Lele, *Large-Eddy Simulation of Jet Mixing in Supersonic Crossflows.* AIAA Journal, 2010. 48(9): p. 2063-2083.**
19. **Tam, C.-J., R.A. Baurle, and M.R. Gruber. *Numerical Study of Jet Injection into a Supersonic Crossflow*. in *35th AIAA/ASME/SAE/ASEE Joint Propulsion Conference and Exhibit*. 1999. Los Angeles, california.**
20. **Spalart, P.R., S. Deck, M.L. Shur, K.D. Squires, M.K. Strelets, and A. Travin, *A New Version of Detached-Eddy Simulation, Resistant to Ambigious Grid Densities.* Theoritical Computational Fluid Dynamics, 2006. 20: p. 181-195.**
21. **Maddalena, L., T.L. Campioli, and J.A. Schetz, *Experimental and Computational Investigations of Light-Gas Injectors in Mach 4.0 Crossflow.* Journal of Propulsion and Power, 2006. 22(5).**
22. **Nichols, R.H. and R. Tramel, *Applications of a Highlt Efficient Numerical Method for Overset Mesh Moving Body Problems.* AIAA, 1997. 97-2255.**
23. **Sinha, N., S. Dash, and N. Chidambaram, *A Perspective on the Simulation of Cavity Aeroacoustics.* AIAA, 1998. 98-0286.**
24. **Spalart, P., W. Jou, and M. Strelets, *Comments on the Feasibility of Les for Wings and Ona Hybrid Rans/Les Approach*, ed. C. Liu and Z. Liu. 1997: Greyden Press, Columbus, OH.**
25. **Smagorinsky, J., *General Circulation Experiments with the Primitive Equations: I. The Basic Equations.* Mon. Weather Rev., 1963. 91: p. 99-164.**
26. **Lilly, D.K., *The Representation of Small Scale Turbulence in Numerical Simulation Experiments*, in *Proc. IBM Scientific Computing Symp. In Environmental Sciences*, H.H. Goldestine, Editor. 1967. p. 195-210.**
27. **Boles, J.A., J.R. Edwards, and R.A. Baurle, *Large-Eddy/Reynolds-Averaged Navier-Stokes Simulations of Sonic Injection into Mach 2 Crossflow.* AIAA Journal, 2010. 48(7): p. 1444-1456.**
28. **Chapman, D.R., *Computational Aerodynamics Development and Outlook.* AIAA Journal, 1979. 17(12): p. 1293-1313.**
29. **Hassan, E., H. Aono, J. Boles, D. Davis, and W. Shyy. *Multi-Scale Turbulence Model in Simulation of Supersonic Crossflow*. in *49th AIAA Aerospace Sciences Meeting including the New Horizon Forum and Aerospace Exposition* 2011. Orlando, Florida.**
30. **Hassan, E., H. Aono, J. Boles, D. Davis, and W. Shyy, *Adaptive Turbulent Schmidt Number Approach for Multi-Scale Simulation of Supersonic Crossflow* in *20th AIAA Computational Fluid Dynamics Conference*. 2011: Honolulu, Hawaii.**

31. **Hassan, E., H. Aono, J. Boles, D. Davis, and W. Shyy, *Multi-Scale Turbulence Model in Simulation of Supersonic Crossflow Part 2: Inclined Injection*, in *50th AIAA Aerospace Sciences Meeting including the New Horizon Forum and Aerospace Exposition* 2012: Nashville, TN.**
32. **Shyy, W., H.S. Udaykumar, M.M. Rao, and R.W. Smith, *Computational Fluid Dynamics with Moving Boundaries*. Taylor & Francis, Washington, Dc, (1996, Revised Printing 1997, 1998&2001). 2007, New York: Dover.**
33. **Osher, S. and R.P. Fedkiw, *Level Set Methods and Dynamic Implicit Surfaces*. 2002: Springer.**
34. **Losasso, F., R. Fedkiw, and S. Osher, *Spatially Adaptive Techniques for Level Set Methods and Incompressible Flow.* Computers and Fluids, 2006. 35: p. 995-1010.**
35. **Francois, M.M., S.J. Cummins, E.D. Dendy, D.B. Kothe, J.M. Sicilian, and M.W. Williams, *A Balanced-Force Algorithm for Continuous and Sharp Interfacial Surface Tension Models within a Volume Tracking Framework.* J. Computational Phys., 2006. 213(1): p. 141-173.**
36. **Enright, D., F. Losasso, and R. Fedkiw, *A Fast and Accurate Semi-Lagrangian Particle Level Set Method.* Comput. Struct, 2005. 83(6-7): p. 479-490.**
37. **Sussman, M., K.M. Smith, M.Y. Hussaini, M. Ohta, and R. Zhi-Wei, *A Sharp Interface Method for Incompressible Two-Phase Flows.* Journal of Computational Physics, 2007. 221(2): p. 469-505.**
38. **Gilmanov, A. and F. Sotiropoulos, *A Hybrid Cartesian/Immersed Boundary Method for Simulating Flows with 3d, Geometrically Complex, Moving Bodies.* J. Computational Phys., 2005. 207(2): p. 457-492.**
39. **Wasekar, V.M. and R.M. Manglik, *Short-Time-Transient Surfactant Dynamics and Marangoni Convection around Boiling Nuclei.* Journal of Heat Transfer, 2003. 125(5): p. 858-866.**
40. **Perot, B. and R. Nallapati, *A Moving Unstructured Staggered Mesh Method for the Simulation of Incompressible Free-Surface Flows.* Journal of Computational Physics, 2003. 184(1): p. 192-214.**
41. **Udaykumar, H.S., R. Mittal, P. Rampunggoon, and A. Khanna, *A Sharp Interface Cartesian Grid Method for Simulating Flows with Complex Moving Boundaries.* J. Computational Phys., 2001. 174(1): p. 345-380.**
42. **Sachdev, J.S. and C.P.T. Groth, *A Mesh Adjustment Scheme for Embedded Boundaries.* Commun. Comput. Phys., 2007. 2: p. 1095-1124.**
43. **Tryggvason, G., B. Bunner, A. Esmaeeli, N. Al-Rawahi, W. Tauber, J. Han, Y.J. Jan, D. Juric, and S. Nas, *A Front-Tracking Method for the Computations of Multiphase Flow.* Journal of Computational Physics, 2001. 169(2): p. 708-759.**
44. **Uzgoren, E., J. Sim, and W. Shyy. *Computations of Multiphase Fluid Flows Using Marker-Based Adaptive, Multilevel Cartesian Grid Method*. in *45th AIAA Aerospace Sciences Meeting and Exhibit*. 2007. Reno, NV.**
45. **Uzgoren, E., R. Singh, J. Sim, and W. Shyy. *A Unified Adaptive Cartesian Grid Method for Solid-Multiphase Fluid Dynamics with Moving Boundaries*. in *18th AIAA Computational Fluid Dynamics Conference*. 2007. Miami, FL.**

46. **Singh, R. and W. Shyy, *Three-Dimensional Adaptive Cartesian Grid Method with Conservative Interface Restructuring and Reconstruction.* Journal of Computational Physics, 2007. 224(1): p. 150-167.**
47. **Hassan, E.A., E. Uzgoren, H. Fujioka, J. Grotberg, and W. Shyy, *Adaptive Lagrangian-Eulerian Computation of Propagation and Rupture of a Liquid Plug in a Tube.* International Journal for Numerical Methods in Fluids, 2011. 67(11): p. 1373–1392.**
48. **Uzgoren, E., J. Sim, and W. Shyy, *Marker-Based, 3-D Adaptive Cartesian Grid Method for Multiphase Flow around Irregular Geometries.* Commun. Comput. Phys., 2009. 5(1): p. 1-41.**
49. **Sim, J., C.-K. Kuan, and W. Shyy, *3-D Multiscale Adaptive Eulerrian-Lagrangian Method for Multiphase Flows with Phase Change*, in *48th AIAA Aerospace Sciences Meeting* 2010: Orlando, Florida.**
50. **VanLerberghe, W.M., J.G. Santiago, J.C. Dutton, and R.P. Lucht, *Mixing of a Sonic Transverse Jet Injected into Supersonic Crossflow.* AIAA Journal, 2000. 38(3): p. 470-479.**
51. **Gruber, M.R., A.S. Nejad, T.H. Chen, and J.C. Dutton, *Large Structure Convection Velocity Measurements in Compressible Transverse Injection Flowfields.* Experiments in Fluids, 1997. 22 (1997): p. 397-407.**
52. **Peterson, D. and G. Candler, *Simulations of Mixing for Normal and Low-Angled Injection into a Supersonic Crossflow* AIAA Journal, 2011. 49(12): p. 2792-2804.**
53. **Fujioka, H., S. Takayama, and J.B. Grotberg, *Unsteady Propagation of a Liquid Plug in Liquid Lined Tube.* Physics of Fluids, 2008. 20(062104).**
54. **Castro, J., *Scramjet*, in *AccessScience*. 2008, McGraw-Hill Companies.**
55. **Hallion, R.P., *The Hypersonic Revolution, Volume Ii: From Max Valier to Project Prime*, in *Aeronatical System Center, Air Force Material Command, Wright Patterson Air Force Base*. 1995.**
56. **Fry, R.S., *A Century of Ramjet Propuslion Technology Evolution.* Journal of propulsion and power, 2004. 20(1): p. 27-58.**
57. **NASA, *How Scramjets Work*. 2006, NASA Langley Research Center.**
58. **Andreadis, D. *Scramjets Integrate Air and Space*. the Industrial Physicist: Technology 2004 [cited; Available from: http://www.aip.org/tip/INPHFA/vol-10/iss-4/p24.html.**
59. **Hieser, W.H., D.T. Pratt, D.H. Daley, and U.B. Metha, *Hypersonic Airbreathing Propulsion.* AIAA Educational Series, 1994.**
60. **Portz, R. and C. Segal, *Mixing in High-Speed Flows with Thick Boundary Layers*, in *40th AIAA/ASME/SAE/ASEE Joint Propulsion Conference and Exhibit*. 2004: Fort lauderdale, FL.**
61. **Andrepoulos, J. and W. Rodi, *Experimental Investigations of Jets in a Crossflow.* Journal of Fluid Mechanics, 1984. 138: p. 93-127.**
62. **McDaniel, J.C. and J. Graves., *Laser-Induced Fluorescence Visualization of Transverse Gaseous Injection in a Nonreacting Supersonic Combustor.* Journal of Propulsion and Power, 1988. 4: p. 591-597.**

63. McMillin, B.K., J.L. Palmer, and R.K. Hanson, *Temporally Resolved, Two-Line Fluorescence Imaging of No Temperature in a Transverse Jet in a Supersonic Cross Flow.* Applied Optics, 1993. 32(36): p. 7532-7545.
64. Ben-Yakar, A., M.G. Mungal, and R.K. Hanson, *Time Evolution and Mixing Characteristics of Hydrogen and Ethylene Transverse Jets in Supersonic Crossflows.* Physics of Fluids, Feb,2006. 18(2): p. 026101.
65. Lin, K.-C., M. Ryan, C. Carter, M. Gruber, and C. Raffoul, *Scalability of Ethylene Gaseous Jets for Fueling High-Speed Air-Breathing Combustors*, in *47th AIAA Aerospace Sciences Meeting and Exhibit*. 2009: Orlando, Florida.
66. Schetz, J.A., R.A. Weinraub, and R.E. Mahaffey, *Supersonic Transverse Injection into a Supersonic Stream.* AIAA Journal, 1968. 6(5): p. 933-934.
67. Schetz, J.A. and F.S. Billig, *Penetration of Gaseous Jets Injected into Supersonic Stream.* journal of spacecraft 1966. 3(11): p. 1658-1665.
68. Billig, F.S., R.C. Orth, and M. Lasky, *A Unified Analysis of Gaseous Jet Penetration.* AIAA Journal, 1971. 9(6): p. 1048-1058.
69. Billig, F.S. and J.Schetz, *Analysis of Penetration and Mixing of Gas Jets in Supersonic Cross Flow*, in *AIAA 4th International Aerospace Planes conference*. 1992: Orlando, FL.
70. Campbell, J. and J.A. Schetz, *Analysis of Injection of a Heated Turbulent Jet into a Cross Flow.* 1973. NASA TRR-413.
71. Rogers, R.C., *Mixing of Hydrogen Injected from Multiple Injectors Normal to a Supersonic Airstream.* 1971. NASA TN D-6476.
72. Hersch, M., L.A. Povinelli, and F.P. Povinelli, *A Schlieren Technique for Measuring Jet Penetration into Supersonic Stream.* Journal of spacecraft, 1970. 7(6): p. 755-756.
73. Palekar, A., C.R. Truman, and P. Vorobieff, *Prediction of Transverse Injection of a Sonic Jet in a Supersonic Crossflow*, in *36th AIAA Plasmadynamics on Lasers Conference*. 2005: Toronto, Ontario Canada.
74. Yuan, L.L., R.L. Street, and J.H. Ferziger, *Large-Eddy Simulations of a Round Jet in Crossflow.* Journal of Fluid Mechanics, 1999. 379: p. 71-104.
75. Keislter, P.G., *A Variable Turbulent Prandtl and Schmidt Number Model Study for Scramjet Applications*, in *Mechanical and Aerospace Engineering*. 2009, North Carolina State University: Raleigh, North Carolina.
76. Jones, W.P. and B.E. Launder, *The Prediction of Laminarization with Atwo-Equation Model of Turbulence.* International Journal of Heat and Mass Transfer, 1972. 15.
77. Menter, F.R., *Zonal Two Equations K-W Turbulence Models for Aerodynamic Flows.* AIAA, 1993. 93(2909).
78. Wilcox, D.C., *Simulation of Transition with a Two-Equation Turbulence Model.* AIAA Journal, 1994. 32: p. 247-254.
79. Spalart, P.R. and S.R. Allmaras, *A One-Equation Turbulence Model for Aerodynamic Flows.* AIAA Paper, 1992. 92: p. 0439.
80. Nikitin, N.V., F. Nicoud, B. Wasistho, K.D. Squires, and P.R. Spalart, *An Approach to Wall Modeling in Large-Eddy Simulations.* Physics of Fluids, 2000. 12(7): p. 1629-1632.

81. **Mockett, C. and F. Thiele.** ***Overview of Detached-Eddy Simulation for External and Internal Turbulent Flow Applications*****. in** ***Fifth International Conference on Fluid Mechanics*****. 2007. Shanghai, China: Tsinghua University Press & Springer.**

82. **Shur, M.L., P.R. Spalart, M.K. Strelets, and A.K. Travin,** ***A Hybrid Rans-Les Approach with Delayed-Des and Wall Modelled Les Capabilities.*** **International Journal of Heat and Fluid Flow, 2008. 29(6): p. 1638-1649.**

83. **Johansen, S.T., J. Wu, and W. Shyy,** ***Filter-Based Unsteady Rans Computations.*** **International Journal of Heat and Fluid Flow, 2004. 25: p. 10-21.**

84. **Nichols, R.H. and C.C. Nelson,** ***Application of Hybrid Rans/Les Turbulence Models,*** **in** ***41st Aerospace Science Meeting and Exhibit*****. 2003: Reno , Nevada.**

85. **Reynolds, A.J.,** ***The Prediction of Turbulent Prandtl and Schmidt Numbers.*** **Int. J. Heat and Mass Transfer, 1975. 18: p. 1055-1069.**

86. **Negano, Y., M. Kondoh, and M.Shimada,** ***Multiple Time-Scale Turbulence Model for Wall and Homogenous Shear Flows Based on Direct Numerical Simulation.*** **Int. J. Heat Fluid Flow, 1997. 18(4): p. 347-359.**

87. **Sommer, T.P., R.M.C. So, and H.S. Zhang,** ***Near-Wall Variable Prandtl-Number Turbulence Model for Compressible Flows.*** **AIAA Journal, 1993. 31(1): p. 27-35.**

88. **Guo, Y., G. He, A.T. Hsu, A. Brankovic, S. Syed, and N.S. Liu,** ***The Development of a Variable Schmidt Number Model for Jet-in-Crossflow Using Genetic Algorithms.*** **AIAA Paper, 1999(99-0671).**

89. **Kenzakowski, D.C., J. Papp, and S.M. Dash,** ***Evaluation of Advanced Turbulence Models and Variable Prandtl/Schmidt Number Methodology for Propulsive Flows.*** **AIAA Paper, 2000(2000-0885).**

90. **Brinckman, K.W., D.C. Kenzakowsi, and S.M. Dash,** ***Progress in Practical Scalar Fluctiation Modeling for High Speed Aeropropulsive Flows.*** **AIAA Paper, 2005(2005-0508).**

91. **Segal, C. and W. Shyy,** ***Energetic Fuels for Combustion Applications.*** **J. Energy Resources Technology, 1996. 118: p. 180-186.**

92. **Marchand, A.P., H.G. Kruger, T.D. Power, and C. Segal,** ***Synthesis and Properties of Polycyclic Cage Hydrocarbons (High Energy Density Fuels) and of Polycyclic Cage Organonitro Compounds (Insensitive High-Energy Explosives).*** **Kim Ind., 2002. 51(51-67).**

93. **Yang, V. and V.E. Zarko,** ***Solid Propellant Rocket Motor Interior Ballastics and Combustion of Energetic Materials.*** **Journal of propulsion and power, 1995. 11(4).**

94. **Schetz, J.A.,** ***Injection and Mixing in Turbulent Flows.*** **Progress in Aeronautics and Astronautics, 1980. 68.**

95. **Chigier, N. and R.D. Reitz,** ***Regimes of Break-up and Breakup Mechanisms (Physical Aspects).*** **Progress in Aeronautics and Astronautics, 1996. 166(AIAA): p. 109-135.**

96. **Kush, E.A. and J.A. Schetz,** ***Liquid Jet Injection into Supersonic Crossflow.*** **AIAA Journal, 1973. 11: p. 1223-1224.**

97. **Fuller, R.P., P.K. Wu, K.A. Kirkendall, and A.S. Nejad, *Effect of Injection Angle on Atomization of Liquid Jets in Transverse Flow.* Journal of propulsion and power, 2000. 38: p. 64-72.**

98. **Huh, D., H. Fujioka, Y. Tung, N. Futai, R. Paine, J. Grotberg, and S. Takayama, *Acoustically Detectable Cellular-Level Lung Injury Induced by Fluid Mechanical Stresses in Microfluidic Airway Systems.* Proceedings of the National Academy of Sciences, 2007. 104(48): p. 18886.**

99. **Tavana, H., D. Huh, J.B. Grotberg, and S. Takayama, *Microfluidics, Lung Surfactant, and Respiratory Disorders.* Labmedicine, 2009. 40(4): p. 203-210.**

100. **Bilek, A.M., K.C. Dee, and D.P. Gaver, *Mechanisms of Surface-Tension-Induced Epithelial Cell Damage in a Model of Pulmonary Airway Opening.* Journal of Applied Physiology, 2003. 94(2): p. 770-783.**

101. **Kay, S.S., A.M. Bilek, K.C. Dee, and D.P. Gaver, *Pressure Gradient, Not Exposure Duration, Determines the Extent of Epithelial Cell Damage in a Model of Pulmonary Airway Reopening.* Journal of Applied Physiology, 2004. 97(1): p. 269-276.**

102. **Zheng Y, Fujioka H, Bian S, Torisawa Y, Huh D, Takayama S, and G. JB, *Liquid Plug Propagation in Flexible Microchannels: A Small Airway Model.* Physics of Fluids, 2009. 21(7).**

103. **Howell, P.D., S.L. Waters, and J.B. Grotberg, *The Propagation of a Liquid Bolus Along a Liquid-Lined Flexible Tube.* Journal of Fluid Mechanics, 2000. 406: p. 309-335.**

104. **Waters, S.L. and J.B. Grotberg, *The Propagation of a Liquid Bolus Along a Liquid-Lined Flexible Tube.* Physics of Fluids, 2002. 14(2): p. 471-480.**

105. **Fujioka, H. and J.B. Grotberg, *Steady Propagation of a Liquid Plug in a Two-Dimensional Channel.* Journal of Biomechanical Engineering, 2004. 126: p. 567.**

106. **Fujioka, H. and J. Grotberg, *The Steady Propagation of a Surfactant-Laden Liquid Plug in a Two-Dimensional Channel.* Physics of Fluids, 2005. 17(8): p. -.**

107. **Suresh, V.A. and J.B. Grotberg, *The Effect of Gravity on Liquid Plug Propagation in a Two-Dimensional Channel.* Physics of Fluids, 2005. 17.**

108. **Zheng, Y., H. Fujioka, J.C. Grotberg, and J.B. Grotberg, *Effects of Inertia and Gravity on Liquid Plug Splitting at a Bifurcation.* Journal of Biomechanical Engineering, 2006. 128: p. 707.**

109. **Campana, D.M., S. Ubal, M.D. Giavdoni, and F.A. Saita, *Accurate Representation of Surface Tension Using Level-Contour Reconstruction Method.* Journal of Computational Physics, 2007. 203(2): p. 493-516.**

110. **Erneux, T. and S.H. Davis, *Nonlinear Rupture of Free Films.* Physics of Fluids A: Fluid Dynamics, 1993. 5: p. 1117.**

111. **Scardovelli, R. and S. Zaleski, *Direct Numerical Simulation of Free-Surface and Interfacial Flow.* Annual Review of Fluid Mechanics, 1999. 31(1): p. 567-603.**

112. **Francois, M. and W. Shyy, *Micro-Scale Drop Dynamics for Heat Transfer Enhancement.* Progress in Aerospace Sciences, 2002. 38(4): p. 275-304.**

113. Peskin, C.S., *The Immersed Boundary Method.* Acta Numerica, 2003. 11: p. 479-517.
114. Francois, M. and W. Shyy, *Computations of Drop Dynamics with the Immersed Boundary Method, Part 1: Numerical Algoritm and Buoyancy-Induced Effect.* Numerical Heat Transfer: Part B: Fundamentals, 2003. 44(2): p. 101-118.
115. Ye, T., R. Mittal, H.S. Udaykumar, and W. Shyy, *An Accurate Cartesian Grid Method for Viscous Incompressible Flows with Complex Immersed Boundaries.* Journal of Computational Physics, 1999. 156(2): p. 209-240.
116. Leveque, R.J. and Z. Li, *The Immersed Interface Method for Elliptic Equations with Discontinuous Coefficients and Singular Sources.* SIAM Journal on Numerical Analysis, 1994. 31(4): p. 1019-1044.
117. Li, Z. and M.C. Lai, *The Immersed Interface Method for the Navier-Stokes Equations with Singular Forces.* Journal of Computational Physics, 2001. 171(2): p. 822-842.
118. Ye, T., W. Shyy, and J.C. Chung, *A Fixed-Grid, Sharp-Interface Method for Bubble Dynamics and Phase Change.* Journal of Computational Physics, 2001. 174: p. 781-815.
119. Menter, F.R., *Two-Equation Eddy-Viscosity Turbulence Models for Engineering Applications.* AIAA Journal, 1994. 32(8): p. 1598–1605.
120. Poinsot, T. and D. Veynante, *Theoritical and Numerical Combustion*. 2001: Edwards.
121. Hirschfelder, J.O., R.J. Buehler, H.A. McGee, and J.R. Sutton, *Generalized Equation of State for Gases and Liquids.* Ind Eng Chem, 1958. 50: p. 375-385.
122. Hirschfelder, J.O., R.J. Buehler, H.A. McGee, and J.R. Sutton, *Correction:Generalized Equation of State for Gases and Liquids.* Ind Eng Chem, 1962. 1: p. 224.
123. Chase, M.W.J., *Nist-Janaf Thermodynamical Tables*. 4 ed.
124. Kee, R.J., F.M. Rupley, and J.A. Miller, *Chemkin Ii: A Fortran Chemical Kinetic Package for Modeling Well-Stirred Reactors.* Sandia National Laboratories, 1989. SAND 89-8009B.
125. Pope, S.B., *Turbulent Flows*. 2000: Cambridge University Press.
126. Favre, A., *Statistical Equations of Turbulent Gases*, ed. I. SIAM. 1969: Problems of Hydrodynamics and Continuum Mechanics.
127. Wilcox, D.C., *Turbulence Modeling for Cfd*. 2 ed. 1998: DCW Industries.
128. kuo, K.K., *Principles of Turbulent Combustion*. 2 ed. 2005: Wiley.
129. Spalart, P.R., *Strategies for Turbulence Modelling and Simulations.* International Journal of Heat and Fluid, 2000. 21: p. 252-263.
130. Launder, B.E. and D.B. Spalding, *The Numerical Computation of Turbulent Flows.* Computer Methods in Applied Mechanics and Engineering, 1974. 3(2): p. 269-289.
131. Deadorff, J.W., *A Numerical Study of Three-Dimensional Turbulent Channel Flow at Large Reynolds Numbers.* J. Fluid Mech, 1970. 41: p. 453-480.
132. Boles, J.A., *Hybrid Large-Eddy Simulation/Reynolds-Averaged Navier-Stokes Methods and Predictions for Various High-Speed Flows*, in *Aerospace Engineering*. 2009, North Carolina State University: Raleigh, NC.

133. Boles, J.A. and J.R. Edwards, *Hybrid Les/Rans Simulation of Transverse Sonic Injection into a Mach 2 Flow*, in *46th AIAA Aerospace Sciences Meeting and Exhibit*. 2008: Reno, Nevada.

134. Wilcox, D.C., *Re-Assesment of the Scale-Determining Equation for Advanced Turbulence Models.* AIAA Journal, 1988. 26: p. 1414-1421.

135. Menter, F.R., *Influence of Freestream Values on K −Ω Turbulence Model Predictions.* AIAA Journal, 1992. 30(6): p. 1992.

136. Launder, B.E., G.J. Reece, and W. Rodi, *Progress in the Development of a Reynolds-Stress Turbulence Closure.* Journal of Fluid Mechanics Digital Archive, 2006.

137. Edwards, J.R., A.M. Pinto, K.-C.Lin, and T.A. Jackson. *Simulation of Injection of Supercritical Methane / Ethylene Mixtures into Nitrogen*. in *33rd AIAA Fluid Dynamics Conference and Exhibit*. 2003. Orlando, Florida.

138. Strelets, M., *Detached Eddy Simulation of Massively Separated Flows*, in *39th AIAA Aerospace Sciences Meeting and Exhibit*. 2001, AIAA: Reno, NV.

139. Basu, D., A. Hamed, and K. Das, *Des and Hybrid Rans/Les Models for Unsteady Seperated Turbulent Flow Predictions*, in *43rd AIAA Aerospace Sciences Meeting & Exhibit* 2005: Reno, Nevada.

140. Tseng, C.-C. and W. Shyy, *Modeling for Isothermal and Cryogenic Cavitation.* International Journal of Heat and Mass Transfer, 2010. 5: p. 513-525.

141. Comte-Bellot, G. and S. Corsin, *Simple Eulerian Time Correlation of Full and Narrow-Band Velocity Signals in Grid-Generated 'Isotropic' Turbulence.* Journal of Fluid Mechanics, 1971. 48: p. 273-337.

142. Garnier, E., M. Mossi, P. Sagaut, P. Comte, and M. Deville, *On the Use of Shock-Capturing Schemes for Large-Eddy Simulation.* Journal of Computational Physics, 1999. 153(2): p. 273-311.

143. Mossi, M. and P. Sagaut, *Numerical Investigation of Fully Developed Channel Flow Using Shock-Capturing Schemes.* Computers & Fluids, 2003. 32(2): p. 249-274.

144. Luke, E.A. and P. Cinnella, *Numerical Simulations of Mixtures of Fluids Using Upwind Algorithms.* Computers & Fluids, 2007. 10: p. 1547-1566.

145. Luke, E.A. and T. George, *Loci: A Rule-Based Framework for Parallel Multidisciplinary Simulation Synthesis.* Journal of Functional Programming, 2005. 15(3): p. 477-502.

146. Blazek, J., *Computational Fluid Dynamics: Principles and Applications*. 2001, The Netherlands: Elsevier Ltd.

147. Venkatakrishnan, V., *On the Accuracy of Limiters and Convergence to Steady State Solutions.* AIAA Paper, 1993(93-0880).

148. Walters, R.W., P. Cinnella, D.C. Slack, and D. Halt, *Characteristic-Based Algorithms for Flows in Thermodynamic Nonequilibrium.* AIAA Journal, 1992. 30: p. 1304-1313.

149. Gruber, M.R. and A.S. Nejad, *New Supersonic Combustion Research Facility.* Journal of propulsion and power, 1995. 11(5): p. 1080-1083.

150. Balay, S., W.D. Gropp, L.C. McInnes, and B.F. Smith, *Efficient Management of Parallelism in Object Oriented Numerical Software Libraries*, ed. E. Arge, A.M. Bruaset, and H.P. Langtange. 1997: Birkh user Press.

151. Roe, P.L., *Approximate Riemann Solvers Parameter Vectors and Difference Schemes.* Journal of Computational Physics, 1981. 43: p. 357-372.

152. Boris, J.P., *On Large Eddy Simulation Using Subgrid Turbulence Models.* in Whither Turbulence? Turbulence At The Crossroads, Lecture Notes in Physics, 1990. 357: p. 344-353.

153. Peterson, D.M., P.K. Subbareddy, and G.V. Candler, *Assessment of Synthetic Inflow Generation for Simulating Injection into Supersonic Crossflow*, in *14th AIAA/AHI Space Planes and Hypersonic Systems and Technologies Conference*. 2006.

154. Grinstein, F.F., L.G. Margolin, and W.J. Rider, *Implicit Large Eddy Simulation: Computing Turbulent Fluid Dynamics*. 2007: Cambridge University Press. 546.

155. Raymond, L. and M.M. Jr, *In Defense of the Stethoscope.* Respiratory Care, 2008. 53(3).

156. Pasterkamp, H., S.S. Kraman, and G.R. Wodicka, *Respiratory Sounds. Advances Beyond the Stethoscope.* Am J Respir Crit Care Med, 1997. 156: p. 974–987.

157. Munakata, M., Y. Homma, M. Matsuzaki, H. Ogasawara, K. Tanimura, H. Kusaka, and Y. Kawakami, *Production Mechanism of Crackles in Excised Normal Canine Lungs.* The American Physiological Society, 1986. 0161(7567/86).

158. Uzgoren, E., R. Singh, J. Sim, and W. Shyy, *Computational Modeling for Multiphase Flows with Spacecraft Application.* Progress in Aerospace Sciences, 2007. 43: p. 138-192.

159. Dumbser, M., *Arbitrary High Order Pnpm Schemes on Unstructured Meshes for the Compressible Navier–Stokes Equations.* Computers and Fluids, 2010. 39(1): p. 60-70.

160. Zhu, J. and J. Qiu, *Local Dg Method Using Weno Type Limiters for Convection Diffusion Problems.* journal of Computational Physics, 2011. 230(11): p. 4353-4375.

161. Pirozzoli, S. and F. Grasso, *Direct Numerical Simulation of Impinging Shock Wave/Turbulent Boundary Layer Interaction at M = 2.25.* Physics of Fluids, 2006. 18(6): p. 065113.

162. Herrin, J.L. and J.C. Dutton, *Supersonic Base Flow Experiments in the near Wake of a Cylindrical Afterbody.* AIAA Journal, 1994. 32: p. 77-83.

163. Sozer, E., E. Hassan, S. Yun, S. Thakur, J. Wright, M. Ihme, and W. Shyy. *Turbulence-Chemistry Interaction and Heat Transfer Modeling of H2/O2 Gaseous Injector Flows*. in *48th AIAA Aerospace Sciences Meeting Including the New Horizon Forum and Aerospace Exposition*. 2010. Orlando, Florida.

164. Veluri, S.P. and C.J. Roy, *Comprehensive Code Verification for an Unstructured Finite Volume Cfd Code*, in *48th AIAA Aerospace Sciences Meeting*. 2010: Orlando, Florida.

165. Kuan, C., J. Sim, and W. Shyy, *Parallel, Adaptive Grid Computing of Multiphase Flows in Spacecraft Fuel Tanks* in *50th AIAA Aerospace Sciences Meeting including the New Horizons Forum and Aerospace Exposition*. 2012: Nashville, Tennessee.